Preparation and characterization of powders and pulsed laser deposited thin films of rare-earths doped oxyorthosilicates

By

Ogugua Simon Nnalue

(M.Sc. Physics)

This thesis is submitted in fulfillment of the requirements for the degree

Doctor of Philosophy

in the

Faculty of Natural and Agricultural Sciences

Department of Physics

Bloemfontein campus

at the

UNIVERSITY OF THE FREE STATE

Promoter: Prof. O.M. Ntwaeaborwa

Co – Promoter: Prof. H.C. Swart

November 2017

Quote

A man's gift makes room for him, and brings him before great men.

– Proverbs 18:16–

The lazy man says, "There is a lion outside! I shall be slain in the streets!"

–Proverbs 22:13–

Dedication

Now all glory to God who is able, through His mighty power at work within us, to accomplish infinitely more than we might ask or think.

–Ephesians 3:20–

Declaration

I, Ogugua Simon Nnalue, Student No: 2010062897, affirm solemnly that the content of this thesis is mine and that it has not been submitted previously for any type of degree or qualification of any kind in this or any other University.

–Ogugua Simon Nnalue–

Sign……. at……UFS…….

On the … 6th ……. day of …… 11 …… 2017

Acknowledgments

The African Laser Center (ALC), Department of Science and Technology, the competitive programme for rated researchers (CPRR) (Grantno.CPR20110724000021870) of the National Research Foundation (NRF)-South Africa, and the rental pool programme of the National Laser Centre (NLC) (Grantno.NLC-LREGM) sponsored this work. This work is based on the research supported by the South African Research Chairs Initiative of the Department of Science and Technology and the National Research Foundation of South Africa (84415).

I would also like to express my sincere gratitude to some individual of which without this dissertation could have not been possible:

- ♥ *Prof. Odireleng M. Ntwaeaborwa* (promoter) for giving me the opportunity into the world of research and for addressing my shortcomings politely.
- ♥ *Prof. Hendrik C. Swart* (Co-promoter) for his invaluable advices and contributions to this work.
- ♥ *Dr. Samy K.K. Shaat* for his invaluable contributions to the success of this work.
- ♥ *Miss P.P. Mokoena* for assisting with FE-SEM measurements, *Prof. E. Coetsee-Hugo* for assisting me with XPS measurements, *Dr. M. Duvenhage* for assisting with ToF-SIMS measurements and Prof. R.E. Kroon for the PL measurements.
- ♥ I am grateful to the entire staff and fellow students of physics department for their invaluable contributions.
- ♥ Above all, thanks to Almighty *God* who in His infinite mercy gave me the strength, knowledge and willpower to finish this work. I am also grateful to *Dr. Alexander Ogugua* for his encouragement and supports, *Mrs. Sandra Ogugua* for her prayers and supports and the entire *Ogugua* family for their prayers.

Abstract

Today, phosphor materials have found many technological applications such as in electronic information display, advertising, solid-state lighting, solar cells, theft prevention, medicine, data storage, quality control, optical amplifiers, optical laser, scintillation, etc.

Crystal field determines the chemical nature of the optical center of a phosphor material. Engineering the crystal field of the host matrix can lead to shifting of the wavelength ranges of optical transitions, increasing the rates of radiative transitions and minimizing loss by nonradiative decay and excited state absorption. These objectives can be accomplished by manipulating the unit cell containing the optical center. The unit cell can be manipulated by changing its chemical composition. By varying the molar ratio of La, Gd and Y in mixed $La_{2-x}Gd_xSiO_5$ or $La_{2-x}Y_xSiO_5$ hosts, the unit cells of the host can be manipulated and hence tuning the crystal field strength. These, to large extent, can influence the luminescence properties of Pr^{3+} and Dy^{3+} in these host matrices and can lead to the generation of tunable colour and white light for LED application.

Phosphors are commercially available in powder form. However, for practical purposes, they must be in thin film forms. Hence, we have prepared a series of powder and thin film phosphors. The powder phosphors were prepared using solution combustion synthesis (SCS), before they were deposited on Si(111) substrates using the pulsed laser deposition (PLD) technique. In our previous report [1], we prepared $La_{2-x}Gd_xSiO_5:Dy^{3+}$ (x = 0, 0.5, 1, 1.5 and 2) powder phosphors in which the International Commission of Illumination or CIE colour coordinates calculated from the photoluminescence data showed tunable colour, from blue to yellow through white. A near white emission was obtained from the sample when x = 0.5 (i.e. $La_{1.5}Gd_{0.5}SiO_5:Dy^{3+}$), therefore, we chose to prepare the thin films using this sample. The thin films were deposited in different atmospheres (vacuum, argon and oxygen), different deposition time and different deposition temperatures. Effect of post-annealing on the properties of the films were studied.

We also prepared five sets of $La_{2-x}Y_xSiO_5:Pr^{3+}$ (x = 0, 0.5, 1, 1.5 and 2) powder phosphors. Here we investigated how the molar ratio of the hosts (La_2SiO_5 and Y_2SiO_5) affects the

photoluminescence properties of Pr^{3+}. The luminescence of phosphors based on Pr^{3+} doped matrices showed a strong dependence on the crystal field of the host. When incorporated into hosts with strong crystal field (e.g. La_2SiO_5 or Y_2SiO_5), Pr^{3+} gave green and red emission from $^1P_0$ and $^1D_2$ levels of the 4f state respectively. The intensity of these emissions and the band gaps of the phosphors varied with the molar ratio of La and Y. When Pr^{3+} was co-doped with Dy^{3+} in $La_{2-x}Y_xSiO_5:Pr^{3+}$ (x = 0, 0.5, 1, 1.5 and 2) hosts, it was observed that energy transfer from Pr^{3+} to Dy^{3+} was dependent on the molar ratio of La to Y and post-preparation annealing atmospheres (Ar-H_2 and air). We also demonstrated that the emitted colour from $La_{2-x}Y_xSiO_5:Pr^{3+}$ (x = 0, 0.5, 1, 1.5 and 2) could be tuned by exciting the phosphors at different wavelengths. Finally, we used integrating sphere method to determine the quantum yield of some of the phosphors.

The structure of the phosphors was analyzed using X-ray diffractometer (XRD). The morphologies and chemical composition were analyzed using field emission scanning electron microscopy (FE-SEM) and energy dispersive X-ray spectroscopy (EDS) respectively. Furthermore, X-ray photoelectron spectroscopy (XPS) was used to analyze the chemical and electronic states and the elemental composition of the phosphors. The distribution of molecular and atomic ionic species on the surface region of the phosphors was analyzed using time-of-flight secondary ion mass spectroscopy (ToF-SIMS). The diffuse reflectance, photoluminescence and cathodoluminescence of the phosphors were also measured. Additional characterization techniques such as, atomic force microscopy (AFM) and The Rutherford back scattering (RBS) were used to analyze the topography and the composition and thickness of the thin film samples respectively.

Reference

[1] S.N. Ogugua, H.C. Swart, O.M. Ntwaeaborwa, Tunable multicolour emission from dysprosium-doped mixed rare-earths oxyorthosilicate nanophosphors for application in ultraviolet-pumped multicolour and white light emitting diodes, M.Sc. Thesis, University of the Free State, South Africa (2015) p. 100-123.

Keywords

Combustion synthesis, pulsed laser deposition, powder Phosphors, thin films, X-ray Diffraction, Photoluminescence, Microscopy, Spectroscopy

List of Acronyms

Techniques

XRD: X-ray Diffraction

FE-SEM: Field Emission Scanning Electron Microscope

EDS: Energy Dispersive X-ray Spectrometer

XPS: X-ray Photoelectron Spectroscopy

AFM: Atomic Force Microscope

RBS: Rutherford Backscattering Spectrometry

ToF-SIMS: Time of Flight Secondary Ion Mass Spectroscopy

UV-Vis: Ultraviolet-Visible Spectroscopy

PL: Photoluminescence

Chemical elements and compounds

Dy: Dysprosium

Pr: Praseodymium

La: Lanthanum

Gd: Gadolinium

Y: Yttrium

Si: Silicon

La_2SiO_5: Lanthanum oxyorthosilicate

Gd_2SiO_5: Gadolinium oxyorthosilicate

Y_2SiO_5: Yttrium oxyorthosilicate

$LaGdSiO_5$: Lanthanum gadolinium oxyorthosilicate

$LaYSiO_5$: Lanthanum yttrium oxyorthosilicate

$GdYSiO_5$: Gadolinium yttrium oxyorthosilicate

Table of Contents

CH. 1 Introduction

CH. 2 Materials and sample preparation techniques

CH. 3

Characterization techniques

CH. 5 **The influence of post-deposition annealing on the structure, morphology and luminescence properties of pulsed laser deposited $La_{0.5}Gd_{1.5}SiO_5$ doped Dy^{3+} thin films**

CH. 6 **The dynamics of the photoluminescence of Pr^{3+} in mixed lanthanum yttrium oxyorthosilicate hosts**

CH. 7 **Influence of the ratio of rare earth oxyorthosilicate R_2SiO_5 (R = La, Y) hosts on the structure and optical properties of co-doped Pr^{3+} /Dy^{3+} phosphors.**

CH. 8 **The influence of post-annealing atmospheres on the optical properties and energy transfer between Pr^{3+} and Dy^{3+} in mixed lanthanum-yttrium oxyorthosilicate hosts**

CH. 9 Determination of quantum yield of phosphors using integrating sphere

CH. 10 Summary, future work, presentations and list of publications

CH. 1 Introduction

1.1. Phosphors

Phosphors materials, known for their ability to absorb and emit light (luminescence), are mainly inorganic materials comprising of host lattice, which are purposely doped with impurity known as dopants (activators). The host houses the dopants. In some case, both absorption and emission of light in phosphors are observe from the host matrices and the activator [1]. However, most of the host materials are inert but are transparent to the excitation radiation. The activators are mainly 3d or 4f electron metals [2]. The concentration of the activator is mainly low because, at higher concentrations, it causes decrease in the luminescence efficiency of the phosphor. This phenomenon is known as concentration quenching [1]. In some cases, when the activator ion shows weak emission, a second type of impurity ion (co-activator or co-dopant) called a sensitizer is added, which absorbs the energy and subsequently transfer it to the activator resulting in improved luminescence [1, 2]. The emission colour can be varied by choosing the appropriate activator since each activator has a characteristic colour emission, but the host material may not be changed [1]. Phosphors can be in either in the powder or thin film form [3].

1.1.1. Luminescence phenomena

During luminescence, a material absorbs an external radiation and an electron from an atom in the material is promoted from the valence band (lower energy level) to the conduction band (higher energy level) [4]. This is complimented with a release of energy in the form of light by the excited electron via the *luminescence center* and returning to the valence band (ground state) (Fig. 1.1) [5]. During luminescence, the maximum of the absorption (excitation) spectrum is usually observe at a shorter wavelength (higher energy); while the maximum of the emission spectrum is observed at a higher wavelength (lower energy). The difference between the maximum of the absorption and the emission spectra is known as *Stokes shift* [6].

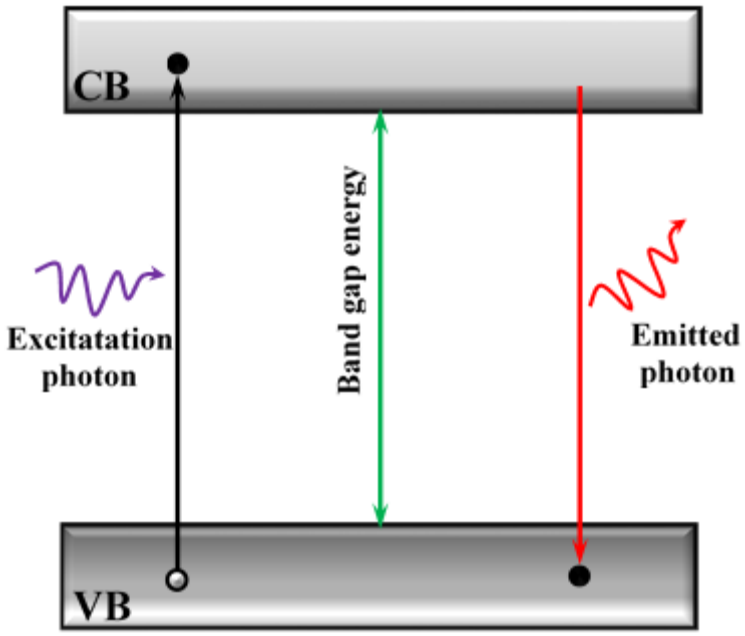

Fig. 1.1: Simplified schematic of absorption and emission process from an atom in a material.

1.1.2. Luminescence center

Luminescence center is a point-lattice defect that is responsible for luminescence in a transparent crystal. In crystalline phosphor, luminescence centers are lattice imperfections that exhibit luminescence in the material [7]. These centers may originate from intrinsic crystal defects such as interstitial atoms and ions or from intentionally incorporated activators. Interstitial atoms or ions originate in a crystal when an atom or ion is displaced from their original position to a new position and it form a point defect, leaving a vacancy defect behind [8]. Luminescence centers that originate from the crystal defects are known as host-crystal center (intrinsic centers) [7, 9]; while those that originate from the activator are called activator centers (extrinsic centers) [7, 10]. The schematic diagram illustrating intrinsic and extrinsic luminescence centers is shown in Fig. 1(a). When a crystalline material with intrinsic defect absorbs an incident radiation, electrons are promoted from the valence band to the conduction band and positively charged holes are created in the valence band [8]. The donor level "D" is occupied by positive defects, and the acceptor level "A" level is occupied by negative defect within the material band gap (Fig. 1.2(a)) [11]. The excited electrons in the conduction band are attracted by a coulombic force of attraction exerted by the positively charged donor.

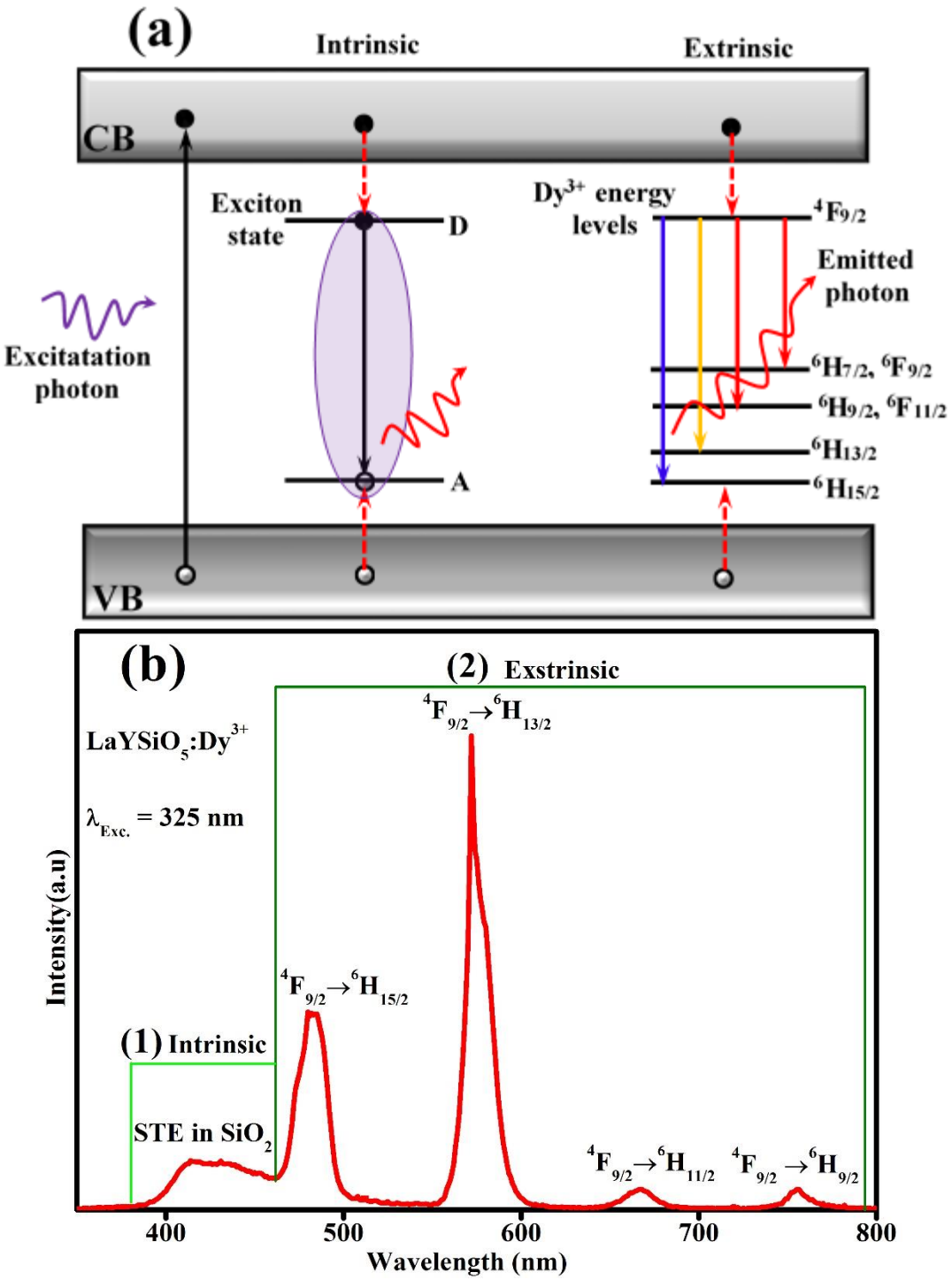

Fig. 1.2: (a) Schematic diagram illustrating the energy levels of an intrinsic and extrinsic luminescence centers, (b) emission spectrum of $LaYSiO_5:Dy^{3+}$ showing (1) an intrinsic emission, (2) extrinsic emission.

Similarly, the holes in valence band are attracted by the negative charge of the acceptor level. Due to the low binding energy of the electrons bound donor and the hole bound acceptor levels, both levels exist shortly at room temperature, and the electrons and the holes recombine and release energy in the form of photons [12]. As mentioned previously, extrinsic centers are normally incorporated into the host lattice purposely. Trivalent dysprosium (Dy^{3+}) is used as an example of an activator (intrinsic center) in Fig. 1.2(a). When excited host electrons relaxes from the conduction band to the energy level of the activator, energy is transferred from the host ions to the activator ions. The activator ion further relax to a lower energy and release energy in the form of photon [13]. It should be noted that direct excitation of activator ions from a lower energy to a higher energy level will also yield luminescence [14].

Fig. 1.2(b) shows a typical example of photoluminescence emission spectrum consisting of intrinsic and extrinsic luminescence emission spectrum. The spectrum was obtained from photoluminescence measurement of lanthanum yttrium oxyorthosilicate doped trivalent dysprosium ($LaYSiO_5:Dy^{3+}$) under the excitation wavelength of 325 nm [15]. The band originating from the intrinsic centers (the broad band with maximum around 415 nm in Fig. 1.2(b1)) is due to self-trapped excitons (STE) in SiO_2 [15, 16]. The peaks originating from the extrinsic centers (Fig. 1.2(b2) are observed around 485, 573, 668, and 756 nm and they are assigned to the $^4F_{9/2}\rightarrow{}^6H_{15/2}$, $^4F_{9/2}\rightarrow{}^6H_{13/2}$, $^4F_{9/2}\rightarrow{}^6H_{15/2}$, $^4F_{9/2}\rightarrow{}^6H_{11/2}$ and $^4F_{9/2}\rightarrow{}^6H_{9/2}$ transitions of Dy^{3+}, respectively [15].

1.1.3. Classification of luminescence

Luminescence can be classified as *fluorescence* or *phosphorescence* based on the duration of the emission. Fluorescence is known for a very short emission lifetime (10 ns), while phosphorescence have longer lifetime (milliseconds to seconds) [17]. In addition, fluorescence is known for temperature-independent decay, while phosphorescence exhibits temperature-dependent decay [13].

The mechanism of fluorescence and phosphorescence can best be explained using the simplified Jabłoński diagram [18] shown in Fig. 1.3. It comprises of singlet ground, first, second and n^{th} energy states denoted by S_0, S_1, S_2 and S_n. Each energy state contains sub vibrational energy levels denoted by 0, 1 and 2. When a phosphor material absorbs external radiation (photon), its electrons can be excited from the ground state (S_0) to the higher vibrational levels of S_1 or S_2. Fluorescence is observed when the excited electrons returns to the ground state (S_0) from the excited state (S_1 or

S_2) after rapidly relaxing to the lowest vibrational level of the S_1 state (internal conversion, IC) within 10 ns. Phosphorescence occurs when emission is observed from electrons in the S_1 state after undergoing spin conversion (change in the original spin state) to the first triplet state T_1. Phosphorescence emission are generally observed at lower energy (higher wavelength) relative to the fluorescence emission. The conversion from S_1 to the T_1 state is termed intersystem crossing (ISC) [17]. Another type of luminescence is the steady-state fluorescence. This is a type of spectroscopy where the intensity of the fluorescence emitted by molecules is excited by constant illumination of light [19].

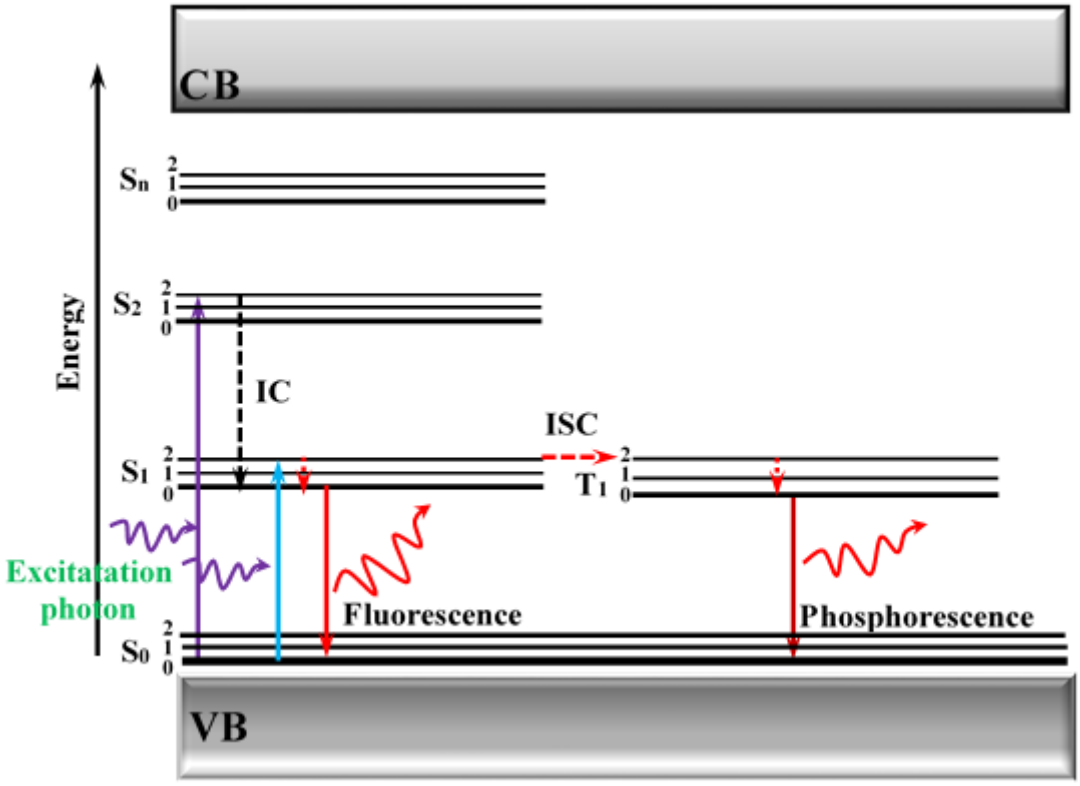

Fig. 1.3: A simplified Jabłoński diagram showing fluorescence and phosphorescence mechanism.

Luminescence can also be classified based on the excitation source. Various types of luminescence phenomenon and the excitation sources are listed in table 1.1.

Table. 1.1: Types of luminescence [20].

Phenomenon	Mode of excitation
Photoluminescence (fluorescence and phosphorescence)	Light (photon) absorption
Cathodoluminescence	Cathode rays (electron beams)
Radioluminescence	Ionizing radiation (X-rays, α, β, and γ and rays)
Electroluminescence	Electric field
Thermoluminescence	Heating after pre-storage of energy (e.g. radioactive irradiation)
Chemiluminescence	Chemical processes (e.g. oxidation)
Sonoluminescence	Ultrasounds
Triboluminescence	Frictional and electric forces
Bioluminescence	Biochemical processes

1.1.4. Application of phosphors

Today, phosphor materials have found many technological applications such as in electronic information display, advertising, solid-state lighting [21], solar cells [22, 23], theft prevention [24, 25], medicine [26-29], data storage, quality control [30], optical amplifiers [31], optical laser [32, 33], scintillation [34-37], etc. Among all these applications, our focus in this section will be on light emitting diodes (LEDs).

1.1.5. Light emitting diodes

LED belong to the family of solid-state lighting (SSL). In the recent years, LEDs have been the preferred lighting sources for many lighting applications. This system of lighting is the most matured technology in modern lighting applications, and may provide up to 50 % of lighting solution by 2025 [38]. Compare to other sources of lighting, LEDs have shown higher efficiency, e.g., between 2012 and 2014, the efficiency of LED has improved from 60 to 100 lumens per watt. However, the efficiency of compact fluorescent light (CFL) improved from 55 to 70 lumens per watt, and that of incandescent bulbs improved from 13 to 18 lumens per watt [39]. Furthermore,

the efficiency of LED is expected to improve to 150 lumens per watt by 2020 [40]. A study carried out for 25,000 h (Fig.1. 4) to compare cost saving of LED to incandescent bulb showed that about $ 236 per bulb can be saved [41]. Other advantages of LED over compact fluorescent lights (CFL) and incandescent bulbs are listed in table 1.2.

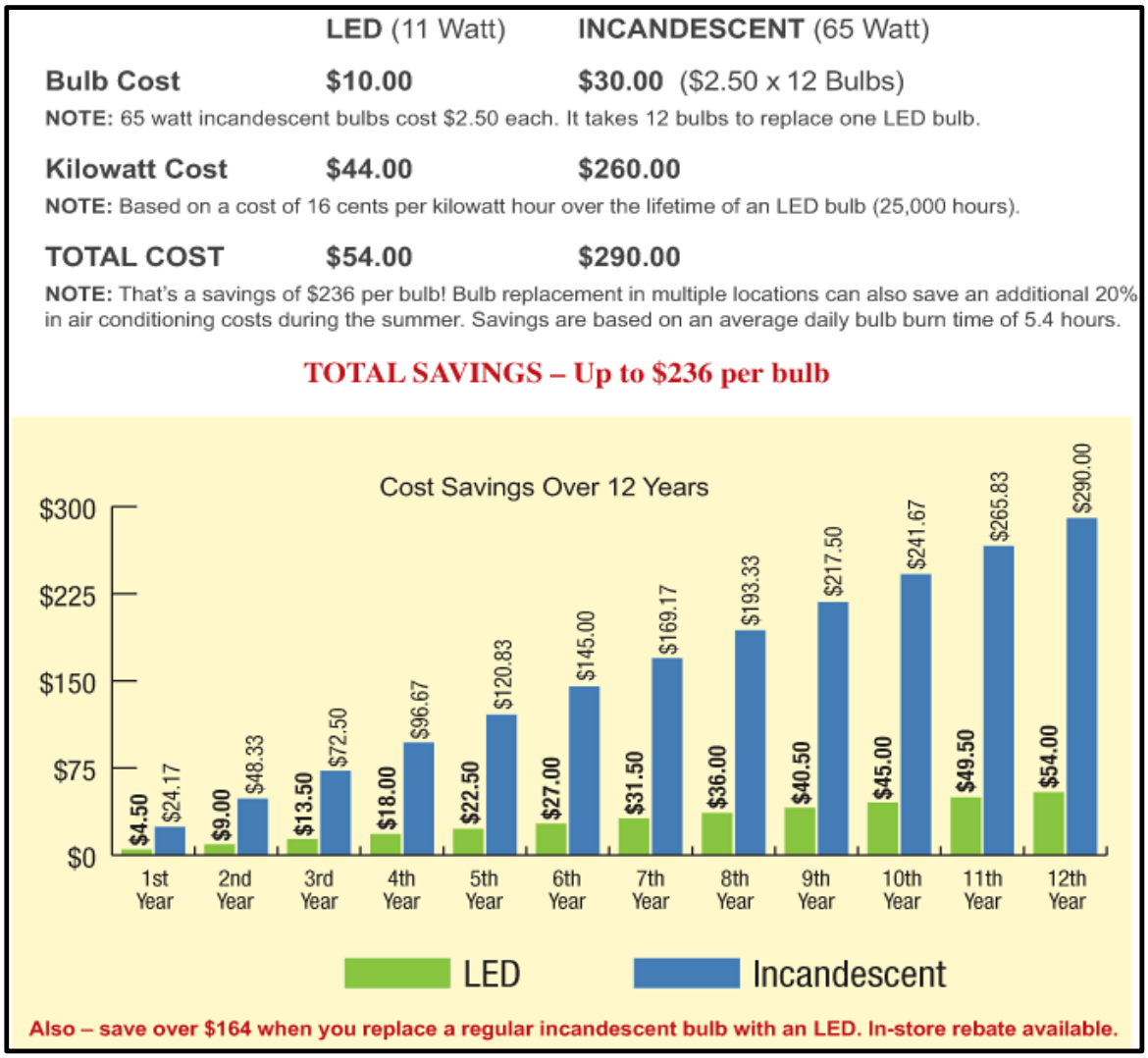

Fig. 1.4: Cost savings of LED bulb vs incandescent bulb over 25, 000 h [41].

Table 1.2: Advantages of LED over compact fluorescent lights (CFL) and incandescent bulbs.

Features	LED	Incandescent	CFL	Ref.
Sensitivity to low temperature	None	Some	Yes - may not work below −12 ºC or above 49 ºC	[42]
Sensitivity to humidity	No	Some	Yes	[42]
On/off cycle	No effect	Some	Yes - can reduce the lifespan	[42]
Turn on instantly	Yes	Yes	No – takes some time to warm up	[42]
Durability	Very durable – can handle bumping and jarring	Not very durable – glass or filament can break easily	Not very durable – glass can break easily	[42]
Heat emitted	3.6 KJ/h – 4 %	90 KJ/h – 100 %	32 KJ/h – 35 %	[42]
Failure	Not typical	Some	Yes – can catch fire, smoke, or emit odour	[42]
CO_2 emission (30 bulbs per year)	205 Kg/yr.	2041.2 Kg/yr.	477 Kg/yr.	[43]
Mercury	No	No	Yes	[43]
light output (lumen)/Power(Watt)	100 lm/ W	18 lm/W	70 lm/ W	[39]
Lifespan	15,000 h+	1,100 h	8,000 h	[44]

1.1.6. Applications of LEDs

Nowadays, LEDs are the lighting solution for general lighting applications. They have shown advantages such as low power consumption, durability, the possibility of direct mounting on circuit boards, mercury-free composition and brightness over other light sources [45]. LEDs have found applications in every area of life. Some of the fascinating possibilities offered by LEDs include;

indoors and outdoors applications, decorative and functional uses, signs, display applications, electronic backlighting, etc. [45-47]. Some of these applications are shown in Fig. 1.5.

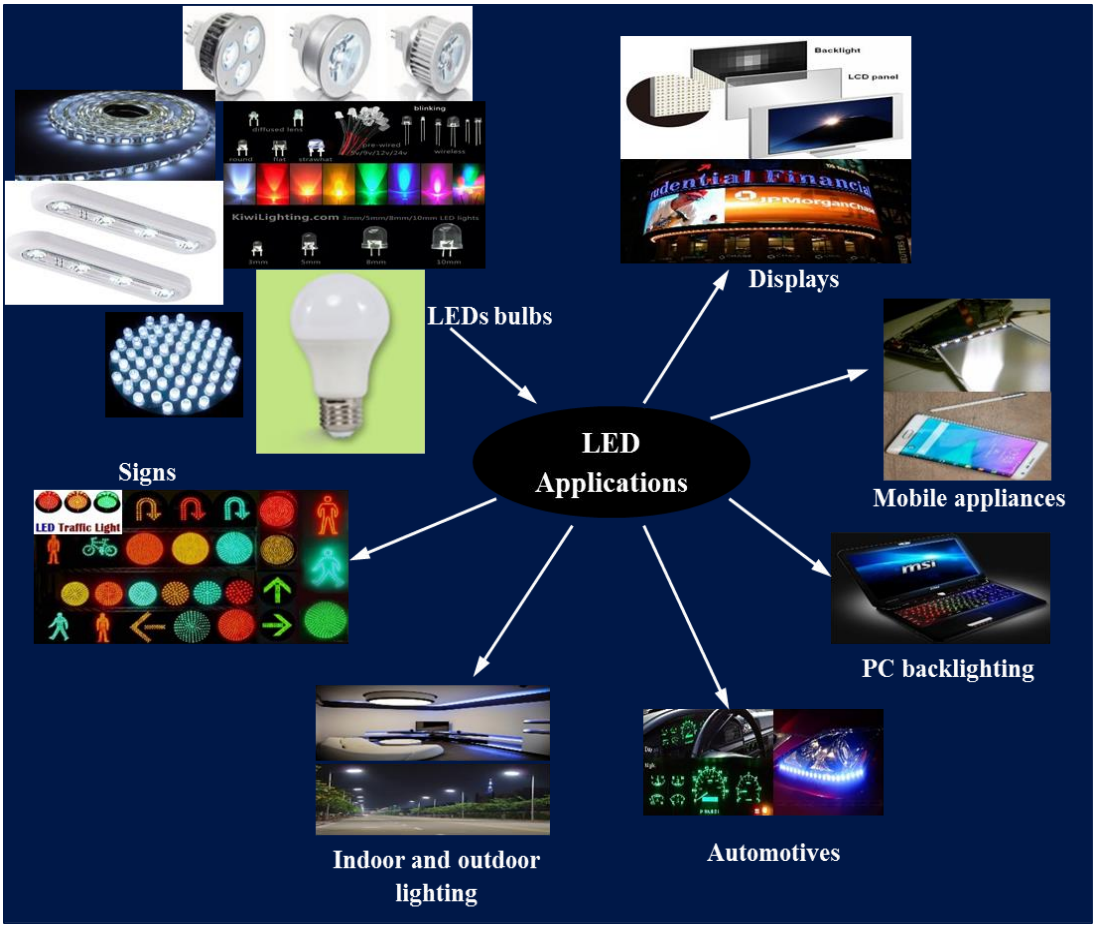

Fig. 1.5: Different applications of LEDs.

1.1.7. Different approaches of generating white light in LED

White LEDs can be generated through four different set-ups, namely:

(1) **Mixed coloured white LED**: In this set-up, three LED emitting red, green and blue are combined in a single device to generate white light through colour addition (Fig. 1.6(a)). Phosphors are not required in this type of set-up [48].

(2) **UV-pumped triple-doped phosphor (RGB-phosphors):** This arrangement involves the excitation of tripled-doped phosphors which emit red, green and blue (RGB) light with ultraviolet (UV) LED (Fig. 1.6(b)) [49]. Since human eyes are not sensitive to UV-light [50], combination of the RGB light give white light.

(3) **UV-pumped blue and yellow emitting phosphor**: This is similar to the arrangement in "2" above. However, in this case, blue and yellow emitting phosphors are excited using UV-emitting LED (Fig. 1.6(c)) [48].

(4) **Yellow phosphor converted white light**: This arrangement involves the excitation of a yellow emitting phosphor using blue LED. When the phosphor is excited, part of the blue light will be absorbed while some will contribute to the blue component of the white light [48, 49] (Fig. 1.6(d)).

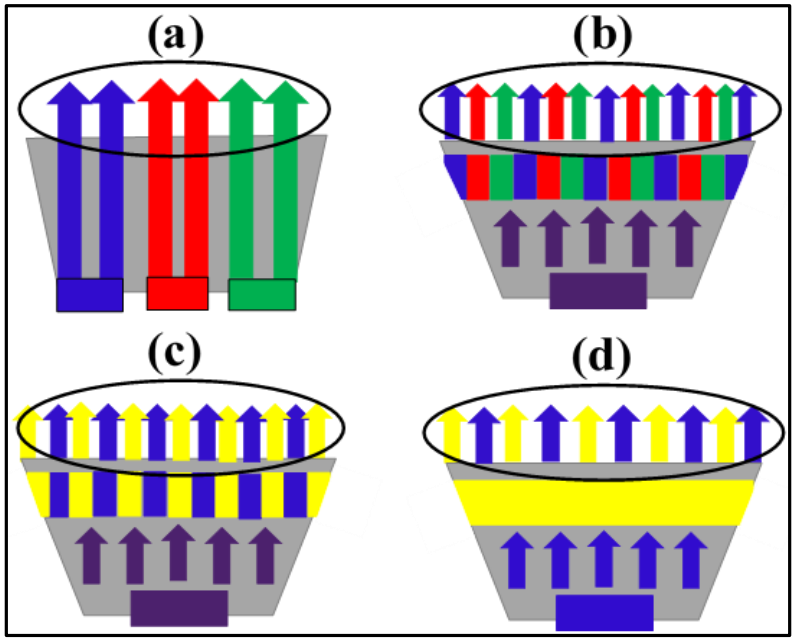

Fig. 1.6: Four arrangement for generating white light in LEDs: (a) RGB LEDs, (b) UV LED + RGB phosphors, (c) UV LED + blue and yellow phosphors, (d) Blue LED + yellow phosphor.

1.2. Problem statement

Energy management is very crucial for economic growth of a nation. Excessive energy bills will not only lead to energy shortage but will also harm the standard of living and socio-economic development. To a large extent, excessive energy consumption will affect the price of commodities (e.g. cloths, water, food etc.). Fixing the global energy crisis is not just about generation of more electricity. However, more focus should be on management of energy. The department of energy study United State of America in 2002 reported that the use of solid-state lighting such as white light LEDs would reduce the amount of carbon dioxide emission by 258 million tons and reduce the need for new power stations by 133 for the period of over 20 years. They also reported that the use of LEDs in place of filament light could decrease energy usage for lighting by 50% and at the same time providing better quality lighting [51].

Research has shown that the price of LEDs across Europe have decreased by 80 - 90 % between 2010 and 2016 [52]. This is because of immense amount of research input in this area for the past years. However, the price of LED is currently eight times higher than incandescent lamp and four times higher than CFL [53].

The demand for white light emitting applications in household and industries has led an endless quest to producing white light that will be cheaper, less energy consuming, more efficient and brighter. In contribution to this quest, we aim to prepare set of powder and thin film phosphors that can emit tunable colour and with light for LED application using cheap material and cheap synthesis method.

1.3. Objectives of the study

R_2SiO_5 (R_2 = La, Gd, Y) doped rare earth elements, has shown wide band gap, fast decay time, high quantum efficiency, high density and minimal self-absorption [54]. The quantum efficiency of some R_2SiO_5 is twice that of bismuth germanium oxide (BGO), and their lifetime is about five times smaller than that of BGO [55, 56]. They are good luminescence hosts for rare-earth dopant ions to prepare light emitting materials (phosphors) and their chemical stability is high [57].

Dy^{3+} doped matrices have found applications in white light emitting phosphors [58]. However, the choice of host matrix plays important role in accomplishing this goal. Two major emission peaks in Dy^{3+} doped matrices characterize Dy^{3+}, namely: the bluish emission (observed around 485 nm,

$^4F_{9/2} - {}^6H_{15/2}$ transition of Dy^{3+}) and the yellowish emission (observed around 575 nm, $^4F_{9/2} - {}^6H_{13/2}$ transition of Dy^{3+}). The yellowish emission dominates the bluish emission in most Dy^{3+} doped host matrices (with the ligand field at low symmetry). On the other hand, for host matrices with the ligand field at the low symmetry, the bluish emission gives stronger emission. However, in a case where the ligand field is situated in or very close to the inversion symmetry in the host matrix, both the blue and yellow emissions give equivalent emission intensities, which can result to white colour.

The luminescence of phosphors based on Pr^{3+} doped matrices shows a strong dependence on the crystal field of the host. For a hosts with strong crystal field (e.g. La_2SiO_5, Y_2SiO_5 or Gd_2SiO_5), Pr^{3+} give emission which the intensity can vary with crystal field in the visible range of the spectrum [59].

Crystal field determines the chemical nature of the optical center of a phosphor material. Engineering the crystal field of the host matrix can lead to shifting of the wavelength ranges of optical transitions, increasing the rates of radiative transitions and minimizing loss by nonradiative decay and excited state absorption. These objectives can be accomplished by manipulating the unit cell containing the optical center. The unit cell can be manipulated by changing its chemical composition [60].

By varying the molar ratio of La, Gd and Y in mixed $La_{2-x}Gd_xSiO_5$, $La_{2-x}Y_xSiO_5$ or $Gd_{2-x}Y_xSiO_5$ host, the unit cells of the host can be manipulated and hence tuning the crystal field strength. These to large extent can influence the luminescence properties of Pr^{3+} and Dy^{3+} in these host matrices and can lead to the generation of tunable emission.

To actualize these goals, we have designed this work in the following ways:

- Ψ Prepare powder and thin film phosphors and characterize them with different techniques.
- Ψ Deposit mixed lanthanum gadolinium oxyorthosilicate ($La_{0.5}Gd_{1.5}SiO_5$) doped with 1 mol% Dy^{3+} powder phosphor on a Si (111) substrate using pulsed laser deposition (PLD) technique.
- Ψ Deposit the films in different atmosphere (Vacuum, Ar and O_2)
- Ψ Choose the atmosphere that give the best luminescence property, vary the deposition temperature (substrate temperature), and study its effect on the properties of the thin film.

- Choose the films with the best luminescence properties and post-anneal them at high temperature.
- Prepare mixed lanthanum yttrium oxyorthosilicate ($La_{2-x}Y_xSiO_5$, x = 0, 0.5, 1, 1.5 and 2) doped with 1 mol% Pr^{3+} powder phosphors. Study the how the change in molar ratio of La and Y effect the photoluminescence property of Pr^{3+}.
- Co-dope Pr^{3+} and Dy^{3+} in mixed $La_{2-x}Y_xSiO_5$ (x = 0, 0.5, 1, 1.5 and 2) hosts.
- Post-anneal the aforementioned phosphors in different environments (air and ($Ar-H_2$)) and study the influence on the properties of the phosphors.
- Determine the quantum yield (QY) of some of the phosphors.

1.4. The makeup of the thesis chapters

Chapter 1: A brief introduction to phosphor and luminescence mechanisms were discussed.

Chapter 2: This chapter focused on the synthesis methods used to prepare the powder and the thin film samples.

Chapter 3: In this chapter, we discussed the characterization techniques we used to characterize our samples.

Chapter 4: Studied the effect of deposition atmospheres, substrate temperatures, and deposition time on the properties of $La_{0.5}Gd_{1.5}SiO_5:Dy^{3+}$ thin films.

Chapter 5: Studied the effect of post-annealing temperature on the properties of $La_{0.5}Gd_{1.5}SiO_5:Dy^{3+}$ thin films.

Chapter 6: The influence of variation of the molar ratio of La and Y in $La_{2-x}Y_xSiO_5$ (x = 0, 0.5, 1, 1.5 and 2) hosts on the photoluminescence properties of Pr^{3+}.

Chapter 7: The photoluminescence properties of co-doped Pr^{3+} and Dy^{3+} in $La_{2-x}Y_xSiO_5$ (x = 0, 0.5, 1, 1.5 and 2) hosts.

Chapter 8: The influence of post-annealing atmospheres on the photoluminescence properties of co-doped Pr^{3+} and Dy^{3+} in $La_{2-x}Y_xSiO_5$ (x = 0, 0.5, 1, 1.5 and 2) hosts.

Chapter 9: How to determine the QY of a phosphor using $La_{2-x}Gd_xSiO_5$ (x = 0, 0.5, 1, 1.5 and 2) doped Dy^{3+} as example.

Chapter 10: Summary, future works, list of publications and conferences.

1.5. References

[1] C.R. Ronda, Emission and excitation mechanisms of phosphors, In, C. Ronda (Ed.), "*Luminescence: From theory to applications*", WILEY-VCH Verlag, (2008) p. 3.

[2] K.N. Shinde, S.J. Dhoble, H.C. Swart, K. Park. Phosphate phosphors for solid-state lighting, Springer-Verlag Berlin Heidelberg (2012) p. 43.

[3] S. Shionoya, Introduction to the handbook, In, M. William, Y.S. Shionoya, H. Yamamoto (Ed.), "*Phosphor handbook*", 2nd Edi., CRC Press, Taylor & Francis Group, NY. (2007) p. 1-2.

[4] K.V.R. Murthy, H.S. Virk, Luminescence phenomena: An introduction, DDF 347 (2014) 1.

[5] C.R. Ronda, Emission and excitation mechanisms of phosphors, In, C. Ronda (Ed.), "*Luminescence: From theory to applications*", WILEY-VCH Verlag, (2008) p. 4.

[6] K.G. Fleming, Fluorescence theory, In, J. Lindon, G.E. Tranter, D. Koppenaal (Ed.), "*Encyclopedia of spectroscopy and spectrometry*", 3rd Edi., Academic Press, USA, (2016) p. 647-653.

[7] Encyclopedia2.thefreedictionary.com, Luminescence center, Retrieved October, (2017) from http://encyclopedia2.thefreedictionary.com/Luminescent+Center.

[8] R.C. Ropp, Luminescence and the solid state, Elsevier Science Publishers B.V., Amsterdam, Netherlands (2012) p.42.

[9] F. Stavale, N. Nilius, H.J. Freund, J. Phys. Chem. Lett. 4 (2013) 3972.

[10] I. Pelant, J. Valenta, Luminescence spectroscopy of semiconductors, Oxford University Press, Oxford, UK. (2012) p. 4.

[11] R.E. Hummel, Electronic properties of materials, 3rd Edi., Springer-Verlag, NY, USA, (2000) p. 113.

[12] C.T. Sah, Fundamentals of solid-state electronics, World Scientific Publishing Co. Pte. Ltd. London (1996) p. 165-166.

[13] K.N. Shinde, S.J. Dhoble, H.C. Swart, K. Park. Phosphate phosphors for solid-state lighting, Springer-Verlag Berlin Heidelberg (2012) p. 13-14.

[16] K.N. Shinde, S.J. Dhoble, H.C. Swart, K. Park. Phosphate phosphors for solid-state lighting, Springer-Verlag Berlin Heidelberg (2012) p. 119-122.

[15] S.N. Ogugua, S.K.K. Shaat, H.C. Swart, O.M. Ntwaeaborwa, J. Phys. & Chem. Sol. 83 (2015) 109.

[16] C. Itoh, K. Tanimura, N. Itoh, J. Phys. C: Solid State Phys. 21 (1988) 4693.

[17] J.R. Lakowickz, Principles of fluorescence spectroscopy, 3rd Edi., Springer Publishers, NY (2006) p. 1-5.

[18] A. Jabłoński, Efficiency of anti-Stokes fluorescence in dyes, Nature 131 (1933) 839.

[19] Royal Society of Chemistry, Steady-state fluorescence spectroscopy, Retrieved April, (2018) fromhttp://www.rsc.org/publishing/journals/prospect/ontology.asp?id=CMO:0002714&MSID=C2TA01318E.

[20] S.N. Ogugua, M.Sc. Thesis, University of the Free State, South Africa (2015) p. 15.

[21] A. Lakshmanan, Luminescence and display phosphors: phenomena and applications, Nova Science Poblishers, Inc., NY (2008) p.1-3.

[22] N. Yao, J. Huang, K. Fu, X. Deng. M. Ding, X. Xu, RSC. Adv. 6 (2016) 17546.

[23] W. He, T.S. Atabaev, H.K. Kim, Y.H. Hwang, J. Phys. Chem. C. 117 (2013) 17894.

[24] W. Wang, X. Lei, Z. Ye, N. Zhao, H. Yang, J. Alloys. Compd. 705 (2017) 253.

[25] V. Sharma, A. Das, V. Kumar, Mater. Res. Express 3 (2016) 015004.

[26] D. Cavouras, I. Kandarakis, C.D. Nomicos, G.S. Panayiotakis, I. Fezoulidis, Appl. Radiat. Isot. 52 (2000) 119.

[27] P. Leblans, D. Vandenbrouke, P. Willems, Materials 4 (2011) 1034.

[28] T. Lécuyer, E. Teston, G.R. Garcia, T. Maldiney, B. Viana, J. Seguin, N. Mignet, D. Sherman, C. Richard, Theranostics 6 (2016) 2488.

[29] P.P. Mokoena, H.C. Swart, O.M. Ntwaeaborwa, Physica B (2017) https://doi.org/10.1016/j.physb.2017.06.040.

[30] H. von Seggern, Braz. J. Phys. 29 (1999) 254.

[31] F. Hu, X. Liu, R. Chen, Y. Liu, Y. Mai, R. Maalej, Y. Yang, J. Rare Earth 35 (2017) 964.

[32] K. Yoshimura, K. Annen, H. Fukunaga, M. Harada, M. Izumi, K. Takahashi, T. Uchikoshi, R.J. Xie, N. Hirosaki, Jpn. J. Appl. Phys. 55 (2016) 042102.

[33] A.A. Kaminskii, Phys. Status Solidi A 200 (2003) 215.

[34] G.C. Tyrrell, Nucl. Instr. Meth. Phys. Res. A 546 (2005) 180.

[35] G. Blasse, Scintillator materials, Chem. Mater. 6 (1994) 1465.

[36] G.V. Bramhe, S.J. Dhoble, S.V. Moharil, Radiat. Eff. Defects Solids 160 (2005) 219.

[37] G. Kertzscher, S. Bedder, Phys. Med. Biol. 62 (2017) 5046.

[38] Lrc.rpi.edu, Solid-State Lighting Program at the LRC, Retrieved October, (2017) from http://www.lrc.rpi.edu/programs/solidstate/SSLWhat.asp.

[39] Cleantechnica.com, LED lighting efficiency jumps roughly 50% since 2012, Retrieved October, (2017) from https://cleantechnica.com/2014/11/05/led-lighting-efficiency-jumps-roughly-50-since-2012/.

[40] Cleantechnica.com, LED lamp efficiency to continue improving as cost decreases, Retrieved October (2017) from https://cleantechnica.com/2014/03/24/led-lamp-efficiency-continue-improving-cost-decreases/.

[41] Wolfers.com, Learn about LED bulbs, Retrieved October (2017) from http://www.wolfers.com/learn-about-led-bulbs-4/.

[42] J. Westbrook, LED lighting - benefits over CFL and incandescent, Retrieved October, (2017) from https://iesdistributors.com/blog/led-lighting-benefits-over-cfl-and-incandescent/.

[43] Yourgreensolutions.com.au, Advantages of LED lights over CFL & incandescent bulbs, Retrieved October, (2017) from http://www.yourgreensolutions.com.au/advantages-led-lights-cfl-incandescent-bulbs/.

[44] K. Alt, LED vs CFL vs Incandescent vs Fluorescent: Which Shines Cleanest? Retrieved October, (2017) from https://www.earthsfriends.com/led-vs-cfl-vs-incandescent-vs-fluorescent/.

[45] J. Silver, R. Withnall, Color conversion phosphors for LEDs, In, A. Kitai (Ed.), "*Luminescent Materials and Application*", John Wiley, England, (2008) p. 75-109.

[46] Futureelectronics.com, What is an LED display? Retrieved October, (2017) from http://www.futureelectronics.com/en/optoelectronics/led-displays.aspx.

[47] A. Reggiani, A. Farini, LEDs and use of white LED for lighting, In, P. Sansoni, L. Mercatelli, A. Farini (Ed.), "*Sustainable Indoor Lighting*", Springer-Verlag, London (2015) p. 127-149

[48] S. Pimputkar, J.S. Speck, S.P. DenBaars, S. Nakamura, Nat. Photonics 3 (2009) 179.

[49] D.A. Steigerwald, J.C. Bhat, D. Collins, R.M. Fletcher, M.O. Holcomb, M.J. Ludowise, P.S. Martin, S.L. Rudaz, IEEE J. Sel. Top. Quantum Electron 8 (2002) 310.

[50] C. Berger, Dragonflies, Stackpole books, Mechanicsburg, PA, USA (2004) p. 22.

[51] OIDA (www.oida.org), The promise of solid state lighting for general illumination, light emitting diodes (LEDs) and organic light emitting diodes (OLEDs), U.S. Department of Energy (2002).

[52] M. Scholand, Fast learning curves – LED lighting's rapid reduction in price, CLASP Europe (2016).

[53] H. Johnson, Light bulb showdown: LED vs. CFL vs. incandescent, Retrieved October, (2017) formhttps://www.thesimpledollar.com/the-light-bulb-showdown-leds-vs-cfls-vs-incandescent-bulbs-whats-the-best-deal-now-and-in-the-future/.

[54] D.W. Cooke, E.A. McKigney, R.E. Muenchausen, B.L. Bennett, US Patent. Sr. No. 60/752, 981 (2005).

[55] K. Takagi, T. Fukazawa, Appl. Phys. Lett. 32 (1983) 43.

[56] H. Ishibashi, K. Shimizu, K. Susa, IEEE Trans. Nucl. Sci. 36 (1989)170.

[57] C. Li, C. Wyon, R. Moncorge, IEEE J. Quant. Electron. 28 (1992) 1209.

[58] G. Han, Y. Wanga, C. Wua, J. Zhang, Mater. Res. Bull. 44 (2009) 2255.

[59] J. Ganem, W.M. Denis, W.M. Yen, J. Lumin. 54 (1992) 79.

[60] B. Henderson, R. Bartram, Crystal-field engineering of solid-state laser materials, Cambridge University Press, New York (2000) p. 253.

CH. 2 Materials and sample preparation techniques

2.1. Introduction

This chapter give some insight into the materials used in this thesis. The properties of the host materials (lanthanum, gadolinium and yttrium oxyorthosilicates) were discussed. We also looked at some important properties of the dopants (activators). Finally, the methods used for the synthesis of the powders and the thin films samples were discussed.

2.2. Rare earth oxyorthosilicates

Rare-earth oxyorthosilicate (R_2SiO_5) are created from binary rare-earth silicate (R_2O_3-SiO_2) system with 1:1 composition. Base on the size of the radius of the rare-earth ion, they can be classified into two groups of monoclinic structures namely, the small (La-Tb) and large (Dy-Lu, Y, Sc) ionic radius rare-earth ions. Lanthanum oxyorthosilicate (La_2SiO_5) and gadolinium oxyorthosilicate (Gd_2SiO_5) belong to the small ionic radius rare-earth ions, while yttrium oxyorthosilicate (Y_2SiO_5) belong to the large ionic radius rare-earth ions in rare-earth oxyorthosilicates crystals. R_2SiO_5 can also be classified base on their crystal structures as monoclinic crystallographic point group with space group *P21/c* and *I2/a* [1-4], and monoclinic crystallographic point group with space group *C2/c* and *B2/b*. The space groups *P21/c* and *C2/c* are the low temperature (*X*1) phase, while the space groups *I2/a* and *B2/b* are the high temperature (*X*2) phase. La_2SiO_5 and Gd_2SiO_5 belong to the *P21/c* and *I2/a* space group, while Y_2SiO_5 belong to the *C2/c* and *B2/b* space group. In the low temperature phase, R_2SiO_5 have two non-equivalent crystallographic sites R1 and R2 coordinated by nine and seven oxygen atoms, respectively (Fig. 2.1(a)) [1-4]. In the high temperature phase however, seven and six oxygen atoms coordinates the two sites (R1 and R2, using Y_2SiO_5 as an example in Fig. 2.1(b)), respectively. In each phase, a tetrahedra Si (SiO_4) links the two R sites [5]. A phase transformation temperature of 1190 ºC and 1250 ºC from *X1* to *X2* phase have been reported for Y_2SiO_5 [1, 6]. The lattice parameters of La_2SiO_5, Gd_2SiO_5 and Y_2SiO_5 are listed in table 2.1.

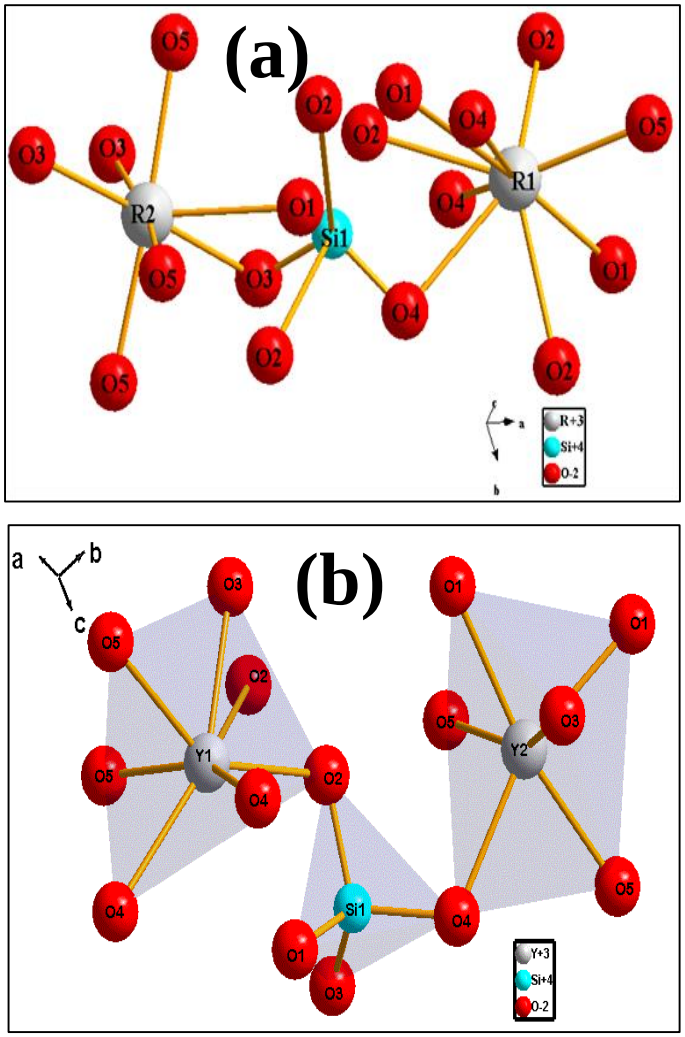

Fig. 2.1: Crystal structure of R_2SiO_5 in the (a) *X1* phase, (b) *X2* phase.

Table 2.1: Lattice parameters of La_2SiO_5, Gd_2SiO_5 and Y_2SiO_5.

R_2SiO_5	*a* (nm)	*b* (nm)	*c* (nm)	*β* (°)	*V* (nm^3)	Ionic radius (nm)		Ref.
						R1	R2	
La_2SiO_5	0.93329	0.75087	0.70337	108.675	0.4669	0.1216	0.110	[7]
Gd_2SiO_5	0.91105	0.69783	0.68544	107.141	0.4164	0.1107	0.100	[7-9]
Y_2SiO_5	1.44300	1.04100	0.67330	122.130	0.3974	0.0960	0.090	[7, 1]

These crystals have demonstrated excellent properties like wide band gap, fast decay time, high quantum efficiency, high density and minimal self-absorption and also possess great ability to accommodate rare-earth ions [10]. They have been used as host to prepare light emitting materials or phosphors for different applications [11-17]. In rare earth oxyorthosilicates (R_2O_3-SiO_2), SiO_2 can give broad blue emission from self-trapped excitons (STE) [18, 19].

2.3. Praseodymium

Praseodymium with the atomic number 59, atomic weight 140.91 $g.mol^{-1}$, represented by the chemical formula Pr is the second element in the lanthanide series and it is a rare earth element. It was discovered in 1885 by an Austrian Chemist Baron Carl Auer von Welsbach [20]. Some of the properties of Pr are shown in table 2.2. The electronic configuration of Pr is $(1s)^2\,(2s)^2\,(2p)^6\,(3s)^2\,(3p)^6\,(3d)^{10}\,(4s)^2\,(4p)^6\,(4d)^{10}\,(5s)^2\,(5p)^6\,(4f)^2\,(5d)^1\,(6s)^2$ normally written as $[Xe]4f^25d^16s^2$

Table 2.2: Properties of praseodymium.

Colour	silvery-yellow
Structure	Hexagonal
Density	6.80 g/cm^3 at 20 ℃
Melting point	935 ^0C
Boiling point	3130 ^0C
State	Solid
Solubility	Soluble in dilute acids
Atomic radius	0.182 nm
Ionic radius	0.101 nm

, showing that it has 2 valence 4f electrons. The 4f electrons have orbital quantum number $l = 3$ ($l = 0, 1, 2, 3\ldots$ also represented as *s*, *p*, *d*, *f*… shells) [21]. The magnetic quantum number m_l takes

value from $-l \ldots 0 \ldots l$ and spin angular momentum (S) takes the value of 1/2 × the number of unpaired electrons. The two valence 4f electrons of Pr are all spin up as shown in table 2.3. Hence the maximum value of $S = 1/2 \times 2 = 1$ and the maximum value of L = +2 +3 = 5. Since the shell is less than half filled, the total angular momentum is given by, $J = L - S$, which gives the total value of 4 and the spin multiplicity given by $(2S+1)$ is 3.

Table 2.3: Electronic spins of Pr^{3+}.

m_l	↑	↓
3	•	-
2	•	-
1	-	-
0	-	-
-1	-	-
-2	-	-
-3	-	-

According to the spectroscopic notation, L, S and J system is written as $^{(2S+1)}L_J$, where L, which is represented as S, P, D, F, G, H … corresponds to $L = 0, 1, 2, 3, 4, 5 \ldots$ In general, the ground state of Pr can be written as $^3H_4$, which further splits into $^3H_5$, and $^3H_6$ sub-levels according to $^3H_{J+1}$. Pr can exist in trivalent (Pr^{3+}) or tetravalent (Pr^{4+}) state.

It is well known that the $4f^n \rightarrow 4f^n$ electronic transitions are parity forbidden and that these transitions are forced by the mixing of the crystal field configuration. Hence, they appears to be weak and sharp. On the contrary, the interconfigurational $4f^{n-1}5d \rightarrow 4f^n$ transitions are parity-allowed and they are known for short lifetime and their emission bands appears broad with high intensity and are observed in the UV region [22-26]. In Pr^{3+}-doped matrices, both the $4f^n \rightarrow 4f^n$ and $4f^n \rightarrow 4f^{n-1}5d$ transitions exists depending on the host matrix and the position of the $^1S_0$ energy level of the $4f^2$ electronic configuration with respect to the $4f^15d$ electronic configuration [27]. Therefore, the emission spectra of Pr^{3+}-doped matrices shows strong dependence on the host lattice. In other words, they depend on the site symmetry and the crystal field strength of the host. When doped into host lattice such as YF_3, which exert weak crystal field on Pr^{3+} ions, the crystal

field component of the $4f^15d$ electronic configuration is located energetically above the $^1S_0$ level of the 4f state (Fig. 2.2) [28]. The emission spectra of Pr^{3+} in the UV region shows broad band when doped into host lattices with crystal field strong enough such that the lowest crystal field component of the $4f^15d$ electronic configuration is situated below the $^1S_0$ state [29]. The five transitions observed between $4f^15d$ and $4f^2$ electronic configurations ($^3H_4$, $^3H_5$, $^3H_6$, $^3F_2$ and $^3F_3$) are located in the UV-B and UV-C range. When Pr^{3+} is doped into a host lattice with very strong crystal field such as YAG, the $4f^15d \rightarrow 4f^2$ transitions are situated in the UV-A region. In this case, the lowest crystal field component of the $4f^15d$ configuration is situated very close to the ^3P_J levels, which lead to the population of the 4f states. As a result, electronic transitions from the $^3P_0$ levels to the ^3H_J and ^3F_J states of Pr^{3+} are observed in the visible region.

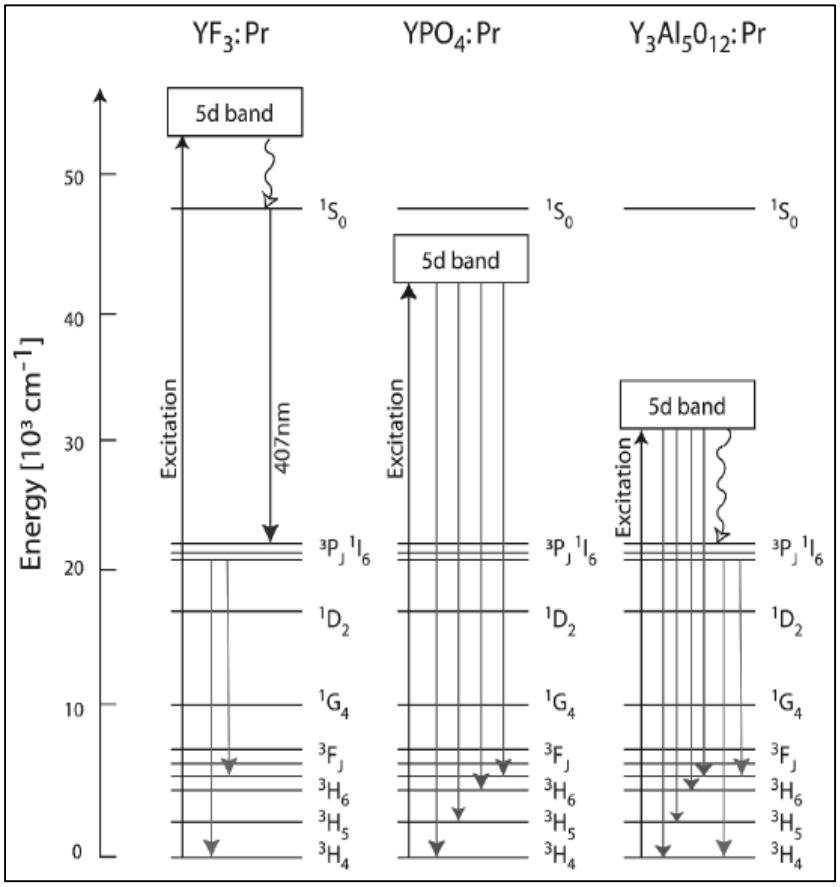

Fig. 2.2: Energy level scheme of Pr^{3+} [30].

Pr^{3+} doped matrices have found applications in laser [31-36] - because most of its transitions have the ability to produce stimulated emission, thermographic phosphor for planar gas phase

thermometry [37], white light from the $^3P_0 \rightarrow {}^3H_{4,5,6}$ and $^1D_2 \rightarrow {}^3H_4$ transitions [38], scintillators [39] information processing and all-optical network [40] and as an up-conversion material [41].

2.4. Dysprosium

A French chemist Paul Émile Lecoq de Boisbaudran discovered dysprosium in 1886. It is the tenth element in the lanthanide series and it is a rare-earth metal with chemical symbol Dy [42]. The electronic configuration of Dy is $(1s)^2\ (2s)^2\ (2p)^6\ (3s)^2\ (3p)^6\ (4s)^2\ (3d)^{10}\ (4p)^6\ (5s)^2\ (4d)^{10}\ (5p)^6$ (4f)9 $(5d)^1\ (6s)^2$, often written as $[Xe]4f^9 5d^1 6s^2$. Some of the properties of Dy are listed in table 2.4.

Table 2.4: Properties of Dy.

Atomic no	66
Atomic weight	162.50 $g.mol^{-1}$
Colour	Silvery-white
Structure	Hexagonal
Density	8.559 g/cm^3
Melting point	1441 ^0C
Boiling point	2560 ^0C
State	Solid
Solubility	Soluble in dilute acids
Atomic volume	19. 032 cm^3/g
Atomic radius	0.1773 nm
Ionic radius	0.0908 nm

The outermost shell of Dy is $4f^9$ showing that it has 9 valence f electrons. Hence, one can determine the ground state of its 4f shell using Hund's rules [43]. The orbital quantum number (l) for f electrons is $l = 3$ ($l = 0, 1, 2, 3,\ldots$ often denoted as *s*, *p*, *d*, *f*,… shells). The magnetic quantum number (m_l) takes values from $-l \ldots 0 \ldots l$. The spin angular momentum S is ½ multiplied by the number of the unpaired electrons (5 from table 2.5) [21]. Hence, S have the maximum value of 5/2. From table 2.5, the orbital angular momentum (L) is L = -3 -2 -1 0 +1 +2 +3 +2 +3 = 5 and the total angular momentum (J) = $L + S$ (+ because the shell is more than half filled) is 15/2. J, L and S are known as spectroscopic terms and is written as $^{(2S+1)}L_J$, with $(2S+1)$ representing the spin multiplicity and L is normally denoted as (S, P, D, F, G, H…) and it takes value from 0, 1, 2, 3, 4…. In general, the state of any element can be written as $^{(2S+1)}L_J$. For Dy, $(2S+1) = 6$, $L = 5$ and $J = 15/2$, hence $^{(2S+1)}L_J = {}^6H_{15/2}$. Where H is the corresponding value of L, i.e. 5.

Table 2.5: Electronic spins of Dy^{3+}.

m_l	↑	↓
3	•	•
2	•	•
1	•	-
0	•	-
-1	•	-
-2	•	-
-3	•	-

Four emission peaks in the visible region of the electromagnetic spectrum characterize the luminescence spectrum of Dy^{3+} doped host matrices. These peaks are located around 485, 573, 668 and 756 nm and are ascribed to the $^4F_{9/2} \rightarrow {}^6H_{15/2}$, $^4F_{9/2} \rightarrow {}^6H_{13/2}$, $^4F_{9/2} \rightarrow {}^6H_{11/12}$, and $^4F_{9/2} \rightarrow {}^6H_{9/2}$ 4f→4f transitions of Dy^{3+} respectively [44]. However, the peaks at 485 nm (blue) and 573 nm (yellow) are pronounced than the other two. The peak at 485 nm is magnetic dipole in nature (hardly vary with its environment), while the peak at 573 nm is electric dipole in nature (easily vary with its environment) [45]. When incorporated in most host matrix, the yellow emission of Dy^{3+} normally dominate the blue emission i.e. in a host matrix where Dy^{3+} ions are located at low

symmetry (host matrix without inversion center). Examples of these type of host matrices are La_2SiO_5, Gd_2SiO_5, Y_2SiO_5 [46], YVO_4 [47], $Ca_3La_2(BO_3)_4$ [48], ZANP glasses [49], $CaMoO_4$ [50]. When incorporated into a host matrix with an inversion center (Dy^{3+} are located at the higher symmetry), e.g. $Ca_5(PO_4)_3F$ [51], PKAlCaF glasses [52], PbF_2 glasses [53], the blue emission becomes stronger than the yellow emission. In some other host materials, Dy^{3+} are incorporated in or very close to the inversion symmetry, e.g. ZTFB glasses [54], BaY2ZnO5 [55], the intensity of the blue and yellow emission becomes comparable. Eight peaks located around 294, 325, 349, 362, 387, 424, 454 and 474 nm characterize the absorption spectrum of Dy^{3+} in Dy doped matrices. These peaks are assigned to $^6H_{15/2}\rightarrow{}^4K_{13/2}$, $^6H_{15/2}\rightarrow{}^4K_{15/2}$, $^6P_{3/2}$, $^6H_{15/2}\rightarrow{}^6P_{7/2}$, $^4M_{15/2}$, $^6H_{15/2}\rightarrow{}^6P_{5/2}$, $^6H_{15/2}\rightarrow{}^4I_{13/2}$, $^6H_{15/2}\rightarrow{}^4G_{11/2}$, $^6H_{15/2}\rightarrow{}^4I_{15/2}$, and $^6H_{15/2}\rightarrow{}^4F_{9/2}$ 4f→4f excitation of Dy^{3+}, respectively [44].

2.5. Combustion synthesis

Combustion is redox (red-ox = reduction-oxidation) reaction, or electron transfer process in which the oxidizer gain an electron and increase in its oxidation state and the reducer lose an electron and reduce in its oxidation state to form a product [56a, 57]. The reducing agent is said to be oxidized and the oxidizing agent is said to be reduced. In general, the reducer is an element or a compound that donates and the oxidizer is an element that gains electron during redox reaction [57]. Redox reaction is illustrated schematically using Fig. 2.3. Oxidation involves the addition of oxygen or any electronegative element (or nonmetals). Reduction involve addition of hydrogen or any electropositive element (or metals). Typical example of redox reaction is shown in Eq. 2.1.

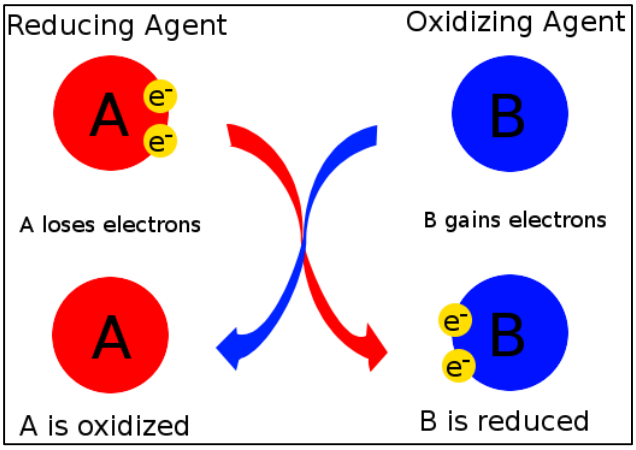

Fig. 2.3: Schematic illustration of redox reaction [57].

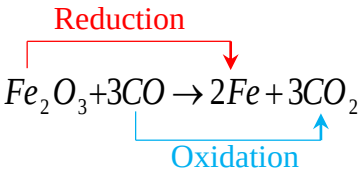

(2.1)

In Eq. 1.1, the iron (III) oxide (Fe_2O_3) is the oxidizing agent and the carbon monoxide (CO) is the reducing agent. The Fe_2O_3 donated oxygen to the CO. Some examples of oxidizing and reducing agents are shown in table 2.6.

Table 2.6: Some oxidizing and reducing agents.

Oxidizing agents	Reducing agents
O_2	H_2
O_3	Fe
F_2	Zn
Br_2	Li

During combustion synthesis (CS), redox reaction is use to produce inorganic solid materials [56b]. CS is also known as self-propagation high temperature synthesis (SHS). It is an important synthesis technique for preparation of advanced ceramics (structural and functional, nanomaterials, alloys, composites, catalysts, and intermetallics. CS process is known for high

activation energies, high exothermic reactions, and high reaction temperature (500 – 4000 K, 226.85 – 3726.85 ºC) [56a].

2.5.1. Types of combustion synthesis

Depending on the state of the reactants (solid, liquid or gas), the adiabatic temperature, CS can be classified as low-temperature combustion synthesis (LTCS) [58], self-propagation high temperature synthesis (SHS) [59], volume combustion synthesis (VCS) (thermal explosion) [60], emulsion combustion synthesis [61], sol-gel combustion synthesis [62], gel-combustion synthesis [63], solid-state combustion (SSC) [64], solution combustion synthesis (SCS) [64], etc.

2.5.2. Modes of combustion synthesis

Combustion synthesis can be classified based on the rate of temperature increase and the duration of combustion as, volume combustion synthesis (VCS) and self-propagating high-temperature synthesis (SHS) [65-67]. In VCS mode, combustion takes place at very high rate (~600 ºC/s), attaining high temperature at a very short time (~10 s) [68]. It requires the sample to be heated uniformly in a controllable manner until combustion reaction is ignited. VCS uses weak exothermic reaction and the reaction occurs in the entire volume of the sample. It requires preheating (~150 – 200 ºC) before ignition [69]. In SHS however, combustion last longer [68]. Its initial exothermic reaction is ignited by an external heat source at a very high temperature (1000 – 3000 ºC). Once ignited, the reaction propagates through the entire sample in a self-sustained manner without any external energy source [69]. SHS mode are more energy saving compared to the VCS mode.

Some advantages of combustion synthesis include:

- Ψ High purity product.
- Ψ Very low cost of production.
- Ψ Can be used to produce any size or shape of particle.
- Ψ Does not require sophisticated equipment.
- Ψ It is time saving.
- Ψ Low energy consumption.
- Ψ High productivity.

2.5.3. Solution combustion synthesis

SCS is a type of CS process where exothermic redox reactions in solutions is used for preparation of samples. It uses self-sustaining reaction between metal salts such as nitrites, sulfates and oxides as the oxidizing agents and fuels such as urea, glycine, sucrose, etc. are use as the reducing agents [70]. Once ignited, a self-sustaining reaction between a fuel and an oxygen containing species can generate enough heat to sustain the entire reaction [71]. In practices, SCS is achieved by dissolving admixture of metal nitrates and fuel in distilled water, stir with a magnetic stirrer on a hot plate set to certain temperature (about 100 ºC) to obtain homogeneous mixture (Fig. 2.4). The solution is transferred into a preheated (about 600 ºC) muffle furnace, leading to evaporation of water, and followed by self-ignition of the reactants. Subsequently, crispy crystalline product is formed, which can be ground to fine powder using agate mortar and pestle.

Some advantages of SCS include:

- Ψ Fast reaction process.
- Ψ Mixing of reactants at molecular level.
- Ψ Products exhibits high purity due to vaporization of all volatile species.
- Ψ Formation of nanocrystalline grains.
- Ψ Formation of complex oxides nanopowder for different applications.

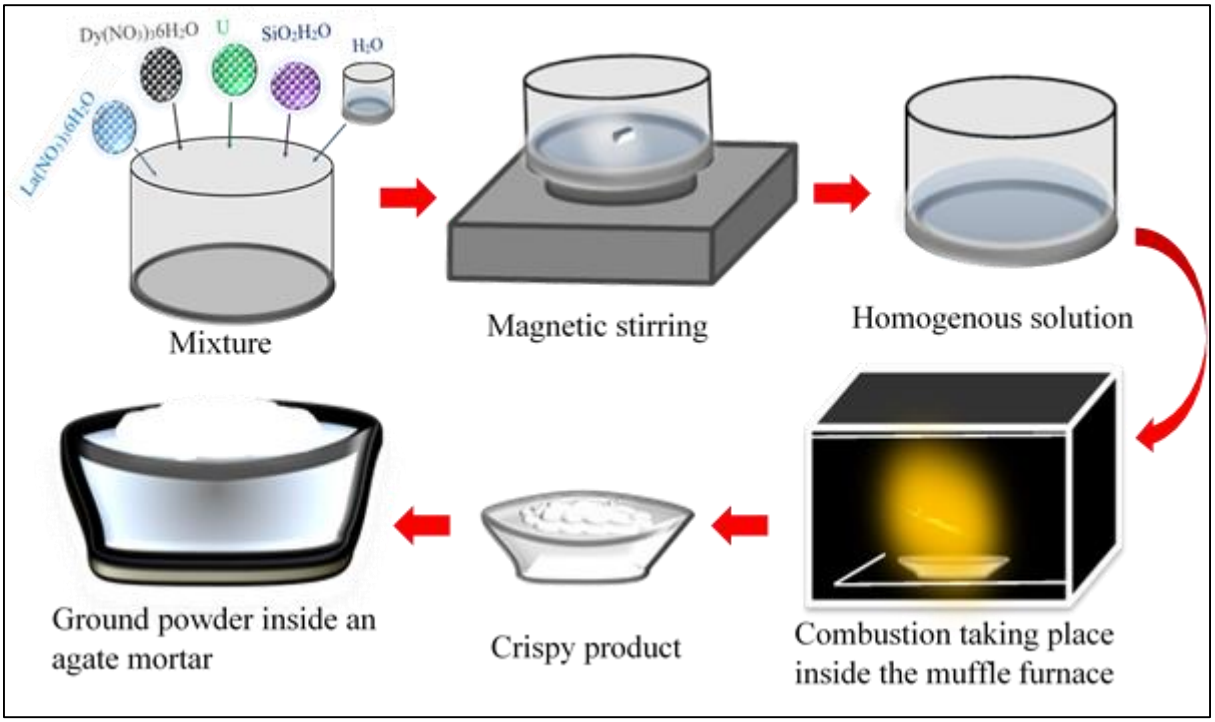

Fig. 2.4: Schematic diagram illustrating SCS process.

Some fuels and the corresponding metal salts used for SCS are listed in table 2.7. See Ref. [72] for list of more fuels.

Table 2.7: Some of the fuels used for SCS.

Metal salts	Fuels	Ref.
$NiFe_2O_4$	U	[73]
$NiFe_2O_4$	Gl	[73]
$NiFe_2O_4$	Su	[73]
$NiFe_2O_4$	Gly	[73]
$LaFeO_3/LaMnO_3$	Ethy	[68]
$LaFeO_3/LaMnO_3$	Gl	[68]
ZrO_2	Gl	[74]
La_2SiO_5	U/AN	[46]
Gd_2SiO_5	U/AN	[46]
Y_2SiO_5	U/AN	[46]

ZrO_2	H	[75]
CeO_2	H	[75]
α-Al_2O_3	H	[75]
MAl_2O_4(M = Ca, Mg, Zn, Ni)	H	[75]
$LaMO_3$(M = Mn, Cr, Al)	H	[75]

U = urea, Gl = glycine, Su = sucrose, Gly = Glycerol, Ethy = ethylene glycol, AN = ammonium nitrate, H = Hexamethylenetetramine.

2.6. Pulsed laser deposition (PLD)

2.6.1. Introduction

In 1962, Breech and Cross reported the first study on excitation and ionization in the vapor plume of a surface vaporized using pulsed laser [76]. First laser deposition was performed in 1965 by Smith and Turner using a pulsed ruby laser to deposit thin films in vacuum [77]. The films however, were of inferior quality to the films obtained using techniques such as molecular beam epitaxy and chemical vapor deposition. Nonetheless, in 1987, Dijkkamp et al [78] recorded a major breakthrough when they laser-deposited $YBa_2Cu_3O_7$ thin film with superior quality film than films deposited using the alternative techniques. This process of deposition was termed Pulsed Laser Deposition (PLD) [79, 80] or Laser Ablation Deposition (LAD). Defined as a "flash evaporation" technique, in PLD, small volume of a material when heated to a high temperature evaporates quickly such that the target material have the same composition as the deposit. Most of the modern PLD systems uses excimer lasers [81, 82]. Since its invention, PLD has been used to deposit varieties of complex oxides, nitrides, carbides, borides, semiconductors, insulators, biological materials and polymer, metal composites [80, 83].

2.6.2. Mechanisms of PLD

In contrast to the simplicity of PLD system set-up, its principle involves a complex physical phenomenon. It includes all the physical processes during laser-material interaction, formation of plasma plume, transfer of the ablated material through the plasma plume unto the heated substrate and the growth process. Hence, PLD process is divided into four stages:

i. The interaction of the laser beam with the target.
ii. The dynamics of ablation of materials and plume formation.
iii. The evaporation of the ablated materials onto the substrate.
iv. The nucleation and growth of a thin film on the surface of the substrate.

2.6.3. The interaction of the laser beam with the target

The laser beam is focused onto the surface of the target at an incidence angle of 45° (to avoid spatial overlap between the plume and the incident laser) as shown in Fig. 2.5. On hitting the surface of the target, the target absorbs the incident laser and it induces oscillations of the electrons in the material by transferring of energy to the electrons. The energy absorbed per unit area by the target material depend on the fluence of the laser (time integral of laser intensity over the pulse duration).

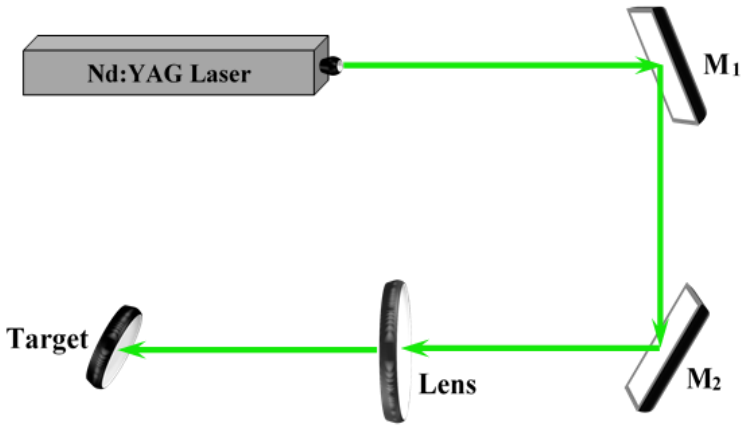

Fig. 2.5: Schematic diagram illustrating the interaction of laser beam with the target.

Collision cascade created among the atoms in the material due to the absorbed incident laser energy creates oscillation field. The oscillation of the electrons leads to electron excitations, which leads to electron-lattice (ions) energy transfer. To eject an atom from the surface of the target material, the energy delivered by the laser pulse to a single atom must be greater than the binding energy of the atom [84]. At a sufficient energy density (at a very short pulse), the elemental species on the surface of the target are heated to their evaporation temperature. This leads to a stoichiometrical evaporation (pulsed-laser ablation) of materials from the surface of the target. The rate of ablation is dependent on the laser fluence hitting the target. The intensity of the laser light impinging on the surface of the target is defined by Lambert-Beer's law [85] given as

$$I(x) = I(x_0)e^{-\alpha(x-x_0)} \tag{2.2}$$

where $I(x)$ is the reduced intensity at an ablated-layer of thickness *x* below the surface of the target, $I(x_0)$ is the intensity just before the incident laser light hit the target material, and α is the absorption coefficient of the target material. The attenuation length (δ) (the optical penetration depth) is defined as [86]

$$\delta = \frac{1}{\alpha} \tag{2.3}$$

The α of any material is related to its refractive index (*n*) by [87]

$$\alpha = \frac{4\pi\kappa_\alpha}{\lambda} = \frac{4\pi n\kappa_0}{\lambda} \tag{2.4}$$

where $\lambda = 2\pi c/\omega$ is the wavelength of the laser [84], *c* the speed of light, ω is the angular frequency,$\kappa_\alpha = n\kappa_0$ is the absorption index and κ_0 is the attenuation index. Comparing Eq. (2.3) and (2.4) shows that the δ is directly proportional to the λ (inversely proportional to energy of the laser light) and inversely proportional to the *n* of the material.

2.6.4. The dynamics of ablation of materials and plume formation

Laser ablation has been analyzed based on thermal, mechanical, photophysical, photochemical and defect models. In all these models, ablation was described based on the dominant mechanism. As stated earlier, ablation process begins with single-phonon or multiphonon excitation in the material. Instantaneous transformation of the excitation energy into heat changes the optical properties of the material with increasing temperature. The increase in temperature of the surface of the target material results in (thermal) material ablation (vaporization) with or without surface melting [86b]. Depending on the target material and the laser wavelength, the ablation threshold ranges from 0.1-1J/cm^2 [84]. Once the ablation threshold of the target material is reached, the ionization of the target material induces plasma (plume) formation (Fig. 2.6), with stoichiometry similar to the target. The plume is collected on a substrate (Fig. 2.6) placed at a short distance from the target.

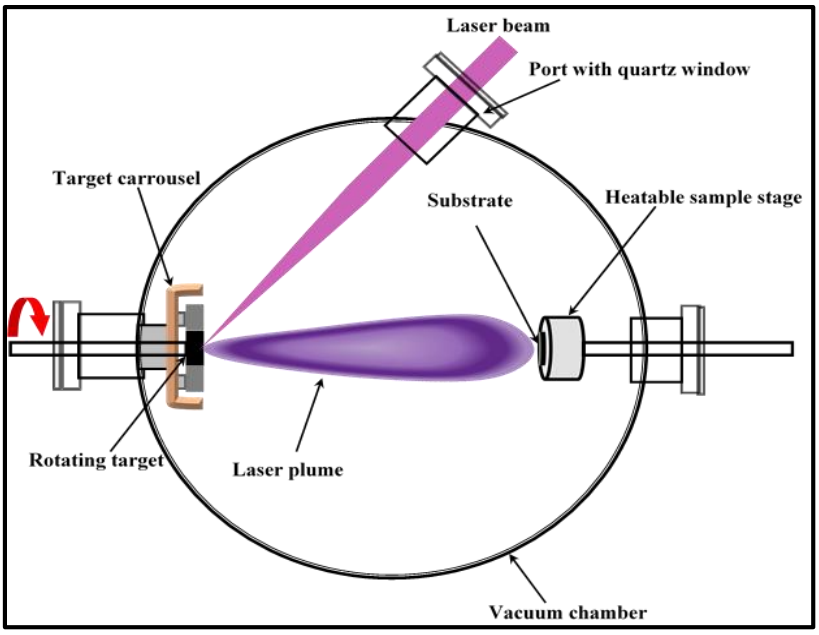

Fig. 2.6: Simplified schematic diagram illustrating PLD set-up.

2.6.5. The evaporation of the ablated materials onto the substrate

The evaporation of the plume onto the substrate plays a crucial rule on the quality of the thin film. Different laser parameters such as the laser energy, pulse repetition rate, and number of pulses can influence the energy of ejected species impinging on the substrate [88]. If the average intensity of the laser beam exceeds the ionization threshold of the material, the target material can ionize early in the laser pulse leading to a high density plume [14]. A very high density plume can induce various type of damages to the substrate. Fig. 2.7 illustrates the mechanisms of interaction between the incident plume flux and the substrate. The energetic incident plume sputters some atom from the surface of the substrate. This creates a collision region (thermalized region) between the incident plume and the sputtered atoms. This region serves as particle condensation source; hence, film growth takes place after the formation of the thermalized region.

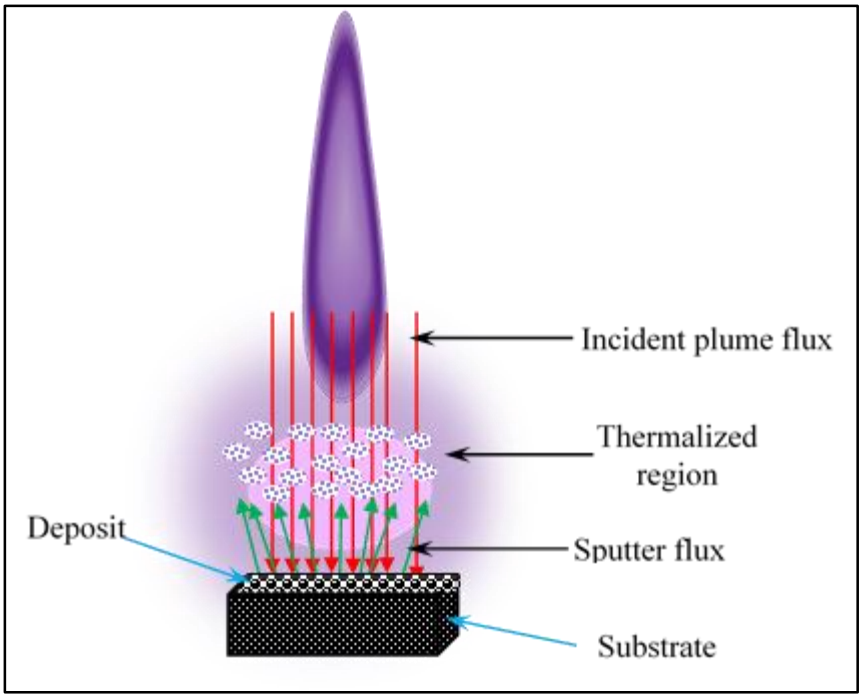

Fig. 2.7: Schematic diagram illustrating the mechanism of interaction between the plume and the substrate.

2.6.6. The nucleation and growth of a thin film on the surface of the substrate

During nucleation and growth stage of PLD, there is a transition from plasma (plume) phase to a crystalline (solid) phase on the substrate surface. Crystalline thin films nucleation and growth depends on several factors, namely, the laser energy, pulse repetition rate, density and degree of ionization of the ablated material, substrate temperature, physico-chemical properties of the substrate, and background pressure. However, the two major thermodynamic parameters involve in the growth mechanism are the substrate temperature T_s, and the supersaturation S, that takes place between the plasma and solid phase of the material during crystallization. These two parameters are related by

$$S = k_B T_s \ln(R / Re) \tag{2.5}$$

where k_B is the Boltzmann constant, R is the rate of deposition and Re is the equilibrium deposition value at temperature T [89]. Eq. (2.5) shows that supersaturation varies directly with the substrate temperature. A small value of supersaturation is characterized by large nuclei, which leads to

creation of dispersed patches (islands) of the films on the surface of the substrate. At this low value of the supersaturation, the inter-step distance between the islands increases and in turn the growing surface becomes smooth [90]. As the number of the clusters impinging on the surface of the substrate increases, the island density increases [91] and the nucleus of the islands shrinks to atomic level as the supersaturation increases [89]. For a further increase in the supersaturation value (at high substrate temperature) the islands emerges via coalescence phenomenon (which is liquid-like for some cases) [91]. High supersaturation rate may be required to initiate nucleation. However, a low supersaturation rate is needed at later stage to facilitate a single crystal film growth [92]. The mean thickness *t* at which the growing and discontinuous thin film reaches continuity is given by

$$t = A(1/R)^{1/3} \exp(-1/T_s) \tag{2.6}$$

where T_s is the substrate temperature, R is the deposition rate and A is a constant related to the properties of the material [93].

Generally, there are three modes of thin film growth, namely, Island or Volmer–Weber mode, Layer-by-layer or Frank–van der Merwe mode, and Layer plus island or Stranski–Krastanov mode.

2.6.6.1. Island or Volmer–Weber mode

An island growth occur when the cohesion between the atoms of the target material is greater than the adhesion between the target atoms and the substrate. As a result, the adatoms are more bound to each other than to the substrate, hence forming clusters [91]. This mode of growth is characterized by three-dimensional (3D) islands (Fig. 2.8 (a)).

2.6.6.2. Layer-by-layer or Frank–van der Merwe mode

Layer-by-layer growth occur when the adhesion between the adatoms and the substrate is greater than the cohesion between the adatoms. This mode of growth generally results to 2D growth with the adatoms forming smooth monolayers on the surface of the substrate [94] (Fig. 2.8 (b)).

2.6.6.3. Layer plus island or Stranski–Krastanov mode

Layer plus island growth mode occurs when islands are formed after the formation of one or two monolayers on the surface of the substrate (Fig. 2.8 (c)) [91].

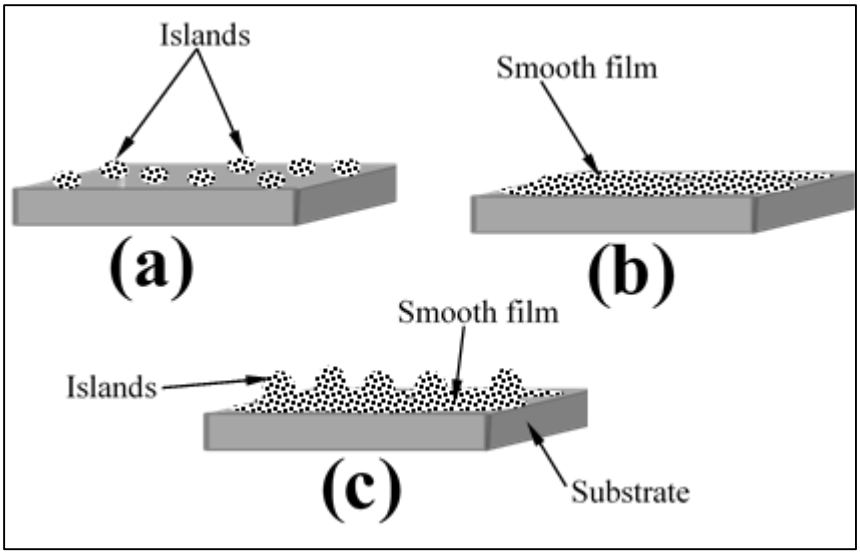

Fig. 2.8: Modes of thin film growth (a) Island (b) Layer-by-layer and (c) Layer plus island.

2.6.7. Advantages and disadvantages of PLD

Compared to other popular thin film deposition techniques, such as physical vapor deposition and chemical vapor deposition (CVD), pulsed laser deposition (PLD) has shown some outstanding advantages. In CVD, precursors are used as the starting material, while in PLD solid targets are deposited on a substrate using laser ablation. In PLD, the rate of the film growth can be controlled by changing background gas, adjusting the laser parameters, deposition time, substrate to target distance, etc. [95]. Some of the major features of PLD are the transfer of the stoichiometry of the target material deposited on the substrate, deposition at high temperature and high deposition rate [88, 79]. Another advantage of PLD is that a very short time frame is required for deposition.

A major disadvantage of PLD is the non-uniformity of the particulate size across the surface of the film. This non-uniform distribution of particulate size is due to the presence of molten material (up to ~ 10 μm) in the ablated material.

2.7. References

[1] J. Felsche, The crystal chemistry of the rare-earth silicates, In, R.A. Penneman, R.R. Ryan, A. Rosenzweig, R. Reisfeld, J. Felsche, C.K. Jørgensen, "*Structure and Bonding*" Springer, Berlin, 13 (1973) p. 99-197.

[2] Y.I. Smolin, S.P. Tkachev, Kristalografiya 14 (1969) 22.

[3] K. Fukuda, T. Iwata, Powder Diffr. 21 (2006) 300.

[4] R. Lisiecki, G. Dominiak-Dzik, P. Solarz, W. Ryba-Romanowski, M. Berkowski, M. Glowacki, Appl. Phys. B 98 (2010) 337.

[5] J. Wen, C.K. Duan, L. Ning, Y. Huang, S. Zhan, J. Zhang, M. Yin, J. Phys. Chem. A 118 (2014) 4988.

[6] E.M. Rabinovich, J. Shmulovich, V.J. Fratello, N.J. Kopylov, Am. Ceram. Soc. Bull. 66 (1987) 1505.

[7] R.D. Shannon, Acta. Crystallogr. 32 (1976) 751.

[8] A.A. Bosak, C. Dubourdieu, J.P. S*é*nateur, O. Yu. Gorbenko, A.R. Kaul.. Crystal Engineering 5 (2002) 355.

[9] R. Lisiecki, G. Dominiak-Dzik, P. Solarz, W. Ryba-Romanowski, M. Berkowski, M. Glowacki. Appl. Phys. B 98 (2010) 337.

[10] D.W. Cooke, E.A. McKigney, R.E. Muenchausen, B.L. Bennett, U.S. Patent No. 60/752,981. (2005).

[11] T.E. Peters, J. Electrochem. Soc. 116 (1969) 985.

[12] J. Wang, S. Tian, G. Li, F. Liao, X. Jing, J. Electrochem. Soc. 148 (2001) H61.

[13] R.Y. Lee, F.L. Zhang, J. Penczek, B.K. Wagner, P.N. Yocom, C.J. Summers, J. Vac. Sci. Technol. B 16 (1998) 855.

[14] C.M Michail, A. Toutountzis, I.G. Valais, I. Seferis, M. Georgousis, G. Fountos, I.S. Kandarakis , G.S. Panayiotakis, e-JST 2 (2010) 25.

[15] T. Kamae, Y. Fukazawa, N. Isobe, M. Kokubun, A. Kubota, S. Osone, T. Takahashi, N. Tsuchida, H. Ishibashi, Nucl. Instr. Meth. Phys. Res. A 490 (2002) 456.

[16] V. Avdeichikov, B. Jakobsson, V. A. Nikitin, V. Nomokonov, A. Wegner, Nucl. Instr. Meth. Phys. Res. A 484 (2002) 251.

[17] W. Mangesha, T.D. Taulbee, J.D. Valentine, B.D. Rooney, Nucl. Instr. Meth. Phys. Res. A 486 (2002) 448.

[18] I. Warshaw, R. Roy, Am. Ceram. Soc. Bull. 38 (1959) 169.

[19] C. Itoh, K. Tanimura, N. Itoh, J. Phys. C: Solid State Phys. 21 (1988) 4693.

[20] D. Stewart. Praseodymium. Chemicool. com, Retrieved October, (2017) from http://www.chemicool.com/elements/praseodymium.html.

[21] J.-C.G. Bünzli, S.V. Eliseeva. Basics of lanthanide photophysics. Laboratory of lanthanide supramolecular chemistry, E ´ cole Polytechnique Fe´de´rale de Lausanne, Switzerland (2011).

[22] R.T. Wegh, A. Meijerink, Phys. Rev. B 60 (1999) 10820.

[23] J.C. Krupa, M. Queffelec, J. Alloys & Comp. 250 (1997) 287.

[24] J. Becker, J.Y. Gesland, N.Y. Kirikova, J.C. Krupa, V.N. Makhov, M. Runne, M. Queffelec, T.V. Uvarova, G. Zimmerer, J. Lumin. 78 (1998) 91.

[25] A.N. Belsky, P. Chevallier, J.Y. Gesland, N.Y. Kirikova, J.C. Krupa, V.N. Makhov, P. Martin, P.A. Orekhanov, M. Queffelec, J. Lumin. 146 (1997) 72.

[26] E.G. Gumanskaya, M.V. Korzhik, S.A. Smirnova, V.B. Pawlenko, A.A. Fedorov, Opt. Spectrosc. 72 (1992) 86.

[27] I. Sokolska, S. Kück, M. Baluka, Investigation of high-energetic transitions in some Pr^{3+}-doped fluoride and oxide crystals, Proc. SPIE 4412 (2001) 236.

[28] a) J.L. Sommerdijk, A. Bril, A.W. de Jager, J. Lumin. 8 (1974) 341. b) W.W. Piper, J.A. deLuca, F.S. Ham, J. Lumin. 8 (1974) 344.

[29] G. Blasse, J.P.M. Vliet, J.W. M. Verwey, R. Hoogendam, M. Weigel, J. Phys. Chem. Solids

50 (1989) 583.

[30] T. Juestel, W. Mayr, P.J. Schmidt, Tuning the 4f15d-4f2 UV emission of Pr^{3+}, 200^{th} Meeting of the Electrochemical Society, San Francisco, CA, USA, September (2001).

[31] G.G. Grigoryan, Y.V. Orlov, E.A. Petrenko, A.Y. Shashkov, N.V. Znamenskiy, Laser Phys. 15 (2005) 602.

[32] A.A. Kaminskii, L. Li, A.V. Butashin, V.S. Mironov, A.A. Pavlyuk, S.N. Bagayev, K, Ueda, Jpn. J. Appl. Phys. 36 (1997) L107.

[33] N.V. Kuleshov, V.G. Shcherbitsky, A.A. Lagatsky, V.P. Mikhailov, B.I. Minkov, T. Danger, T. Sandrock, G. Huber, J. Lumin. 71 (1997) 27.

[34] R.M. Percival, M.W. Phillips, D.C. Hanna, A.C. Tropper, IEEE J. Quantum Electron. 25 (1989) 2119.

[35] S. Watanabe, K. Ogasawara, M. Yoshino, T. Nagasaki. Phys. Rev. B 81 (2010)125128.

[36] V.N. Boikov, N.V. Kuleshov, B.I. Minkov, V.P. Mikhailov, D.S. Umreiko, J. Appl. Spectro. 62 (1995) 123.

[37] J. Jordan, D.A. Rothamer. Thermographic phosphor based planar thermometry using the trivalent Praseodymium ion (Pr^{3+}) doped into a yttrium aluminum garnet (YAG) crystal. Spring Technical Meeting of the Central States Section of the Combustion Institute April 22–24 (2012).

[38] A.P. Vink, P. Dorenbos, C.W.E. Vijk, Phys. Rev. B 66 (2002) 075118.

[39] A. Novoselov, H. Ogino, A. Yoshikawa, M. Nikl, J. Pejchal, J.A. Mares, A. Beitlerova, C. D'Ambrosio, T. Fukuda, J. Cryst. Growth 287 (2006) 309.

[40] H-H, Wang, Z-H. Kang, Y. Jiang, Y-J. Li, D-M. Du, X-G. Wei, J-H. Wu, J-Y. Gao, Appl. Phys. Lett. 92 (2008) 011105.

[41] L.E. Cates, J.H. Kim, Opt. Mat. 36 (2013)2347.

[42] Slashdocs.com (2009). Dysprosium. Retrieved October, (2017) from http://www.slashdocs.com/hohohohohohohohok/Atomic%20Symbol.html.

[43] G.L. Miessler, D.A. Tarr, Inorganic Chemistry, 2nd Edn., Prentice-Hall, New Jersey, USA (999) p. 358–360.

[44] S. Chemingui, M. Ferhi, K.H. Naifer, M. Ferid, J. Lumin. 166 (2015) 82.

[45] S.N. Ogugua, H.C. Swart, O.M. Ntwaeaborwa, Physica B 480 (2016) 131.

[46] S.N. Ogugua, S.K.K. Shaat, H.C. Swart, O.M. Ntwaeaborwa, J. Phys. Chem. Solids 83 (2015) 109.

[47] M.N. Luwang, R.S. Ningthoujam, S.K. Srivastava, R.K. Vasta, J. Mater. Chem. 21 (2011) 5326.

[48] S.D. Meetei, M.D. Singh, S.D. Singh, J. Appl. Phys. 115 (2014) 204910.

[49] K. Brahmachary, D. Rajesh, Y.C. Ratnakaram, Optik. 126 (2015) 4050.

[50] S. Dutta, S. Som, S.K. Sharma, Dalton Trans. 42 (2013) 9654.

[51] K.N. Shinde, I.M. Nagpure, S.J. Dhoble, S.V. Godbole, M.K. Bhide, Indian J. Phys. 83 (2009) 503.

[52] Sk.N. Rasool, L.R. Moorthy, C.K. Jayasankar, Solid State Sci. 22 (2013) 82.

[53] C.R. Kesavulu, C.K. Jayasankar, Mat. Chem. & Phy. 130 (2011) 1078.

[54] P. Suthanthirakumar, K. Marimuthu, J. Mol. Struct. 1125 (2016) 443.

[55] C-H. Liang, L-G. Teoh, K.T. Liu, Y-S. Chang, J. Alloys Compd. 517 (2012) 9.

[56] M. Lackner, Combustion synthesis: Novel routes to novel materials, Bentham Science Publishers, UAE (2009) a) p. 1, b) p. 2.

[57] Chem.libretexts.org, Oxidizing and reducing agents, Retrieved October, (2017) from https://chem.libretexts.org/Core/Analytical_Chemistry/Electrochemistry/Redox_Chemistry/Oxidizing_and_Reducing_Agents.

[58] P.P. Sarangi, N.N. Ghosh, Low temperature combustion synthesis of α-Fe_2O_3 and $Ni_{(1-x)}Zn_xFe_2O_4$ nanopowder, In, M. Lackner (Ed.), "*Combustion synthesis: Novel routes to novel materials*", Bentham Science Publishers, UAE (2009) p. 123 - 131.

[59] X. Su, F. Fu, Y. Yan, G. Zheng, T. Liang, Q. Zhang, X. Cheng, D. Yang, H. Chi, X. Tang, Q. Zhang, C. Uher, Nat. Commun. 5 (2014) 4908.

[60] H. Zarrinpour, S. Firoozi, V. Milani, Ceram. Int. 42 (2016) 11217.

[61] J. Chandradass, M. Balasubramanian, K.H. Kim, Emulsion combustion synthesis, In, M. Lackner (Ed.), "*Combustion synthesis: Novel routes to novel materials*", Bentham Science Publishers, UAE (2009) p. 25 - 32.

[62] E. Mercadelli, C. Galassi, A.L. Costa, S. Albonetti, A. Sanson, J. Sol. Gel. Sci. Technol. 46 (2008) 39.

[63] C. Fu, G. Li, D. Luo, J. Zhang, L. Li, J. Mater. Chem. A 2 (2014) 1471.

[64] K.C. Patil, S.T. Aruna, T. Mimani, Curr. Opin. Solid State Mater. Sci. 6 (2002) 507.

[65] A.S. Mukasyan, C. Costello, K.P. Sherlock, D. Lafarga, A. Varma, Spar. Purif. Technol. 25 (2001) 117.

[66] K. Deshpande, A. Mukasyan, A. Varma, J. Am. Ceram. Soc. 86 (2003) 1149.

[67] A. Varma, A.S. Rogachev, A.S. Mukasyan, S. Hwang, Adv. Chem. Eng. 24 (1998) 79.

[68] T. Striker, J.A. Ruud, J. Am. Ceram. Soc. 93 (2010) 2622.

[69] A.S. Mukasyan, P. Epstein, P. Dinka, Proc. Combust. Inst. 31 (2007) 1789.

[70] A.K. Alves, C.P. Bergmann, F.A. Berutti, Novel synthesis and characterization of nanostructured materials, Springer-Verlag Berlin Heidelberg (2013) p. 12.

[71] J.W. McCauley, J.A. Puszynski, Int. J. Self-Propag. High-Temp. Synth. 17 (2008) 58.

[72] S.N. Ogugua, M.Sc. Thesis, University of the Free State, South Africa (2015) p. 51-52.

[73] T. Lazarova, M. Georgieva, D. Tzankov, D. Voykova, L. Aleksandrov, Z. C-Zheleva, D. Kovacheva, J. Alloys Compd. 700 (2017) 272.

[74] B.S.B. Reddy, I. Mal, S. Tewari, K. Das, S. Das, MMTA. 38A (2007) 1786

[75] A.S. Prakash, A.M.A. Khadar, K.C. Patil, M.S. Hegde, J. Mater. Synth. Process. 10 (2002) 135.

[76] F. Breech, L. Cross, Appl. Spectroscopy 16 (1962) 598.

[77] H.M. Smith, A.F. Turner, Appl. Opt. 4 (1965) 147.

[78] D. Dijkkamp, T. Venkatesan, X.D. Wu, S.A. Shareen, N. Jiswari, Y.H. Min-Lee, W.L. McLean, M. Croft, Appl. Phys. Lett. 51 (1987) 619.

[79] J.T. Cheung, History and fundamentals of pulsed laser deposition, In, D.B. Chrisey, G.K. Hubler (Ed.), "*Pulsed laser deposition of thin films*", (1St Edi.) Wiley Interscience (1994) p. 1-19.

[80] D.P. Norton, Pulsed laser deposition of complex materials: Progress toward applications, In, R. Eason (Ed.), "*Pulsed laser deposition of thin films: Applications-led growth of functional materials*", Wiley Interscience (2007) p 1-28.

[81] J.A. Greer, H.J. Van Hook, Mater. Research Soc. Symposium Proc. 191 (1990) 171.

[82] A.J. Greer, J. Phys. D: Appl. Phys. 47 (2014) 034005.

[83] H-U. Krebs, M. Weisheit, J. Faupel, E. Süske, T. Scharf, C. Fuhse, M. Störmer, K. Strum, M. Seibt, H. Kijewski, D. Nelke, E. Panchenko, M. Buback, Pulsed laser Deposition (PLD) – a Versatile Thin Film Technique, In, B. Kramer (Ed.), "*Advances in Solid State Physics*" Springer-Verlag Berlin Heidelberg 43 (2003) p. 505-517.

[84] E.G. Gamaly, A.V. Rode, B.L. Davies, Ultrafast laser ablation and film deposition, In, R. Eason (Ed.) "*Pulsed laser deposition of thin films – Applications-led growth of functional materials*", John Wiley & Sons, Inc., Hoboken, New Jersey, (2007) p. 99-129.

[85] W.M. Steen, Laser material processing, Springer-London, (1991) p. 81-89.

[86] D. Bäuerle, Laser processing and chemistry, (3rd Edi.), Springer-Verlag Berlin Heidelberg, (2000), a) p. 221, b) p. 226.

[87] D. Bäuerle, Laser processing and chemistry, (4th Edi.), Springer-Verlag Berlin Heidelberg, (2011) p 20.

[88] J. Schou, Laser beam–solid Interactions: Fundamental aspects, In, Y. Pauleau (Ed.), "*Materials surface processing by directed energy techniques*", (1st Edi.), E-MRS, Great Britain (2006) p. 35–66.

[89] S. Soltan, Interaction of superconductivity and ferromagnetism in YBCO-LCMO heterostructures, Cuvillier Verlag, Göttingen, Germany, (2005) p. 63.

[90] T. Nishinaga, H.J. Scheel, Crystal growth aspects of high-Tc superconductors, Proceedings ISS'95, In H. Hayakawa, Y. Enomoto (Ed.), "*Advances in superconductivity VIII*", Springer, Tokyo, 1 (1996) p. 33-38.

[91] P.H. Le, C.W. Luo, Thermoelectric and topological insulator bismuth chalcogenide thin films grown using pulsed laser deposition, In, D. Yang (Ed.), "*Applications of laser ablation - thin film deposition, nanomaterial synthesis and surface modification*" InTech, Rijeka, Croatia, (2016) p. 55-84.

[92] J.J. Richardson, F.F. Lange, Low temperature continuous circulation reactor for the aqueous synthesis of ZnO films, nanostructures, and bulk single crystals, US patent No: US 8,926,750 B2, (2015).

[83] S. Metev, K. Meteva, Appl. Surf. Sci. 43 (1989) 402.

[94] C.W. Schneider, T. Lippert, Laser ablation and thin film deposition, Paul Scherrer Institut, materials group, general energy research department, Villigen PSI, Switzerland (2010).

[95] S.N. Ogugua, R.L. Nyenge, P.T. Sechogela, H.C. Swart, O.M. Ntwaeaborwa, J. Vac. Sci. Technol. A 34 (2016) 021520.

CH. 3

Characterization techniques

3.1. Introduction

This chapter gives brief description of the various characterization techniques used in this thesis. These techniques includes X-ray diffraction (XRD), X-ray Photoelectron Spectroscopy (XPS), Time of Flight Secondary Ion Mass Spectroscopy (Tof-SIMS), Scanning Electron Microscope (SEM), Energy dispersive X-ray spectroscopy (EDS), Atomic Force Microscope (AFM), Rutherford Backscattering Spectrometry (RBS), Ultraviolet-Visible Spectroscopy and Photoluminescence Spectroscopy.

3.2. X-Ray Diffraction

X-ray diffraction (XRD) is a non-destructive analytical technique used for structural characterization of crystalline compounds and for face identification. XRD technique based on the principle Bragg's law. Consider X-ray beam (I) with wavelength λ incident on a perfect crystal as shown in Fig. 3.1. If the incident and the reflected beam (R) meet Bragg's condition [1], then Bragg's law is written as

$$n\lambda = 2dSin\theta \qquad (3.1)$$

where n is the other of reflection and can take any positive integer, d is the interplanar spacing and θ is the incident angle.

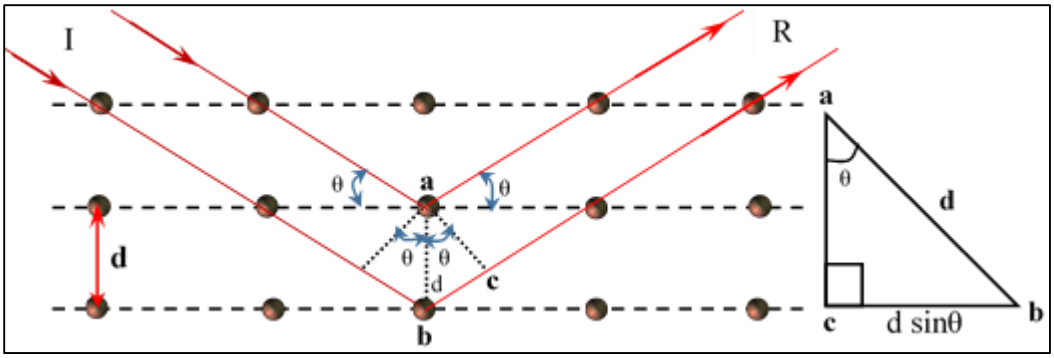

Fig. 3.1: Schematic diagram of X-ray diffraction from the surface of a perfect crystal.

The experimental set-up for X-ray diffraction is made of tree basic components, namely, an X-ray tube, a sample holder and an X-ray detector (Fig. 3.2). The X-rays tube contain a copper block connected to anode and cathode made respectively of a metal and a tungsten filament. The copper block is cool down using water. Electrons generated by heating up the tungsten filament (cathode) are accelerated to the anode by applying a very high potential different between the anode and the cathode. By bombarding the metal anode with these stream of electrons, characteristic X-rays are produced (mainly CuK_β and CuK_α with wavelengths 1.39 and 1.54 Å, respectively). The CuK_β radiation is absorbed using a Nickel filament, which absorbs below 1.54 Å. This wavelength (monochromatic X-ray) is use to excite the sample [2, 3].

In X-ray diffraction, X-ray tube, sample and detector arrangement is based on the Bragg-Brentano geometry. This geometry can be in $\theta - \theta$ or $\theta - 2\theta$ configuration. The $\theta - \theta$ configuration allows the sample to be fixed at the center of the goniometer, and the X-ray source and the detector rotates around a common axis located at the center of the goniometer. Here the sample lies on a horizontal plane that forms vertical planes at angle θ with both the X-ray source and the detector. The X-ray source and the detector rotate at the same angular velocity enabling them to maintain equal angles with the surface of the sample. With this condition, the reflected beam is captured once diffraction occur at the Bragg angle. In the $\theta - 2\theta$ configuration, the X-ray source is fixed at position forming an angle θ with the non-stationary sample. Thus, the variation in the angle of the incident X-ray beam is due to the sample's movement. The sample rotate in the same axis with the detector but the detector move at twice the speed of the sample, hence the diffraction angle 2θ, is always twice the glancing angle, θ [4].

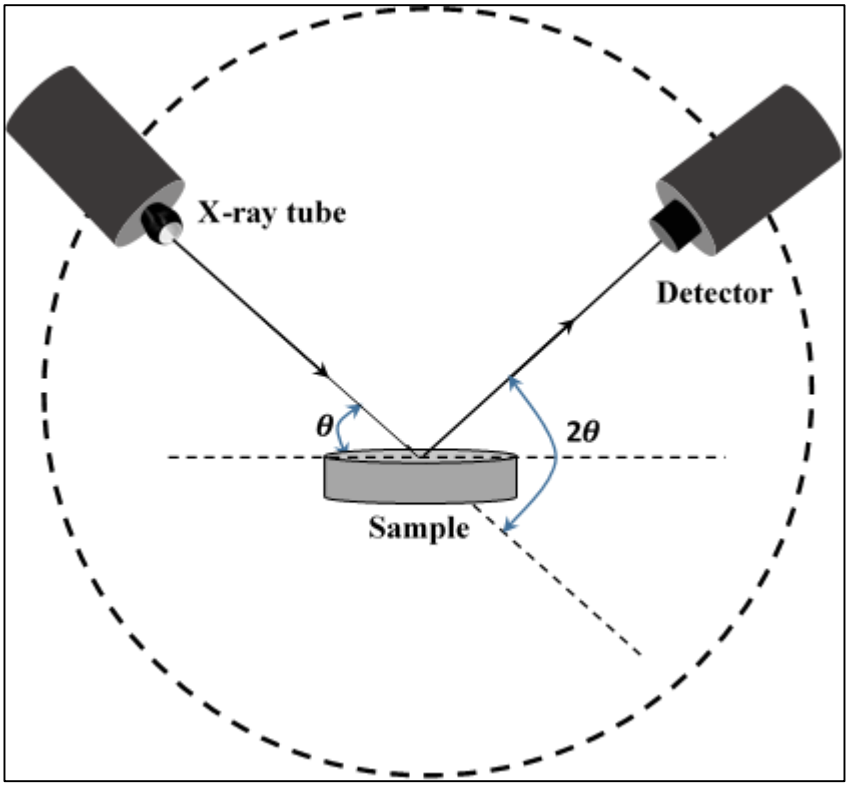

Fig.3.2: Schematic diagram of an X-ray diffractometer.

3.3. X-ray Photoelectron Spectroscopy

X-ray photoelectron spectroscopy (XPS) is an in-situ analytical technique for qualitative and quantitative study of the elemental composition, oxidation state, chemical and electronic states of elements in the surface region of a material. The standard laboratory energy source for XPS are MgKα and AlKα with energies of 1253.3 and 1486.6 eV, respectively. XPS is based on the principle of photoelectric effect [5]. An incident X-ray beam is used to eject characteristic photoelectron from the core level (K shell) of an atom (Fig. 3.3), and a high sensitive analyzer is used to determine the kinetic energy of the electron. The kinetic energy of the ejected photoelectron gives information about its binding energy. The distribution of the binding energies gives information on the chemical composition of the sample, since binding energies are characteristic for each element. The binding energy of the photoelectron (E_B) is related to the kinetic energy of the photoelectron measured by analyzer (E_k) by

$$E_B = h\nu - E_k - \varphi_A \tag{3.2}$$

where $h\nu$ is the energy of primary X-ray beam, and φ_A is the work function of the analyzer. Eq. (3.2) shows that the binding energy of the photoelectron is independent of the work function of the specimen. Hence, once the kinetic energy is measured by the XPS spectrometer and the X-ray energy and the work function of the analyzer are known, the binding energy of the photoelectron can be determined. All XPS measurements are performed under ultra-high vacuum (UHV) chamber ($\sim 10^{-11}$mbar).

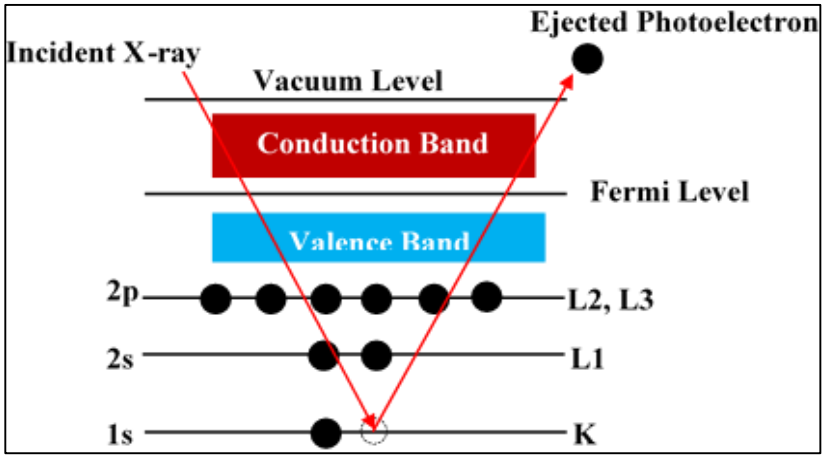

Fig. 3.3: Schematic diagram of the XPS process, showing photo-ionization of an atom by the ejection of a K electron.

A typical XPS set up is shown in a schematic diagram in Fig. 3.4. It is made of for components, namely, a fixed energy X-ray source, electron energy analyzer to measure the energy of electrons of the same energy, electron detector and a recorder. The angles α and θ are the X-ray grazing-incidence angle and the photoelectron emission angles, respectively, relative to the surface normal. During XPS, the sample is rotated with respect to the entrance of the photoelectron analyzer to maintain the surface sensitivity of the technique (photoelectrons are generated from 0-10 nm top layers of the sample). The concentric hemispherical analyzer (CHA) filters the electrons that enters into the detector with respect to their energies. The CHA consists of two entrance lenses (lens 1

and lens 2) which focus the incoming electrons onto the entrance aperture, two hemispherical electrodes held at negative voltage and an exit slit [6]. The lens system also retards the photoelectrons to the pass energy (the retarding voltage applied at the entrance slit to slow the electrons down so that they can be captured by the detector) of the analyzer. The pass energy is the potential difference between the two hemispheres and it is fix (~10 to 100 eV). Only photoelectrons with kinetic energy equal the pass energy are allowed to enter the analyzer. As mentioned earlier, laboratory X-ray sources for XPS analysis are Al Kα (E = 1487 eV) and Mg Kα (E = 1254 eV), hence, the emitted photoelectrons will have kinetic energies in the range of 0 - 1480 eV or 0 – 1250, respectively.

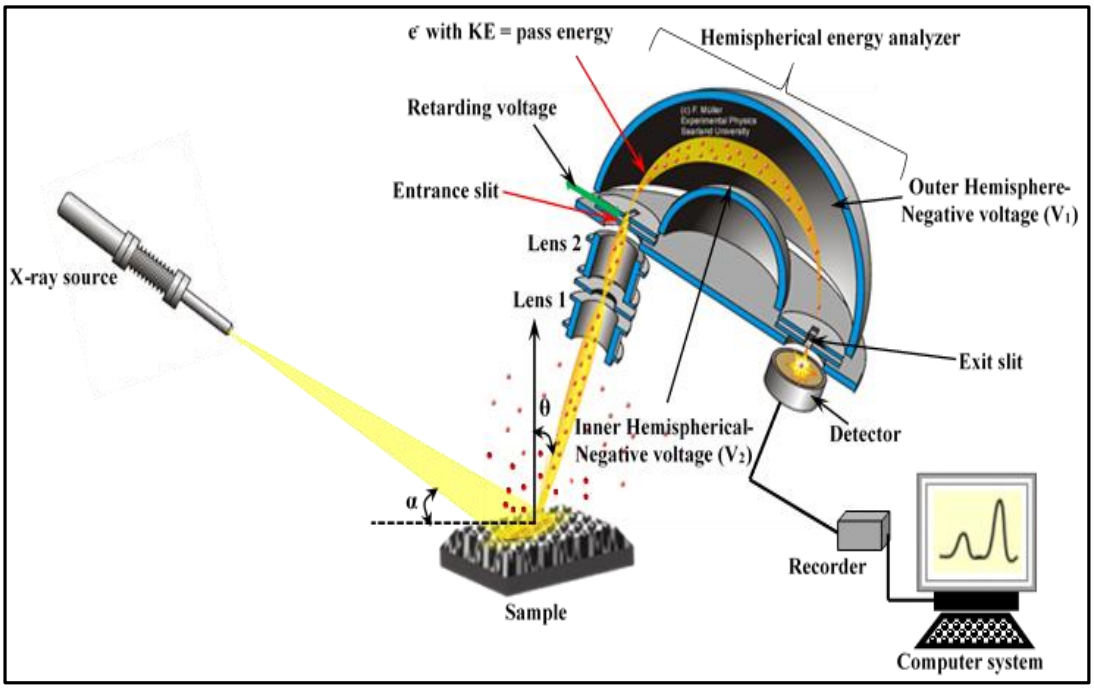

Fig. 3.4: Schematic set-up of XPS system.

3.4. Time-of-Flight Secondary Ion Mass Spectroscopy

Time-of-flight secondary ion mass spectroscopy (ToF-SIMS) is based on the emission of secondary ions from the surface of a material after impact on the surface by KeV energy pulsed primary ion beam (Cs or micro-focused Ga) [7, 8]. Over 95% of the secondary ions emanate from

the outermost 1-2 layers of the sample, hence defining ToF-SIMS as a surface sensitive technique [9]. Because of its surface sensitivity, ToF-SIMS has been used to characterize varieties of conducting and non-conducting surfaces. Common applications include metals, semiconductors, biomaterials, ceramics, lubricants, polymers, glasses, catalysts, pharmaceuticals, thin films and paper [9]. ToF-SIMS is also applied in depth profiling. During ToF-SIMS depth profiling, a low energy ion gun is operated in DC mode for sputtering with high depth resolution. Data acquisition is accomplished using the same or a second ion gun operated in pulsed mode. Depth profiling by ToF-SIMS allows monitoring of all species of interest simultaneously with high-mass resolution to remove any interference [10].

The basic set-up for a ToF-SIMS experiment is shown in Fig. 3.5. The impinging primary ion beam transfer energy and moment to the atoms in the sample. This results to collision cascade within the atoms in the sample. These energetic interactions produces a cloud of atoms and molecules among which some are ionized. The ionized particles of one polarity, atomic and molecular secondary ions are accelerated by electric field through a 2 m field-free tube, where the secondary ions are separated according to their mass-to-charge ratio (Eq. (3.3)) into a reflectron type spectrometer.

$$\frac{m}{z} = 2eEs(t/d)^2 \tag{3.3}$$

where m is the mass, e is elementary charge, z is the number of elementary charges, s is the length of the tube over which an extraction potential $E = V/s$ is applied, t is time-of-flight, V is the applied voltage and d is the length of the secondary ions trajectory tube. The spectrum obtained with each primary ion pulse is collected and summed over many pulses (typically 105 – 107). Finally, the spectrum is converted from a ‘time-of-flight’ scale into a mass scale via mass calibration using a number of known secondary ions [11].

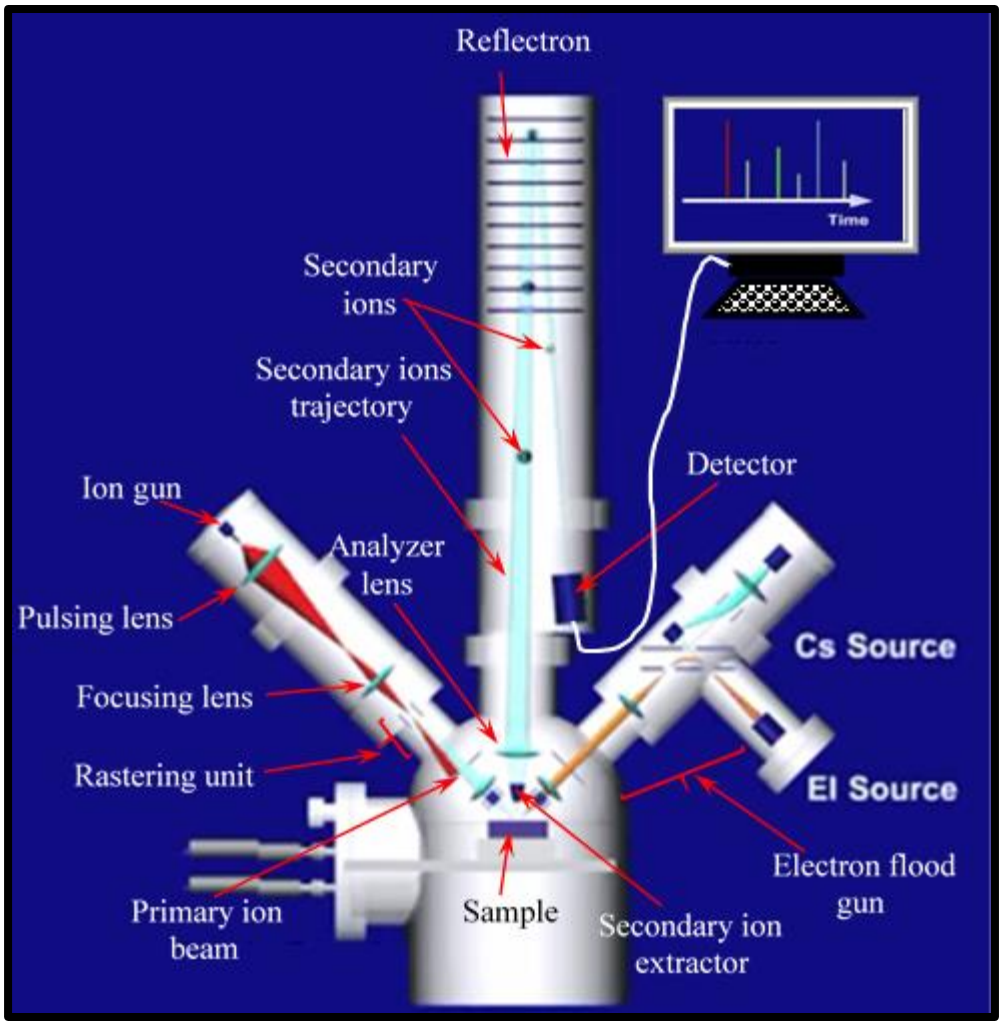

Fig. 3.5: Schematic set-up of ToF-SIMS system.

3.5. Scanning Electron Microscope

Scanning electron microscope (SEM) is use to generate a high-magnified image of an object by scanning a focused energetic electron beam across the surface of a sample and detecting the signal that arise from different depths of the sample due to the interaction of the electron beam and the object (Fig. 3.6) [12]. The signals generated include secondary ions, backscattered electrons, characteristic X-ray, cathodoluminescence, absorbed current and transmitted electrons. This signal gives information about the sample's external morphology, chemical composition, crystalline structure and the orientation of materials the sample is made of [12]. The secondary electrons are

generated due to inelastic scattering process close to the surface layers (100 nm) of a sample, hence, they have very low energy. SEM image is produce by the secondary electrons. Backscattered electrons are generated due to electron reflected from the sample through elastic scattering, hence, they have energy comparable to that of the incident electrons [13]. The intensity of backscattered electrons are related to the atomic number of the sample, hence, backscattered electron image can provide information about elemental distribution in the sample. Characteristic X-ray are generated when electron from higher orbital fill the orbital of an electron removed from the inner shell (K-shell) and emit energy (Fig. 3.7) [14]. Characteristic X-rays gives the composition and abundance of elements in the sample. Energy dispersive X-ray spectrometer (EDS) is used in SEM for detecting the characteristic X-rays that are generated and emitted from the sample [15].

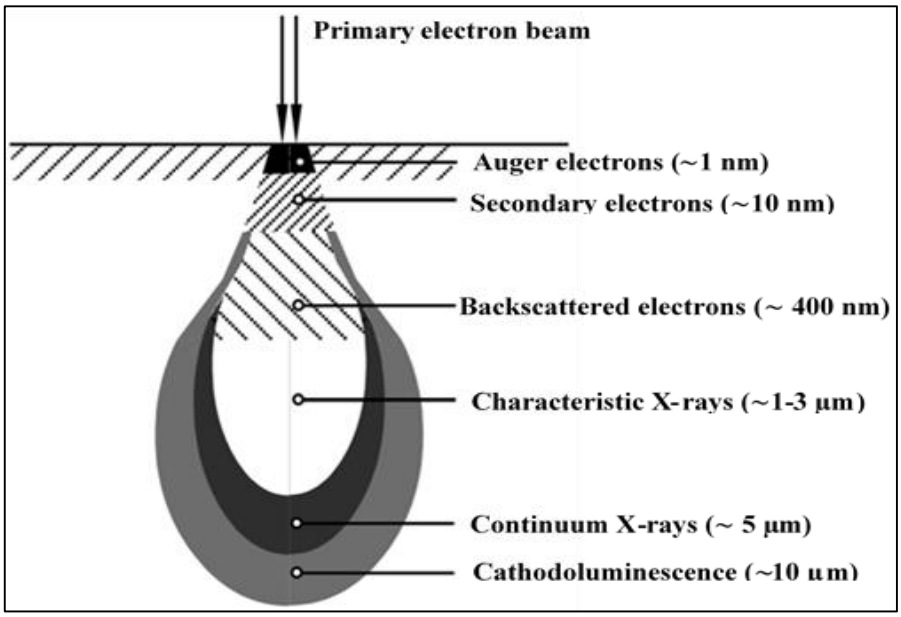

Fig. 3.6: Illustration of the interaction volume of an electron beam on a sample.

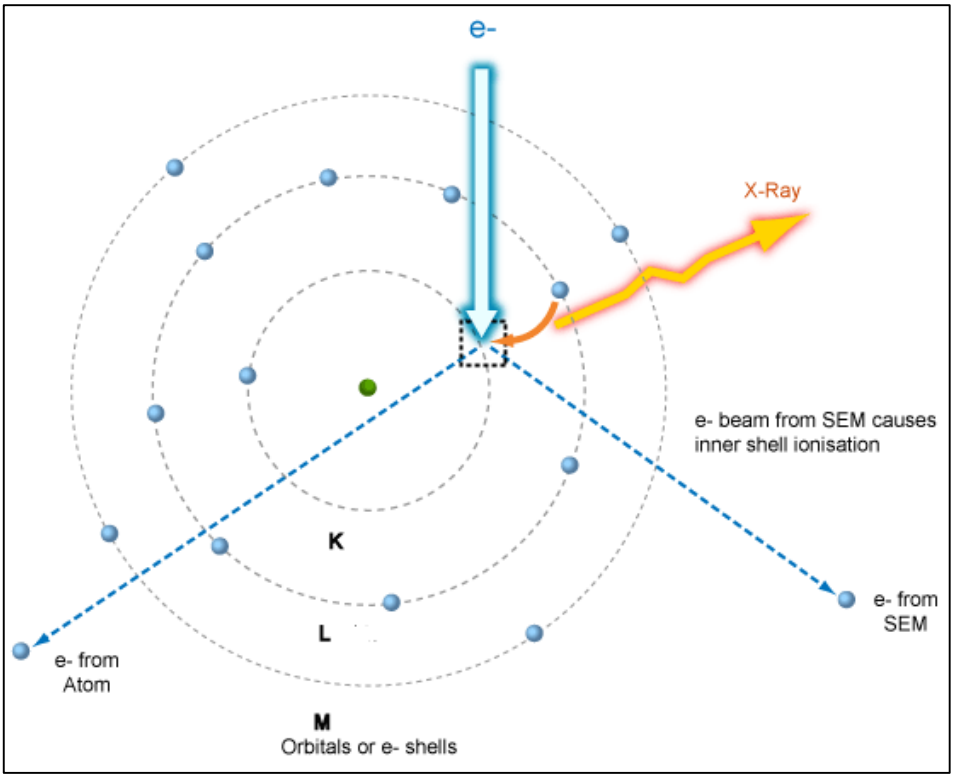

Fig. 3.7: Generation of characteristic X-ray from a sample.

The schematic diagram of SEM system is shown in Fig. 3.8. It is composed of an electron gun, an anode, set of lenses, sample stage and detectors. SEM operates in a very low vacuum pressure. The electron gun uses Schottky field emission (strong electric field is used to pull electrons from the atoms) to generate electrons with beam diameter in the order of 10−100 nm. The anode accelerates the electrons with a typical voltage of 0.1-50 KeV. The condenser lenses further narrowed the electron beam to the diameter of 1−10 nm before they arrive onto the surface of the specimen with electron-probe current in the range of 10^{-9}−10^{-12} A [16]. The objective lens is used to finely scan the electron beam across the surface of the sample, by varying the potential difference between the plates of the lens. The different detectors, secondary electron detector, backscattered electron detector and the X-ray detector are used to detect the secondary electrons, backscattered electrons and the characteristic X-rays, respectively.

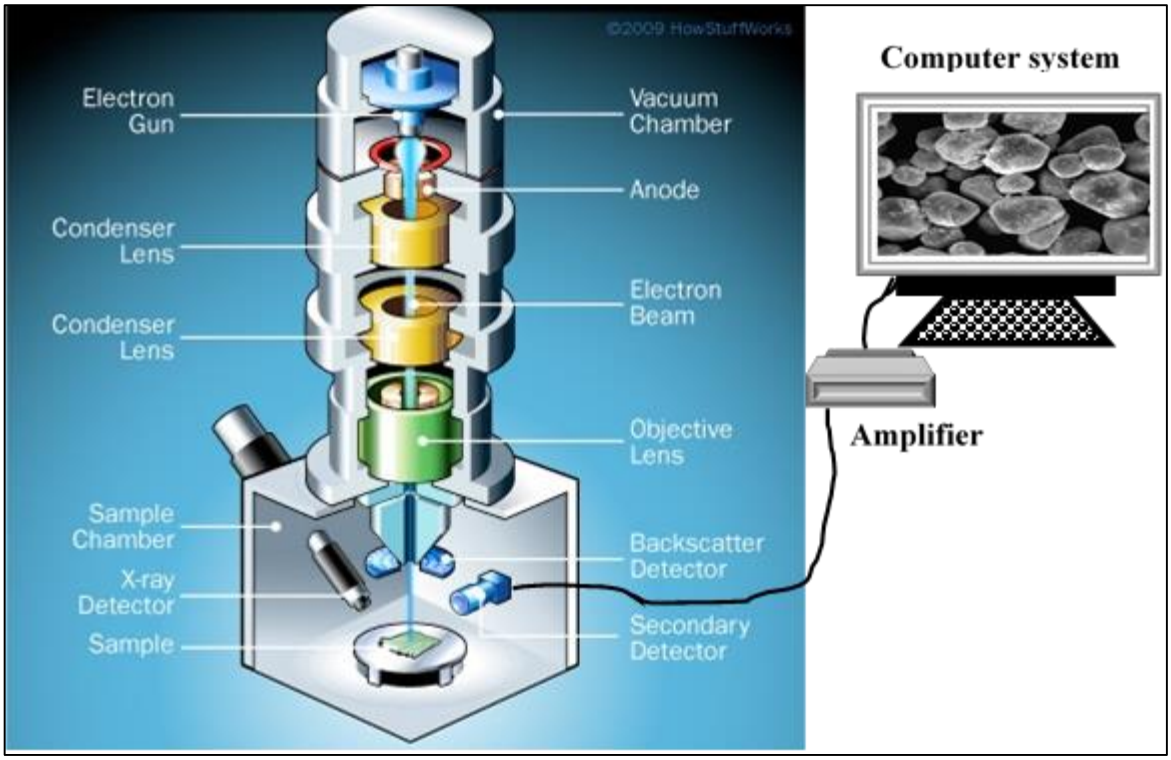

Fig. 3.8: Schematic diagram of SEM system.

3.6. Atomic Force Microscope

The atomic force microscope (AFM) belong to the family of scanning probe microscopes (SPMs). Invented in 1982 by Binning and Rohrer [17], this family of microscopes uses a very sharp probe to scan across a surface of a sample and the interactions between the probe and the surface of the sample is used to generate a very high-resolution topographic image of the sample surface. Depending on the technique and the sharpness of the tip of the probe, the resolution of a SPM can be in the sub-nanometer scale. AFM uses a stylus probe, which on direct or indirect contact with the surface of the sample produces a high-resolution three-dimensional topographic image of the sample surface by measuring the repulsive and attractive forces that exist between the probe and the sample surface.

Fig. 3.9 shows a schematic set-up of one of the models of AFM. It consist of three major components, the AFM head and base stage, the high voltage electronics (HVE), and the digital signal processor (DSP) and the data processing system.

(i) ***The AFM head and base stage:*** The AFM head consists of the laser, cantilever, the photodiode, the position mechanism for focusing the laser beam on the backside of the cantilever and the photodiode (the beam splitter and the mirror respectively). It is also comprises of an electronic device which processes the signal coming from the photodiode [17].

(ii) ***The high voltage electronics (HVE):*** It amplifies the low signal coming from the digital signal processor (DSP) to a high voltage (about 100 V) to derive the piezoelectric scanner. The HVE also send the analog voltage signals from the photodiode to the DSP.

(iii) ***The digital signal processor (DSP) and the data processing system:*** The DSP processes the signals and calculate the real-time involve in AFM operation. It transforms the digital signal coming from the computer to analog signals using the digital to analog converter (DAC). It also converts the analog signal from the HVE to digital signal using an analog to digital converter (ADC). Finally, the data processing system uses a computer base software to run the whole set-up [18].

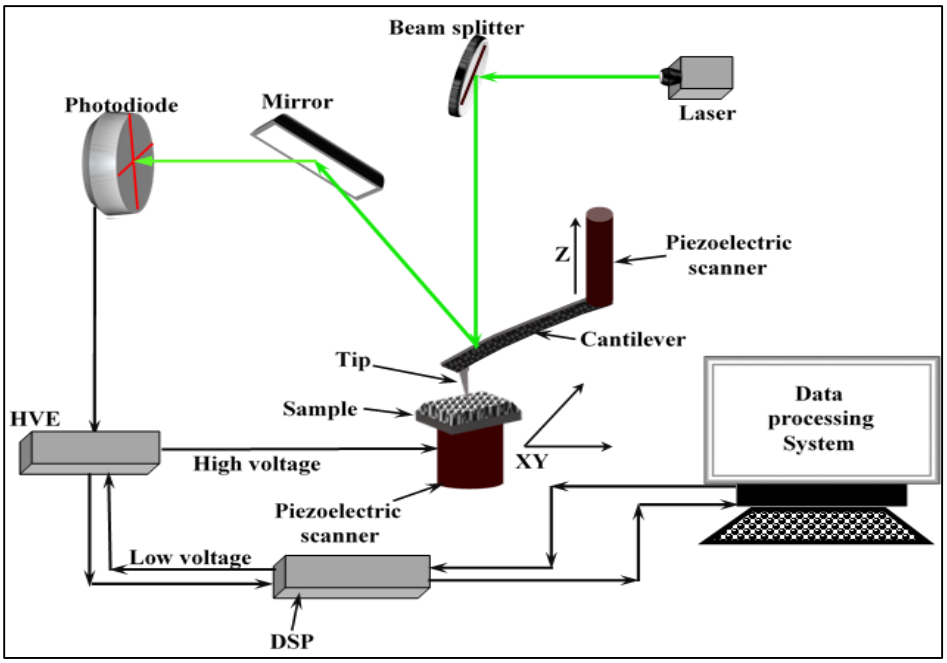

Fig. 3.9: Schematic diagram set-up of AFM technique.

3.6.1. The principle of operation of the AFM

The light from the laser is focused on the backside of the cantilever by the beam splitter and the mirror on the photodiode focuses the reflected light. Two piezoelectric scanners are used for the movement of the cantilever and the sample. One scanner moves the cantilever up and down in the Z-direction, while the other scanner moves the sample back and forth in the x- and y-direction. The deflection of the cantilever with respect to the repulsive or attractive forces between the tip and sample surface depend on the spring constant of the cantilever, and the distance between the tip and the sample surface. As the tip approaches the surface, the attractive force between the tip and the surface causes the cantilever to bend towards the surface. However, as the cantilever bends closer to the surface, the increasingly repulsive force between the cantilever and the surface causes the cantilever to bend away from the surface. This force, F can be described using Hooke's law:

$$F = -kx \tag{3.4}$$

where k is the cantilever spring constant and x is cantilever deflection [19]. The up and down deflection of the cantilever changes the direction of the deflection of the laser beam, and hence produces a change in the position of the laser spot on the photodiode. The photodiode is divided into quadrant of different sensitivities. Depending on the position of the laser beam on the photodiode, a corresponding analog voltage is recorded by the HVE.

3.6.2. Mode of operation

AFM operate in three different modes, namely, contact mode, non-contact mode and tapping mode. In ***contact mode***, the tip is brought into soft mechanical contact with the surface of the sample [20]. Contact mode allows tip to either scans at a constant small height above the sample surface or under a constant force. The cantilever deflection x is proportional to the force acting on the tip according to Eq. (3.4). Contact mode allows fast scanning. However, its major disadvantage is that the excessive tracking forces applied by the probe to the sample can cause damage on the sample surface. In ***non-contact mode***, there is no tip-sample interaction, but the probe operates base on the attractive Van der Waals forces acting between the tip and the sample. Although, a very low force is exerted on the sample in this mode, however, the image resolution is low. In ***tapping (intermittent contact) made***, the tip contacts with the sample surface intermittently, hence

avoiding dragging the tip across the surface. Tapping mode overcomes problems associated with friction, adhesion, electrostatic forces, etc. Tapping mode allows high resolution topographic imaging of the sample surface; however, a slow scanning is required [21].

3.6.3. Applications of AFM

AFM have found application in: biochemistry for biological molecular structure imaging, cellular components imaging and cell or tissues imaging; Chemistry, material science and nanotechnology applications for polymer imaging, nanostructure and other material imaging; physics and biophysics for measurement of forces between the probe tip and the sample surface [22].

3.7. Rutherford Backscattering Spectrometry

Rutherford backscattering spectrometry (RBS) is one of the analytical techniques used for quantitative analysis of elemental composition, thickness and depth profiles of a solid sample near the surface region ($\sim 2\,\mu$). RBS is based on the principles of Rutherford scattering [23]. In this method of analysis, charged incident particles elastically scattered by the nuclei of the analyzed sample are detected and their energies are analyzed. The amount of energy loss by the incident particle during collision with the nuclei of the sample depends on the atomic number Z of each element present in the sample.

3.7.1. Scattering fundamentals

Consider a flux of known particles (ions) of mass M_1, atomic number Z_1 and a given energy E_0, focused on a sample containing particles of mass M_2 and atomic number Z_2, as illustrated in Fig. 3.10. The force between the incident and the target nucleus is purely Coulombic, hence, some of the impinging positively charged ions (+) would be repelled by the positively charged nucleus according to the inverse square law [24]. This repulsive force causes the path of a scattered incident particle to form a hyperbola. The scattering angle (θ) is the angle between the asymptotes and the hyperbola.

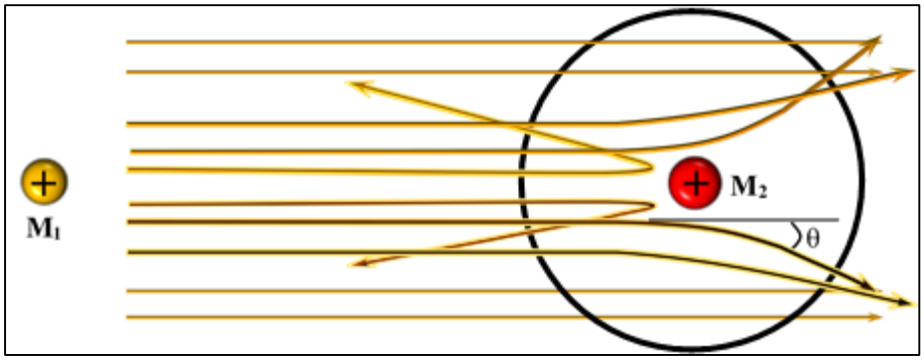

Fig. 3.10: Collision between two positively charged particles.

In RBS, a monoenergetic $^4He^+$ ion (α-particle) beam coming from an accelerator are focused on the sample (Fig. 3.11). When the α-particle beam interact with the sample, some of the ions will be elastically scattered by the surface atoms of the sample, while others will penetrate the sample. The ions that penetrate the sample will lose some energy and will be backscattered at various depths in the sample. The backscattered α-particles are detected and analyzed and a spectrum of backscattered α-particles as a function of energy is obtained. Every information on the nature and depth distribution of individual element present in the sample can be determined from the RBS energy spectrum.

The ratio of the reduced energy of the incident particle (E_1) after scattering and its energy before scattering (E_0) is the kinematic factor K, which is related to the scattering angle by

$$\frac{E_1}{E_0} = K = \left[\frac{\left(M_2^2 - M_1^2 \sin^2\theta\right)^{1/2} + M_1 \cos\theta}{M_2 + M_1} \right]^2 \qquad (3.5)$$

where M_1 is the mass of the incident α-particles and M_2 is the mass of the target atom. According to Eq. (3.5), when E_0 is fixed, the energy of the backscattered particles (KE_0) will depend only on the nature of the atoms in the surface of the sample [25].

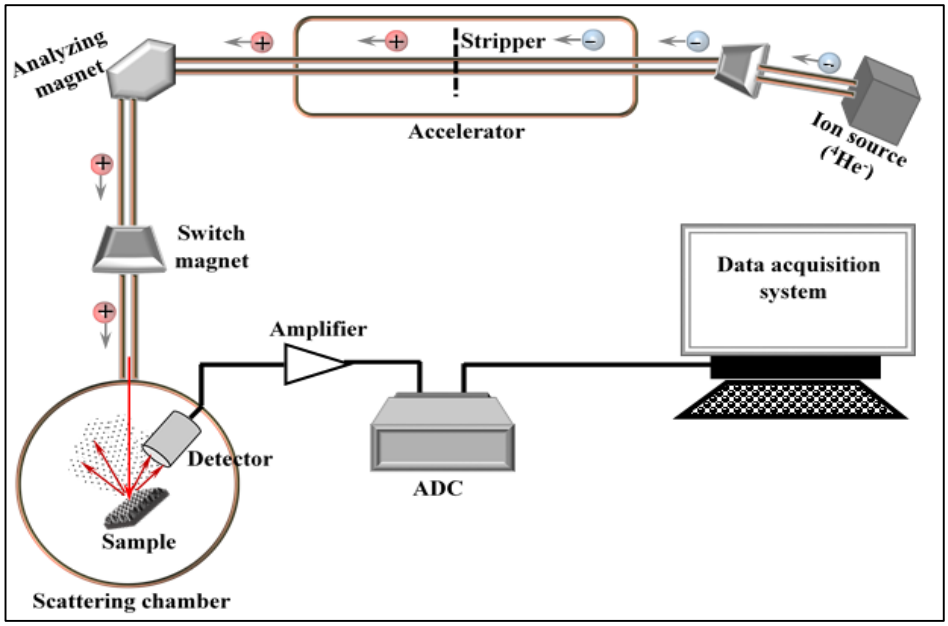

Fig. 3.11: Schematic diagram showing the set-up of RBS technique.

3.8. Ultraviolet-Visible Spectroscopy

When a light beam is incident on the surface of an absorbing medium, three phenomenon occur, reflection, absorption and transmission. As illustrated in Fig. 3.12, some of the light is reflected from the surface of the material, while the rest of the light propagates through the material and is transmitted at other side of the material. Absorption occurs in a material during propagation if the frequency of the incident light is in resonance with the transition energies of the atoms in the material [26]. The coefficient of transmission or transmissivity T is related to the coefficient of reflection or reflectivity R and the absorption coefficient α by

$$T = (1-R)^2 e^{-\alpha l} \tag{3.6}$$

where l is the thickness of the material.

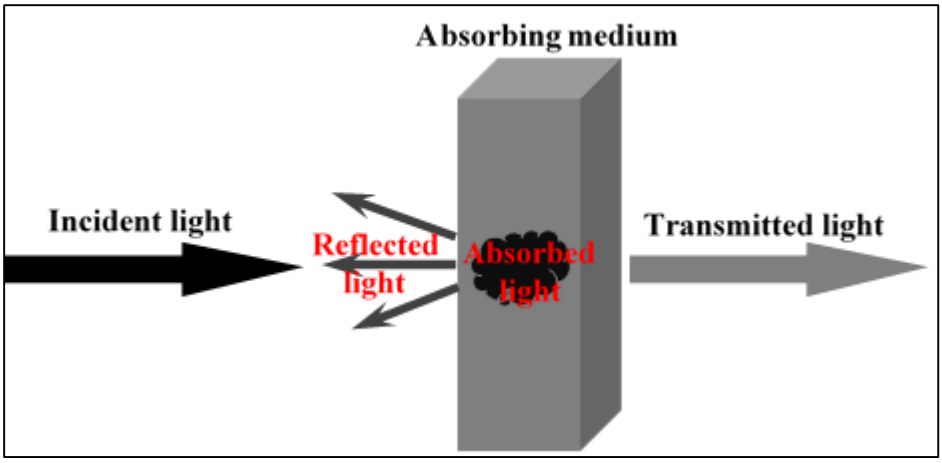

Fig. 3.12: Schematic diagram showing incident, reflected and transmittance light propagating through an absorbing medium.

Ultraviolet-visible (UV-vis) spectroscopy is used for absorbance, reflectance and transmittance measurement of materials [27]. As the name implies, UV-vis spectroscopy can be used to measure the aforementioned properties of a material from the ultraviolet (UV) range (100 - 400 nm) and the visible range (400 - 750 nm) of the electromagnetic spectrum. However, due to application reasons, must of the techniques are designed to scan from 200 - 800 nm. From UV-vis measurement, electrical and optical properties of a material can be determined. Absorbance mode allows the measurement of the concentration of a substance in a liquid solution according to the Beer-Lambert law [26]. In absorption spectroscopy, the intensities of a liquid sample placed between a light source and a photodetector are compared before and after it passes through the sample. The transmission spectroscopy is similar to the absorption spectroscopy, but it compares the light that pass through the sample to the light that does not pass through the sample, and it can be used for solid, liquid and gas samples [27]. Reflectance spectroscopy on the other hand can be used for only solid samples.

The basic set-up of UV-vis spectrometer is depicted in Fig. 3.13. The monochromator transmits a selected wavelength of light. The chopper controls the light path by alternating it between the sample, shutter and blank [28]. By doing this, the chopper allows light to hit both the sample and the reference at a small interval. The detector (photomultiplier tube, PMT) detects the intensity of the light that pass through the reference (which suffer insignificant or no absorption) and the

intensity of the light that pass through the sample. The ratio of these two signals are compared using the signal processor and the output is displayed on the screen [29]. Most UV-vis spectrometers uses two light sources. For instance, Lambda 950 UV-Vis spectrophotometer uses a Deuterium lamp for short wavelength scan (190 - 370 nm) and a Tungsten Halogen lamp for long wavelength (320 - 1100 nm) scan [30, 31].

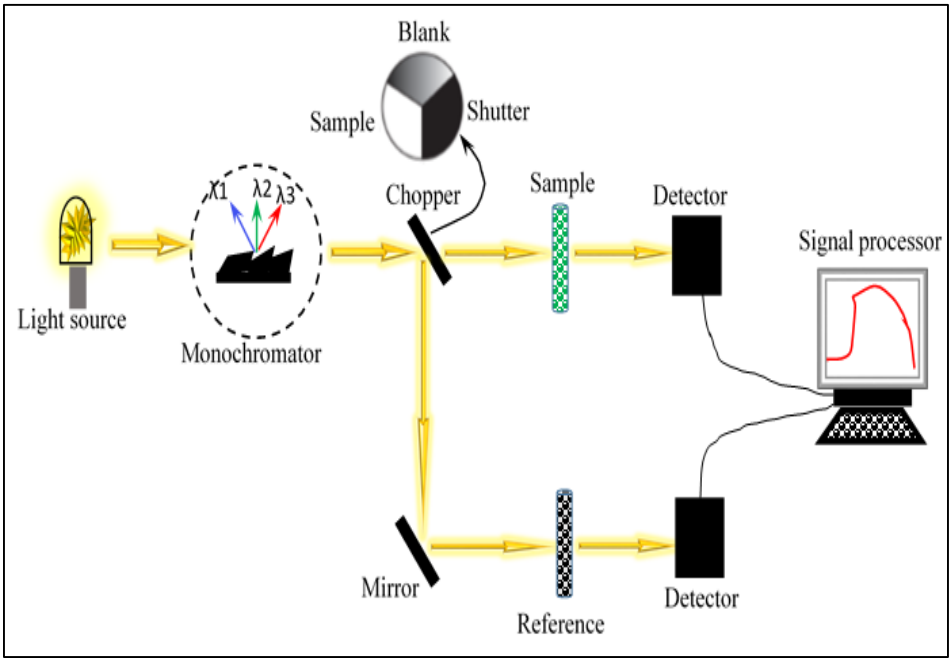

Fig. 3.13: Schematic diagram of a UV-vis spectrometer.

3.9. Photoluminescence Spectroscopy

Photoluminescence (PL) emission spectrum is obtained from photoluminescence spectrometer by choosing a fixed excitation wavelength (often at the peak of the absorption spectrum) and scanning the emission as a function of wavelength. The PL excitation spectrum is generated under the inverse condition, i.e., the emission spectrum is fixed at the emission maximum and the excitation source is scanned over the wavelength range of the absorption of the material [32].

Fig. 3.14 shows the basic set-up of PL spectrometer. It comprises of two wavelength selectors (monochromators). One wavelength selector selects the excitation wavelength from the light source and other selects the emission wavelength from the sample after excitation [33]. The common excitation sources are high-pressure Xe flash lamp with continuous emission spectrum in the wavelength range of 160 - 2000 nm [34] or lasers with a monochromatic wavelength [35]. The detector is usually PMT.

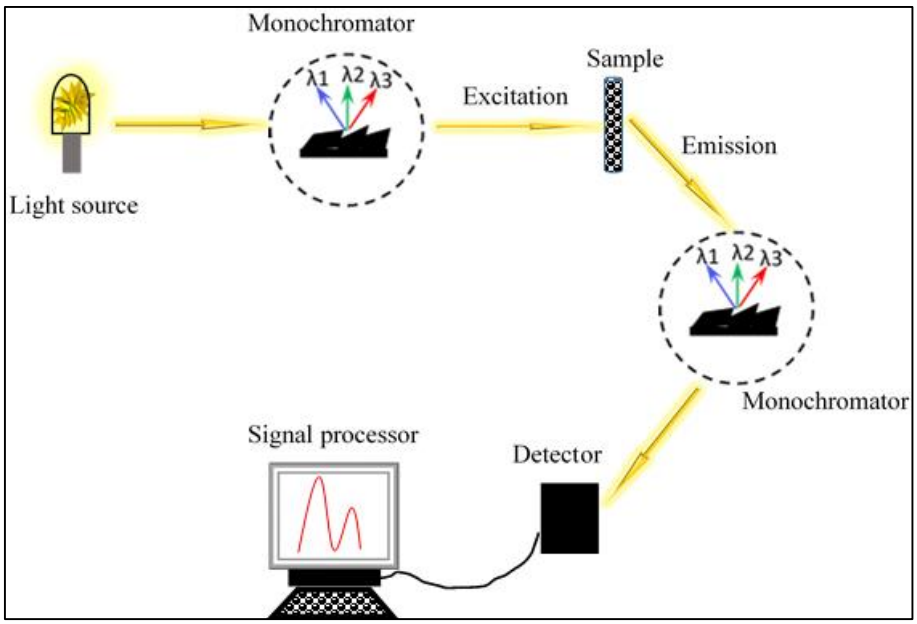

Fig. 3.14: Schematic diagram of a photoluminescence spectrometer.

3.10. References

[1] B.D. Cullity and S. R. Stock Elements of X-ray Diffraction, (3rd Edi.), Prentice Hall (2001) p. 95.

[2] Chem.libretexts.org (2017), X-ray Diffraction, Retrieved August (2017) from: https://chem.libretexts.org/Core/Analytical_Chemistry/Instrumental_Analysis/Diffraction_Scattering_Techniques/X-ray_Diffraction.

[3] D.M. Moore, R.C. Reynolds (Jr.), X-ray diffraction and the identification and analysis of clay minerals, Oxford Press, New York (1989).

[4] A. Monshi, M. Foroughi, M. Monshi, WJNSE, 2 (2012) 154.

[5] K.K. Darrow, Rev. Sci. Instrum. 4 (1933) 467.

[6] H. Lüth, Surfaces and interfaces of solid materials, (3rd Edi.), Springer-Verlag Berlin Heidelberg (1995) p. 27.

[7 P.Q. Vanbellingen, N. Elie, M.J. Eller, S.D. Negra, D. Touboul, A. Brunelle, Rapid Commun. Mass Spectrom. 29 (2015) 1187.

[8] A. Benninghoven, Angew. Chem. Int. Ed. 33 (1994) 1023.

[9] L. vanVaeck, A. Adriaens, R. Gijbels, Mass Spectrom. Rev. 18 (1999) 1.

[10] A. Adriaens, L. vanVaeck, F. Adams, Mass Spectrom. Rev. 18 (1999) 48.

[11] F.M. Green, I.S. Gilmore, M.P. Seah, J. Am. Soc. Mass Spectr. 17 (2006) 514.

[12] S. Swapp. Scanning Electron Microscopy (SEM), Retrieved August, (2017) from http://serc.carleton.edu/research_education/geochemsheets/techniques/SEM.html.

[13] Mee-inc.com, Scanning electron microscopy (SEM), Retrieved August, (2017) from http://www.mee-inc.com/hamm/scanning-electron-microscopy-sem/.

[14] Ammrf.org.au, Characteristic X-rays, Retrieved September (2017) from http://www.ammrf.org.au/myscope/analysis/eds/xraygeneration/characteristic/.

[15] I.M. Watt, The principles and practice of electron microscopy, (2nd Edi.), Cambridge University Press, (1997) p. 44.

[16] L. Reimer. Scanning electron microscopy: Physics of image formation and microanalysis, Springer-Verlag Berlin Heidelberg (1998) p. 1.

[17] G. Binnig, H. Rohrer, Helv. Phys. Acta. 55 (1982) 726.

[18] D. Johnson, N. Hilal, W.R. Bowen, Basic principles of atomic force microscopy, (2009) DOI: 10.1016/B978-1-85617-517-3.00001-8.

[19] A.V. Clemente, K. Gloystein, N. Frangis, Principles of atomic force microscopy (AFM), Physics of Advanced Materials Winter School (2008).

[20] G. Binnig, C.F. Quate, C. Gerber, Phys. Rev. Lett. 56 (1986) 930.

[21] H.Q. Li (1997), The common AFM modes, Retrieved August (2017) from: http://www.chembio.uoguelph.ca/educmat/chm729/afm/details.htm.

[22] Nature.com (2017), Applications of AFM, Retrieved August (2017) from: https://www.nature.com/subjects/applications-of-afm.

[23] B. Schmidt, K. Wetzig, Ion beams in materials processing and analysis, Springer Science & Business Media, Berlin, Germany (2012) p. 312-323.

[24] E.R. Williams, Z.E. Faller, H.A. Hill, Phys. Rev. Lett. 26 (1971) 721.

[25] J. Perriére, Vacuum 37 (1987) 429.

[26] M. Fox, Optical properties of solids, Oxford University Press, New York (2001) p. 1-3.

[27] Andor.com, Absorption/transmission/reflection spectroscopy, Retrieved August (2014) from: http://www.andor.com/learning-academy/absorption-transmission-reflection-spectroscopy-an-introduction-to-absorption-transmission-reflection-spectroscopy.

[28] Chem.libretexts.org, UV/Vis and IR spectroscopy, Retrieved August (2017) from: https://chem.libretexts.org/Textbook_Maps/Analytical_Chemistry_Textbook_Maps/Map%3A_Analytical_Chemistry_2.0_(Harvey)/10_Spectroscopic_Methods/10.3%3A_UV%2F%2FVis_and_IR_Spectroscopy.

[29] H. H. Perkampus, UV-Vis spectroscopy and its application, Springer laboratory 1 (1992).

[30] Perkinelmer.com, Retrieved September (2017) from: http://www.perkinelmer.com/lab-solutions/resources/docs/BRO_LAMBDA8509501050.pdf.

[31] Biochrom.co.uk, Glossary of UV vis spectroscopy, Retrieved September (2017) from: http://www.biochrom.co.uk/content/1/91/glossary-of-uv-vis-spectrophotometry.html.

[32] R.W. Redmond, introduction to fluorescence and photophysics, In, M. Mycek, B.W. Pogue (Ed.) "*Handbook of biomedical fluorescence*" Marcel Dekker, Inc. New York (2003) p. 1-27.

[33] Chem.libretexts.org, UV/Vis and IR spectroscopy, Retrieved August (2017) from: https://chem.libretexts.org/Textbook_Maps/Analytical_Chemistry_Textbook_Maps/Map%3A_Analytical_Chemistry_2.0_(Harvey)/10_Spectroscopic_Methods/10.3%3A_UV%2F%2FVis_and_IR_Spectroscopy.

[34] Photonics.com, A guide to selecting lamps, Retrieved September (2017) from: https://www.photonics.com/Article.aspx?AID=44487.

[35] P.K. Studts, D.J. Studts, J.A. Huth, Fluorometry and fluorescence polarization, In, M.C. Haven, G.A. Tetrault, J.R. Schenken (Ed.), "*Laboratory instrumentation*", (4th Edi.), John Wiley & sons, Inc. New York (1995) p. 135-156.

CH. 4

The influence of deposition atmosphere and substrate temperature on the structure, morphology and photoluminescence of pulsed laser deposited $La_{0.5}Gd_{1.5}SiO_5:Dy^{3+}$

4.1. Introduction

Rare-earth oxyorthosilicates (R_2SiO_5) have generated interest in the past few years due to excellent properties such as high density, high quantum efficiency, minimal self-absorption, wide band gap, high stability and fast decay times [1]. These properties, combined with the ability to incorporate substantial amount of luminescent rare earth ions have made R_2SiO_5 exceptional host matrices to rare-earth ions for numerous luminescence applications [2-8]. The structural properties of R_2SiO_5 have been studied extensively [9-12]. In an attempt to leverage the best qualities out of these materials, researchers have mixed various compound rare-earth oxyorthosilicates [13-19]. For instance, R_2SiO_5 have two crystallographic sites [9-12], therefore mixing two R_2SiO_5 is believed to provide more sites in the crystal lattice to accommodate Dy^{3+} dopant ions. Furthermore, mixing compound R_2SiO_5 at different molar ratios can tune the properties of these materials. The growth of cerium doped $(Lu_{1-x}Gd_x)_2SiO_5$ changed the melting temperature, structure, density, optical absorption edge and light yield of the material depending on the Lu/Gd molar ratio [20]. $Gd_{1.99-x}Y_xCe_{0.01}SiO_5$ showed a similar structure as $Ce:Gd_2SiO_5$ but the optical transmittance and the luminescence intensities of $Gd_{1.99-x}Y_xCe_{0.01}SiO_5$ (x = 0.0995, 0.199) were higher than those of $Ce:Gd_2SiO_5$ [21]. Also Dy^{3+}-doped $(Lu_{1-x}Gd_x)_2SiO_5$ (x = 0, 0.2, 0.6, 0.8 and 1) showed no change in the structural, physical and optical properties of Lu_2SiO_5 but the inhomogeneous broadening of Dy^{3+} spectral band was observed due to structural disorder of the host [15].

Phosphors can be synthesized in either powder or thin film form. Many researchers [22-24] have compared the properties of powder and thin film phosphors. Different methods have been used in the deposition of thin films [25, 26]. Compared to other popular thin film deposition techniques, such as physical vapor deposition (PVD) and chemical vapor deposition (CVD), pulsed laser deposition (PLD) has shown some outstanding advantages. In CVD, precursors are used as the starting material, while in PLD, solid targets are deposited on a substrate using laser ablation. In PLD, the rate of the film growth can be controlled by changing background gas, adjusting the laser

parameters, deposition time, substrate to target distance, etc. Some of the major features of PLD are the transfer of the stoichiometry of the target material deposited on the substrate, deposition at high temperature and high deposition rate [27, 28]. Since its invention in 1965 [29], the principles of PLD have been vastly discussed by many authors [30, 31]. PLD has been applied successfully in the deposition of different types of materials on thin films, such as complex oxides, polymer-metal composites, nitrides, borides and carbides [30-32].

In this study, $La_{0.5}Gd_{1.5}SiO_5:Dy^{3+}$ phosphor thin films for possible application in UV-pumped white light emitting diodes (LED) were deposited on Si (111) substrates using the PLD technique. In our previous work, we prepared $La_{2-x}Gd_xSiO_5:Dy^{3+}$ (x = 0, 0.5, 1.0, 1.5 and 2) phosphor powder and the CIE colour coordinates calculated from the data obtained when the phosphors were excited using a 325 nm He-Cd laser showed a tunable colour from blue to yellow through white [33]. A near white light was obtained when x = 0.5 (i.e. $La_{0.5}Gd_{1.5}SiO_5:Dy^{3+}$), hence we chose to prepare the thin film at this composition.

4.2. Experimental

4.2.1. *Sample preparation:*

A $La_{0.5}Gd_{1.5}SiO_5:Dy^{3+}$ powder was prepared by urea and ammonium nitrate-assisted solution combustion method as discussed in our previous work [13]. The phosphor powder was then pressed using a hydraulic press to make a target for laser ablation. The target (pellet) was pre-annealed in air using an oven at 250 ºC for 3 hours to get remove moisture and other adsorbed volatile substances. The silicon substrates (Si (111)) were cut into smaller sizes (2.5×2.5 cm^2) and were cleaned first using distilled water and subsequently immersed in a glass beaker containing acetone and ethanol respectively placed in an ultrasonic bath for about 15 min. The cleaned substrates were then blown-dry using nitrogen. The Si substrate was mounted on the substrate holder that was 4.5 cm away from the target that was mounted on a rotatable target holder. The deposition chamber was pumped down to a base pressure of 3.25×10^{-6} Torr. The laser energy and the pulse repetition rate were fixed at 40 mJ and 10 Hz respectively. The films were deposited in three different working atmospheres namely; vacuum, Ar and O_2. The substrate temperature was varied from 50 to 500 ºC while the deposition time was 15, 30 and 50 min. The Nd:YAG wavelength was set to 266 nm for all thin film depositions.

4.2.2. *Characterization:*

The crystal structures of the films were analyzed using a Bruker D8-Advanced X-ray diffractometer operating with a CuK_α radiation source ($\lambda = 0.15406$ nm). The chemical composition and the thickness of the films were determined using Rutherford backscattering spectroscopy (RBS). The RBS spectra were recorded when the films were bombarded with $^4He^+$ ions with irradiation energy of 2 MeV at a scattering angle of 165° and detector resolution was set at 20 KeV. The pressure in the chamber was 3.87×10^{-5} mbar and the beam current was in the range of 40-50 nA. SIMNRA program was used to perform the simulation to obtain best-fit curves [34, 35]. The surface topography and particle morphology studies and the elemental analysis were carried out using a Shimadzu SPM-9600 Scanning Probe Microscope and a JEOL JSM-7800F field emission scanning electron microscope (FE-SEM) fitted with Oxford Aztec 350 X-Max80 energy-dispersive X-ray spectroscopy (EDS). The electronic and chemical states were investigated using a PHI 5000 Versaprobe-scanning X-ray photoelectron spectroscopy (XPS). The photoluminescence (PL) spectra were measured using a Cary Eclipse fluorescence spectrophotometer with a 150 W xenon lamp as excitation source.

4.3. Results and discussion

Fig. 4.1(a) and (b) show the XRD patterns of $La_{0.5}Gd_{1.5}SiO_5:Dy^{3+}$ thin films deposited in different atmospheres (Ar, vacuum and O_2 at a substrate temperature of 200 ºC for 30 min) and at different substrate temperatures (50, 200, 300, 400 and 500 ºC) in O_2 atmosphere for 30 min. From Fig. 4.1(a), it is clear that the films deposited in O_2 and Ar were crystalline while the one deposited in vacuum was amorphous. This could be due to the presence of more particles in the films deposited in O_2 and Ar when compared to the film deposited in vacuum (see Fig. 4.3). It is well known that the characteristics of a thin film strongly depend on the pressure of the background gas during PLD, since the ambient particles interact with the particles in the plume [36]. The collision between the ambient gas atoms and the particles in the plume will decrease the kinetic energies of the particles and hence increases the amount of time the particles stay in the plume. This gives the particles enough time to nucleate, agglomerate and grow into bigger particles prior to their arrival on the substrate [36, 37]. On the other hand, the particles ejected in vacuum moves freely and are expected to have higher mean free path and thus they do not have enough time to nucleate. This could explain why better films were obtained in O_2 and Ar when compared to vacuum atmosphere.

Fig. 4.1(b) show the XRD pattern of $La_{0.5}Gd_{1.5}SiO_5:Dy^{3+}$ thin film deposited at different substrate temperatures (50, 200, 300, 400 and 500 ºC) in O_2 atmosphere for 30 min. As can be seen from Fig. 4.1(b), the crystallinity of the films increased with the increase in the substrate temperatures with the samples deposited at 400 and 500 ºC appearing to be more crystalline than the rest. The XRD pattern showed only the (002) diffraction peak from Gd_2SiO_5 and the (012) diffraction peak from La_2SiO_5, indicating that $La_{0.5}Gd_{1.5}SiO_5:Dy^{3+}$ films have a preferred orientation [38]. The Gd_2SiO_5 and La_2SiO_5 peaks matched with the standard data referenced in JCPDS 74-1795 and 40-0234 respectively. The XRD data clearly indicate that Gd_2SiO_5 and La_2SiO_5 combined to form clusters of like materials, i.e. the mixing was not at the particle level to form a new compound whose properties are independent of the two components. The higher intensity of the (002) peak could be a result of the higher ratio of Gd_2SiO_5 in the sample. The shift to the lower 2θ value observed in the diffraction peaks with increasing substrate temperature could be due to residual stress emanating from a change of lattice parameters [38].

RBS is an important technique for the quantification of the chemical composition and the area density (atom/cm^2) of a thin film. The thickness of a thin film can also be determined using RBS if the atomic density (g/cm^3) of the compound is known [39]. The RBS spectra for the films deposited in O_2 at the substrate temperatures of 50 and 500 ºC are shown respectively in Fig. 4.2(a) and (b). No significant change was observed in the spectra. The peaks of La, Gd and Dy are located around 1.7 MeV, while O_2 and Si peaks are located around 0.65 and 0.9 MeV, respectively.

In RBS, beams of charged atomic particles ($^4He^+$ in our case) are used to probe thin films. The ions are slowed down when traversing the thin film and the depth analysis of the material is based on the energy lost by the probing particle [40]. The stopping power S can be defined in terms of the amount of energy lost ΔE per unit distance Δx as

$$S = \frac{\Delta E}{\Delta x} \tag{4.1}$$

The distance Δx is the thickness of the film which we will denote by t. The stopping cross-section ε is defined as

$$\varepsilon = \frac{\Delta E}{Nt} \tag{4.2}$$

where $N(\text{atoms/cm}^3)$ is the atomic density. Hence, the film thickness can be written as

$$t = \frac{\Delta E}{\varepsilon N} \tag{4.3}$$

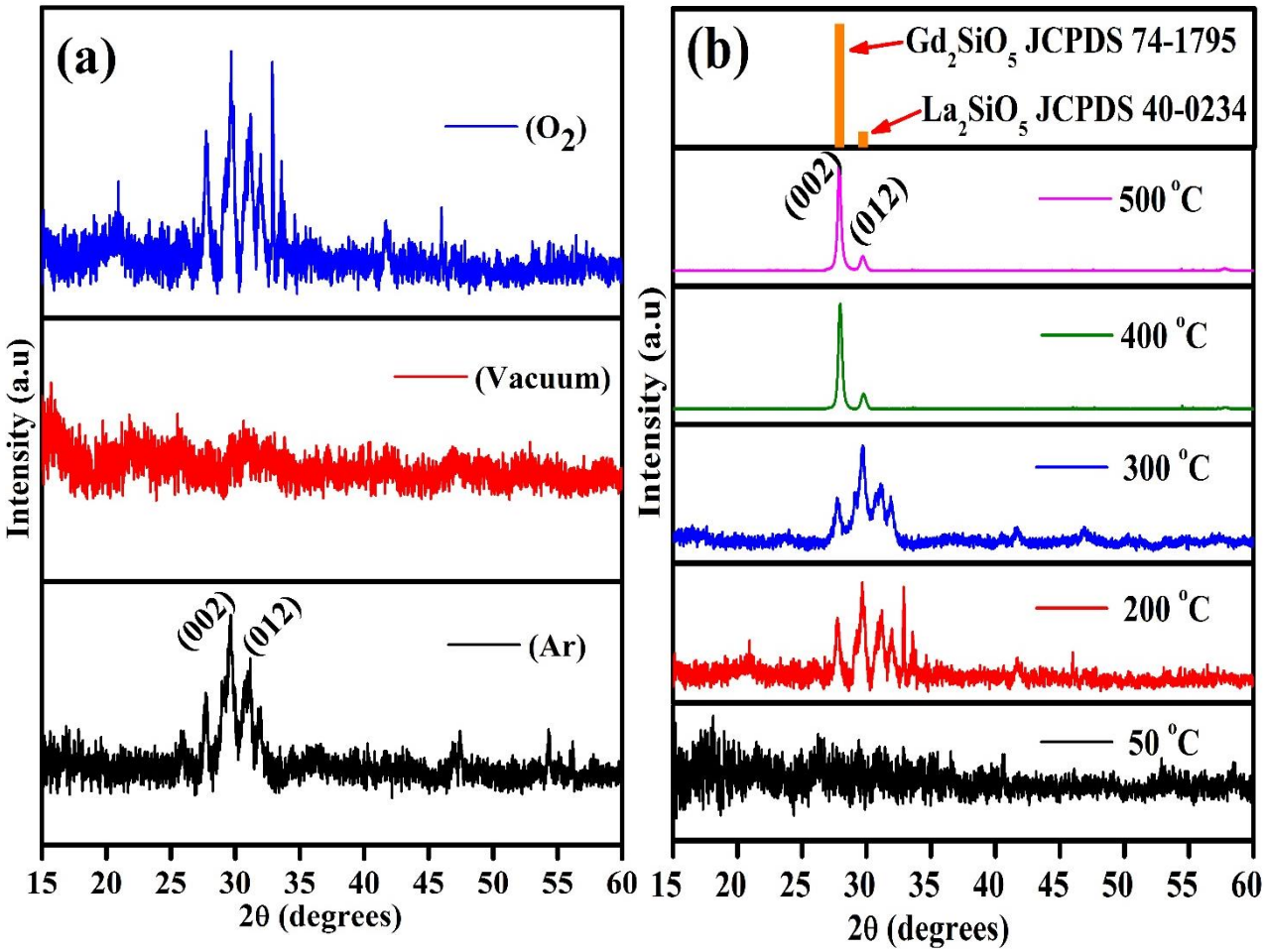

Fig. 4.1: The XRD pattern of $La_{0.5}Gd_{1.5}SiO_5:Dy^{3+}$ thin films, as a function of temperature, (a) deposited in O_2 (blue), vacuum (red) and Ar (black) at 200 ºC for 30 min, (b) deposited at 50 (black), 200 (red), 300 (blue), 400 (green), and 500 ºC (magenta) in O_2 for 30 min.

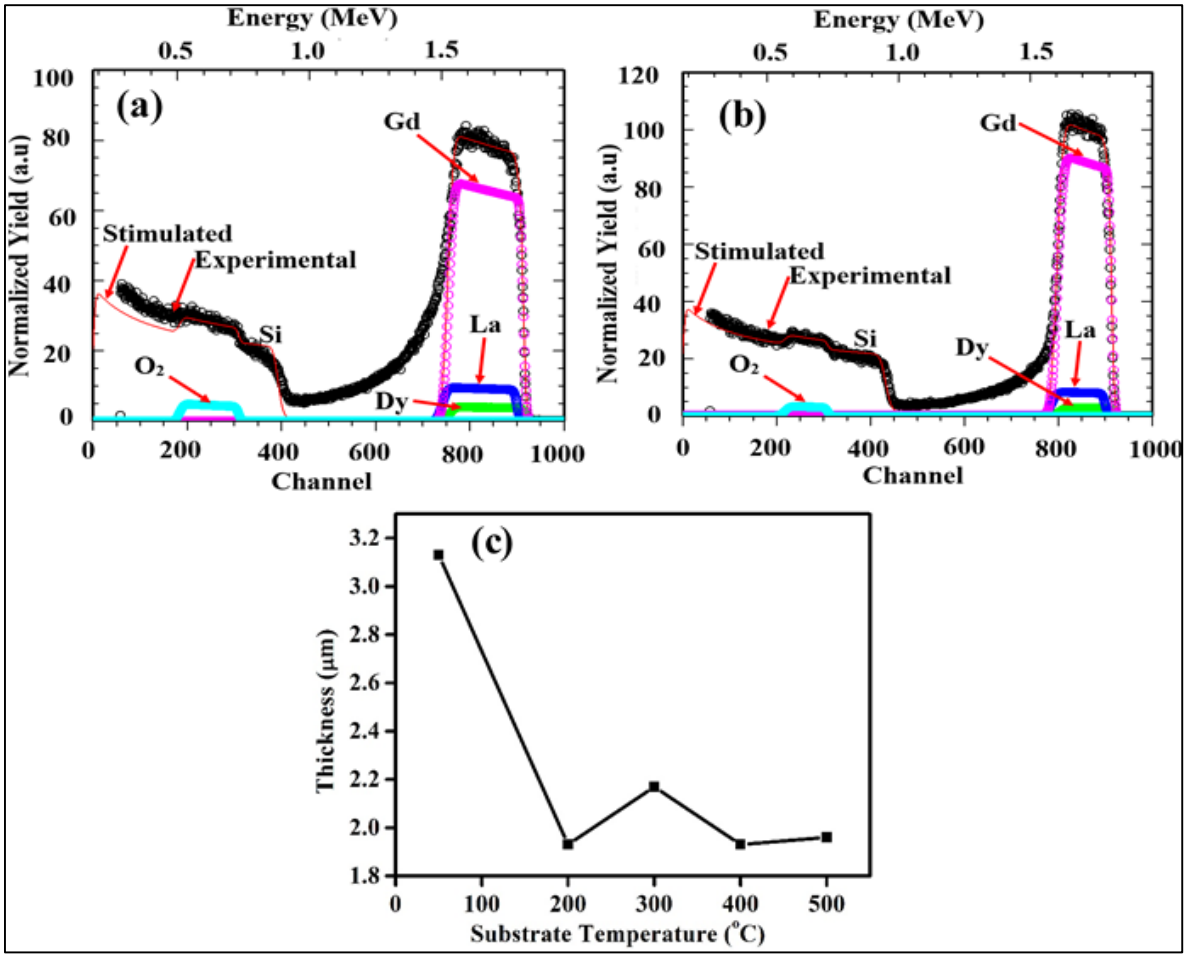

Fig. 4.2: RBS spectra of $La_{0.5}Gd_{1.5}SiO_5:Dy^{3+}$ thin films deposited in O_2 at substrate temperatures of (a) 50 ºC and (b) 500 ºC. (c) Variation of film thickness with substrate temperature.

If the stopping power is in $eV/$ cm, and the stopping cross-section is in $eV\text{cm}^2/\ 10^{15}$atoms, then, $\Delta E/\varepsilon$ will be in 10^{15} atoms/cm^2. The density of $La_{0.5}Gd_{1.5}SiO_5:Dy^{3+}$ is 6.87 g/cm^3 and its atomic density was determined to be 8.34×10^{21} atoms/cm^3. The values $\Delta E/\varepsilon$ from the stimulated data are 737 and 1980×10^{15} atoms/cm^2 for the samples deposited in vacuum and Ar respectively. For the samples deposited in O_2 at the substrate temperatures of 50, 200, 300, 400 and 500 ºC, the values of $\Delta E/\varepsilon$ were 2610, 1610, 1810, 1610 and 1640×10^{15} atoms/cm^2 respectively. Using Eq. (4.3), the thicknesses of the films were determined and are shown in table 4.1. Fig. 4.2(c) shows how the thickness of the films changed with substrate temperature. As can be seen, the thickness of the films reduced sharply between the films deposited at the substrate temperatures of 50 and 200 ºC and afterwards, it started varying in no definite manner with the substrate temperature.

Table 4.1: The thickness of the films and stoichiometry (ratio) of elements in $La_{0.5}Gd_{1.5}SiO_5:Dy^{3+}$.

Deposition atmosphere	Substrate temperature (ºC)	Thickness (μm)	Stoichiometry (at. %)				
			La	Gd	Si	O	Dy
Vacuum	200	0.88	0.036	0.192	0.015	0.764	0.013
Ar	200	2.37	0.036	0.320	0.015	0.796	0.011
O_2	50	3.13	0.035	0.199	0.015	0.764	0.011
O_2	200	1.93	0.036	0.290	0.015	0.764	0.013
O_2	300	2.17	0.045	0.330	0.015	0.764	0.011
O_2	400	1.93	0.045	0.380	0.015	0.764	0.011
O_2	500	1.96	0.043	0.370	0.015	0.764	0.011

Fig. 4.3 (a-c) shows the 3D-AFM images of the $La_{0.5}Gd_{1.5}SiO_5:Dy^{3+}$ films deposited respectively in vacuum, Ar and O_2 atmospheres. The films exhibit spherical particles with distinct number of particles. The films deposited in O_2 and Ar contained the higher number of particles with the same rms roughness value of 70.0 nm. The film deposited in vacuum contained the lowest number of particles with rms roughness value of 18.8 nm. As mentioned earlier, films deposited in a background gas are higher quality than films deposited in vacuum since the background gas interact with the particles in the plume resulting in increased residence time to nucleate, agglomerate and grow into bigger particles [36, 37].

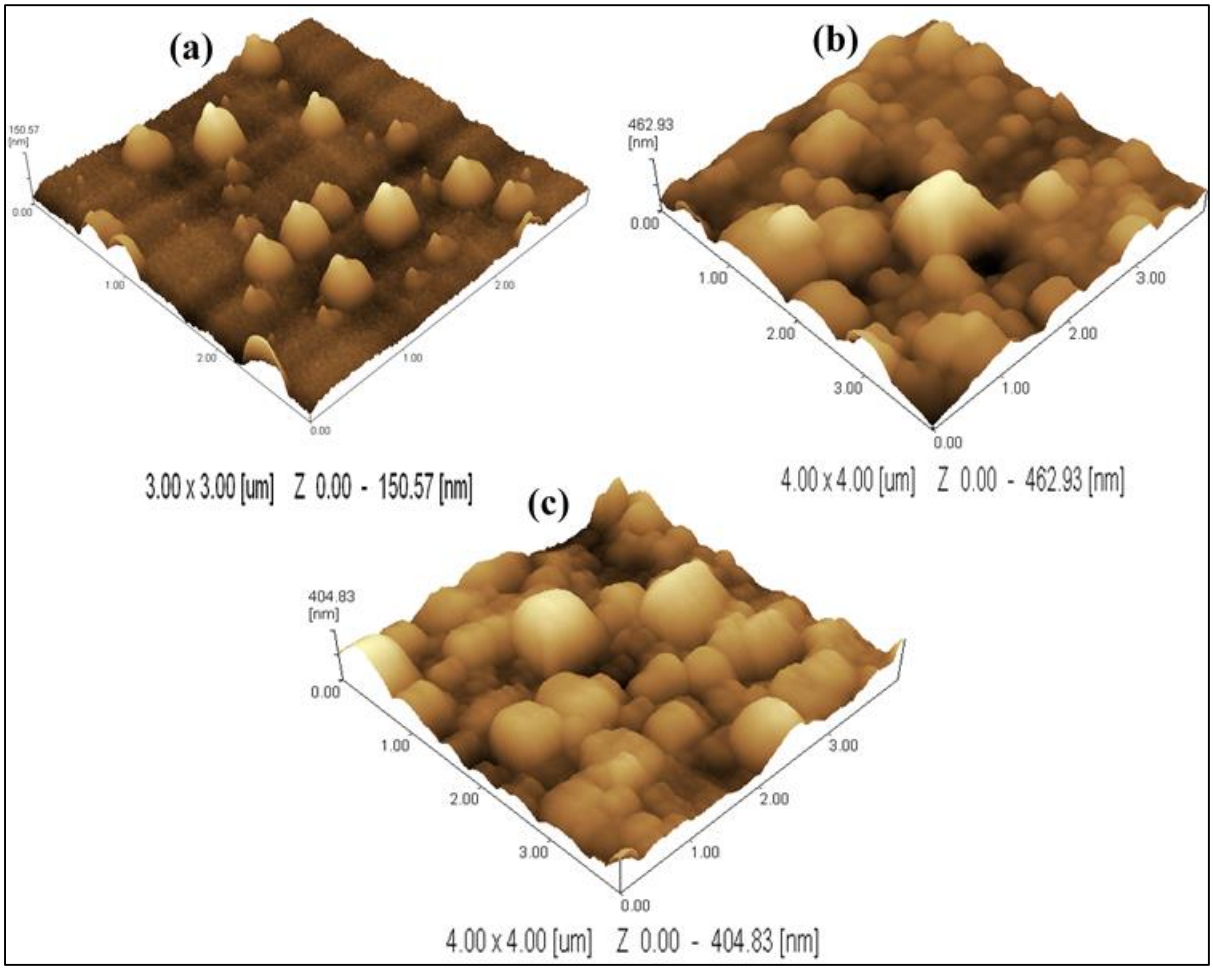

Fig. 4.3: The 3D-AFM images of $La_{0.5}Gd_{1.5}SiO_5:Dy^{3+}$ films deposited in, (a) vacuum, (b) Ar and (c) O_2 at 200 ºC for 30 min.

Fig. 4.4(a-e) shows the 3D-AFM images of the surface of $La_{0.5}Gd_{1.5}SiO_5:Dy^{3+}$ films deposited in O_2 atmosphere for 30 min at 50, 200, 300, 400 and 500 ℃ substrate temperatures respectively. The plot of the surface rms roughness values of the films as a function of substrate temperature is shown in Fig. 4.5. The rms roughness value initially decreased with increase in the substrate temperature, from 84.1 nm at 50 ºC to 70.1 nm at 200 ºC. However, at higher substrate temperatures (300 and 400 ºC) the rms roughness value increased to 72.3 nm and 77.7 nm respectively, but decreased to 39.1 nm when the substrate temperature was increased to 500 ºC. In Fig. 4.4(a), the grain boundaries are indistinct and the surface of the film is highly coarse. However, when the substrate temperature was increased, the adatoms began to form crystalline

particulates with defined boundaries, making the surface of the films smoother. At 500℃, however, the number of the adatoms decreased leading to decrease in the rms roughness value of the film. At low substrate temperatures, the atoms diffuse on the surface of the film with low kinetic energy. Thus, the adatoms have sufficient time to nucleate on the surface of the substrate along with some mixed 3D growth, leading to indistinct boundaries and coarse surface. As the substrate temperature is increased, the kinetic energy of the atoms on the surface of the film increases, and hence the atoms can diffuse on the surface of the substrate and grow more crystalline grains with smoother surface. At 500 ºC, the kinetic energy of the atoms becomes very high leading to the deterioration of the growth orientation of the grains [41].

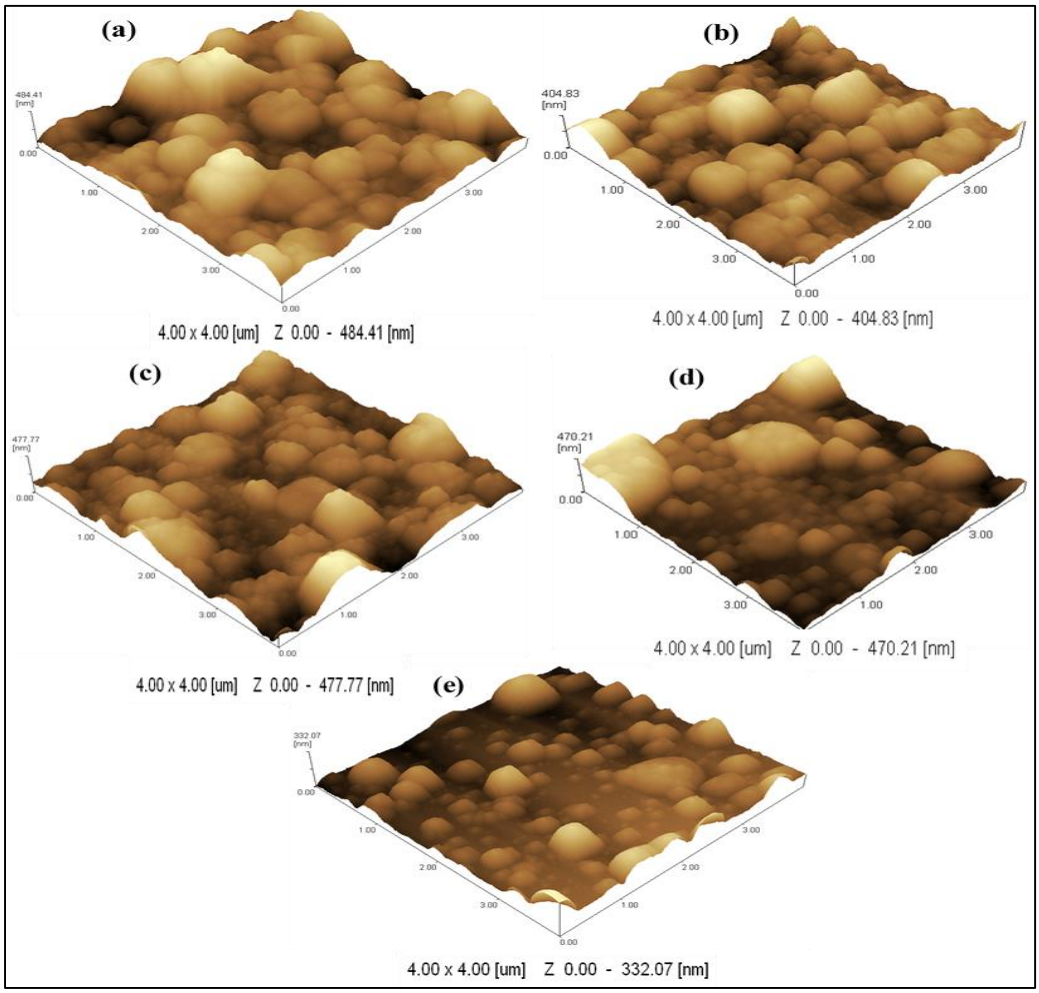

Fig. 4.4: The 3D-AFM images of $La_{0.5}Gd_{1.5}SiO_5:Dy^{3+}$ films deposited in O_2 for 30 min at, (a) 50, (b) 200, (c) 300, (d) 400 and (e) 500 ºC.

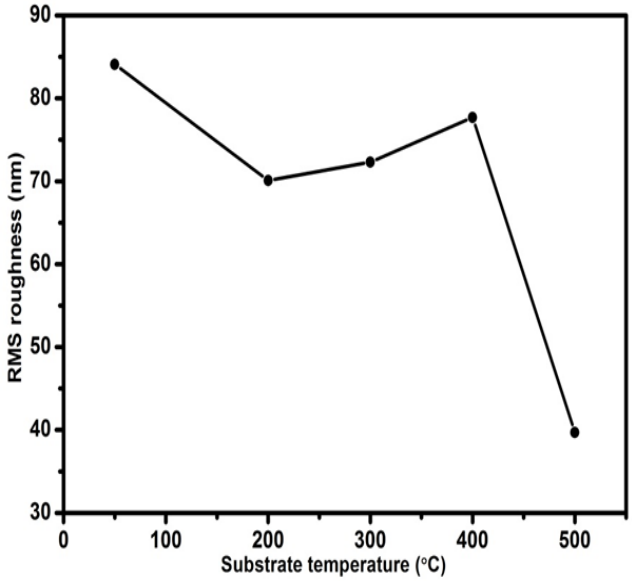

Fig. 4.5: rms roughness values of $La_{0.5}Gd_{1.5}SiO_5:Dy^{3+}$ thin films deposited at different temperatures.

Fig. 4.6(a-c) depicts the FE-SEM images of the surface morphology of the $La_{0.5}Gd_{1.5}SiO_5Dy^{3+}$ films deposited in vacuum, Ar and O_2 atmosphere respectively. The micrographs constitute spherically shaped particulates with distinct sizes. The film deposited in vacuum contained the lowest number of particles followed by the film deposited in Ar while the film deposited in O_2 has the highest number of particles. The FE-SEM results are in agreement with the AFM results and the possible causes of the differences in the number of particles contained in each film is due to their different deposition atmosphere as discussed in the AFM data.

Fig. 4.7(a-e) shows the FE-SEM images of $La_{0.5}Gd_{1.5}SiO_5:Dy^{3+}$ thin films deposited in an O_2 background atmosphere for 30 min, at substrate temperatures of 50, 200, 300, 400 and 500 ºC respectively. It is evident that the number of the particles deposited on the surface of the films decreased with increasing substrate temperature. The factor behind this, as explained in the AFM images, is that the adatoms possess low kinetic energy on arriving at the surface of the substrate at the lower temperatures and hence they will have sufficient time to diffuse and orient. At high temperatures, the kinetic energy increases as they arrive on the surface of the substrate and they collide with each other and re-evaporate [42].

The elemental composition of $La_{0.5}Gd_{1.5}SiO_5:Dy^{3+}$ thin films were investigated using EDS. Fig. 4.8(a) and (b) 8×12 μm EDS scan of $La_{0.5}Gd_{1.5}SiO_5:Dy^{3+}$ thin film deposited in O_2 at the substrate

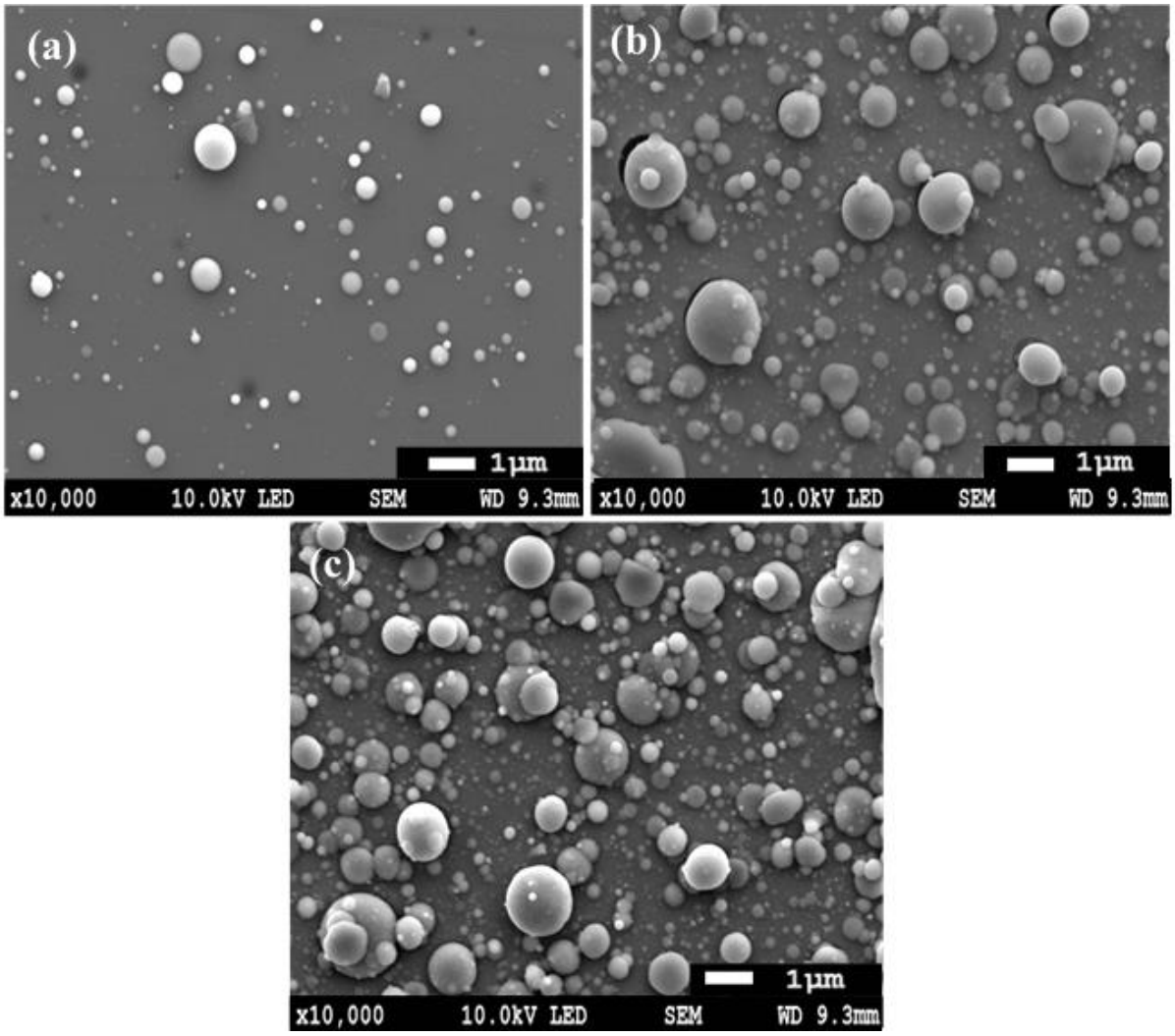

Fig. 4.6: The FE-SEM images of $La_{0.5}Gd_{1.5}SiO_5:Dy^{3+}$ films deposited at 200 ºC for 30 min in, (a) vacuum, (b) Ar, and (c) O_2.

temperatures of 50 and 500 ºC respectively. Carbon (C) was probably coming from the atmospheric hydrocarbons. La, Gd, Dy, Si and O_2 were observed in the samples as expected. Low count of Dy in the spectra is due to its low concentration in the samples. The inset in Fig. 4.8(a) and (b) are the respective elemental maps. It can be seen from the map that all the elements were evenly distributed on the surface of the films. Notice that the O_2 peak decreased at higher substrate temperature. This may be due to the crystallization of the films at higher temperature leading to desorption of the O_2 species [43].

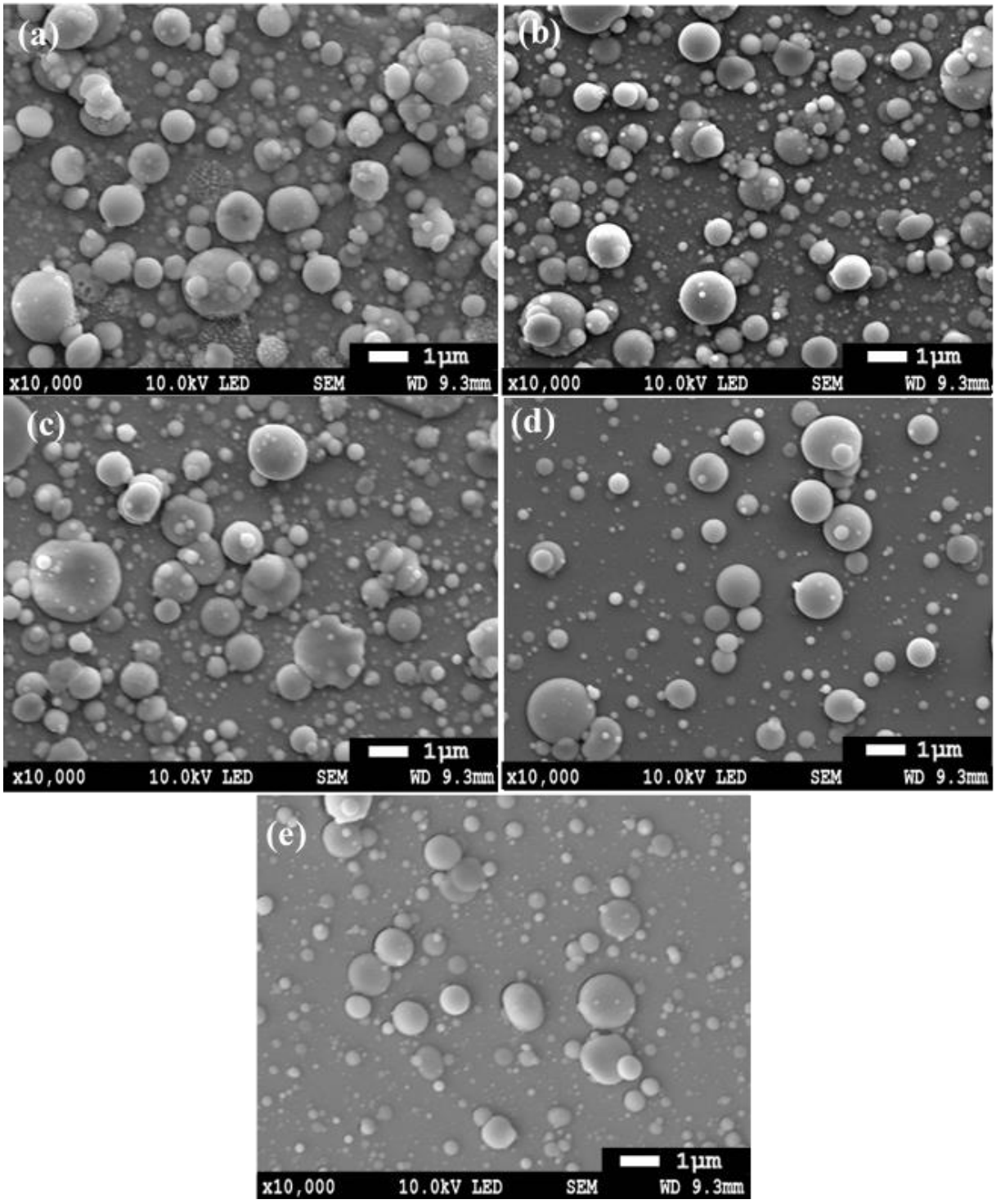

Fig. 4.7: The FE-SEM images of $La_{0.5}Gd_{1.5}SiO_5:Dy^{3+}$ films deposited in O_2 for 30 min at substrate temperatures of, (a) 50, (b) 200, (c) 300, (d) 400 and (e) 500 ºC.

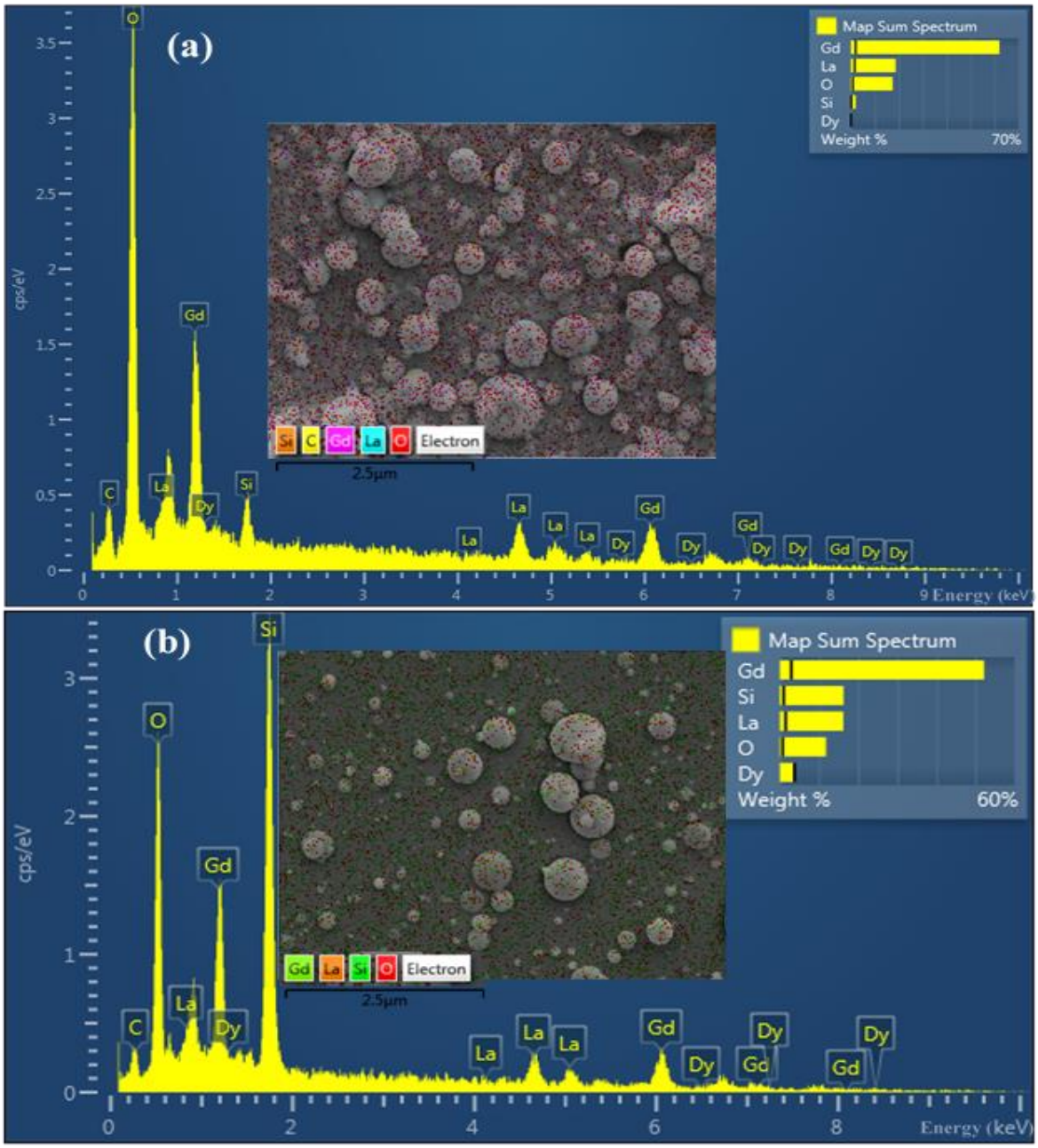

Fig. 4.8: EDS spectra of $La_{0.5}Gd_{1.5}SiO_5:Dy^{3+}$ thin films deposited in O_2 at substrate temperatures of, (a) 50 ºC and (b) 500 ºC.

The XPS technique was used to analyze the electronic and chemical states of the thin films and the results are shown in Fig. 4.9 and 4.10. Fig. 4.9(a) shows the fitted O 1s XPS spectrum of $La_{0.5}Gd_{1.5}SiO_5:Dy^{3+}$ thin film. The five fitted peak at 529.3, 530.3, 531.0, 531.6 and 532.3 eV are ascribed respectively to $LaGdO_3$, SiO_x (x < 2), $LaGdSiO_5$, SiO_2 and SiO_4. The $LaGdO_3$ peaks comprise of the La_2O_3 and Gd_2O_3 peaks while the $LaGdSiO_5$ peak comprises of the La_2SiO_5 and Gd_2SiO_5 peaks [44-51]. Fig. 4.9(b) shows the fitted Si 2p XPS spectrum for the $La_{0.5}Gd_{1.5}SiO_5:Dy^{3+}$ thin film. The Si 2p spectrum consists of five peaks ascribed to Si, SiO_x (x < 2), $LaGdSiO_5$, SiO_2 and SiO_4 with binding energies positioned respectively at 100.7, 102.3, 104.1, 105.1 and 106.0 eV [48, 52, 53].

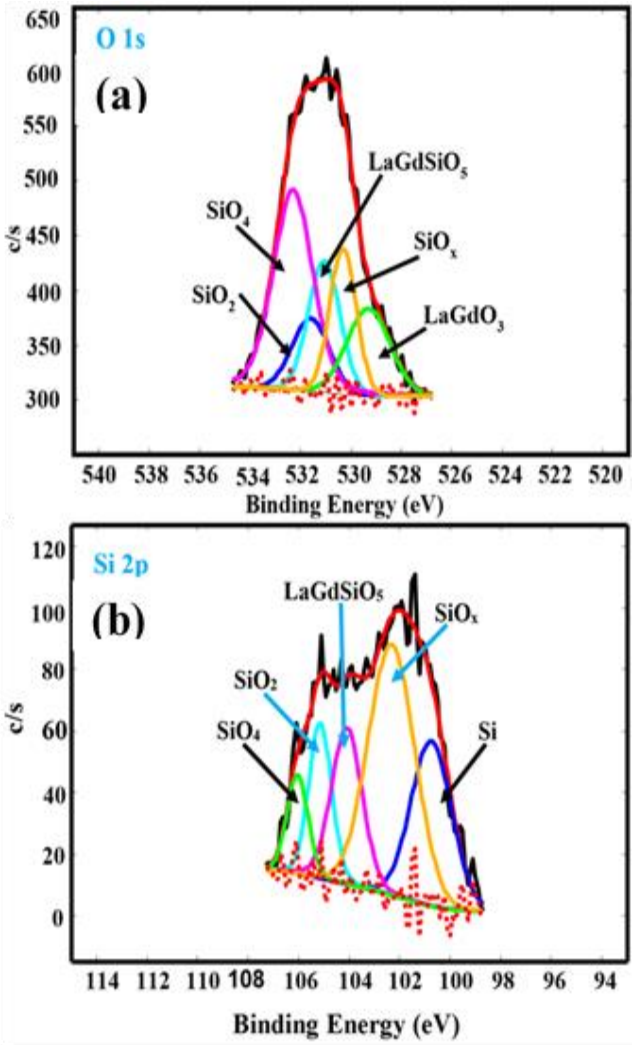

Fig. 4.9: Fitted XPS spectra for (a) O 1s and (b) Si 2p peaks for $La_{0.5}Gd_{1.5}SiO_5:Dy^{3+}$ film.

The 3d core-levels XPS spectra of all rare earth compounds are similar. They are double peak structured, consisting of $3d_{5/2}$ and $3d_{3/2}$ peaks and their energy loss lines [54]. The double structure is due to spin-orbit splitting. By and large, the spectrum is made up of XPS and energy loss lines. The major XPS peaks originate from photoexcitation of core-level electrons and arises as a result of electrons traveling to the surface of the solid without suffering energy loss. On the other hand, the energy loss lines arises as a result of electrons which lost energy during travel through the solid. The energy loss lines can be either intrinsic or extrinsic. Energy loss lines are intrinsic when they are due to the de-excitation of photoholes, which are neutralized by electrons that are localized in the site of photoemission process. This causes change in the energy of the state from which the photoemission occurred. Extrinsic energy loss lines are excited by the outgoing photoelectron in the solid in the process of its travel to the surface [55]. The photoelectrons which suffer no energy loss will have energy E_0 and energy loss lines at $E_0 - \hbar\omega_p$, $E_0 - 2\hbar\omega_p$, $E_0 - 3\hbar\omega_p$ etc., where $\hbar\omega_p$ is energy loss lines energy [56]. The fitted XPS spectrum of La 3d core-levels is shown in Fig. 4.10(a). The spin-orbit splitting of 16.8 eV is observed between the $3d_{5/2}$ and $3d_{3/2}$ double structure peaks of the La 3d core-level. During the photoionization process, individual states ($3d_{5/2}$ and $3d_{3/2}$) split into two final states labeled I and II in Fig. 4.10(a). The final state I is a $3d^14f^0$ final state configuration (a core hole) and it is due to the La-O bond in La_2O_3 and it is observed around 833.3 and 852.1 eV for $3d_{5/2}$ and $3d_{3/2}$ states respectively. The final state II is a $3d^1f^1$ final state configuration (a core hole with the transfer of an electron from the O_{2p} valence band to an empty 4f orbital) and it is due to La-OH bond in $La(OH)_3$. The final state II is further divided into J = 1 (a strong signal) and J ≠ 1 (a cluster of weak signals) terms because of electron-hole exchange interaction. In the $3d_{5/2}$ and $3d_{3/2}$ states, the J = 1 term lines were observed respectively around 837.5 and 854.3 eV whilst the J ≠ 1 term lines were observed respectively around 836.0 and 852.1 eV [57-59]. The La $3d_{5/2}$ and $3d_{3/2}$ energy loss lines are observed around 848.9 and 865.9 eV respectively [44, 57, 59-61]. The fitted XPS spectrum of the Gd 3d core-levels is shown in Fig. 4.10(b). Spin orbit splitting of 32.0 eV was observed between the $3d_{3/2}$ and $3d_{5/2}$ states of the Gd 3d core-levels. The two peaks observed around 1184.1 and 1187.0 eV in the $3d_{5/2}$ state are respectively assigned to Gd and Gd_2O_3. Likewise, two peaks were observed in the $3d_{3/2}$ state around 1217.3 and 1219.4 eV and they are assigned respectively to Gd and Gd_2O_3, respectively [62-65]. The small peak around 1201.8 is also assigned to the energy loss line of the Gd $3d_{5/2}$ state [61]. The broad peak around 1217.3 eV correlates with the Gd $4f^7 \rightarrow 3d^94f^7$ electronic configuration

usually observed in trivalent Gd compounds due to the $3d4f^7$ final state multiplet structure [66]. The Dy 4d core-levels fitted XPS spectrum is shown in Fig. 4.10(c). The XPS peaks observed around 156.6 and 158.5 eV are ascribed to Dy $4d_{5/2}$ and Dy $4d_{3/2}$, respectively [67]. These two peaks are due multiplet splitting. The multiplet splitting is a phenomenon usually observed in lanthanides 4d levels. This phenomenon gives rise to extra structures in the 4d state of lanthanides owing to the electrostatic interaction between a core-level and the partially filled 4f state [55]. The multiplet splitting in the Dy 4d core-level originates from the electrostatic interaction between the 4d and 4f states because these two shells have the same quantum number [68, 69]. The broad peak observed in the higher binding energy centering around 170 eV is ascribed to Dy-O bond in Dy_2O_3. The XPS deconvoluted peaks showed four peaks which arise due to the final Dy states with 4d and 4f spins parallel and anti-parallel. The two peaks observed at 167.9 and 169.5 eV are ascribed to the electrons with their spin anti-parallel to the spin of the electrons in the material and their satellites peaks respectively, while the peaks observed at 171.1 and 173.1 eV are attributed respectively to the electrons with their spins parallel to the spin of the electrons in the material and their satellites peaks. Photoelectrons with spins aligning in the same configuration (spins parallel) with the magnetization of the material will move freely from the core-level of the solid, while the movement of the photoelectrons which their spin are configured anti-parallel to the spin of the electrons in the material will suffer collision with the electrons in the material as they travel from the core-level of the solid. In general, the anti-parallel spin electrons suffer energy loss due to their collision with the electrons in the material and hence they have lower energy than the parallel spin electrons [70].

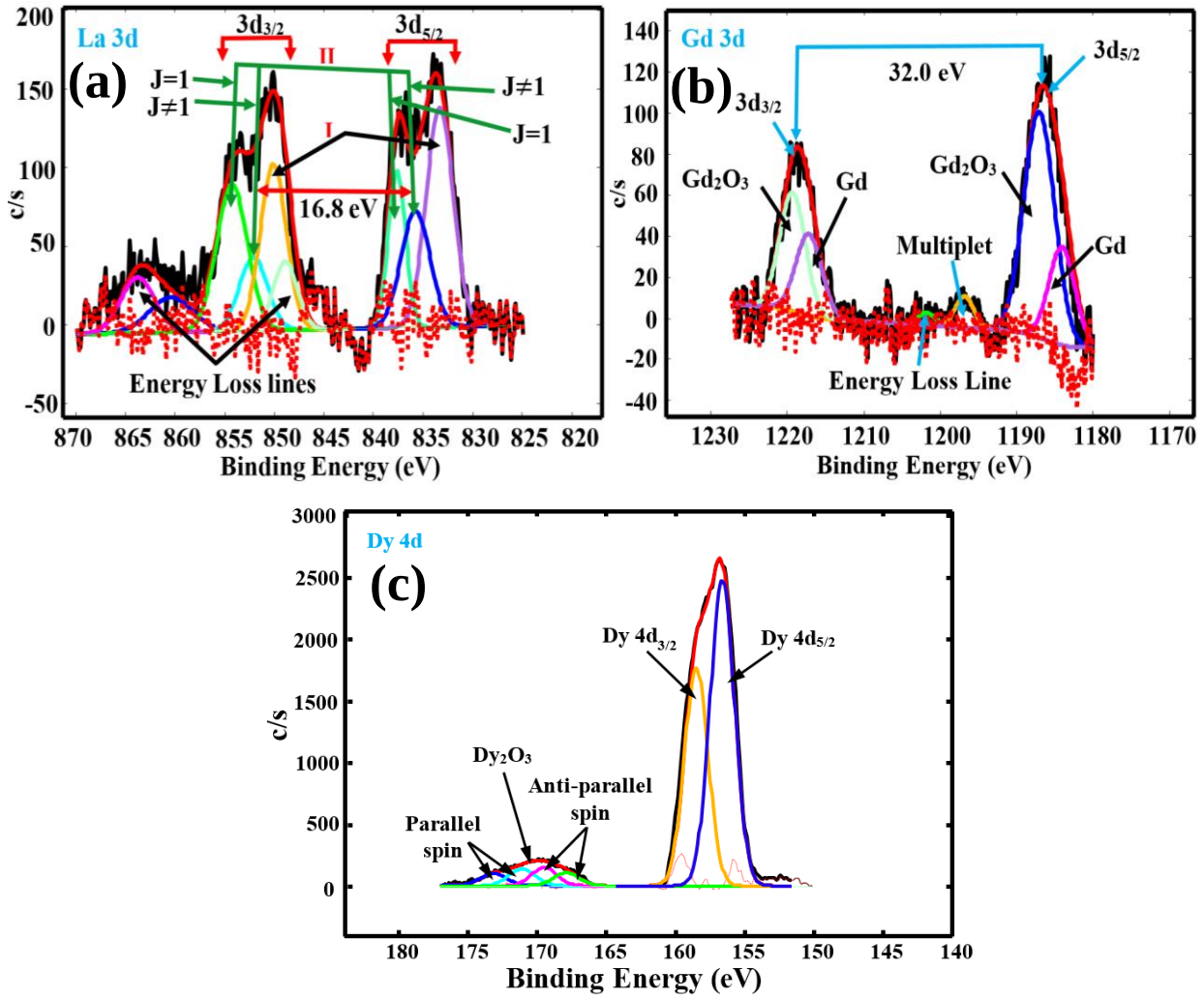

Fig. 4.10: Fitted XPS spectra of (a) La 3d peak, (b) Gd 3d peak and (c) Dy 4d peak.

Fig. 4.11(a) and (c) shows PL excitation spectra of $La_{0.5}Gd_{1.5}SiO_5:Dy^{3+}$ films deposited respectively in different atmosphere and at different deposition temperature. The excitation spectra were recorded when monitoring the emission at 578 nm. The excitation spectra comprises of one major peak at 226 nm and other minor peaks in the range of 275 to 400 nm. The insets in Fig. 4.11(a) and (c) are magnified excitation spectra in the range of 300 to 400 nm. The broad bands with maximums at 226 nm are attributed to the electronic transition from oxygen 2p (O2p) valence band to the La (5d6s) and Gd (5d6s) conduction bands [71, 72]. The other excitation peaks observed at 275 and 313 nm are assigned respectively to $^8S_{7/2} \rightarrow {}^6I_J$ and $^6P_J \rightarrow {}^8S_{7/2}$ f-f forbidden transition of Gd^{3+}, while those at 325, 351 and 386 nm are attributed to $^6H_{15/2} \rightarrow {}^6P_{3/2}$, $^6H_{15/2} \rightarrow {}^6P_{7/2}$ and $^6H_{15/2} \rightarrow {}^4I_{13/2}$ f-f transition of Dy^{3+} respectively [13, 73-75].

The corresponding PL emission spectra were recorded when the films were excited at the wavelength of 226 nm and they are shown in Fig. 4.11(b) and (d). The emission spectra comprise of four emission lines, two major (488 and 578 nm) and two minor (668 and 756 nm) peaks which are ascribed to $^4F_{9/2} \rightarrow {}^6H_{15/2}$, $^4F_{9/2} \rightarrow {}^6H_{13/2}$, $^4F_{9/2} \rightarrow {}^6H_{11/12}$ and $^4F_{9/2} \rightarrow {}^6H_{9/2}$ f-f electronic transition of Dy^{3+} respectively[72]. From the excitation and the emission spectra of the films deposited in different atmospheres (Fig. 4.11(a) and (b) respectively), as expected from the AFM and the FE-SEM images, the film deposited in O_2 gave the highest PL intensity followed by the film deposited in Ar while the one deposited in vacuum have the least intensity.

Furthermore, in the PL excitation and emission spectra of the films deposited at different substrate temperatures (50, 200, 300, 400 and 500 ºC), (Fig. 4.11(c) and (d) respectively), the PL intensity increased with the substrate temperature up to 200 ºC. It can be observed from the XRD pattern in Fig. 4.1(b) that the crystallinity of the films increased with the substrate temperature. Hence, the PL data is not in full agreement with the XRD data when considering from the crystallinity perspective, since it is believed that the intensity of the UV peaks depends strongly on the crystalline quality of a material [76]. However, it has also been suggested that the PL intensity does not solely depend on the crystallinity of a material but depends also on its stoichiometry [77-79]. During PLD, there is usually an interplay between the background gas (O_2 in this case), pressure, and the substrate temperature [80], since the mobility of the particles on the surface of the film depends strongly on these two parameters. Therefore, the best films are obtained when there is a balance between the substrate temperature and the background gas pressure, and this defines the best stoichiometry of the material. From the XRD and the FE-SEM results, the films deposited at the substrate temperature of 400 and 500 ºC have the best crystallinity, but the film deposited at substrate temperature of 200 ºC have the highest emission intensity. Therefore, in our case, the balance between the substrate temperature and the background gas pressure was attained at the substrate temperature of 200 ºC.

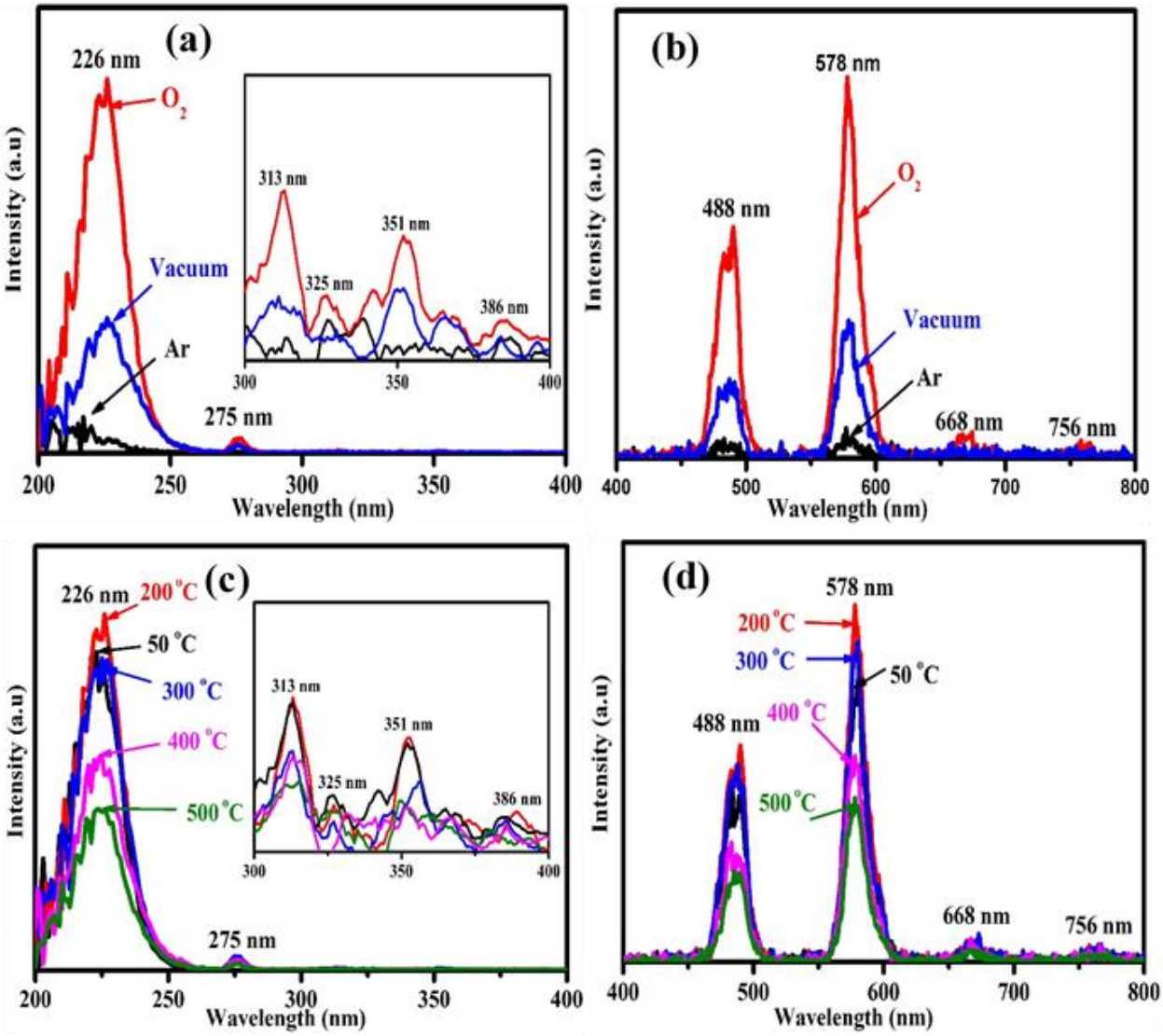

Fig. 4.11: PL spectra of $La_{0.5}Gd_{1.5}SiO_5:Dy^{3+}$ films, (a) excitation and (b) emission spectra of the films deposited in Ar (blue), vacuum (black) and O_2 (red), (c) and (d) excitation and emission spectra of films deposited in O_2 at the substrate temperature of 50 (black), 200 (red), 300 (blue), 400 (purple) and 500 ºC (green).

Fig. 4.12(a) and (b) show the photoluminescence excitation and emission spectra, respectively, for the thin films deposited in O_2 atmosphere at 200 ºC for 15, 30 and 50 min. The film deposited for 15 shown the lowest photoluminescence intensity, while there is no significant difference between the intensities of the films deposited for 30 and 50 min.

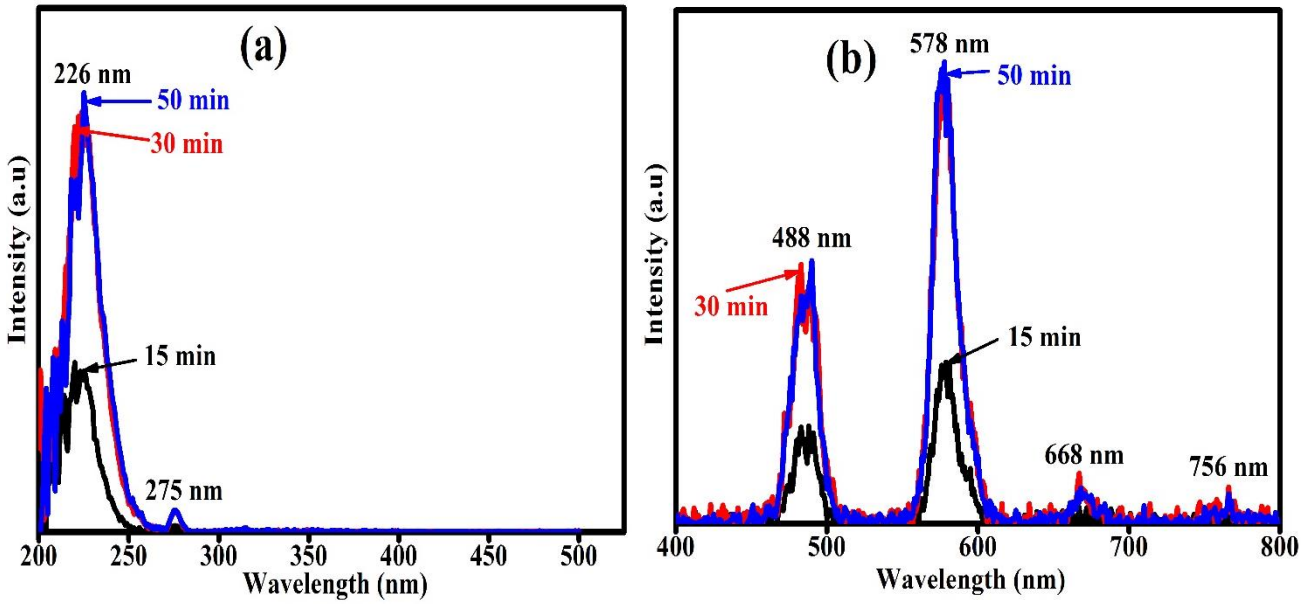

Fig. 4.12: PL (a) excitation and (b) emission spectra of $La_{0.5}Gd_{1.5}SiO_5:Dy^{3+}$ films deposited in O_2 atmosphere at the substrate temperature of 200 ºC for 15, 30 and 50 min.

4.4. Conclusions

Mixed lanthanum gadolinium oxyorthosilicate doped with dysprosium ($La_{0.5}Gd_{1.5}SiO_5:Dy^{3+}$) thin films were successfully deposited on Si (111) substrates using PLD. The films were deposited in different atmosphere and substrate temperatures. The structure, compositions, morphology, electronic states, and the photoluminescence properties were investigated. The XRD showed that the crystallinity of the films increased with substrate temperature, with the highest quality crystalline films obtained at 400 and 500 ºC. However, the photoluminescence emission showed that films deposited at 200 ºC in O_2 have the highest intensity. Furthermore, the films deposited in O_2 gave higher emission intensity than those deposited in Ar and vacuum environments. This suggests that O_2 is a better atmosphere to deposit $La_{0.5}Gd_{1.5}SiO_5:Dy^{3+}$ thin films. The thickness of the films varies from 3.12 to 1.93 µm. The excitation showed a prominent peak at around 226 nm from which the emission were measured. Emission lines associated to f-f electronic transition of Dy^{3+} were also observed at 488, 578, 668 and 756 nm.

4.5. References

[1] D.W. Cooke, E.A. McKigney, R.E. Muenchausen, B.L. Bennett, U.S. Patent No. 7,525,094 B2 (28 April 2008).

[2] T.E. Peters, J. Electrochem. Soc. 116 (1969) 985.

[3] J. Wang, S. Tian, G. Li, F. Liao, X. Jing, J. Electrochem. Soc. 148 (2001) h61.

[4] R.Y. Lee, F.L. Zhang, J. Penczek, B.K. Wagner, P.N. Yocom, C.J. Summers, J. Vac. Sci. Technol. 16 (1998) 855.

[5] C.M. Michail, A. Toutountzis, I.G. Valais, I. Seferis, M. Georgousis, G. Fountos, I.S. Kandarakis, G.S. Panayiotakis, e-J. Sci. Technol. 2 (2010) 5.

[6] T. Kamae, Y. Fukazawa, N. Isobe, M. Kokubun, A. Kubota, S. Osone, T. Takahashi, N. Tsuchida, H. Ishibashi, Nucl. Instrum. Methods Phys. Res. A. 490 (2002) 456.

[7] V. Avdeichikov, B. Jakobsson, V.A. Nikitin, V. Nomokonov, A. Wegner, Nucl. Instrum. Methods Phys. Res. A. 484 (2002) 251.

[8] W. Mangesha, T.D. Taulbee, J.D. Valentine, B.D. Rooney, Methods Phys. Res. A. 486 (2002) 448.

[9] J. Felsche, The crystal chemistry of the rare-earth silicates, In, R.A. Penneman, R.R. Ryan, A. Rosenzweig, R. Reisfeld, J. Felsche, C.K. Jørgensen, "*Structure and Bonding*" Springer, Berlin 13 (1973) p. 99–197.

[10] D. Meiss, W. Wischert, S. Kemmler-Sack, Phys. Status Solidi. A. 133 (1992) 575.

[11] M. Yin, C. Duan, W. Zhang, L. Lou, S. Xia, J.C. Krupa, J. Appl. Phys. 86 (1999) 3751.

[12] E.M. Rabinovich, J. Shmulovich, V.J. Fratello, N.J. Kopylov, Am. Ceram. Soc. Bull. 66 (1987) 1505.

[13] S.N. Ogugua, S.K.K. Shaat, H.C. Swart, O.M. Ntwaeaborwa, J. Phys. & Chem. Sol. 83 (2015) 109.

[14] G.B. Loutts, A.I. Zagumennyi, S.B. Lavrishev, Y.D. Zavartsev, P.A. Studenikin, J. Crystal Growth. 174 (1997) 331.

[15] G.D. Dominiak, W. R. Romanowski, R. Lisiecki, P. Solarz, B. Macalik, M. Berkowski, M. Gzowacki, V. Domukhovski, Crystal Growth & Design. 10 (2010) 3522.

[16] W. Drozdowski, K. Brylew, A. J. Wojtowicz, J. Kisielewski, M. Świrkowicz, T. Łukasiewicz, J. T.M. de Haas, P. Dorenbos, Opt. Matt. Exp. 4 (2014) 1207.

[17] W. Li, S. Xu, H. Pan, L. Ding, H. Zeng, Opt. Expr. 14 (2006) 6681.

[18] O. Sidletskiy, Funct. Mat. 14 (2010) 414.

[19] W. Tian, J. Zhu, Z. Wang, J. Wang, Z. Wei, Chinese Opt. Lett. 12 (2014) 1.

[20] G.B. Loutts, A.I. Zagumennyi, S.V. Lavrishchev, Y.D. Zavartsev, P.A. Studenikin, J. Cry. Growth. 174 (1997) 331.

[21] M. Jie, G. Zhao, X, Zeng, L. Su, H. Pang, X. He, J. Xu, J. Cryst. Growth. 277 (2005) 175.

[22] J.Y. Choe, Mat. Res. Innovat. 6 (2002) 238.

[23] G.A. Hirata, J. McKittrick, M. Avalos-Borja, J.M. Siqueiros, D. Devlin, Appl. Surf. Sci. 113/l 14 (1997) 509.

[24] R.B. Mueller-Mach, G.O. Mueller, U.S. Patent No. 6,696703 B2 (24 February 2004).

[25] M. Ohring, The material science of thin films, Academic press, San Diego, California (1992).

[26] K. Seshan, Handbook of thin-film deposition processes and techniques principles, methods, equipment and applications, Noyes publications/William Andrew publication, New York,USA (2002).

[27] J. Schou, Laser beam-solid interactions: Fundamental aspects, In, Y. Pauleau (Ed.) "*Materials surface processing by directed energy techniques*" 1st Ed. E-MRS (2006) p. 35–66.

[28] D. B. Chrisey, G. K. Hubler, Pulsed laser deposition of thin films, Wiley, New York, (1994) p. 2.

[29] H.M. Smith, A.F. Turner, Appl. Opt. 4 (1965) 147.

[30] T. Venkayesan (Ed.), Symposium I: Recent Advances in the Pulsed Laser Deposition of Thin Films and Nanostructures, MRS Singapore ICMAT Symposia Proceedings, available in Procedia Engineering, Elsevier (2013).

[31] D.P. Norton, Pulsed laser deposition of complex materials: progress towards applications, In, R. Eason (Ed.), "*Pulsed laser deposition of thin films – applications-led growth of functional materials*" Wiley-Interscience (2006) p. 4–5.

[32] H.U. Krebs, M. Weisheit, J. Faupel, E. Süske, T. Scharf, C. Fuhse, M. Störmer, K. Strum, M. Seibt, H. Kijewski, D. Nelke, E. Panchenko, M. Buback, Adv. Sol. Sta. Phys. 43 (2003) 505.

[33] S.N. Ogugua, S.K.K. Shaat, H.C. Swart, O.M. Ntwaeaborwa, Structure, scanning electron microscopy, and spectroscopy of $La_{2-x}Gd_xSiO_5:Dy^{3+}$ nanophosphors (manuscript in preparation).

[34] M. Mayer, SIMNRA User's Guide, Report IPP 9/113, Max-Planck-Institut für Plasmaphysik: Garching (1997) p. 4–47.

[35] M. Mayer, Nucl. Instrum. Methods Phys. Res. B. 332 (2014) 176.

[36] M. Liu, B.Y. Man, C.S. Xue, H.Z. Zhuang, H.C. Zhu, X.Q. Wei, C.S. Chen, Appl. Phys. A. 85 (2006) 83.

[37] L. Chen, Particulates generated by pulsed laser ablation, In, D.B. Chrisey, G.K. Hulber (Ed.) "*Pulsed Laser Deposition of Thin Films*, John Wiley & Sons, Inc, New York (1994) p. 167 – 196.

[38] Y. Wang, B. Chu, Q. He, J. Xu, App. Surf. Sci. 254 (2008) 6799.

[39] A. Kitahara, S. Yasuna, K. Fujikawa, Trans. Mat. Res. Soci. Japan. 34 (2009) 613.

[40] E. Rauhala, Scattering methods, In, Z.B. Alfassi (Ed.) "*Instrumental multi-element chemical analysis*" Springer Science and Business Media Dordrecht (1998) p. 379–437.

[41] M. Liu, B.Y. Man, X.C. Lin, X.Y. Li, C.S. Chen, Appl. Surf. Sci. 253 (2007) 9291.

[42] M. Liu, X.Q. Wei, Z.G. Zhang, G. Sun, C.S. Chen, C.S. Xue, H.Z. Zhuang, B.Y. Man. App. Surf. Sci. 252 (2006) 4321.

[43] P. Chetri, A. Choudhury, Physica E. 47 (2013) 257.

[44] F.S. Aguirre-Tastado, M. Milojevic, B. Lee, J. Kim, R.M. Wallace. Appl. Phys. Lett. 93 (2008) 172907.

[45] T. Gougousi, M.J. Kelly, D.B. Terry, G.N. Parsons. J. Appl. Phys. 93 (2003) 1691.

[46] W.S. Kim, S.K. Park, D.Y. Moon, B.W. Kang, H.D. Kim, J.W. Park, J. Korean Phys. Soc. 55 (2009) 590.

[47] C. Li, Y. Shen, S. Zhu, S. Shen, RSC Adv. 4 (2014) 29107.

[48] E. Coetsee. J.J. Terblans, H.C. Swart, Appl. Surf. Sci. 256 (2010) 6641.

[49] J.L. Her, M.H. Wu, Y.B. Peng, T.M. Pan, W.H. Weng, S.T. Pang, L. Chi, Int. J. Electrochem. Sci. 8 (2013) 606.

[50] O.E. Filatova, A.A. Sokolov, V.I. Kozhevnikov, Studying the internal structure of high-K dielectric films by hard X-ray photoelectron spectroscopy and TEM, In, H. Gang, S. Zhaoqi (Ed.) "*High-k gate dielectric for CMOS technology*" Wiley-VCH, Weinheim (2012) p. 236.

[51] G. He, M. Liu, L.Q. Zhu, M. Chang, Q. Fang, L.D. Zhang, Surf. Sci. 576 (2005) 67.

[52] C. Logofatu, C.C. Negrila, R.V. Ghita, F. Ungureanu, C. G. Manea, M.F. Lazarescu. Study of SiO_2/Si interface by surface techniques. Intech, Rejika, Croatia (2011).

[53] E. Coetsee, J.J Terblans, H.C. Swart, J. Lumin. 126 (2007) 37.

[54] A.J. Signorelli, R.G. Hayes, Phys. Rev. B. 8 (1973) 81.

[55] S. Hufner, Photoelectron Spectroscopy: Principles and Applications, Springer-Verlage Berlin Heideberg (2003) p. 173.

[56] A. Bahadur, S.K. Srivastava, Trakia J. Sci. 8 (2010) 29.

[57] D.F. Mullica, C.K. Lok, H.O. Perkins, Phy. Rev. B. 31 (1985)4039.

[58] T.H. Yang, Y.W. Harn, K.C. Chiu, C.L. Fan, J.M. Wu, J. Mater, Chem. 22 (2012) 17071.

[59] S. Mickevicius, S. Grebinskij, V. Bondarenka, H. Tvardauskas, B. Vengalis, K. Sliuzienne, B.A. Orlowski, W. Drube, Opt. Appl. XXXVI (2006) 235.

[60] L.A. Qian, P.T. Lai, W.M. Tang, Appl. Phys. Lett. 104 (2014) 123505.

[61] J.F. Moulder, W.F. Stickle, P.E. Sobol, K.D. Bomben, Handbook of X-ray photoelectron spectroscopy, J. Chastain (Ed.), Perkin-Elmer Corporation, Physical Electronics Division, USA, (1992) p. 20.

[62] J.F. Moulder, W.F. Stickle, P.E. Sobol, K.D. Bomben, Handbook of X-ray photoelectron spectroscopy, J. Chastain (Ed.), Perkin-Elmer Corporation, Physical Electronics Division, USA, (1992) p. 152-153.

[63] D. Raiser, J.P. Deville, J. Electron Spectrosc. Relat. Phenom. 57 (1991) 91.

[64] M. Ahren, L. Selegard, F. Soderlind, M. Linares, J. Kauczor, P. Norman, P. Kall, K. Uvdal, J. Nanopart. Res. 14 (2012) 1006.

[65] P.P. Mokoene, I.M. Nagpure, V. Kumar, R.E. Kroon, E.J. Olivier, J.H. Neethling, H.C. Swart, O.M. Ntwaeaborwa, J. Phys. & Chem. Sol. 75 (2014) 998.

[66] J. Chung, J. Park, J.G. Park, B.H. Choi, S.J. Oh, E.J. Cho, H.D. Kim, Y.S. Known, J. Korean Phys. Soci. 38 (2001) 744.

[67] K.S. Mishra, S. Kannan, Langmuir 32 (2016) 13687.

[68] H. Ogasawara, A. Kotani, B.T. Thole, Phys. Rev. B. 50 (1994) 12332.

[69] V.A. Mode, G.S. Smith, J. Inorg. & Nucl. Chem. 31 (1969)1857.

[70] V.K. Khanna, Nanosensors: physical, chemical, and biological, CRC Press, Taylor and Frances group (2012) p. 403.

[71] G. Li, C. Li, C. Zhang, Z. Cheng, Z. Quan, C. Peng, J. Mater. Chem. 19 (2009) 8936.

[72] M. Jia, J. Zhang, S. Lu, J. Sun, Y. Luo, X. Ren, H. Song, X. Wang, Chem. Phys. Lett. 384 (2004)193.

[73] Y. Li, Y. Chang, Y. Chang, Y. Lin, C. Laing, J. Phys. Chem. C. 111 (2007) 10682.

[74] G.V. Reddy, L.R. Moorthy, T. Chengaiah, B.C. Jamalaiah, Adv. Mat. Lett. 4 (2013)841

[75] W.T. Camal, P.R. Fields, K. Rajnak, J. Chem. Phys. 49 (1968) 4424.

[76] M. Liu, X.Q. Wei, Z.G. Zhang, G. Sun, C.S. Chen, C.S. Xue, H.Z. Zhuang, B.Y. Man, Appl. Surf. Sci. 252 (2006) 4321.

[77] B.L. Zhu, X.H. Sun, X.Z. Zhao, F.H. Su, G.H. Li, X.G. Wu, J. Wu, R. Wu, J. Liu, Vac. 82 (2008) 495.

[78] B.J. Jin, H.S. Woo, S. Im, S.H. Bae, S.Y. Lee, Appl. Surf. Sci. 169/170 (2001) 521.

[79] S. Im, B. J. Jin, S. Yi, J. Appl. Phys. 87 (2000) 4558.

[80] L. Zhao, J. Lian, Y. Liu, Q. Jiang, Appl. Surf. Sci. 252 (2006) 8451.

CH. 5

The influence of post-deposition annealing on the structure, morphology and luminescence properties of pulsed laser deposited $La_{0.5}Gd_{1.5}SiO_5$ doped Dy^{3+} thin films

5.1. Introduction

Some interesting properties of rare earth oxyorthosilicates (R_2SiO_5) such as high quantum efficiency, wide band gap, high chemical and thermal stability, fast decay time, high density and minimal self-absorption have attracted the attention of many researchers [1]. They have emerged as preferred host for rare-earths dopant ions for various luminescence applications due to similar ionic radii and their wide band gap [2-11]. There are many reports in the literature on the structural properties of R_2SiO_5 [12-16]. Both La_2SiO_5 and Gd_2SiO_5 belong to the rare earth oxyorthosilicate family with monoclinic crystal structure system and the *P21/C* space group. Dy^{3+} doped matrices are a promising phosphors for white light emitting applications such as white light emitting diodes (LEDs) [17], field emission displays (FED) [18] and other white colour display devices [19]. The possibility of generating white emission from Dy^{3+} doped matrices is based solely on the branching ratio of its two major emission lines located at ~485 nm (bluish-green) and ~575 nm (yellowish) [20].

Thin film technology plays measure role in the fabrication of devices used in different technological applications. However, important category of thin film based technologies are mostly in luminescence materials [21]. The luminescence properties of pulsed laser deposition (PLD) based thin films can be improved by varying parameters such as deposition time, substrate to target distance, substrate temperature, laser parameters, and by changing the background gas [22]. In addition, post-deposition annealing (hereafter referred to as post-annealing) of films deposited using PLD have shown a substantial improvement on crystallinity and optical properties of the films [21, 23-26]. At higher annealing temperatures, films are crystalline, more chemical and thermally stable and show higher luminescent intensity [23]. Hence, in this study, $La_{0.5}Gd_{1.5}SiO_5$:Dy^{3+} thin films deposited on Si(111) substrate at different substrate temperatures were post annealed at 1000 ^oC temperature for 1hr. The influence of post-annealing on the structure, morphology and luminescence properties of the films were studied and are discussed.

5.2. Experimental

5.2.1. *Preparation*

A $La_{0.5}Gd_{1.5}SiO_5:Dy^{3+}$ was prepared in powder form by using urea-assisted solution combustion method (a detailed synthesis method used for the powder preparation can be found in [20]). The target (pellet) was prepared by pressing the powder phosphor using a hydraulic press. It was sintered in air using an oven set at 250 ^oC for 3hr to get rid of adsorbed moisture and other volatile substances. The Si (111) substrates were mounted one at a time on the substrate holder inside the vacuum chamber set 4.5 cm away from the rotating target holder. The deposition chamber was pumped to a base pressure of 3.25×10^{-6} Torr. The repetition rate of the laser and the laser energy were fixed respectively at 10 Hz and 40 mJ throughout the deposition. The films were deposited in oxygen atmosphere at different deposition temperature (50, 200 and 500 ^oC) for 30 min using 266 nm Nd: YAG pulsed laser. After deposition, the films were annealed at 1000 ^oC for 1hr before characterization.

5.2.2. *Characterization*

A Bruker D8-Advanced X-ray diffractometer using $CuK_\propto$ radiation with an incident wavelength of 0.15406 nm under a voltage of 40 kV and a current of 40 mA. The surface topography and particle morphology of the surface of the films were analyzed using a Shimadzu SPM-9600 Scanning Probe Microscope and a JEOL JSM-7800F Field Emission Scanning Electron Microscope (FE-SEM) respectively. The elemental analysis was performed using Oxford Aztec 350 X-Max80 Energy-Dispersive X-ray Spectroscopy (EDS) fitted in the JEOL JSM-7800F FE-SEM system. The photoluminescence (PL) spectra were measured using (i) a Carry Eclipse fluorescence spectrometer equipped with 150 W xenon lamp and (ii) a PL system consisting of a 325 nm He–Cd gas laser as an excitation source, a spectrometer, a photomultiplier tube (PMT) detector and a lock-in amplifier. The cathodoluminescence (CL) spectra were measured using a Gatan MonoCL4 fitted to the JEOL JSM-7800F FE-SEM system.

5.3. Results and discussion

Fig. 5.1 depicts the XRD patterns of $La_{0.5}Gd_{1.5}SiO_5:Dy^{3+}$ thin films deposited in oxygen background at 50, 200 and 500 ^oC and post-annealed for 1hr at 1000 ^oC. Compare to the as-deposited films reported in our previous work [22], the XRD of the annealed films appeared to be crystalline (especially the film deposited at 500 ^oC). The peaks marked with an asterisk (*) are from La_2SiO_5 while those with # are from Gd_2SiO_5. The XRD patterns are consistent with the JCDPS file no: 40-0234 and 74-1795 of La_2SiO_5 and Gd_2SiO_5 respectively. The XRD patterns of the films shows four diffraction peaks assigned to the (200), (002), $(\bar{2}12)$ and $(\bar{3}11)$ diffraction peaks of Gd_2SiO_5 and three diffraction peaks assigned to the (012), (013) and (330) peaks of La_2SiO_5. The insets, (1) and (2), of Fig. 5.1 are the magnified XRD patterns of the film deposited at 500 ^oC and 200 ^oC in the 2θ ranges of $25-60^o$ and $20-25^o$, respectively. The (111) diffraction pattern from Gd_2SiO_5 and La_2SiO_5 are apparent in insets (1).

The surface topography of the $La_{0.5}Gd_{1.5}SiO_5:Dy^{3+}$ films were studied using atomic force microscope (AFM). Fig. 5.2(a-c) depicts the 3D AFM images of 4×4 μm area scan of the films deposited at 50 ^oC, 200 ^oC and 500 ^oC respectively, and post-annealed at 1000 ^oC for 1hr. Particle morphology and roughness of the films are different from those of as-deposited films reported in ref [22]. Post-annealing resulted in a considerable increase in the size of the grains causing the grains to agglomerate together and the grain boundaries fades.

Unlike spherical shape formed by the as-deposited films [22], the surface of the annealed films appeared smoother with terraces. In agreement with the FE-SEM images (Fig. 5.3), the films deposited at 50 and 200 ^oC appear to have bigger and closely packed grains compared to the film deposited at 500 ^oC. For the films deposited at 200 and 500 ^oC, the root mean square (rms) roughness values increased from 70 and 39 nm to 73 and 64.5 nm respectively after annealing. The increase in rms value indicates roughness of the film surface after annealing, suggesting increase in crystallinity of the films [27]. On the other hand, the rms value of the film deposited at 50 ^oC, decreased from 84 nm to 78 nm after annealing [28], thus indicating smoothness of the surface after annealing. The smoothness of the surface of the low temperature (50 ^oC) deposited film after annealing could be due to high impurity content observe in low temperature deposited films which evaporates after post-annealing [28].

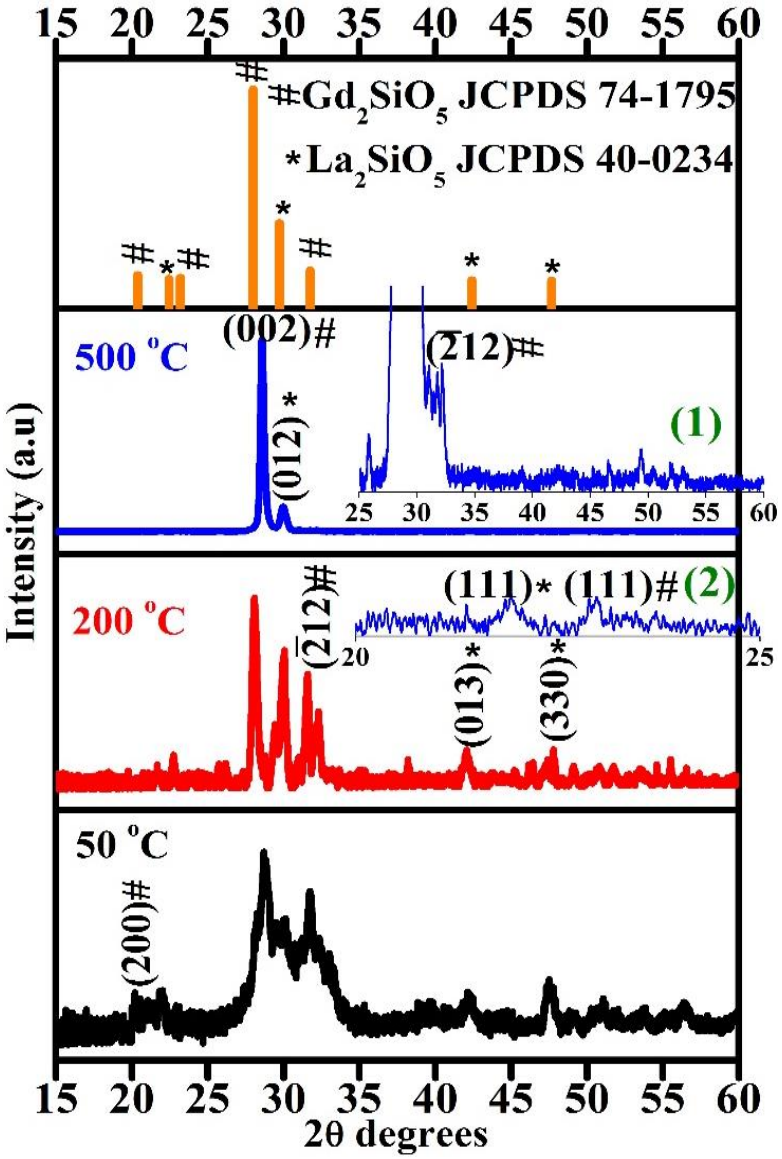

Fig. 5.1: The XRD pattern of $La_{0.5}Gd_{1.5}SiO_5:Dy^{3+}$ thin films deposited in oxygen atmosphere at different substrate temperature (50, 200 and 500 ^oC) and post-annealed at 1000 ^oC for 1hr.

Fig. 5.3 depicts the FE-SEM images of the films pulsed laser deposited at different substrate temperatures and post-annealed in air at 1000^oC. Fig. 5.3(a) and (b), (c) and (d), and (e) and (f) shows the low magnification (x10, 000) and high magnification (x50, 000) of the encircled spots for the films deposited at 50, 200 and 500 ^oC respectively. The low magnification micrographs depict spherically shaped particulates with discrete sizes. However, from the high magnification micrographs, it was observed that the spherically shaped particulates comprised of smaller

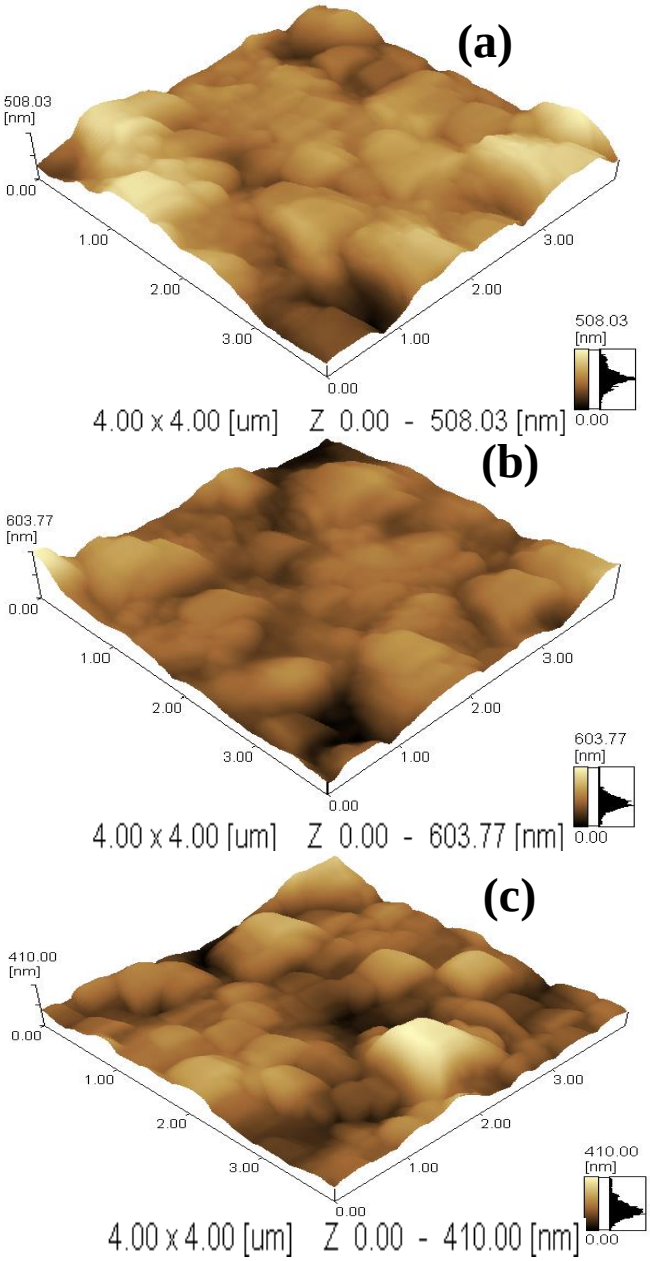

Fig. 5.2: The AFM micrograph of $La_{0.5}Gd_{1.5}SiO_5:Dy^{3+}$ thin films deposited in oxygen atmosphere at different substrate temperature (a) 50 ºC, (b) 200 ºC and (c) 500 ºC and post-annealed at 1000 ºC for 1h.

agglomerated spherically shaped particles. This could be due to the splashing phenomenon as explaining in detail in refs [29-31]. Furthermore, it can be seen that the films deposited at 50 ^{o}C (Fig. 5.3(a)) comprises of large amount of particulates, followed by the film deposited at 200 ^{o}C, while the film deposited at 500 ^{o}C contains the least number of particles. Compare to the SEM images of the as-deposited films [22], the particle size generally increased after post-annealing treatment.

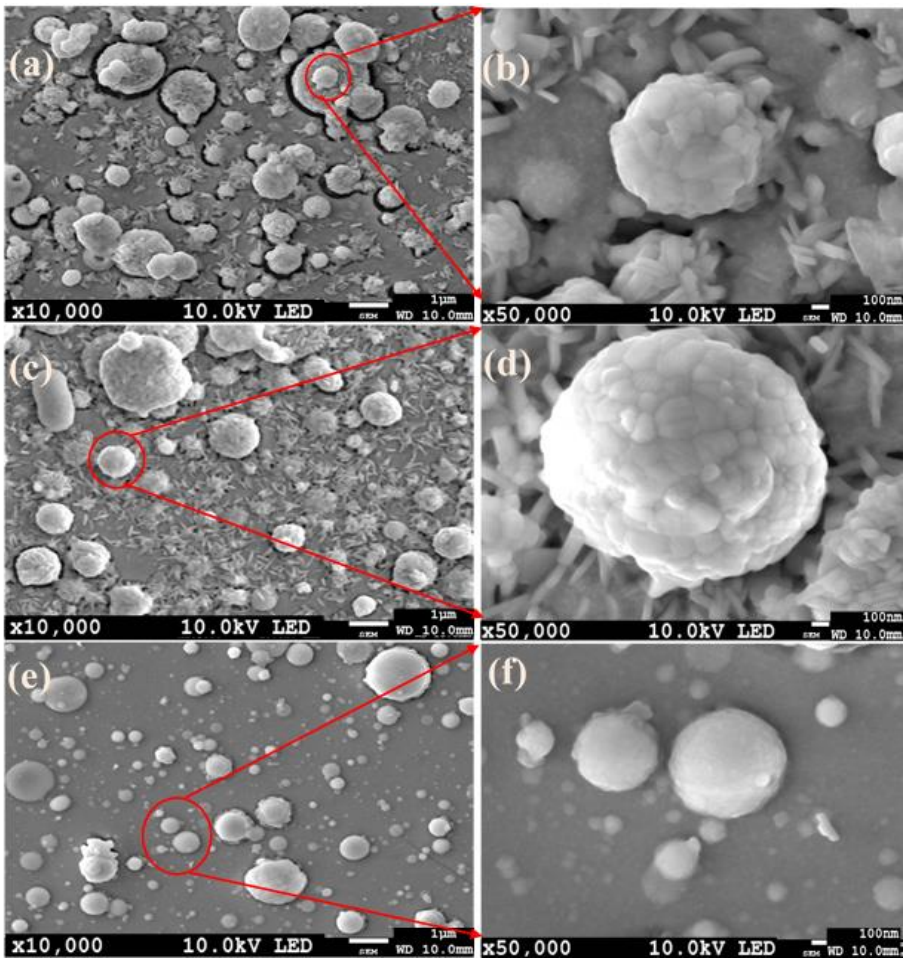

Fig. 5.3: FE-SEM images of $La_{0.5}Gd_{1.5}SiO_5:Dy^{3+}$ thin films deposited in oxygen atmosphere at different substrate temperature (a) 50 ^{o}C, (c) 200 ^{o}C and (e) 500 ^{o}C and post-annealed at 1000 ^{o}C for 1hr. (b), (d) and (f) are the magnification of the encircled region of (a), (c) and (e) respectively.

The elemental composition of the films was analyzed using EDS. Fig. 5.4(a-c) show the EDS scan of $La_{0.5}Gd_{1.5}SiO_5:Dy^{3+}$ films deposited at 50, 200 and 500 ^oC respectively. All the elements (La, Gd, Si, O_2, and Dy) were observed at their respective energy positions in the spectra. The low count of Dy in the spectra can be linked to its low concentration in the films (the concentration of Dy is 1mol% in the powder sample before deposition).

In ToF-SIMS, pulsed ion beam is used to eject and ionize atomic and molecular species from the uppermost layers of a material. The resulting secondary ions are accelerated into a mass spectrometer where they are separated in space according to their mass and a spectrum of intensity versus atomic mass is obtained. By scanning the finely focused beam across the surface of the sample, the chemical image of the sample can be generated to visualize the distribution of individual species across the surface of the sample. Fig. 5.5(a) and (b) shows the ToF-SIMS positive mass spectra of the atomic and molecular species generated from $La_{0.5}Gd_{1.5}SiO_5:Dy^{3+}$ thin film deposited at 50 ^oC and annealed at 1000 ^oC for 1h in the atomic mass range of 12-46 u and 138-181 u respectively. Each spectrum shows the atomic mass unit corresponding to the specie/species in question.

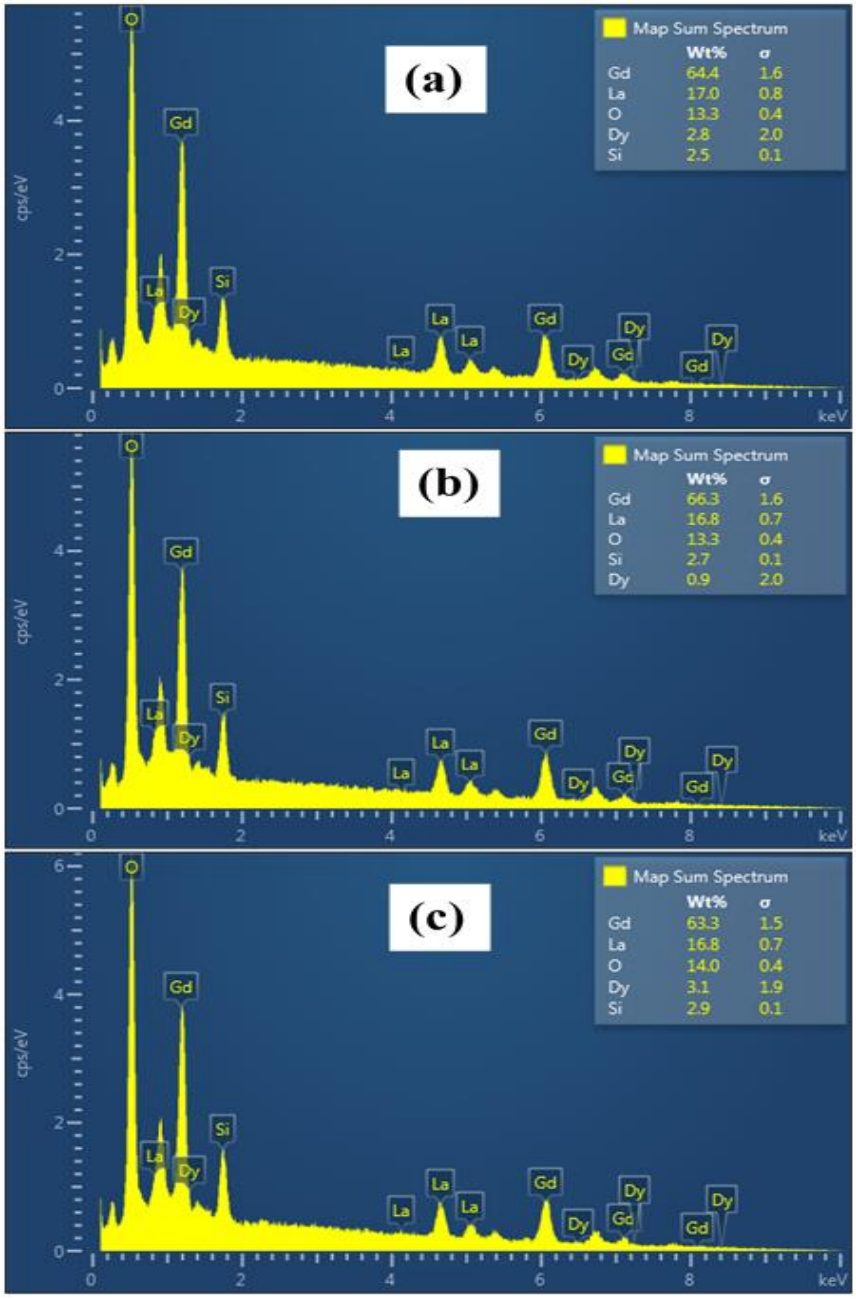

Fig. 5.4: The EDS spectra of $La_{0.5}Gd_{1.5}SiO_5:Dy^{3+}$ thin films deposited in oxygen atmosphere at different substrate temperature (a) 50 ºC, (b) 200 ºC and (c) 500 ºC and post-annealed at 1000 ºC for 1hr.

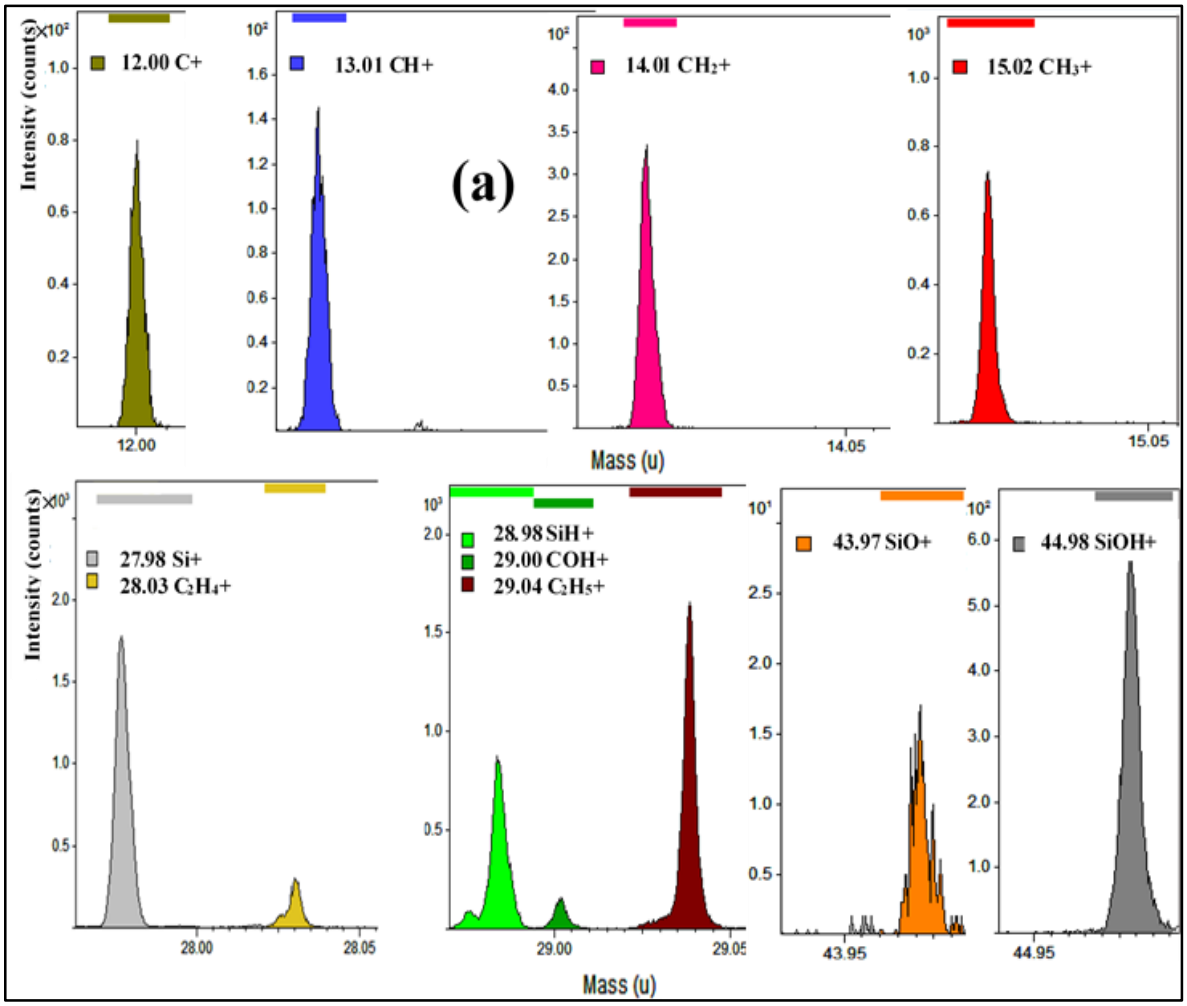

Fig. 5.5(a): The positive ToF-SIMS spectra of molecular and ionic species in the atomic mass range of 12-46 u from $La_{0.5}Gd_{1.5}SiO_5:Dy^{3+}$ film deposited at 50 ^oC and annealed at 1000 ^oC for 1h.

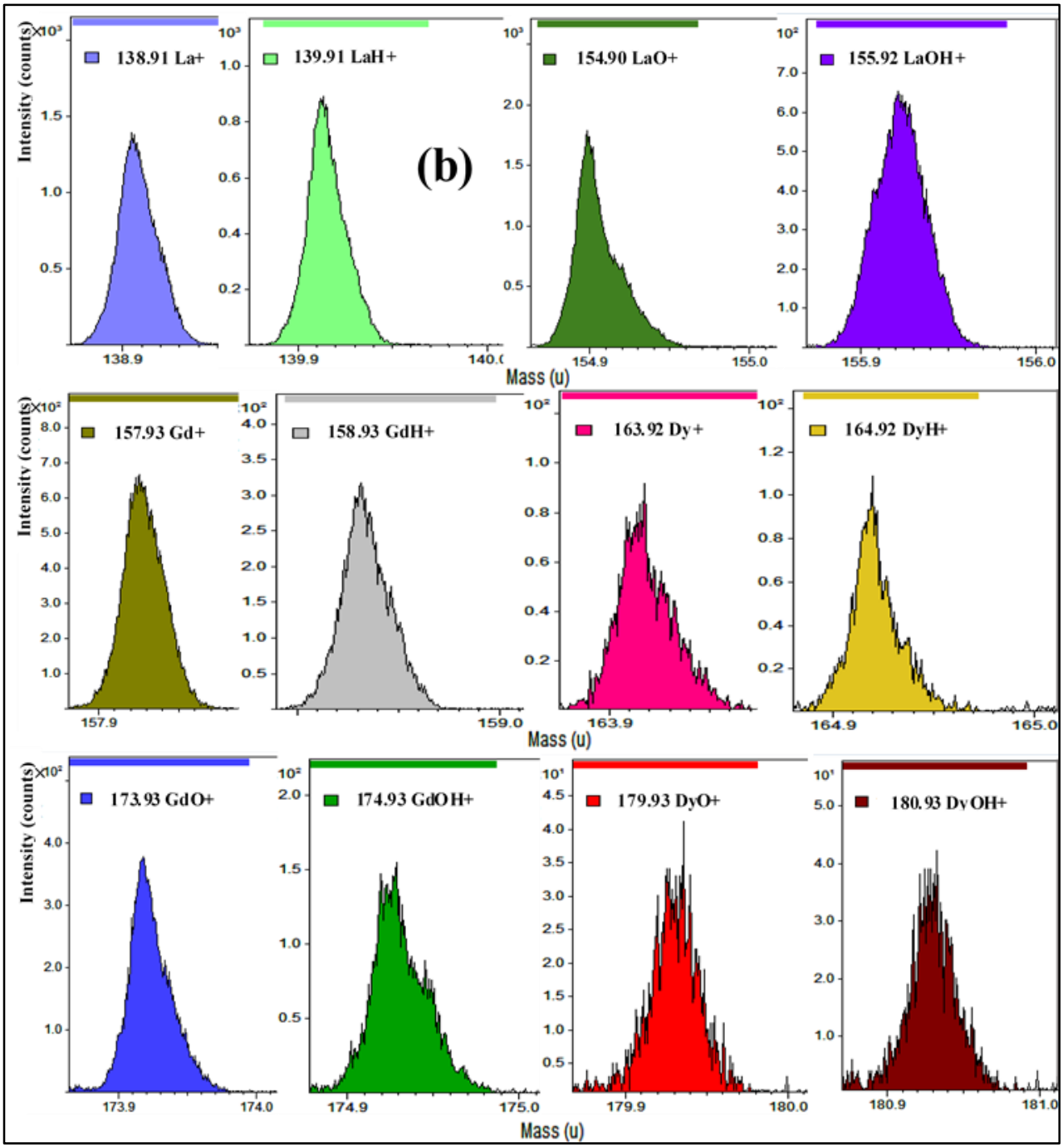

Fig. 5.5(b): The positive ToF-SIMS spectra of molecular and ionic species in the atomic mass range of 138-181 u from $La_{0.5}Gd_{1.5}SiO_5:Dy^{3+}$ film deposited at 50 ^oC and annealed at 1000 ^oC for 1h.

Table 5.1 shows all the atomic and molecular species generated from the films and their corresponding atomic mass units. All the carbon related species (C^+, CH^+, CH_2^+, CH_3^+, $C_2H_4^+$, COH^+ and $C_2H_5^+$) could be from the atmospheric carbon and contaminants from the sample holder [32].

Table 5.1: The atomic and molecular ions and their corresponding atomic mass units obtained from positive ToF-SIMS measurement of $La_{0.5}Gd_{1.5}SiO_5:Dy^{3+}$ thin film deposited at 50 ^oC and annealed at 1000 ^oC for 1h.

Atomic/molecular ions	Mass (u)	Atomic/molecular ions	Mass (u)
C^+	12.00	Gd^+	157.93
CH^+	13.01	GdH^+	158.93
CH_2^+	14.01	Dy^+	163.92
CH_3^+	15.02	DyH^+	164.92
Si^+	27.98	GdO^+	173.93
$C_2H_4^+$	28.03	$GdOH^+$	174.93
SiH^+	28.98	DyO^+	179.93
COH^+	29.00	$DyOH^+$	180.93
$C_2H_5^+$	29.04		
SiO^+	43.97		
$SiOH^+$	44.98		
La^+	138.91		
LaH^+	139.91		
LaO^+	154.90		
$LaOH^+$	155.92		

Fig. 5.6(a-d) shows the 100 × 100 μm^2 ToF-SIMS positive images of LaO^+ (blue), GdO^+ (red), DyO^+ (green) and the overlaid image of the three molecular compounds respectively, obtained from $La_{0.5}Gd_{1.5}SiO_5:Dy^{3+}$ film deposited at 50 ^oC and annealed at 1000 ^oC for 1h. The vertical bar at the right side of each image represent the intensity of the signal emanating from each specie. Region with high colour intensity represent high concentration while region with low intensity

represent low concentration of the specie in question. It can be seen from Fig. 5.6(a-d) that all the species are evenly distributed across the surface of the scanned area of the film.

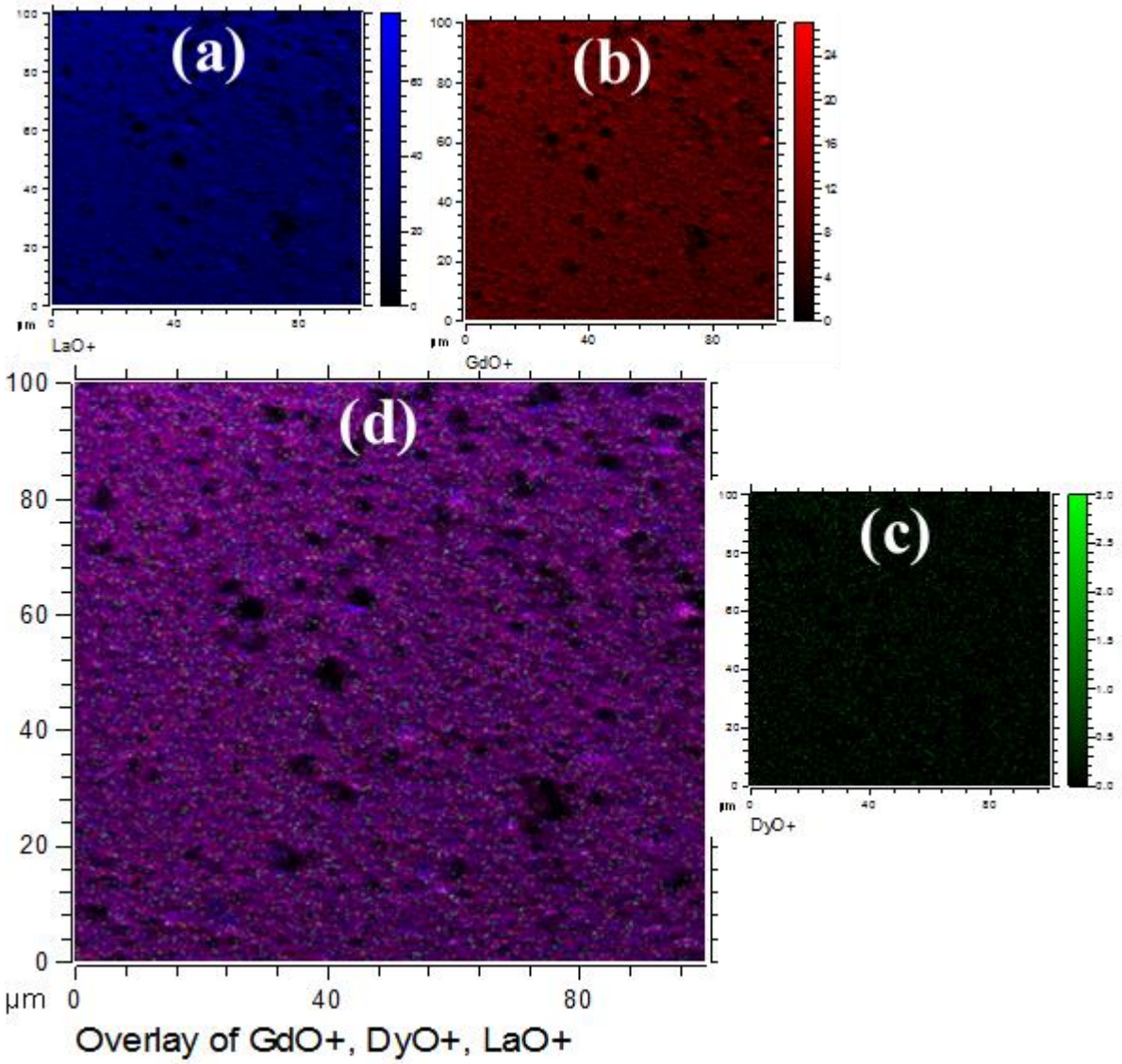

Fig. 5.6: The positive ToF-SIMS images of (a) LaO^+, (b) GdO^+, (c) DyO^+ and (d) overlay images of LaO^+, GdO^+ and DyO^+ of $La_{0.5}Gd_{1.5}SiO_5:Dy^{3+}$ thin film deposited at 50 ^oC and annealed at 1000 ^oC for 1h.

The PL excitation and emission of the films measured using a monochromatized xenon lamp as excitation source are shown in Fig. 5.7. The excitation spectra were measured by monitoring the $^4F_{9/2} \rightarrow {}^6H_{13/2}$ (578 nm) transition of Dy^{3+} and are shown in Fig. 5.7(a). Fig. 5.7(c) is the magnified

excitation spectra in the wavelength range of 265−370 nm. The excitation peak observed at 226 nm is assigned to the electronic transition from oxygen 2p (O2p) valence band to the La (5d6s) and Gd (5d6s) conduction band. The peaks observed at 275 and 313 nm are ascribed to $^{8}S_{7/2}\rightarrow{}^{6}I_{J}$ and $^{6}P_{J}\rightarrow{}^{8}S_{7/2}$ f→f transitions of Gd^{3+} respectively, while the peak at 351 nm is attributed to the $^{6}H_{15/2}\rightarrow{}^{6}P_{7/2}$ f→f transition of Dy^{3+} [22].

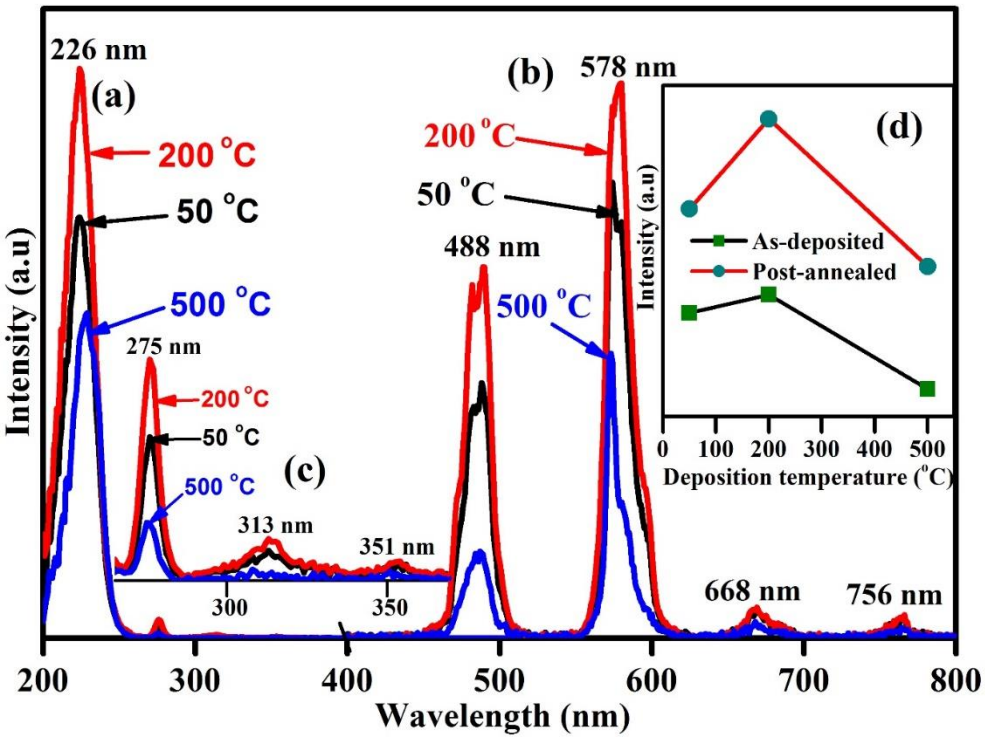

Fig. 5.7: The PL (a) excitation spectra and (b) emission spectra of $La_{0.5}Gd_{1.5}SiO_5:Dy^{3+}$ thin films deposited in oxygen atmosphere at different substrate temperature (50, 200 and 500 °C) and post-annealed at 1000 °C for 1hr. (c) is the magnification of the excitation spectra in the wavelength range of 265−370 nm and (d) is the comparison of the luminescence intensities of the as-deposited [22] and the post-annealed films.

The PL emission spectra were measured by monitoring the 226 nm excitation peak and are shown in Fig. 5.7(b). Four emission lines were observed at 484, 578, 668 and 756 nm and are ascribed to the $^{4}F_{9/2}\rightarrow{}^{6}H_{15/2}$, $^{4}F_{9/2}\rightarrow{}^{6}H_{13/2}$, $^{4}F_{9/2}\rightarrow{}^{6}H_{11/2}$ and $^{4}F_{9/2}\rightarrow{}^{6}H_{9/2}$ electronic transition of Dy^{3+}, respectively [22]. Defined as hypersensitive transition, the yellow (578 nm) emission is an electric dipole transition and is strongly influenced by the crystal field environment around the Dy^{3+} ions.

The blue (484 nm) emission is a magnetic dipole transition and hardly varies with the crystal field around Dy^{3+} [33]. As can be seen from Fig. 5.7, the film deposited at 200 ^{o}C has the highest luminescence intensity, followed by the film deposited at 50 ^{o}C, while the film deposited at 500 ^{o}C has the least intensity. Fig. 5.7(d) is the plot of deposition temperature versus photoluminescence intensity of the as-deposited and the post-annealed films. It is evident that the intensity of the post-annealed films is almost twice that of the as-deposited films. The cathodoluminescence (CL) emission spectra of the films deposited at 50, 200 and 500 ^{o}C and annealed at 1000 ^{o}C for 1hr after exposure time of 50 seconds are shown in Fig. 5.8. The CL spectra show similar emission lines from Dy^{3+} as observed in the PL emission spectra (Fig. 5.7(b)) except for a little shift in the peak positions and a broad background band. The broad band is host related and is more evident when the films were excited with 325 nm He-Cd laser (Fig. 5.9). It can also be seen from Fig. 5.8 that the CL intensities of the films are in agreement with the PL spectra, with the film deposited at 200 ^{o}C having the highest intensity and the film deposited at 500 ^{o}C having the smallest intensity. This suggests that the number of photons absorbed by each film during photoexcitation is proportional to the number of photons emitted by the film under electron bombardment.

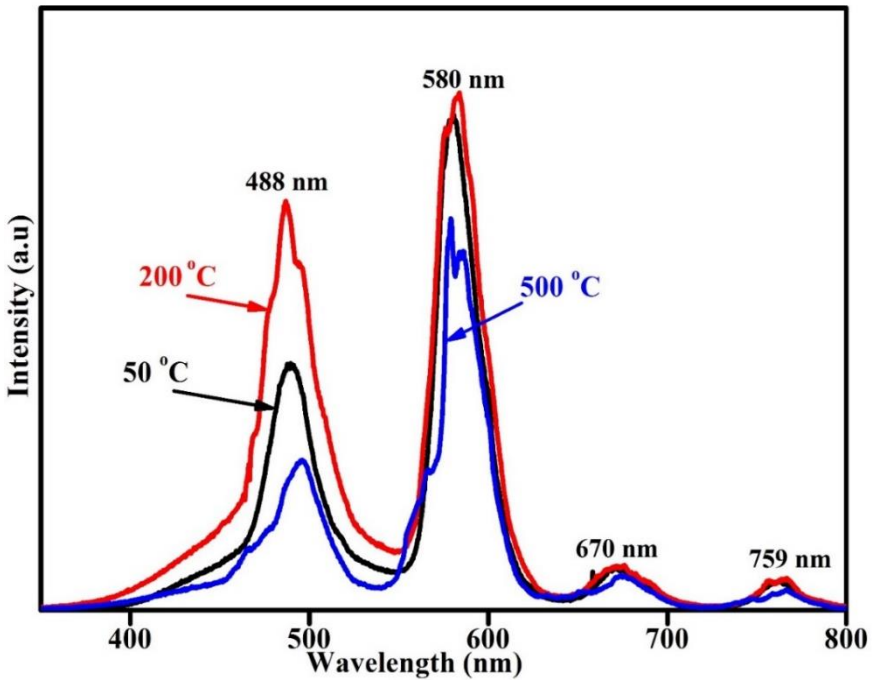

Fig. 5.8: The CL spectra of $La_{0.5}Gd_{1.5}SiO_5:Dy^{3+}$ thin films deposited in oxygen atmosphere at different substrate temperature (50, 200 and 500 ^{o}C) and post-annealed at 1000 ^{o}C for 1hr.

The PL emission of the as-deposited (Fig. 5.9(a)) and the post-annealed (at 1000 ^{o}C for 1hr) (Fig. 5.9(b)) $La_{0.5}Gd_{1.5}SiO_5:Dy^{3+}$ films deposited at 50 ^{o}C, 200 ^{o}C and 500 ^{o}C in oxygen background were recorded using 325 nm He-Cd laser as the excitation source. As shown in Fig. 5.9(a) and (b), the emission spectra consist of all the emission lines observed in Fig. 5.7(b) and Fig. 5.8. In addition, the broad blue emission observed in the CL spectra (Fig. 5.8) is more pronounced (Fig. 5.9) in the wavelength range of 365−600 nm and is assigned to self-trapped excitons (STE) in SiO_2 [34]. The broad blue emission was not observed in the emission spectra in Fig. 5.9(b) because different mode of excitation was used in both cases. The spectra in Fig. 5.7(b) was excited in phosphorescence mode, while the spectra in Fig. 5.9 was excited in fluorescence mode. The STE emission of the as-deposited films (Fig. 5.9(b)) have its maximum at 422 nm, but the maximum shifted to higher wavelength (460 nm) upon annealing in Fig. 5.9(b). The blue emission of Dy^{3+} ions (488 nm) is very close to the STE emission, so the two bands overlaps effectively. Due to the overlapping, the 488 nm emission of Dy^{3+} was highly enhanced. Lü et al [35], Liu et al [36] and Liu et al [37] have reported similar results. It can be seen from the emission spectra of the as-deposited and annealed films that the films deposited at 50 ^{o}C has the highest emission intensity followed by the film deposited at 200 ^{o}C, while the film deposited at 500 ^{o}C has the smallest emission intensity. The inset of Fig. 5.9(a) compares the intensities of the STE bands, 488 and 578 nm emissions as a function of deposition temperature for the as-deposited and the annealed films. As can be seen from the inset, for example, the emission intensity of the 488 nm line for the post-annealed film deposited at 50 ^{o}C has the highest emission intensity followed by that of the film deposited at 200 ^{o}C, while the film deposited at 500 ^{o}C has the smallest intensity. It can also be seen that except from the film deposited at 500 ^{o}C, the annealed films have higher intensities than the as-deposited films for the three major emission bands (STE, 488 and 578 nm). The increase of in luminescence intensity with annealing observed in the films deposited at lower temperature (50 ^{o}C and 200 ^{o}C) can be attributed to the crystallization of the films after post-annealing [23]. On the other, the decrease in the luminescence intensity observed in the film deposited at 500 ^{o}C after post-annealing treatment could be due to the change in the local environment of Dy^{3+} atoms from low to high temperature O_2 coordination of the host materials [12, 38].

The CIE chromaticity coordinates of the data obtained when the films were excited using a 325 nm He-Cd laser as the excitation source and the CL data were calculated and the results are shown in Fig. 5.10(a) and (b) respectively. Table 5. 2 shows the (x, y) colour coordinates of the films.

The correlated colour (CCT) of the films were calculated using the McCamy empirical formula [39, 40] (Eq. 5.1) given by

$$CCT = -473n^3 + 3601n^2 - 6861n + 5514.31 \quad (5.1)$$

In Eq. 5.1, $n = (x - x_e)/(y - y_e)$ with $x_e = 0.3320$ and $y_e = 0.1858$ is the chromaticity epicenter.

Table 5.2: The CIE coordinates for the 325 nm He-Cd laser and the CL data of $La_{0.5}Gd_{1.5}SiO_5:Dy^{3+}$ thin films deposited in oxygen atmosphere at different substrate temperature (50, 200 and 500 ^oC) and post-annealed at 1000 ^oC for 1hr.

Deposition temperature (^oC)	Chromaticity coordinates (x, y)		CCT (K)	
	As-deposited	Post-annealed	As-deposited	Post-annealed
325 nm He-Cd laser				
50	(0.246, 0.249)	(0.217, 0.249)	22619	32554
200	(0.276, 0.282)	(0.219, 0.265)	10815	23903
500	(0.259, 0.301)	(0.259, 0.288)	11419	12412
Cathodoluminescence				
50		(0.361, 0.363)		4486
200		(0.348, 0.351)		4883
500		(0.372, 0.401)		4360

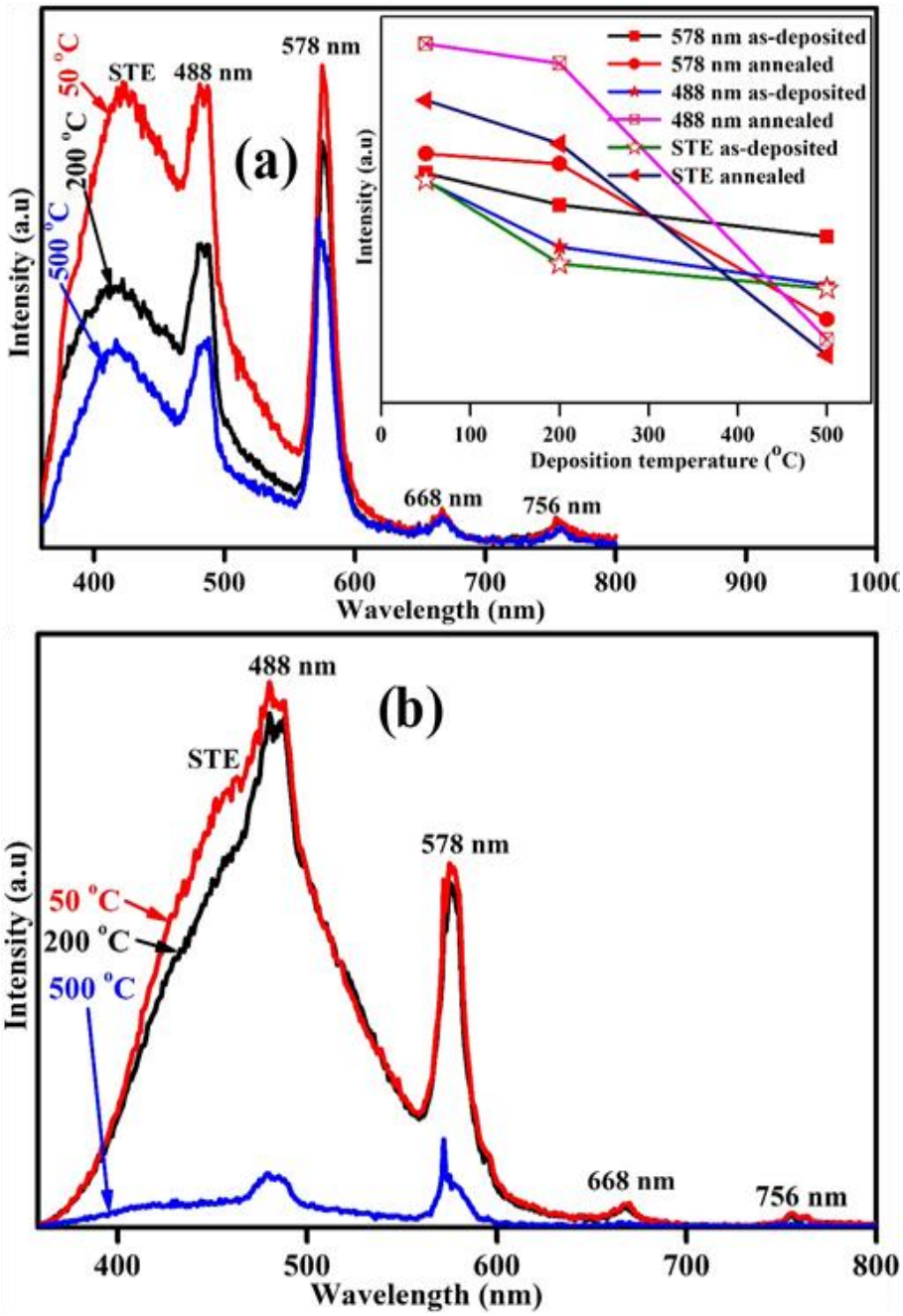

Fig. 5.9: The 325 nm He-Cd laser excited PL spectra of $La_{0.5}Gd_{1.5}SiO_5:Dy^{3+}$ thin films deposited in oxygen atmosphere (a) at different substrate temperature (50, 200 and 500 ^oC) and (b) post-annealed at 1000 ^oC for 1hr.

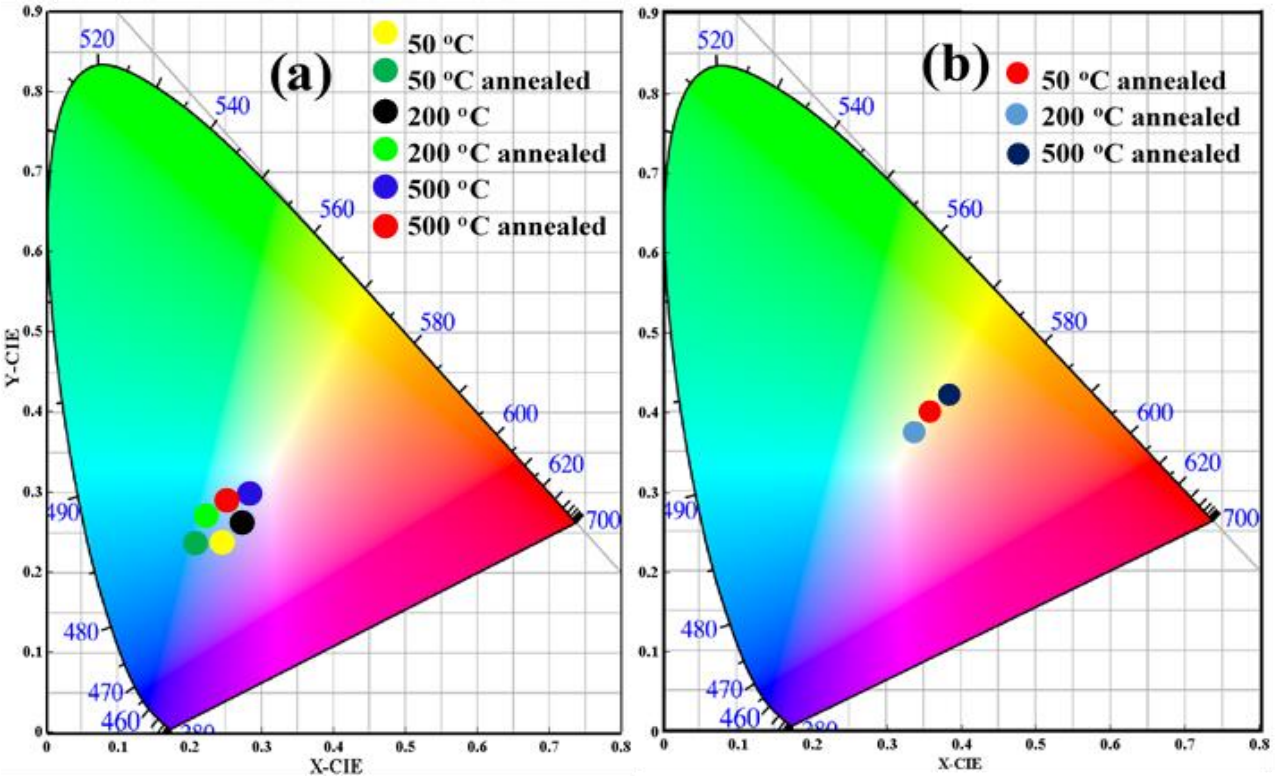

Fig. 5.10: The CIE coordinates diagram of $La_{0.5}Gd_{1.5}SiO_5:Dy^{3+}$ thin films deposited in oxygen atmosphere at different substrate temperature (50, 200 and 500 °C) and post-annealed at 1000 °C for 1hr. (a) from the data when the films were excited with a 325 nm He-Cd laser, (b) from the CL data.

5.4. Conclusion

$La_{0.5}Gd_{1.5}SiO_5:Dy^{3+}$ thin films were successfully deposited on Si(111) substrates at the substrate temperatures of 50, 200 and 500 °C and post-annealed at 1000 °C for 1hr. The XRD patterns showed an improved crystallinity after post-annealing. The FE-SEM images showed that the films were made of agglomerated small particles. The PL studies showed a great luminescence enhancement after post-annealing. From the CIE colour coordinates calculated from the PL and CL data, the films could have potential applications in white lighting devices such as LEDs and FEDs.

5.6. References

[1] D. W. Cooke, E. A. McKigney, R. E. Muenchausen, B. L. Bennett, U.S. patent 7,525,094 B2 (28 April 2008).

[2] D. Kurtsev, O. Sidletskiy, S. Neicheva, V. Bondar, O. Zelenskaya, V. Tarasov, M. Biatov, A. Gektin, Mat. Res. Bul. 52 (2014) 25.

[3] Y. Parganiha, J. Kaur, V. Dubey, D. Chandrakar, Superlattices Microstruct. 77 (2015) 152.

[4] S. Shinde, M. Ghosh, S.G. Singh, S. Sen, S.C. Gadkari, S.K. Gupta, J. Alloy Compd. 592 (2014) 12.

[5] I.V. Khodyuk, P.A. Rodnyi, P. Dorenbos, Instrum. Exp. Tech. 55 (2012) 187.

[6] G. Zhu, Z. Ci, Q. Wang, Y. Wen, S. Han, Y. Shi, S. Xin, Y. Wang, J. Mater. Chem. C, 1 (2013) 449.

[7] H. Yokota, M. Yoshida, H. Ishibashi, T. Yano, H. Yamamoto, S. Kikkawa, J. Alloy Compd. 495 (2010) 162.

[8] X. Zhang, Y. Chen, L. Zhou, Q. Pang, M. Gong, Ind. Eng. Chem. Res. 53 (2014) 6694.

[9] V.V. Seminko, A.A. Masalov, Y.V. Malyukin, Spectroscopically detected segregation of Pr^{3+} ions in Y_2SiO_5 nanocrystals, Proceedings of the international conference nanomaterials: applications and properties, 1 (2012) 04RES04.

[10] M. Trevisani, K.V. Ivanovskikh, N. Grillet, F. Piccinelli, M. Bettinelli, Chem. Phys. Lett. 565 (2013) 80.

[11] G. Ramakrishna, H. Nagabhushana, S.C. Prashantha, S.C. Sharma, B.M. Nagabhushana, Spectrochim. Acta Mol. Biomol. Spectrosc. 136 (2015) 356.

[12] S.N. Ogugua, S.K.K. Shaat, H.C. Swart, O.M. Ntwaeaborwa, J. Lumin. 179 (2016)154.

[13] J. Felsche, The crystal chemistry of the rare-earth silicates, In, R.A. Penneman, R.R. Ryan, A. Rosenzweig, R. Reisfeld, J. Felsche, C.K. Jørgensen, "*Structure and Bonding*" Springer, Berlin 13 (1973) p. 99–197.

[14] K. Fukuda, T. Iwata, Powder Diffr. 4 (2006) 300.

[15] R. Lisiecki, G. Dominiak-Dzik · P. Solarz, W. Ryba-Romanowski, M. Berkowski, M. Głowacki, Appl. Phys. B 98 (2010) 337.

[16] L. Zheng, L. Su, J. Xu, Growth and characterization of ytterbium doped silicate crystals for ultra-fast laser applications, In, N. Kolesnikov, (Ed.) "*Modern aspect of block crystal and thin film preparation*" Intech, Shanghai, China (2012) p. 25–42.

[17] P. Suthanthirakumar, K. Marimuthu, J. Mol. Struct. 1125 (2016) 443.

[18] X. Liu, Y. Lui, D. Yan, H. Zhu, C. Liu, C. Xu, Y. Liu, X. Wang, J. Mater. Chem. 22 (2012) 16839.

[19] M. Dhanalakshmia, H. Nagabhushana, G.P. Darshan, R.B. Basavaraj, B.D. Prasad, J. Sci. Adv. Mater. Dev. 2 (2017) 22.

[20] S.N. Ogugua, S.K.K. Shaat, H.C. Swart, O.M. Ntwaeaborwa, J. Phys. Chem. Sol. 83 (2015) 109.

[21] A. Yousif, H.C. Swart, O.M. Ntwaeaborwa, J. Lumin. 143 (2013) 201.

[22] S.N. Ogugua, R.L. Nyenge, P.T. Sechogela, H.C. Swart, O.M. Ntwaeaborwa, J. Vac. Sci. Technol. A, 34 (2016) 021520.

[23] A. Yousif, H.C. Swart, O.M. Ntwaeaborwa, E. Coetsee, Appl. Surf. Sci. 270 (2013) 331.

[24] M.F. Al-Kuhaili, S.M.A. Durrani, J. Alloy Compd. 509 (2011) 9536.

[25] F.K. Shan, G.X. Liu, J. Korean Phys. Soc. 54 (2009) 916.

[26] D.P. Rueda1, J.M. Vadillo, J.J. Laserna, J. Phys. Conf. Ser. 687 (2016) 012028.

[27] T. Kelwing, S. Mutas, M. Trentzsch, A. Naumann, B. Trui, L. Herrmann, F. Graetsch, C. Klein, L. Wilde, S. Ohsiek, M. Weisheit, A. Peeva, I. Richter, H. Prinz, A. Wuerfel, R. Carter, R. Stephan, P. Kücher, W. Hansch, ECS Trans. 33 (2010) 3.

[28] H. Park, S.Q. Hussain, S. Velumani, A.H. TuanLe, S. Ahn, S. Kim, J. Yi, Mater. Sci. Semicond. Process. 37(2015)29.

[29] L. Égerházi, Zs. Geretovszky, T. Csákó, T. Szörényi, Appl. Surf. Sci. 252 (2006) 4661.

[30] T. Yoshitake, G. Shiraishi, K. Nagayama, Appl. Surf. Sci. 197–198 (2002) 379.

[31] F. Tcheliebou, S. Baik, J. Appl. Phys. 80 (1996) 7046.

[32] S.N. Ogugua, S.K.K. Shaat, H.C. Swart, O.M. Ntwaeaborwa, J. Phys. Chem. Sol. 83 (2015) 109.

[33] J. Kuang, Y. Liu, J. Zhang, J. Solid State Chem. 179 (2006) 266.

[34] C. Itoh, K. Tanimura, N. Itoh, J. Phys. C: Solid State Phys. 21 (1988) 4693.

[35] W. Lü, H. Zhou, G. Chen, J Li, Z. Zhu, Z. You, C. Tu, J. Phys. Chem. C 113 (2009) 3844.

[36] X. Liu, Y. Liu, D. Yan, H. Zhu, C. Liu, C. Xu, Y. Liu, X. Wang, J. Mater. Chem. 22 (2012) 16839.

[37] Y. Liu, B. Lei, C. Shi, Chem. Mater. 17 (2005) 2108.

[38] R. Serna, S.N. Sánchez, P.M. Roque, ECS Trans, 28 (2010) 229.

[39] C. S. McCamy, Color Res. Appl. 17 (1992) 142.

[40] G.A. Kumar, M. Pokhrela, A. Martinez, R.C. Dennis, I.L. Villegas, D.K. Sardara, J. Alloys Comp. 513 (2012) 559.

CH. 6

The dynamics of the photoluminescence of Pr^{3+} in mixed lanthanum yttrium oxyorthosilicate hosts

6.1. Introduction

The luminescence intensities from Pr^{3+} f→f transitions have shown inconsistency in different host materials [1]. Visible emission from Pr^{3+} f→f transition doped matrices are predominantly observed from its $^3P_0$ and $^1D_2$ energy levels. Depending on the crystal field strength of the host material, the luminescence intensity associated with these energy levels can dominate in the emission spectrum, since the crystal field of the host determines where the bottom of the 4f5d level of Pr^{3+} lies with respect to the $^3P_0$ and $^1D_2$ levels [1-4]. The position of the 4f5d level of Pr^{3+} determines the rate of the $^3P_0 \rightarrow {}^1D_2$ non-radiative decay. This non-radiative decay in Pr^{3+} doped matrices has been explained using different mechanisms, such as inter-system crossing due to Pr-to-metal charge transfer [5], multiphonon relaxation [6-10], cross-relaxation between Pr^{3+} ions [11, 12] and inter-system crossing via low-lying 4f5d excited state of Pr^{3+} [3, 4]. However, De Mello Donegá et al [3] in their study of non-radiative relaxation processes of Pr^{3+} in various hosts, demonstrated that the dominant mechanism for $^3P_0 \rightarrow {}^1D_2$ non-radiative decay is relaxation through inter-system crossing via the 4f5d state. Pr^{3+} doped $CaZrO_3$, showed only the $^3P_0$ emission [13]. On the other hand, when doped into Ln_2O_3 (Ln = Sc, Y, Gd) and Lu_2O_3, Pr^{3+} showed only the $^1D_2$ emission [3, 14]. However, both $^3P_0$ and $^1D_2$ transitions were observed with varying branching ratios in some host matrices. When doped into $Na_5La(WO_4)_4$, $Na_5Y(WO_4)_4$ and $CaTa_2O_6$, the $^3P_0$ transition dominates the emission [3, 15]. On the other hand, the $^1D_2$ transition dominated the emission when Pr^{3+} was doped into $RE_2Ti_2O_7$ (RE = La, Gd) and Gd_2TiO_5 [3]. Depending on the ratio of the $^3P_0$ (green) and the $^1D_2$ (red) emission, Pr^{3+} doped matrices can be used in the red [16-19] component of white LED and other display applications.

La_2SiO_5 and Y_2SiO_5 belong to the family of rare earth oxyorthosilicates with monoclinic structure but different space groups. La_2SiO_5 belong to the *P21/c* space group in its low temperature phase (*X1* phase) and *12/a* space group in its high temperature phase (*X2* phase) [20, 21], while Y_2SiO_5 belong to the *C2/c* space group in its low temperature phase and *B2/b* space group in its high temperature phase [20-22]. The difference in space groups of La_2SiO_5 and Y_2SiO_5 will result in

different crystallographic planes, and hence will influence the photoluminescence properties [23], especially when doped with ions like Pr^{3+} whose luminescence properties are highly dependent on the host environment [3]. When doped into Y_2SiO_5, Pr^{3+} exhibited predominantly red emission [24-26]. Although there is no literature on La_2SiO_5:Pr^{3+}, our results show that when Pr^{3+} is doped into La_2SiO_5, the branching ratio of the green and the red emissions are comparable. In this work, we prepared eight different phosphors, namely: undoped lanthanum oxyorthosilicate (La_2SiO_5), undoped yttrium oxyorthosilicate (Y_2SiO_5), undoped lanthanum yttrium oxyorthosilicate ($LaYSiO_5$), Pr^{3+} doped lanthanum oxyorthosilicate (La_2SiO_5:Pr^{3+}), Pr^{3+} doped yttrium oxyorthosilicate (Y_2SiO_5:Pr^{3+}), and Pr^{3+} doped mixed lanthanum yttrium oxyorthosilicates ($La_{1.5}Y_{0.5}SiO_5$:Pr^{3+}, $LaYSiO_5$:Pr^{3+} and $La_{0.5}Y_{1.5}SiO_5$:Pr^{3+}). The three undoped samples are referred to as undoped La_2SiO_5, undoped Y_2SiO_5 and undoped $LaYSiO_5$ throughout this work, while the doped samples are referred to as $La_{2-x}Y_xSiO_5$:Pr^{3+} (x = 0, 0.5, 1, 1.5 and 2), were x = 0 represent La_2SiO_5:Pr^{3+}, x = 0.5 represent $La_{1.5}Y_{0.5}SiO_5$:Pr^{3+}, x = 1 represent $LaYSiO_5$:Pr^{3+}, x = 1.5 represent $La_{0.5}Y_{1.5}SiO_5$:Pr^{3+} and x = 2 represent Y_2SiO_5:Pr^{3+}.

6.2. Experimental

6.2.1. *Sample preparation*

1 mol % Pr^{3+} doped $La_{2-x}Y_xSiO_5$ phosphors were synthesized by urea-assisted solution combustion method using lanthanum nitrate hexahydrate, $La(NO_3)_3.6H_2O$, yttrium nitrate hexahydrate, $Y(NO_3)_3.6H_2O$, praseodymium nitrate hexahydrate, $Pr(NO_3)_3.6H_2O$, and silicic acid, SiO_2H_2O analytical reagents as precursors. Stoichiometric amounts of the aforementioned reagents were added into eight different glass beakers labeled undoped La_2SiO_5, undoped Y_2SiO_5, undoped $LaYSiO_5$, x = 0, x = 0.5, x = 1, x = 1.5 and x = 2. Stoichiometric amounts of the aforementioned precursors, urea, $CO(NH_4)_2$ and ammonium nitrate, NH_4NO_3 were added into different beakers, before 2.0 ml of distilled water was added. Each beaker was placed on a hot plate magnetic stirrer (one at a time) set at the temperature of 100 ^oC and stirred for about 15 min to obtain a homogeneous solution. The homogeneous solution (which looks transparent) was transferred into a clean ceramic crucible boat and instantly into a muffle furnace pre-heated to 600$\pm$10 ^oC. Oxidation took place in about 2 min after placing the solution into the furnace, leading to evaporation of gases such as CO_2, N_2, and H_2O and resulting into a crispy foam-like product. After cooling down the product to room temperature, it was ground into a fine powder using an agate

mortar and pestle and it was further annealed for 1 hr in air at 950 ^{o}C to ensure total evaporation of unwanted gases (CO_2, N_2, and H_2O). Each sample was then stored in a different sample holder for characterization.

6.2.2. *Characterization*

The structure of the powder phosphors was analyzed using a Bruker D8 advanced X-ray diffractometer (XRD) with a monochromatic CuKα radiation of wavelength (λ) = 1.54056 Å. Iontof time of flight secondary ion mass spectroscopy (ToF-SIMS) was used to analyze the atomic and molecular ionic species and dopant ions distribution in the host lattices. The ultraviolet visible (UV-vis) measurements were performed using a Lambda 950 UV-vis spectrometer. The photoluminescence (PL) spectra were measured in the steady state mode and the decay curve in phosphorescence mode using the FLS980 spectrometer - Edinburgh instruments equipped with a 450 W Xenon Lamp (Xe1) as the excitation source and the red-cooled photomultiplier tube (PMT) detector.

6.3. Results and discussion

The XRD patterns of $La_{2-x}Y_xSiO_5:Pr^{3+}$ (x = 0, 0.5, 1, 1.5, 2) and undoped La_2SiO_5 and Y_2SiO_5 powders annealed at 950 ^{o}C for one hour are shown in Fig. 6.1. In general, the powders crystallized in the *X1* phase of both La_2SiO_5 and Y_2SiO_5. The patterns show variation in the crystal planes as the ratio of La to Y was varied in the host matrix, suggesting a change in structure. The change in crystal plane is expected since La_2SiO_5 and Y_2SiO_5 belong to different space groups although they both have a monoclinic structure. La_2SiO_5 belong to the *P21/c* space group (the large ionic radii rare earth ions) while Y_2SiO_5 belong to the *C2/c* space group (the small ionic radii rare earth ions) [21, 22]. It has been shown that mixed rare earth oxyorthosilicates can crystallize in a single phase even at high ratio of the substituent ion. For instance, mixed $Gd_{1.99-x}Y_xCe_{0.01}SiO_5$ (x = 0.199) exhibited the structure of Gd_2SiO_5 (*P21/c*) [27]. In addition, $Lu_{2-x}Gd_xSiO_5$ showed the structure of Lu_2SiO_5 (*C2/c*) up to 80 at% of Gd [28]. In the pure phases of La_2SiO_5 (x = 0) and Y_2SiO_5 (x = 2), the XRD patterns matched with the monoclinic structures of La_2SiO_5 and Y_2SiO_5 referenced respectively in JCDPS file no: 40-0234 and 74-2011. Observe in Fig. 6.1 that some diffraction peaks were suppressed while others were improved upon doping with Pr^{3+}. For instance, the $(\bar{1}02)$, (321), (330) and $(\bar{5}02)$ peaks are more intense for x = 0 ($La_2SiO_5:Pr^{3+}$) but not on the undoped

La_2SiO_5. On the other hand, the (202), (102) and ($\bar{5}$12) peaks are more intense for the undoped La_2SiO_5 but are less intense for the La_2SiO_5:Pr^{3+} (x = 0). These results show that incorporation of Pr^{3+} affected crystallinity of the La_2SiO_5 host lattice. However, the Pr^{3+} incorporation did affect the structure of Y_2SiO_5 (x = 2). This could be due to similarities in the ionic radii of Pr^{3+} (0.1179 nm) and Y^{3+} (0.1075 nm). The ionic radius (0.1216 nm) of La^{3+} is larger than that of the Pr^{3+} and hence can easily accommodate Pr^{3+} on its lattice sites. However, this may lead to small shrinkage in the lattice [21, 29] as confirmed shifting of the (121) peak to higher values of 2θ[30] (Fig. 6.1). Also, observe from Fig. 6.1 is that Pr^{3+} has no effect on the peak positions of Y_2SiO_5 most probably due to similarities in their ionic radii of Pr^{3+} and Y^{3+}.

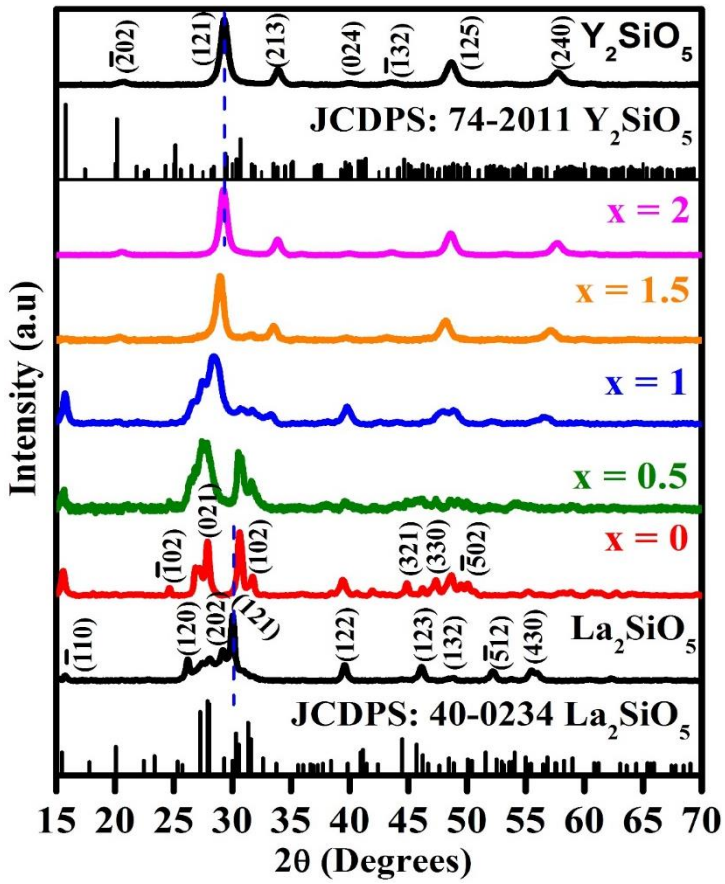

Fig. 6.1: XRD pattern of undoped La_2SiO_5, Y_2SiO_5 and Pr^{3+} doped $La_{2-x}Y_xSiO_5$ (x = 0, 0.5, 1, 1.5 and 2) phosphors compared to the standard JCDPS file.

The differences in the intensities of the diffraction peaks of the undoped and Pr^{3+} doped samples can be related to structure factors (scattering power of atomic planes) of each plane [31]. The structure factor is a function of the atomic scattering factor and since $La^{3+}$and Pr^{3+} have different

atomic scattering factors [32, 33] due to different atomic scattering factors, the intensities of the crystal planes may vary depending on the crystallographic sites occupied by the dopants.

ToF-SIMS can produce the mass spectrum of elemental and molecular species present on the surface of a sample to allow a detailed chemical analysis of the surface of the sample. The mass spectra can be performed in either positive mode (using positively charged primary ion) or negative mode (using negatively charged primary ion) to collect negative or positive secondary ion spectra respectively. The secondary ions are extracted into the analyzer by application of extraction voltage of opposite polarity to the secondary ions (negative extraction voltage for positive secondary ions and vice versa for negative secondary ions). Fig. 6.2(a-f) show the ToF-SIMS positive ion spectra of $LaYSiO_5:Pr^{3+}$. The spectra only depict some of the positive atomic and molecular ions observed in our sample, namely CH_3^+, Si^+, YO^+, LaO^+, PrO^+ and $PrOH^+$ with atomic mass units of 15.02, 27.97, 104.89, 154.89, 156.90 and 157.90 amu respectively. The other atomic species detected from the sample are shown with their corresponding atomic masses in table 6.1. The presence of CH_3^+, Na^+ and K^+ could be associated with contaminants from the sample holder and the atmosphere [20].

Table 6.1: Atomic and molecular ions and their corresponding atomic mass units obtained from positive ToF-SIMS measurement of $LaYSiO_5:Pr^{3+}$ phosphor.

Atomic/molecular ions	Mass/u	Atomic/molecular ions	Mass/u
CH_3^+	15.02	YOH^+	105.90
Na^+	22.99	La^+	138.90
Si^+	27.97	LaH^+	139.91
SiH^+	29.00	LaO^+	154.89
K^+	39.10	$LaOH^+$	155.90
SiO^+	44.05	Pr^+	140.91
$SiOH^+$	44.97	PrH^+	141.91
Y^+	88.90	PrO^+	156.90
YH^+	89.91	$PrOH^+$	157.90
YO^+	104.89		

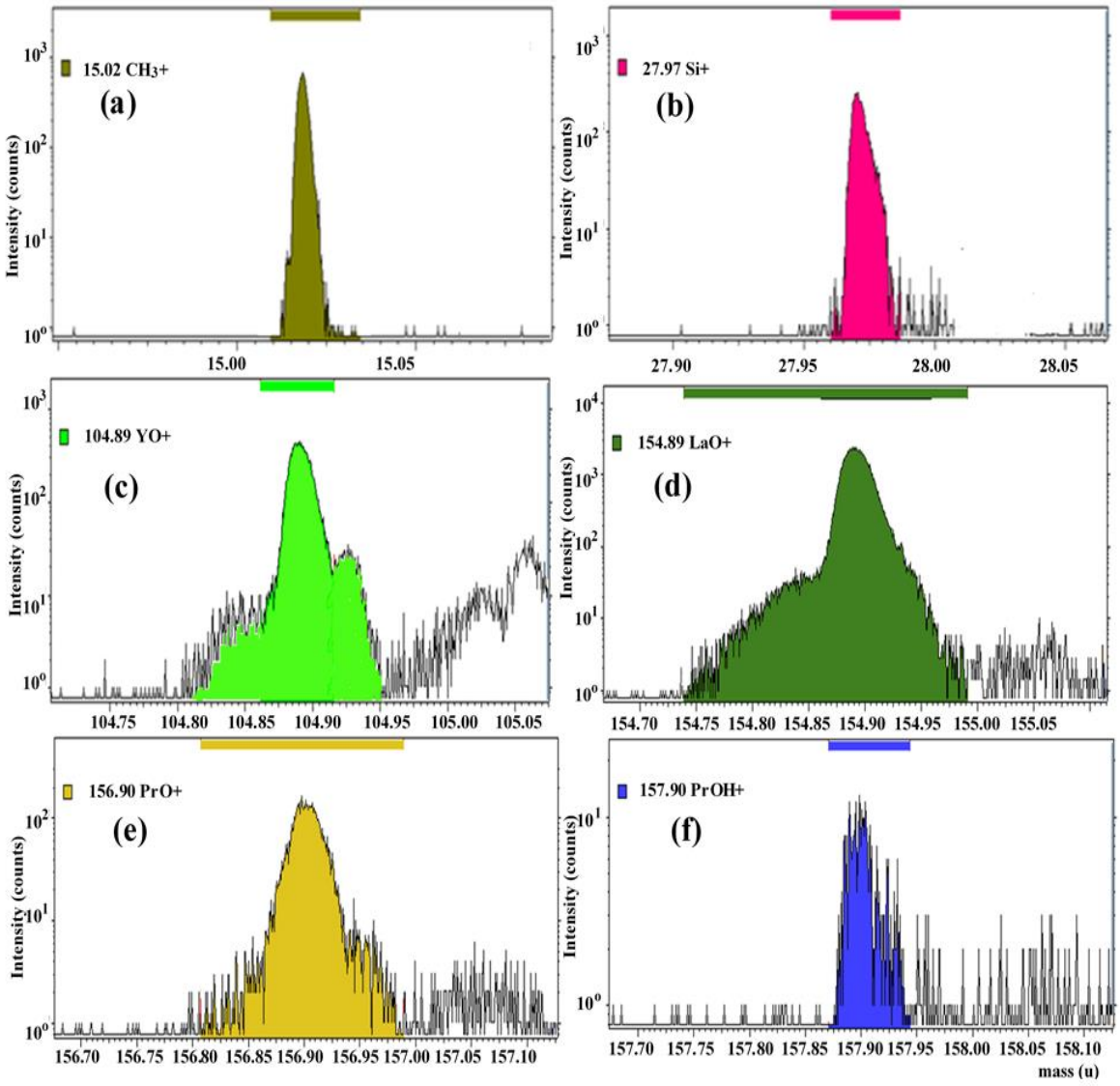

Fig. 6.2: The positive ToF-SIMS spectra showing the spectrum of (a) CH_3^+, (b) Si^+, (c) YO^+ (d) LaO^+, (e) PrO^+ and (f) $PrOH^+$ measured from $LaYSiO_5:Pr^{3+}$ phosphor.

The secondary ion images of the molecular and atomic species present in $LaYSiO_5:Pr^{3+}$ were generated by using the primary ion beam to raster across the surface of the samples. The impinging primary ion beam leads to desorption of secondary ions within the surface region of 2–3 atomic layers. The emitted secondary ions at each point within the area of 100 × 100 μm^2 in the entire cascade volume are captured by the detector. Fig. 6.3(a) depict overlaid images of LaO^+ (red), YO^+ (green) and PrO^+ (blue) labeled as a1, a2 and a3 respectively. The vertical scale bar at the right side of each image portrays the intensities of the signal coming from each ion. Regions with low colour intensity depicts low ionic concentration while region of high intensity indicates high ionic

concentration. The sharpest images were obtained by setting the banning at 4.0 pixels. Fig. 6.3(b) show the overlaid images of LaO^+ (red), YO^+ (green) and $PrOH^+$ (blue) labeled as b1, b2 and b3 respectively. It can be observed from Fig. 6.3 that all the ionic and molecular species are evenly distributed on the surface of 100 × 100 μm^2 area of the sample.

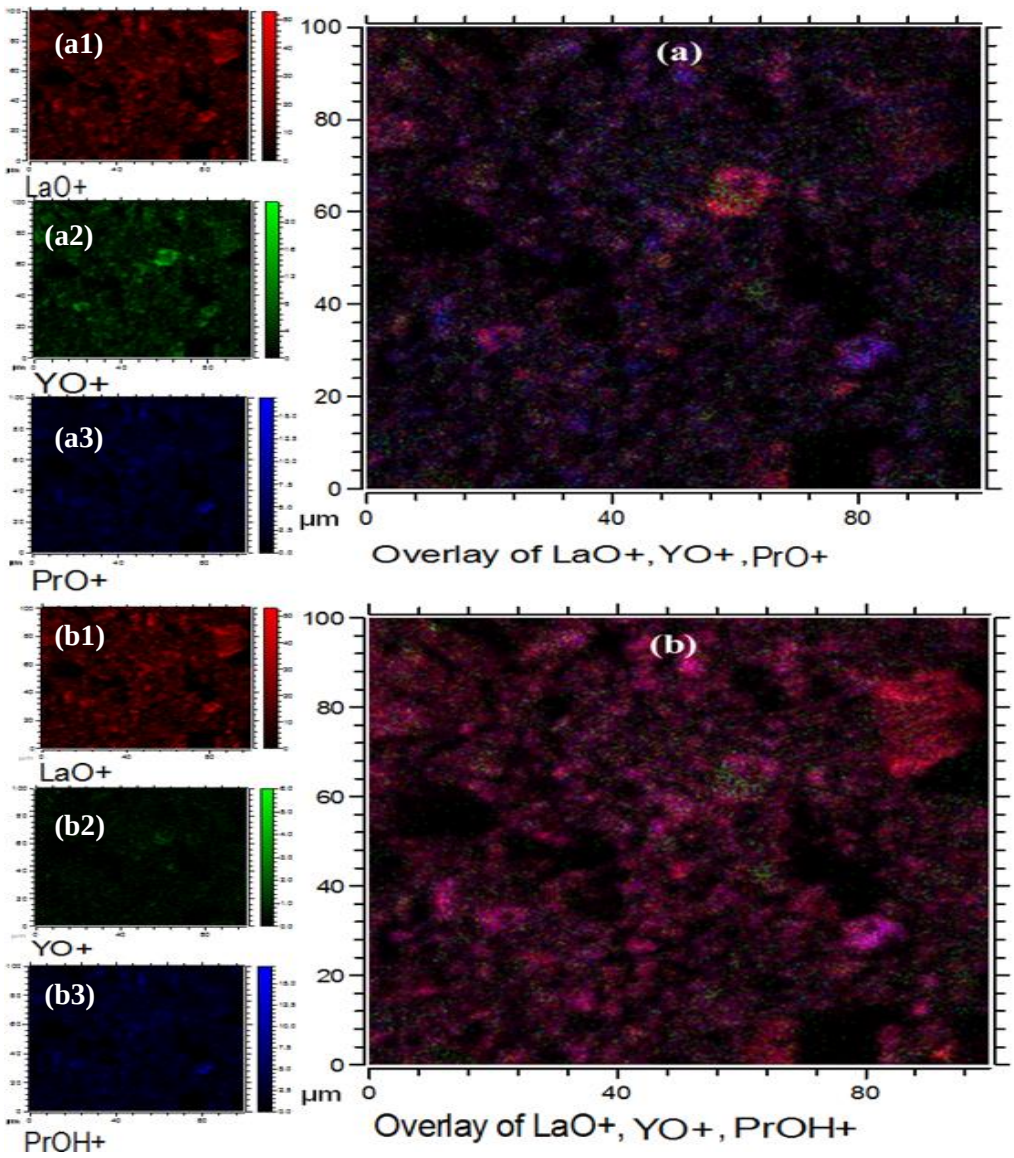

Fig. 6.3: The positive ToF-SIMS images of (a1) LaO^+, (a2) YO^+, (a3) PrO^+ and (a) overlay image of LaO^+, YO^+ and PrO^+, and the positive ToF-SIMS images of (b1) LaO^+, (b2) YO^+, (b3) $PrOH^+$ and overlay image of LaO^+, YO^+ and $PrOH^+$ taken from $LaYSiO_5:Pr^{3+}$ phosphor.

X-ray photoelectron spectroscopy (XPS) technique can be used to measure the elemental composition, chemical and electronic state of elements present in a material. The fitted high resolution O 1s and Si 2p XPS spectra of $LaYSiO_5:Pr^{3+}$ (i.e. $x = 1$) are shown in Fig. 6.4(a & b) respectively. The O 1s peak (Fig. 6.4(a)) showed five peaks assigned to $LaYO_3$ (528.8 eV), SiO_x ($x < 2$) (530 eV), $LaYSiO_5$ (530.9 eV), SiO_2 (531.8 eV), and SiO_4 (532.8 eV) [34].

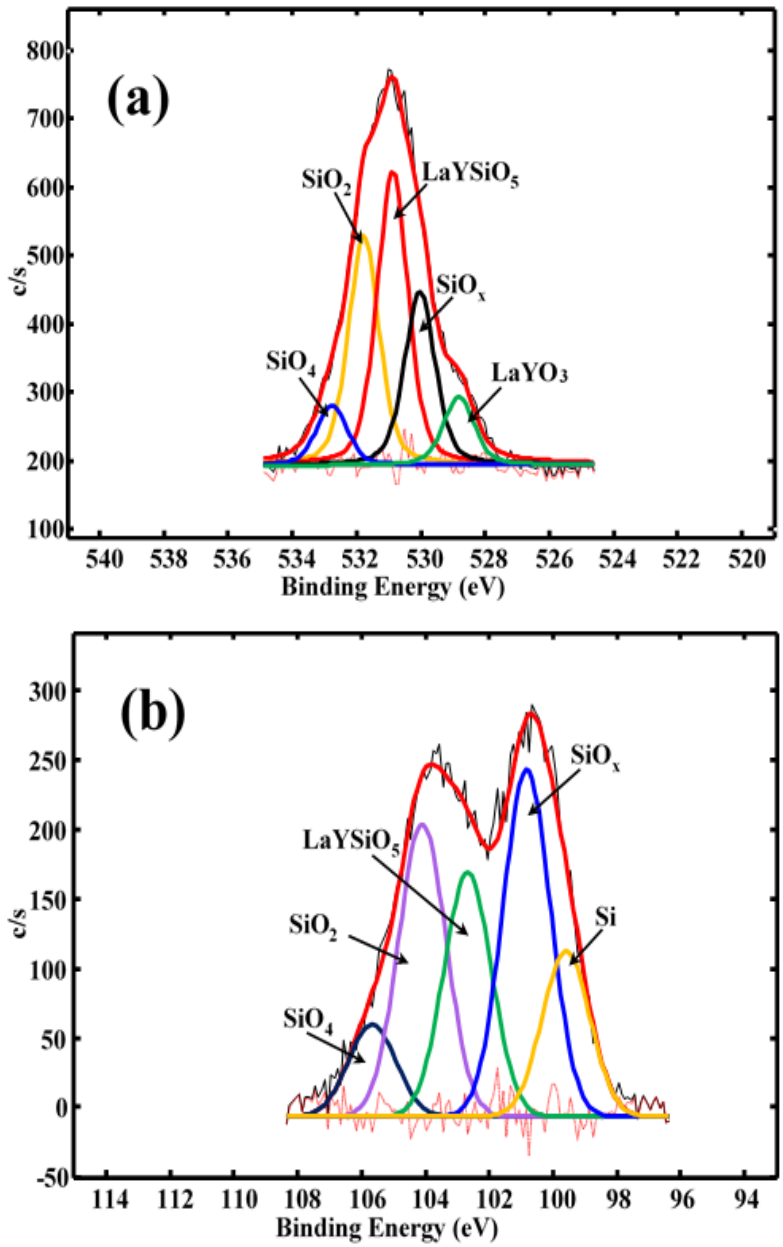

Fig. 6.4: Fitted XPS spectra for (a) O 1s and (b) Si 2p peaks for $LaYSiO_5:Pr^{3+}$.

The Si 2p XPS spectrum (Fig. 6.4(b)) showed peaks from Si, SiO_x (x < 2), $LaYSiO_5$, SiO_2 and SiO_4 at binding energies of 99.6, 100.8, 102.7, 104. 1 and 105.6 eV respectively [34]. The $LaYO_3$ peak in Fig. 6.4(a) originates from La_2O_3 and Y_2O_3, while the $LaYSiO_5$ peak in Fig. 6.4(b) originates from La_2SiO_5 and Y_2SiO_5 respectively.

The XPS 3d core-level spectra of all rare earth compounds usually splits into $3d_{5/2}$ (J = 5/2) and $3d_{3/2}$ (J = 3/2) states due to their spin-orbit splitting [35]. Fig. 6.5(a) shows the La 3d core-level XPS spectrum from $LaYSiO_5:Pr^{3+}$ (i.e. *x* = 1). The spectrum splits into the $3d_{5/2}$ and $3d_{3/2}$ states with a spin-orbit splitting of 16.8 eV. Under photoionization, each state can split into two final states I and II (these represents the two La sites in La_2SiO_5 [36]) as shown in Fig. 6.5(a). The final state I is a core hole state ($3d^14f^0$), while the final state II is a core hole state ($3d^1f^1$) with an electron transfer from the O 2p valence band to an empty 4f orbital. The final state I is ascribed to the La-O bond in La_2O_3 and is observed at 833.7 and 850.5 eV in the $3d_{5/2}$ and $3d_{3/2}$ states respectively. The final state II is ascribed to the La-OH band in $La(OH)_3$. Due to electron-hole exchange, the final state II further splits into two states, J = 1 (a strong signal) and a J ≠ 1 (a cluster of weak signals) in the $3d_{5/2}$ and $3d_{3/2}$ spin-orbital, with the J ≠ 1 terms having lower binding energy than the J = 1 term. The J = 1 term peaks are observed at 838 and 854.9 eV in the $3d_{5/2}$ and $3d_{3/2}$ states respectively, and the J ≠ 1 terms peaks are observed at 835.9 and 852.2 eV in the $3d_{5/2}$ and $3d_{3/2}$ states respectively [37-39]. The peaks observed at 846.9 and 863.5 eV are ascribed to the energy loss lines associated to the La $3d_{5/2}$ and La $3d_{3/2}$ components respectively [37, 39, 40].These peaks are usually observed in XPS due to photoelectrons that loss part of their energy as a result of interaction with other electrons. Consequently, the energy loss lines are observed at higher binding energy of the parent line [40]. Fig. 6.4(b) shows the Y 3d core-level XPS spectrum from $LaYSiO_5:Pr^{3+}$ (i.e. *x* = 1). The $3d_{5/2}$ and $3d_{3/2}$ spin-orbit splitting is 2.05 eV. Two Y_2O_3 peaks belonging to the $3d_{5/2}$ and $3d_{3/2}$ states are observed at 157.2 and 159.1 eV respectively [36]. Each doublet of the Y 3d state (Y $3d_{5/2}$ and Y $3d_{3/2}$) is compose of two Y_2SiO_5 peaks observed at 157.2 and 158 eV for Y $3d_{5/2}$ state and at 159.6 and 160.4 eV for the Y $3d_{3/2}$ state. These peaks are attributed to the two Y sites in Y_2SiO_5 [36]. The Pr 3d core-core level XPS spectrum measured from $LaYSiO_5:Pr^{3+}$ (i.e. *x* = 1) is shown in Fig. 6.5(c). The energy separation between the Pr $3d_{5/2}$ and Pr $3d_{3/2}$ doublets is 20.4 eV. Each doublet contain two pairs of peaks assigned to Pr^{4+} species (e.g. PrO_2 and Pr_6O_{11}) and Pr^{3+} species (e.g. Pr_2O_3 and $Pr(OH)_3$) [41]. In the Pr $3d_{5/2}$ state, the pair of peaks around 928.1 and 932.7 eV are ascribed to Pr^{3+}. The other pair of peaks observed around

930.2 and 934.5 eV are assigned to Pr^{4+} [41]. In the Pr $3d_{3/2}$ state, the Pr^{3+} peaks are observed at 948.7 and 954.1 eV, while the Pr^{4+} peaks are observed at 951.7 and 957.2 eV [42]. The presence of Pr^{4+} peaks is an indication of the oxidation of Pr^{3+} to Pr^{4+} ions in the samples. The energy loss lines are observed around 943.1 and 959.1 eV [40].

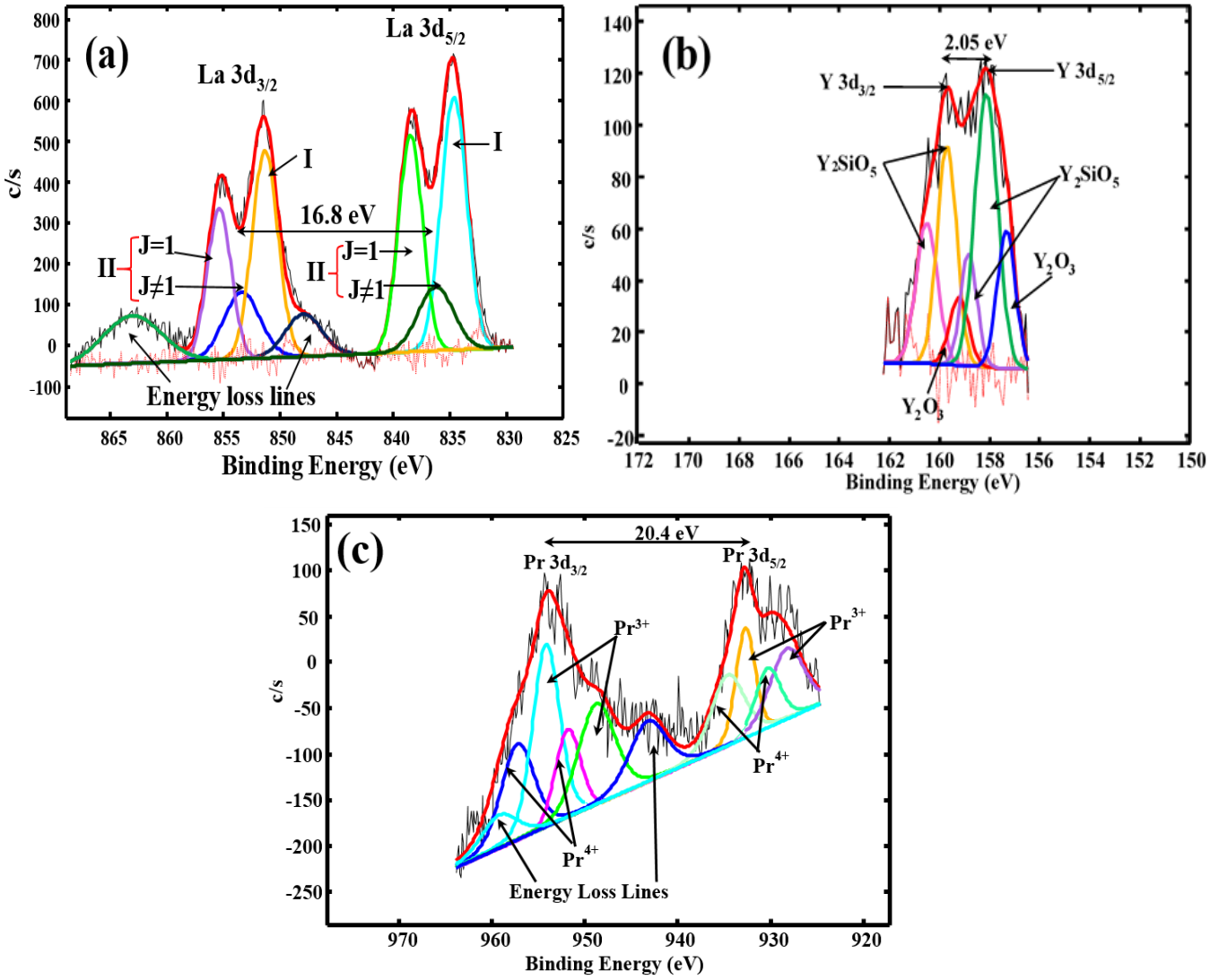

Fig. 6.5: Fitted XPS spectra of (a) La 3d peak, (b) Y 3d peak, and (c) Pr 3d peak from $LaYSiO_5:Pr^{3+}$.

The diffused reflectance spectra of $La_{2-x}Y_xSiO_5:Pr^{3+}$ (x = 0, 0.5, 1, 1.5 and 2) (Fig. 6.6(a)) shows strong UV absorption peaks which varies with the ratio of La to Y in the matrix. The absorption

edges were observed around 207 nm for x = 0 and at 211 nm for x = 0.5, 1, 1.5 and 2. The strong band-edge absorptions may be due to band to band transitions. The strong broad absorption from around 620 nm with maxima at 376 nm is due to $O^{2-} \rightarrow Pr^{4+}$ charge transfer band (CTB). These bands are not accompanied by luminescence and also suppresses the absorption of Pr^{3+} [43, 44]. It has been reported that highly-charge cations such as U^{6+}, Nd^{5+} and W^{6+} can display luminescence [45-47], which can be ascribed to the transitions between metal ion orbitals and ligand molecular orbitals. However, tetravalent rare-earth (RE^{4+}) cannot display luminescence [43, 44] and hence the $O^{2-} \rightarrow Pr^{4+}$ charge transfer band (CTB) is not observed in the excitation spectra (Fig. 6.3). The inability of RE^{4+} to luminesce may be due to radiationless process as a result of interaction between the RE^{4+} and the holes in the ligand molecular orbital [43]. In the tetravalent oxidation state RE^{4+}, rare-earth compounds are normally considered to lose one 4f electron with reference to the trivalent ion RE^{3+}. Pr oxides have been considered as mixed valence compound [48, 49]. In the trivalent state, Pr^{3+} have $4f^2$ configuration, while in the tetravalent state, Pr^{4+} have $4f^1$ configuration [50]. The ground state of Pr ion is made up of the $4f^2$ configuration, which corresponds to the trivalent Pr_2O_3 phase. The covalence hybridization between O 2p−Pr 4f states leads to a minor Pr 4f state which contributes to the upper part of the valence band, mostly dominated by O 2p state. On the other hand, the conduction band minimum is made up of the Pr 4f states with little contribution from antibonding O 2p states [51-53]. In the mixed valence picture, the tetravalent Pr^{4+} ($4f^1$ configuration) and the trivalent Pr^{3+} ($4f^2$ configuration) exist simultaneously in the cation ground state [48]. It has been shown that the $4f^1$ and $4f^2$ configurations are separated by 0.5 eV in the cation ground state of Pr [54]. It can be concluded that Pr_2O_3 are trivalent (Pr^{3+}), while PrO_2 are tetravalent (Pr^{4+}) and that the oxidation process from Pr_2O_3 to PrO_2 harmonize with delocalization of an extra *f* electron [51]. Karnatak et al. proposed the coexistence of localized and delocalized f electrons [52], thus the $4f^1$ ground-state configuration of Pr has can interpreted as being localized [55]. Fig. 6.4(b) shows the plot of $h\nu$ versus $[h\nu F(R_{100})]^{1/2}$ constructed from the diffused reflectance data with the aid of Kubelka-Munk function [56, 57] given by Eq. (6.1).

$$F(R_\infty) = \left(\frac{(1 - R_\infty)^2}{2R_\infty} \right) \tag{6.1}$$

where R_∞ is the reflectance of a semi-infinite medium. $F(R_\infty)$ is directly proportional to the absorption coefficient (α) [57] for a material given by Eq. (6.2).

$$(\alpha h\nu)^{1/n} = A(h\nu - E_g) \tag{6.2}$$

where (E_g) is the band gap of the material, *h* is Planck's constant, *v* is the frequency of vibration, *n* can be 1/2, 3/2, 2 or 3 depending on the nature of the transition and *A* is proportionality constant which is independent of the material chemical composition. For a finite medium with 100 % reflectance, $R_\infty = R_{100}$. Since $F(R_\infty)$ is proportional to α, comparing Eq. (6.1 and (6.2) gives,

$$(F(R_{100})h\nu)^{1/n} = A(h\nu - E_g) \tag{6.3}$$

The band gaps of the annealed $La_{2-x}Y_xSiO_5:Pr^{3+}$ phosphors were determined by extrapolating the point of intersection of a tangent line and the inflection point of the curve to the *hv* axis as shown in Fig. 6.6(b). The estimated band gaps are 5.00, 480, 316, 4.75 and 5.00 eV for *x* = 0, 0.5, 1, 1.5 and 2 respectively. Observe the decrease in the band gaps of the mixed host samples (*x* = 0.5, 1 and 1.5). The variation in the band gap values could be due to lattice mismatch as a result of difference in the lattice parameters of La_2SiO_5 and Y_2SiO_5 [58]. Table 6.2 compare the estimated band gaps with the band gaps of undoped La_2SiO_5, Y_2SiO_5, $LaYSiO_5$ (the spectra are not shown). It can be observed from table 6.2 that the band gaps increased after doping with Pr^{3+}. The widening of the band gaps observed in the samples can be explained by Burstein–Moss (BM) shift (Fig. 6.7) [59]. When Pr^{3+} ions substitute La^{3+} or Y^{3+} lattice sites, it is expected to give n-type doping effect. In n-type materials, the Fermi energy level lies close to the conduction band. When the dopant concentration increases, the position of the Fermi-level is perturbed and it is shifted into the conduction band causing the band gap to widen. Fig. 6.7(a) shows the band structure of an undoped material with the unperturbed valence and conduction bands given respectively by

$$E_V^0(k) = -\hbar^2 k^2 / 2m_V^* \tag{6.4}$$

and

$$E_C^0(k) = E_{g0} + \hbar^2 k^2 / 2m_C^* \tag{6.5}$$

where E_{g0} is the band gap of the undoped material, *k* is the wave number, $\hbar\omega$ is the photon energy, m_C^* and m_V^* are the effective masses at the conduction and valence band respectively. Above the Mott critical density [60] in doped materials, the lowest state of the conduction band is blocked due to partial filling of this state, and hence resulting in the widening of the band gap (Fig. 6.7(b)).

This phenomenon is known as BM shift [59]. Furthermore, above the Mott critical density in the doped materials, the energy shift is observed in the valence and conduction bands due to electron-electron and electron-impurity scattering. The conduction band of the doped material will experience downward shift due to the mutual exchange and Coulomb interaction of the free excited electrons and the electron-impurity scattering.

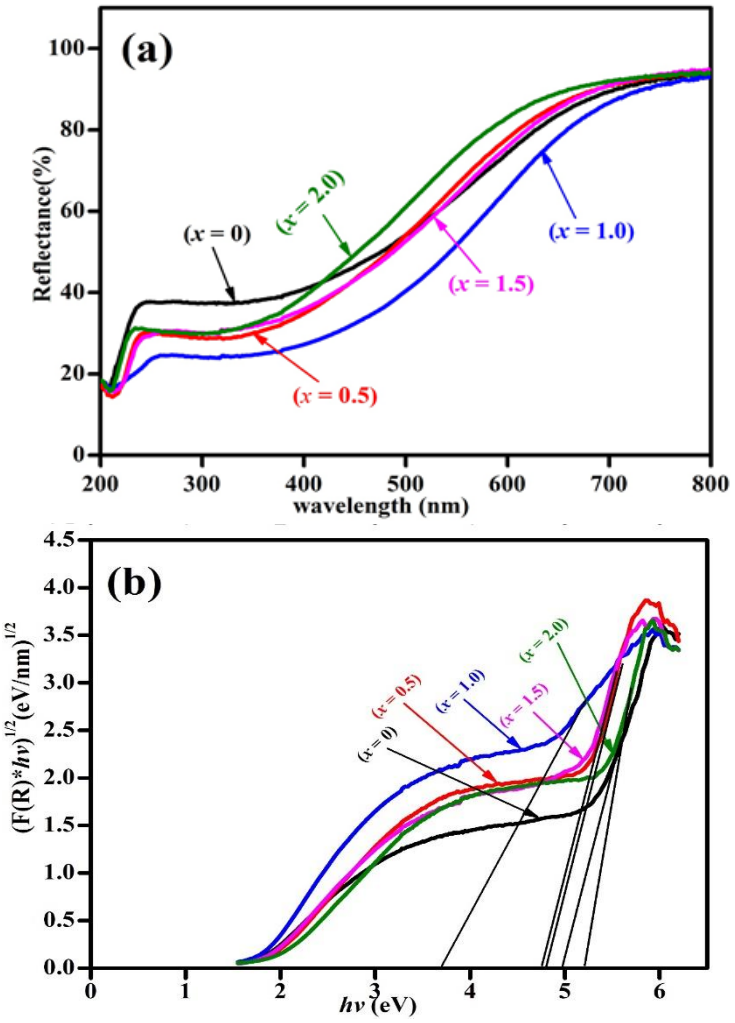

Fig. 6.6: (a) Diffuse reflectance spectra, and (b) $(F(R)*h\nu)^{1/2}$ versus $h\nu$ curve of $La_{2-x}Y_xSiO_5:Pr^{3+}$.

Table 6.2: Band gaps of Pr^{3+} doped and undoped $La_{2-x}Y_xSiO_5$ (x = 0, 0.5, 1, 1.5 and 2).

$La_{2-x}Y_xSiO_5$	$La_{2-x}Y_xSiO_5:Pr^{3+}$ (eV)	Undoped $La_{2-x}Y_xSiO_5$ (eV)
x = 0	5.00	4.65
x = 0.5	4.80	-
x = 1	3.71	3.68
x = 1.5	4.75	-
x = 2	5.20	5.15

Opposite influence is also observed in the valence band. Due to these effects, Eq. (6.4) and (6.5) can be rewritten as follows by replacing the band dispersions by quasiparticle dispersions:

$$E_V(k,\omega) = E_V^0(k) + \hbar\Sigma_V(k,\omega) \tag{6.6}$$

and

$$E_C(k,\omega) = E_C^0(k) + \hbar\Sigma_C(k,\omega) \tag{6.7}$$

where $\hbar\sum_V$ and $\hbar\sum_C$ are self-energies due to electron-electron and electron-impurity scattering. Hence, the band gap of the direct transitions can be expressed as:

$$E_g = E_C(k_F,\omega) - E_V(k_F,\omega) \tag{6.8}$$

where k_F is the Fermi wave number which can be defined as $k_f = (3\pi^2 n_e)^{1/3}$ and n_e is the electron density. Eq. (6.8) can be rewritten as:

$$E_g = E_{g0} + \Delta E_g \tag{6.9}$$

where

$$\Delta E_g = \Delta E_g^{BM} + \hbar\Sigma_C(k_F,\omega) - \hbar\Sigma_V(k_F,\omega) \tag{6.10}$$

and

$$\Delta E_g^{MB} = \frac{\hbar^2}{2m_{VC}^*}k_F^2 = \frac{\hbar^2}{2m_{VC}^*}\left(3\pi^2 n_e\right)^{2/3} \tag{6.11}$$

m_{VC}^{*} is the reduced effective mass and ΔE_g^{MB} is the MB shift. Eq. (6.11) reveals that the energy shift is proportional to $n_e^{2/3}$. The minimum energy separation between the valence and the conduction band in the doped material E_m is defined by [61].

$$E_m \approx E_{g0} + \hbar\Sigma_C(k_F) - \hbar\Sigma_V(k_F) \tag{6.12}$$

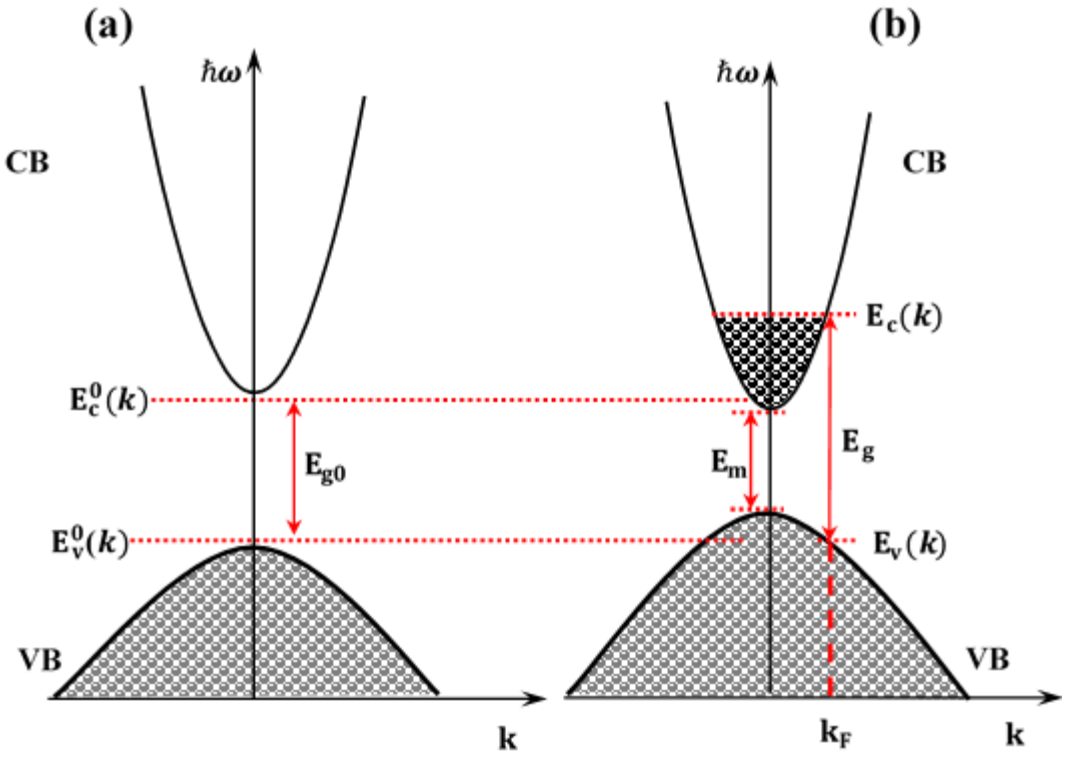

Fig. 6.7: Schematic illustration of the Burstein–Moss shift in Pr^{3+} doped $La_{2-x}Y_xSiO_5$.

To study the effects of crystal field on Pr^{3+} luminescence in $La_{2-x}Y_xSiO_5$ (x = 0, 0.5, 1, 1.5 and 2), we evaluated the photoluminescence (PL) properties of these materials. The PL excitation spectra (Fig. 6.8) exhibited four excitation peaks, one broad band in the UV region and three peaks in the visible region. The broad bands observed in the UV region (235, 237, 237, 237 and 238 nm for x = 0, 0.5, 1, 1.5 and 2 respectively) are assigned to electronic transition from the O2p valence band to La(5d6s) and Y(4d5s) conduction band [20]. The encircled area in Fig. 6.8 (245-290 nm) is ascribed to the 4f-5d transition of Pr^{3+} [62, 63]. The excitation peaks observed in the visible region at 447, 472 and 486 nm (shown in the inset of Fig. 6.8) are assigned to $^3H_4 \rightarrow {}^3P_2$, $^3H_4 \rightarrow {}^3P_1$, $^1I_6$, and $^3H_4 \rightarrow {}^3P_0$ 4f→4f transitions of Pr^{3+} respectively [64]. The PL emission (Fig. 6.9(a-e)) show

three major emission lines at 490 nm (with a shoulder at 500 nm), 611 nm (with a shoulder at 630 nm) and 650 nm. The peaks at 490 and 500 nm are assigned to double manifold of $^3P_0 \rightarrow {}^3H_5$, while those at 611 and 630 nm are double manifold of $^1D_2 \rightarrow {}^3H_4$ 4f→4f transitions of Pr^{3+} [4, 14, 65], whereas, the peak at 650 nm is ascribed to $^3P_0 \rightarrow {}^3F_2$ transition of Pr^{3+} [66]. The three peaks at 528, 540 and 555 nm are assigned to three manifold of $^3P_0 \rightarrow {}^3H_5$ transitions of Pr^{3+} [66], while the peak at 730 nm is assigned to $^3P_0 \rightarrow {}^3F_4$ transition of Pr^{3+} [67]. The broad band observed in the wavelength range of 400-460 nm is assigned to self-trapped excitons (STE) in SiO_2 [20, 68]. Fig. 6.9(f) shows how the intensities of the 490 nm ($^3P_0$) and the 650 nm ($^3P_0$) and 611 nm ($^1D_2$) emission lines varies with *x*. It is obvious that the intensities of both the $^3P_0$ and $^1D_2$ transitions decreased as *x* increased, except for *x* = 1. However, it is apparent that the branching ratio of the $^1D_2$ emission dominates the spectra as the value of *x* increases.

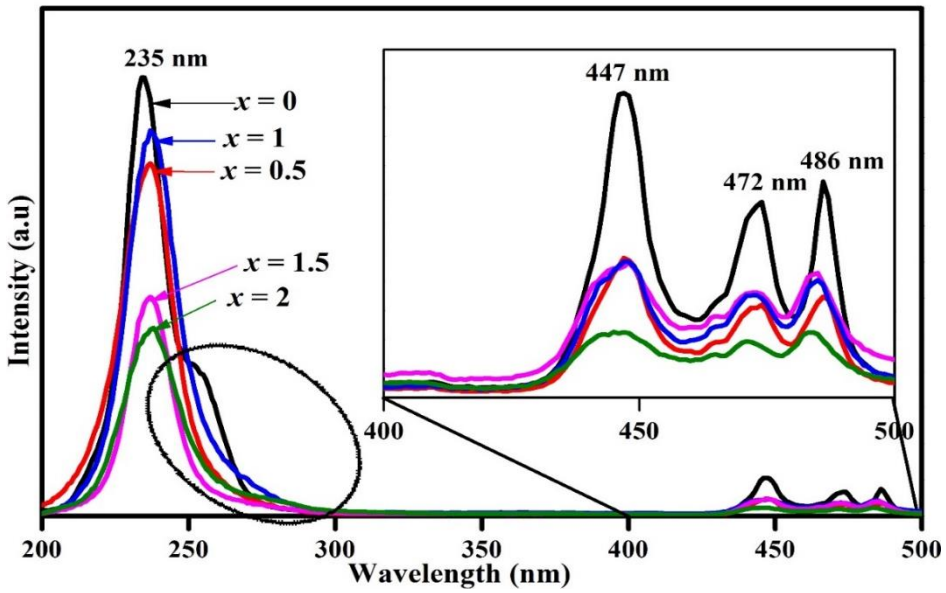

Fig. 6.8: Photoluminescence excitation spectra of $La_{2-x}Y_xSiO_5:Pr^{3+}$ (*x* = 0, 0.5, 1, 1.5 and 2) phosphors recorded under 611 nm emission. The inset and encircled area are the enlarged excitation spectra in the wavelength range of 400-500 nm and the wavelength range of 245-290 nm respectively.

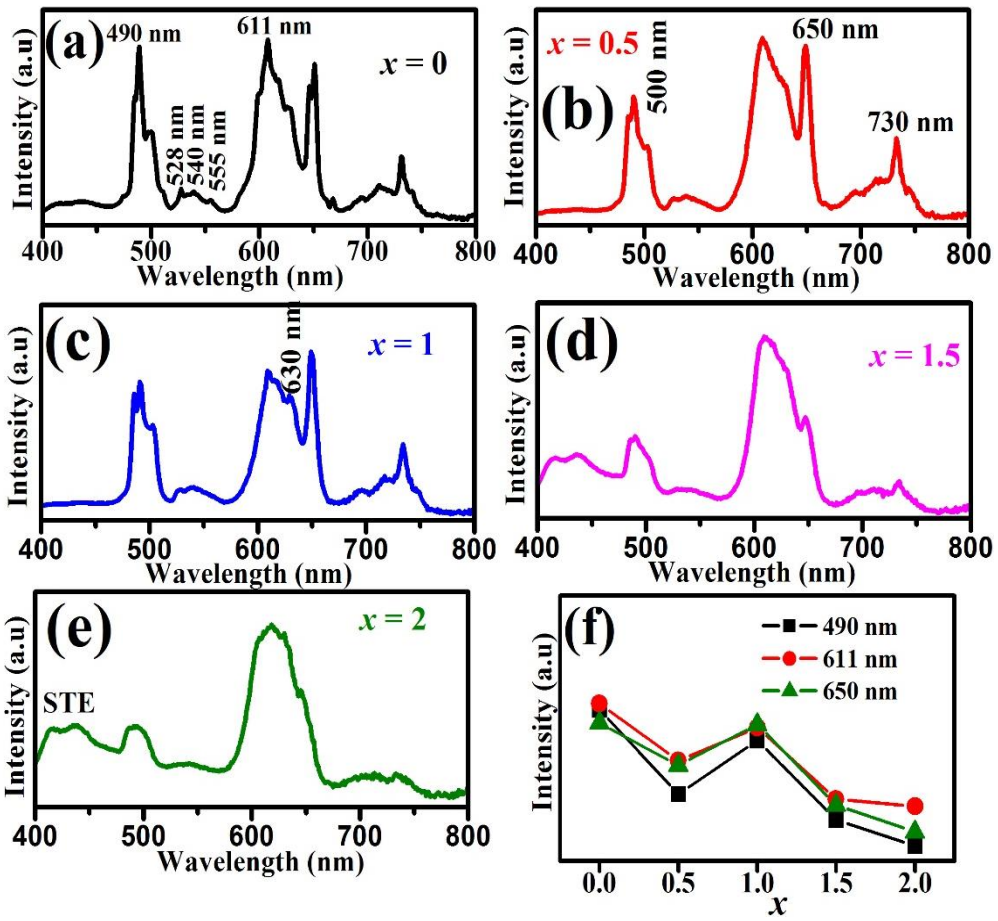

Fig. 6.9: (a-e) Photoluminescence emission spectra of $La_{2-x}Y_xSiO_5:Pr^{3+}$ (x = 0, 0.5, 1, 1.5 and 2) phosphors recorded under 235 nm excitation, (f) the plot of emission intensity versus x for 490, 611 and 650 nm emission lines.

A similar PL emission observed when x = 0 (Fig. 6.9(a)) has been reported by Arai et al [4] in Pr^{3+} doped monoclinic gadolinium sesquioxide (Gd_2O_3). The $^3P_0$ and $^1D_2$ emission lines were attributed to two different sites occupied by Pr^{3+} ions in the host matrix. R_2SiO_5 (R = La, Y) has monoclinic structure with two non-equivalent R crystallographic sites, R1 and R2, which are coordinated by nine and seven oxygen atoms respectively [69]. Hence, Pr^{3+} ions can occupy both R1 and R2 sites in the host matrix and the $^3P_0$ and $^1D_2$ emission of Pr^{3+} can emanate from Pr^{3+} ions occupying any of these sites. Observed from Fig. 6.9(a) that the $^3P_0$ have more or less the same emission intensity height as the $^1D_2$ transition when x = 0 ($La_2SiO_5:Pr^{3+}$), but decreases as x increases (i.e. as Y content increases in the host) (Fig. 6.9(b-e)). Furthermore, when x = 2 ($Y_2SiO_5:Pr^{3+}$) (Fig. 6.9(e)), the $^1D_2$ emission dominates the spectrum. These results suggests two possible cases:

Case I: When $x = 0$, Pr^{3+} occupies the R site which favours $^3P_0$ emission. The behavior of Pr^{3+} ions in such a site is shown schematically in the energy configuration coordinate diagram in Fig. 6.10(a). In this model, the effect of the ligands on the 4f5d level energy is small; hence, the bottom of the 4f5d energy level curve lies slightly above the $^3P_0$ energy level but further away from the $^1D_2$ energy level. These leads to smaller difference in energy between the bottom of the 4f5d curve and the crossing point to the $^3P_0$ curve compared to the bottom of the 4f5d level and the crossing point to the $^1D_2$ curve. Therefore, under UV-excitation, the excited 4f5d state relaxes to the $^3P_0$ level through the bottom of the 4f5d curve and not to the $^1D_2$ level and hence the $^3P_0$ emission intensity is high in the spectrum. In this case, the non-radiative $^3P_0 \rightarrow {}^1D_2$ transition rate is relatively slow.

Case II: When $x = 2$, Pr^{3+} occupies the R site which favours $^1D_2$ emission. In this case, the 4f5d level is highly influenced by the ligands, hence the bottom of the 4f5d energy curve lies between those of the $^3P_0$ and $^1D_2$ curves (Fig. 6.10(b)). Therefore, under UV-excitation, both the $^3P_0$ and the 4f5d state relaxes to the $^1D_2$ level through the bottom of the 4f5d curve. This is due to the bottom of the $^3P_0$ level been close to the crossing point between the $^3P_0$ level and the 4f5d level, hence the $^3P_0$ level empties most of its electrons to the $^1D_2$ state via the 4f5d level, and hence the $^1D_2$ emission intensity dominates the spectrum [4]. In this case, the non-radiative $^3P_0 \rightarrow {}^1D_2$ transition rate is relatively high. The energy gap between the $^3P_0$ and lowest level of $^1D_2$ level has been reported to be about 4000 cm^{-1} [70], and the phonon cut-off energy of Y_2SiO_5 is about 960 cm^{-1} [71, 72] (there is no report on La_2SiO_5 at the moment). So about four phonons are required to bridge the energy gap. Therefore, multiphonon relaxation process for the $^3P_0 \rightarrow {}^1D_2$ energy transfer is negligible. Hence, the $^3P_0$ state can relax non-radiatively to the $^1D_2$ state through the deep lying 4f5d level [14].

By and large, the irregularities in the branching ratios of the emission intensities of energy level transitions in Pr^{3+} doped matrices is as a result of the magnitude of the interaction between these levels and the excited configurations, which is a function of how strong the ligands interact (crystal field strength of the host) with the excited configuration. This anomaly in the interaction between the excited configuration and the multiplets leads to a conditional (with regard to the crystal field strength of the host lattice) non-radiative charge transfer between the excited states and the

multiplets, and between the multiplets [73], with higher rate of non-radiative $^3P_0 \rightarrow {}^1D_2$ transitions observed in host lattices with high crystal field strength [74].

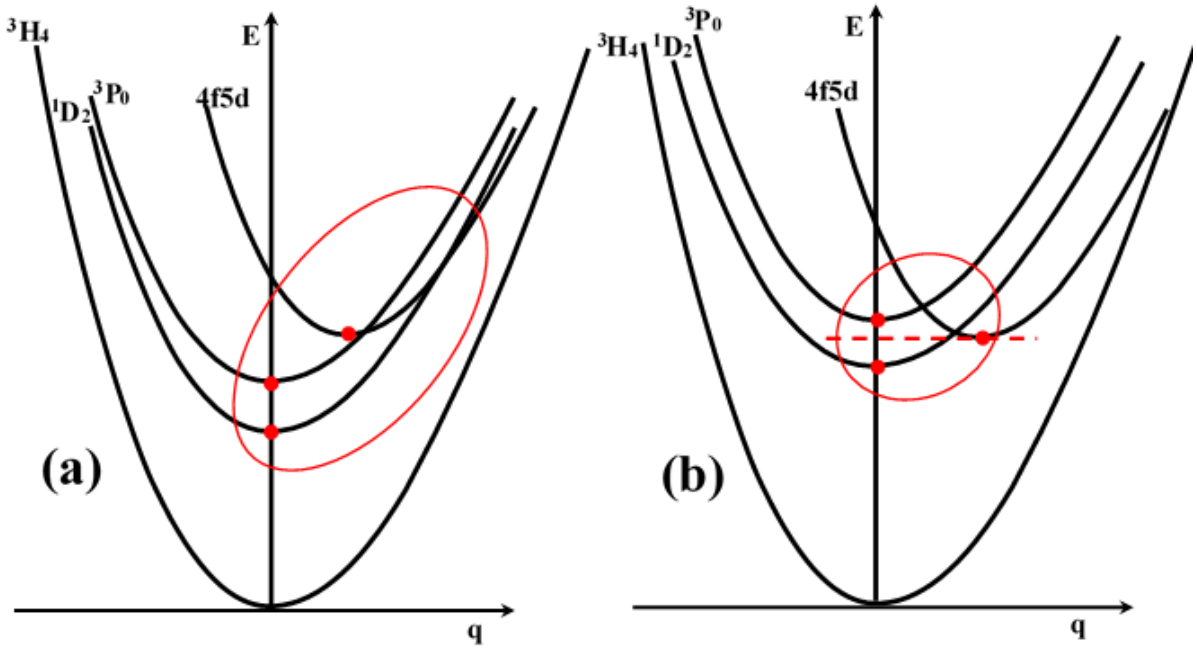

Fig. 6.10: Schematic configuration coordinate diagrams with energy E and configuration coordinate q for Pr^{3+} in $La_{2-x}Y_xSiO_5:Pr^{3+}$ (x = 0, 0.5, 1, 1.5 and 2), (a) the ligands crystal field have small effect on 4f5d level (b) ligands crystal field have high effect on the 4f5d level.

From the two cases reported above, the preferred R sites for Pr^{3+} in La_2SiO_5 and Y_2SiO_5 can be deduced. As mentioned previously, R_2SiO_5 (R = La, Y) have two non-equivalent R crystallographic sites, R1 and R2 (R1 = La1, Y1 and R2 = La2, Y2) coordinated by nine and seven oxygen atoms respectively [75, 76]. The La–O and Y–O distances for the two R sites in La_2SiO_5 and Y_2SiO_5 are listed in table 6.3. The average distance for La1–O and L2–O are 0.2628 and 0.2512 nm, with the maximum distances of 0.3055 and 0.2676 nm respectively. Likewise, the average distances of Y1–O and Y2–O are 0.2456 and 0.2390 nm, with the maximum distances of 0.2951 and 0.2562 nm respectively. It is a well-known phenomenon that for divalent and trivalent rare earth ions, the energy levels difference between the 4f5d and 4f states decreases with an increase in the crystal field strength of the host matrix, which increases with the decrease in the distance between the rare earth ion and the ligands [77, 78]. This implies that there is likely to be less interaction between the ligands and the rare earth ions (Pr^{3+}) occupying the La1 sites compare

to the La2 sites, since La1 site has the higher average rare earth-oxygen distance (0.2628 nm). Also, the La1–O4^{d} (0.3055 nm) distance is very long and hence its effect on the central rare earth ion is negligible. Therefore, in case I, $^{3}P_{0}$ emission emanates from Pr^{3+} occupying La1 sites and $^{1}D_{2}$ emission emanates from Pr^{3+} occupying the La2 sites (Fig. 6.11). Similarly, in case II, the $^{3}P_{0}$ emission emanates from Pr^{3+} occupying the Y1 sites, while the $^{1}D_{2}$ emission emanates from Pr^{3+} ions occupying the Y2 sites (Fig. 6.11). Furthermore, in La_2SiO_5 and Y_2SiO_5, all the oxygen atoms are bonded to silicon except the O5 atoms which form bonds only with R atoms. There are three non-silicon-bonded O5 atoms around R2 sites and only one O5 atom around R1 sites. Consequently, Pr^{3+} in the R2 sites are more covalently bonded than Pr^{3+} in the R1 sites. The covalency of La1 and La2 has been reported to be 2.86 and 3.00 respectively [75]. Therefore, it is fair to conclude that the transition at the higher energy ($^{3}P_{0}$) emanates from Pr^{3+} occupying the La1 and Y1 sites, while the transitions at the lower energy ($^{1}D_{2}$) emanates from Pr^{3+} occupying the La2 and Y2 sites, since crystal field strength increases with covalency [14, 79]. As mentioned earlier, the branching ratio of $^{3}P_{0}$ and $^{1}D_{2}$ transition changes with *x*, with $^{3}P_{0}$ transition dominating when $x = 0$ and $^{1}D_{2}$ transition dominating when $x = 2$ (Fig. 6.9). So it can be deduced that the highest rate of $^{3}P_{0} \rightarrow {}^{1}D_{2}$ non-radiative transition was observed when $x = 2$.

Table 6.3: The La–O and Y–O distances for La1 and La2 sites in La_2SiO_5 and Y1 and Y2 sites in Y_2SiO_5.

Nuclear	d (nm)	Nuclear	d (nm)	Nuclear	d (nm)	Nuclear	d (nm)
La1–O1	0.2654	La2–O1^{f}	0.2676	Y1–O1	0.2391	Y2–O1^{f}	0.2421
La1–O1^{a}	0.2370	La2–O3	0.2575	Y1–O1^{a}	0.2201	Y2–O3	0.2541
La1–O2	0.2666	La2–O3^{f}	0.2656	Y1–O2	0.2611	Y2–O3^{f}	0.2562
La1–O2^{b}	0.2618	La2–O3^{g}	0.2489	Y1–O2^{b}	0.2451	Y2–O3^{g}	0.2342
La1–O2^{c}	0.2516	La2–O5	0.2324	Y1–O2^{c}	0.2461	Y2–O5	0.2342
La1–O4^{d}	0.3055	La2–O5^{h}	0.2506	Y1–O4^{d}	0.2561	Y2–O5^{h}	0.2302
La1–O4^{e}	0.2570	La2–O5^{i}	0.2358	Y1–O4^{e}	0.2951	Y2–O5^{i}	0.2231
La1–O4^{b}	0.2695			Y1–O4^{b}	0.2251		
La1–O5^{c}	0.2509			Y1–O5^{c}	0.2231		
Ave.	0.2628	Ave.	0.2512	Ave.	0.2456	Ave.	0.2390

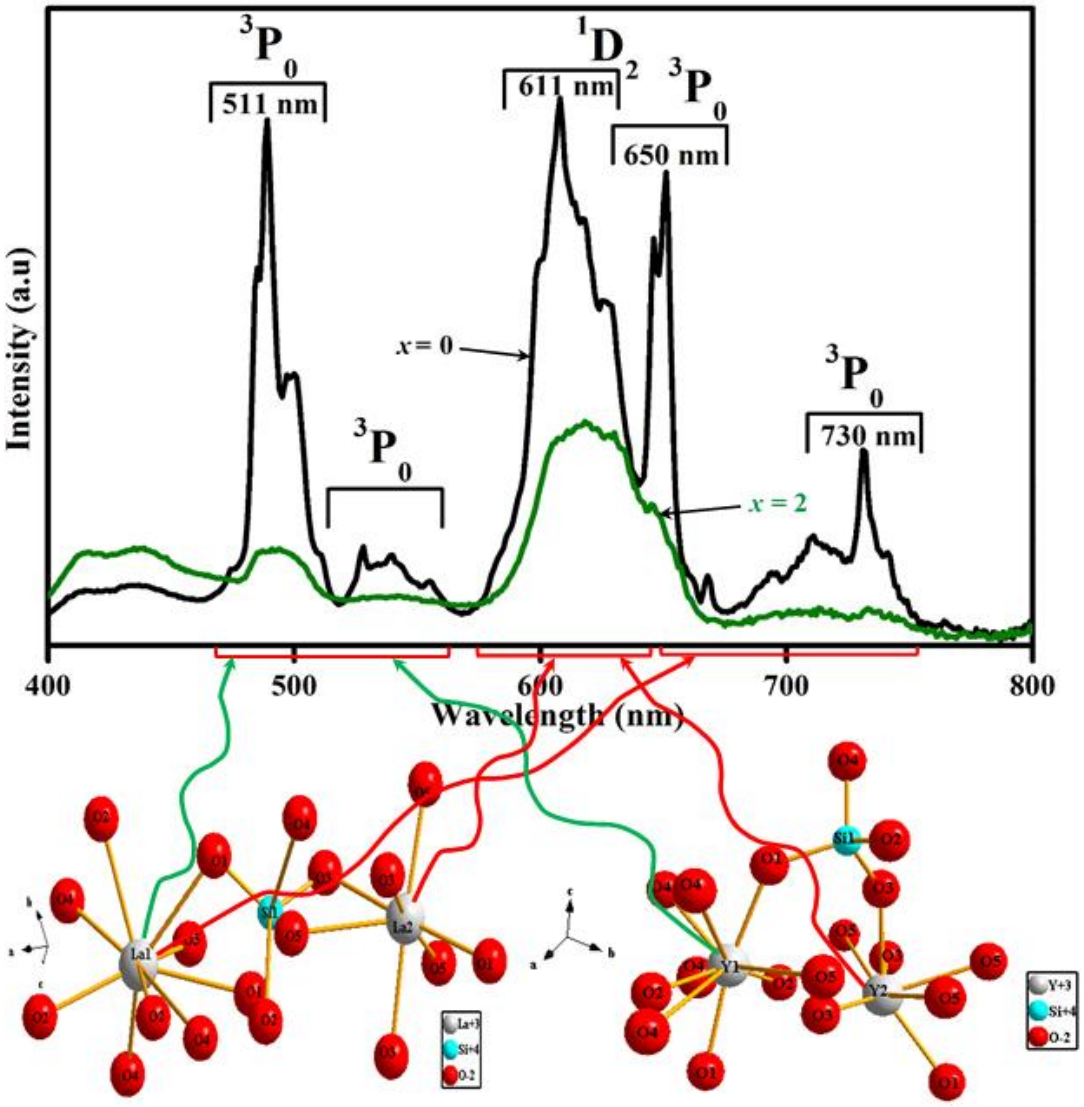

Fig. 6.11: Schematic illustration of crystal sites of La_2SiO_5 (La1 and L2) and Y_2SiO_5 (Y1 and Y2) from which the $^3P_0$ and $^1D_2$ transitions of Pr^{3+} emanates.

Fig. 6.12 shows a schematic energy diagram illustrating the photoluminescence mechanism of Pr3+ in the $La_{2-x}Y_xSiO_5$ hosts. When the samples are excited with 235 nm UV-light, electrons are promoted to from the valence band (VB) of the host (O 2p level) to its conduction band (La(5d62)/Y(4d5s) level) and holes are generated in the VB. The excited electrons can be transferred non-radiatively to the 4f5d energy level of Pr^{3+}, and then to the ^3P_J (J = 0, 1, 2) level and $^1D_2$ level and emissions are observed. As shown in shown in Fig. 6.10, depending on the

position of the 4f5d level of Pr^{3+} relative to the $^3P_0$ and the 1D2 level, either the $^3P_0$ or the $^1D_2$ or both emissions can be observed.

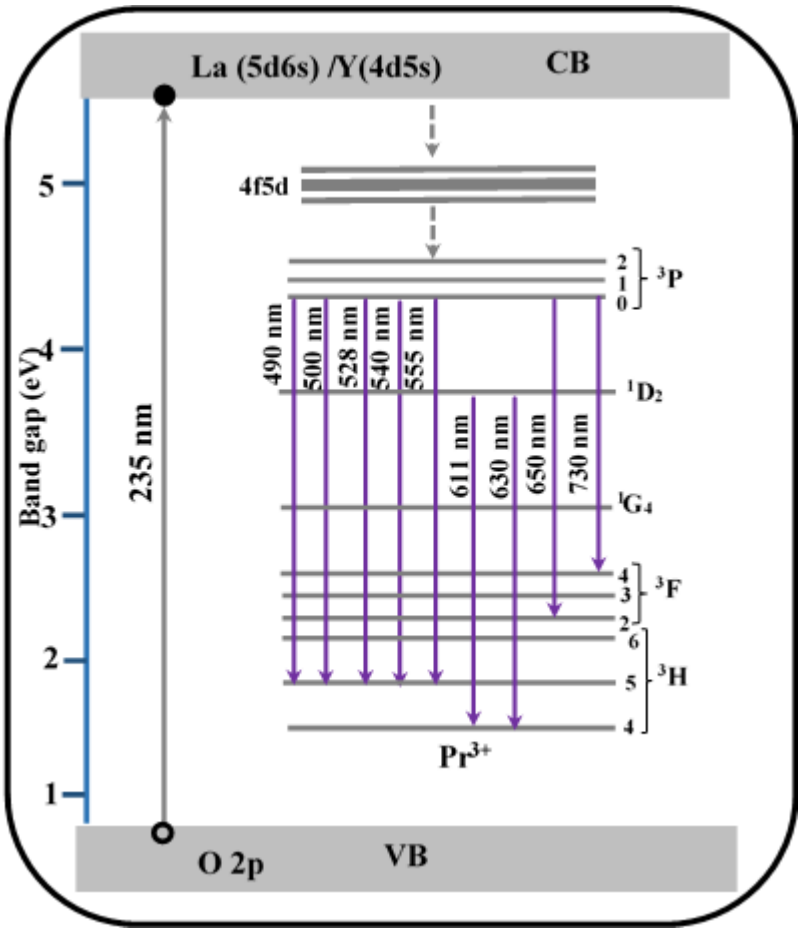

Fig. 6.12: The schematic energy diagram illustrating the energy transitions of Pr^{3+} in $La_{2-x}Y_xSiO_5:Pr^{3+}$ (x = 0, 0.5, 1, 1.5 and 2) phosphors.

The luminescence branching ratio ($B_{JJ'}$) for emission from the J manifold to the J' manifolds is defined as a probability of spontaneous emission for a particular transition $A_{JJ'}$ to the sum of all the transition probabilities from the J manifold [80]. The luminescence branching ratio can be estimated experimentally by taking ratio of the relative intensities of individual emission peaks to that of the total emission intensity peaks [81]. Table 6.4 shows the estimated experimental luminescence branching ratios (β_{Exp}) of $La_{2-x}Y_xSiO_5:Pr^{3+}$ (x = 0, 0.5, 1, 1.5 and 2) phosphors. Observe the variation in the luminescence branching ratios as the value of x changes. For instance, the luminescence branching ratios of the $^3P_0$ emission observed at 490 nm 0.194, 0.144, 0.162¸

0.109 and 0.093 for x = 0, 0.5, 1, 1.5 and 2 respectively, and 0.204, 0.207,0.174, 0.238 and 0.205 for the $^1D_2$ emission at 611 nm. It also be seen that the difference between the β_{Exp} value for the 611 nm line and the 490 nm was highest when x = 2 (in the favour of 611 nm line).

Table 6.4: The experimental luminescence branching ratios of the emission lines observed from $La_{2-x}Y_xSiO_5:Pr^{3+}$ (x = 0, 0.5, 1, 1.5 and 2) phosphors.

Transition	Emission λ (nm)	Experimental luminescence branching ratios (β_{Exp})				
		x = 0	x = 0.5	x = 1	x = 1.5	x = 2
STE	STE	0.025	0.017	0.021	0.084	0.094
$^3P_0$	490	0.194	0.144	0.162	0.109	0.093
$^3P_0$	500	0.101	0.087	0.110	0.086	0.087
$^3P_0$	528	0.036	0.029	0.037	0.040	0.049
$^3P_0$	540	0.036	0.032	0.036	0.037	0.052
$^3P_0$	555	0.025	0.026	0.031	0.030	0.046
$^1D_2$	611	0.204	0.207	0.174	0.238	0.205
$^1D_2$	630	0.125	0.159	0.146	0.197	0.203
$^3P_0$	650	0.177	0.202	0.196	0.130	0.134
$^3P_0$	730	0.075	0.097	0.087	0.048	0.038

The phosphorescence decay curves of $La_{2-x}Y_xSiO_5:Pr^{3+}$ (x = 0, 0.5, 1, 1.5 and 2) phosphors were measured by exciting the phosphors at 235 nm and measuring the time it takes for the 490 nm ($^3P_0$) and 611 nm ($^1D_2$) emission (Fig. 6.13(a & b) respectively) to decay. The insets of Fig. 6.13(a & b) are the log scale plots of the phosphorescence decay curves for the $^3P_0$ and $^1D_2$ emissions respectively. The decay curves show superposition of three exponential components for both $^3P_0$ and $^1D_2$ lines. This suggests that three energy levels were involved in the radiative transitions for these emissions. The lifetimes components were extracted by fitting the decay curve with a third order exponential decay function (Eq. (6.13)).

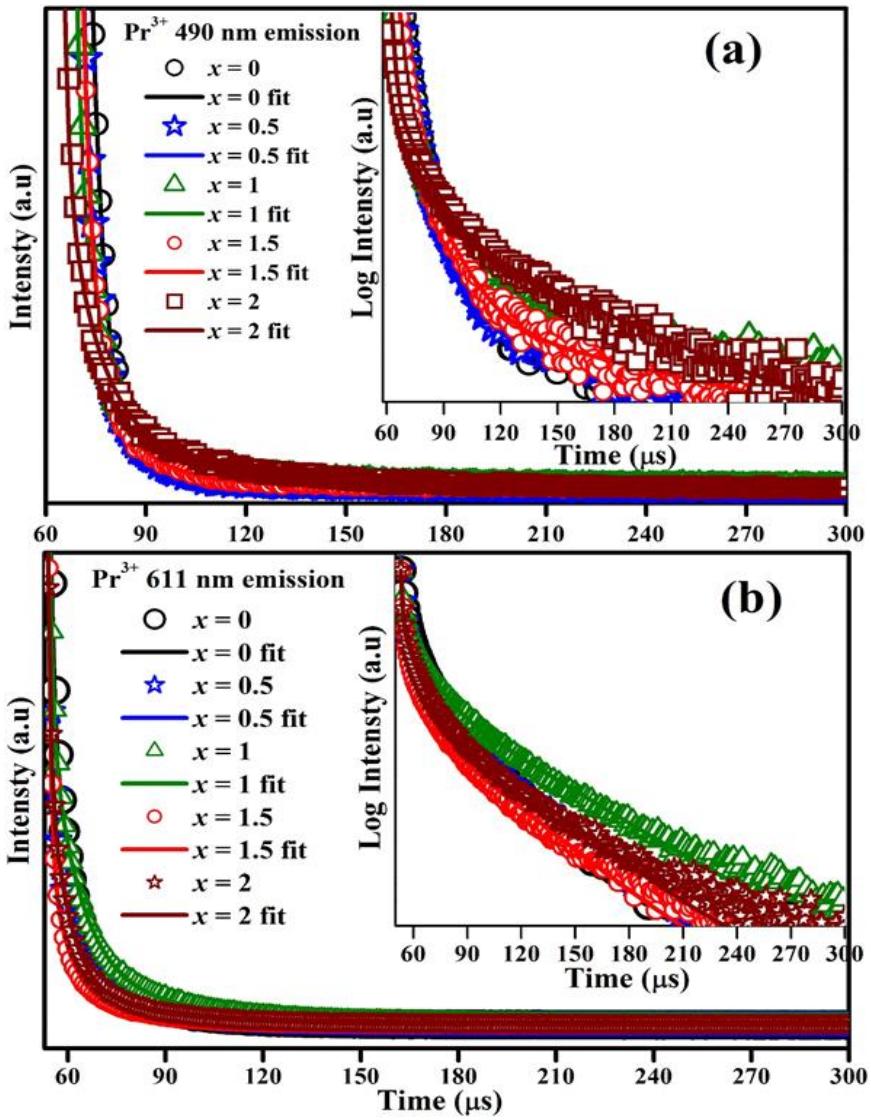

Fig. 6.13: The fitted decay curves of $La_{2-x}Y_xSiO_5:Pr^{3+}$ (x = 0, 0.5, 1, 1.5 and 2) phosphors for the (a) $^3P_0$ (490 nm) and (b) $^1D_2$ (611 nm) Pr^{3+} transition by monitoring the 235 nm excitation.

$$I(t) = Ae^{-t/\tau_1} + Be^{-t/\tau_2} + Ce^{-t/\tau_3} \tag{6.13}$$

where I is the luminescence intensity, t is the phosphorescence time, A, B and C are decay constants, τ_1, τ_2 and τ_3 are the decay times of the first, second and the third lifetime components, respectively [15]. The three lifetime components (τ_1, τ_2 and τ_3) for both $^3P_0$ and $^1D_2$ emission lines are shown in table 6.5 whereas Fig. 6.14 shows the plots of lifetime as a function of x. The inset in Fig. 6.14 shows the magnified graph of first lifetime component (τ_1) versus x for $^3P_0$ and $^1D_2$ emissions. It can be seen from Fig. 6.14 that lifetimes of the $^1D_2$ emission are higher than those

from the $^3P_0$ emission in each case (τ_1, τ_2 and τ_3). For instance, the values of τ_1 for x = 0, 0.5, 1, 1.5 and 2 are 3.83, 2.93, 2.52, 2.90 and 1.45 μs for $^3P_0$ emission and 4.55, 3.67, 3.68, 3.32 and 2.66 μs for the $^1D_2$ emission, respectively. The longer lifetime of the $^1D_2$ state of Pr^{3+} is due to the spin-forbidden nature of the transition [82, 83].

Table 6.5: The values of lifetime (τ) for the $^3P_0$ (490 nm) and $^1D_2$ (611 nm) transitions of Pr^{3+} in $La_{2-x}Y_xSiO_5$ (x = 0, 0.5, 1, 1.5 and 2).

$La_{2-x}Y_xSiO_5:Pr^{3+}$	$^3P_0$ (490 nm) emission			$^1D_2$ (611 nm) emission		
	τ_1 (μs)	τ_2 (μs)	τ_3 (μs)	τ_1 (μs)	τ_2 (μs)	τ_3 (μs)
x = 0	3.83	10.97	26.62	4.55	28.19	99.94
x = 0.5	2.93	11.07	100.00	3.67	29.18	110.00
x = 1	2.52	13.56	110.00	3.68	34.97	140.00
x = 1.5	2.90	12.47	110.00	3.32	34.97	110.00
x = 2	1.45	10.68	61.33	2.66	24.09	120.00

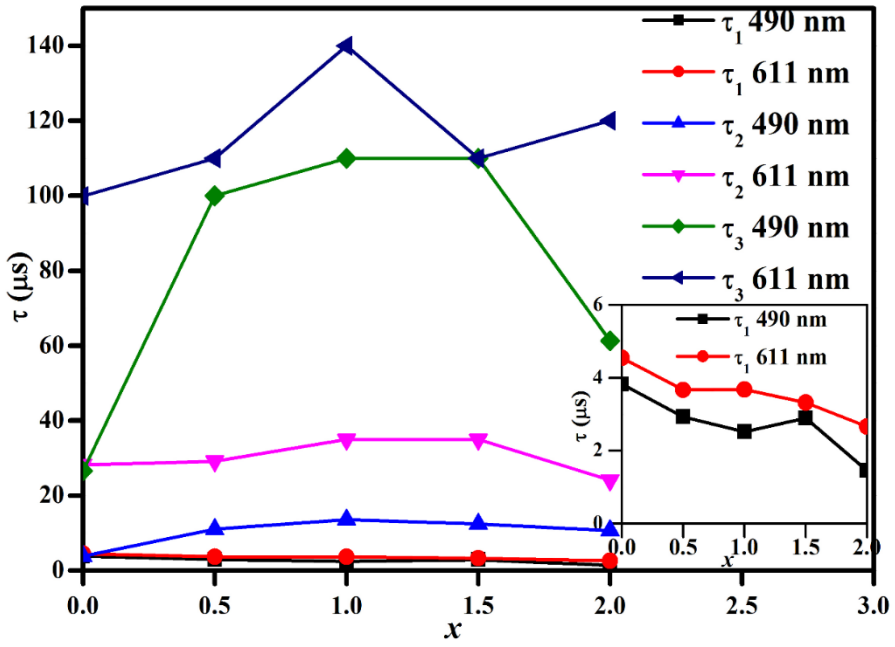

Fig. 6.14: The plots of lifetime (τ_1, τ_2 and τ_3 for $^3P_0$ (490 nm) and$^1D_2$ (611 nm) transitions of Pr^{3+}) versus x for Pr^{3+} in $La_{2-x}Y_xSiO_5$ (x = 0, 0.5, 1, 1.5 and 2). The inset is magnified spectra of τ_1 for the $^3P_0$ (490 nm) and $^1D_2$ (611 nm) transitions.

Fig. 6.15 shows the CIE chromaticity coordinates diagram of $La_{2-x}Y_xSiO_5:Pr^{3+}$. The CIE shows red colours with (x, y) coordinates of (0.464, 0.341), (0.501, 0.350), (0.462, 0.355), (0.432, 0.286) and (0.411, 0.290) for x = 0, 0.5, 1, 1.5 and 2, respectively. The changes observed in the CIE

coordinates is due to the variations observed in the luminescence intensities of the ^3P_J and $^1D_2$ transitions in the emission spectra (Fig. 6.9(a-e)).

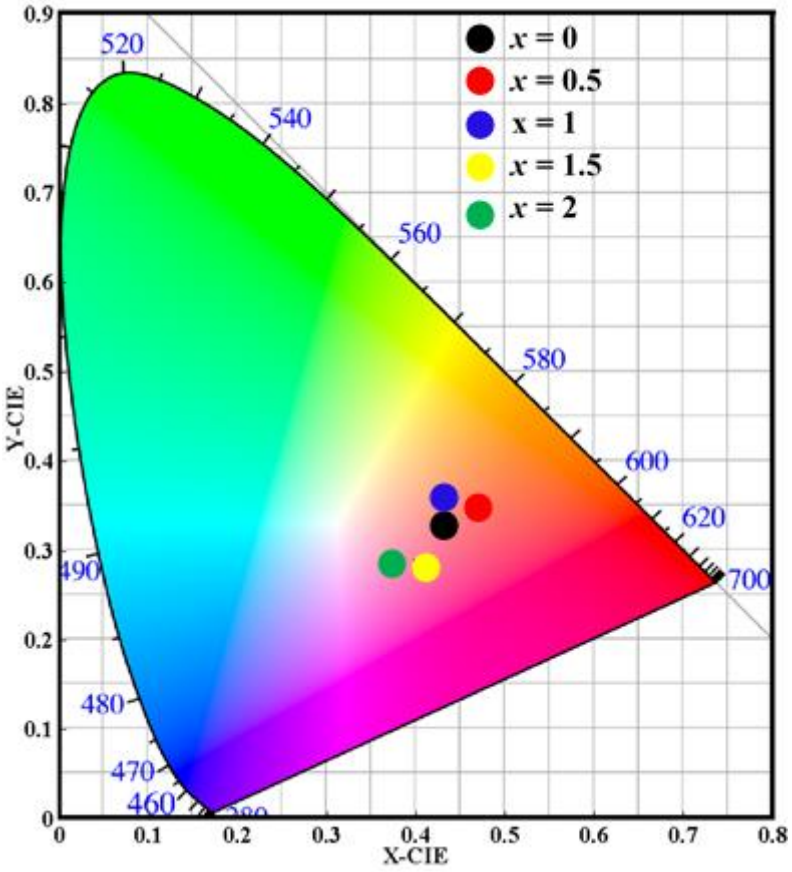

Fig. 6.15: CIE coordinates diagram of $La_{2-x}Y_xSiO_5:Pr^{3+}$ (x = 0, 0.5, 1, 1.5 and 2) phosphors.

6.4. Conclusions

Pr^{3+} doped mixed lanthanum yttrium oxyorthosilicates, $La_{2-x}Y_xSiO_5:Pr^{3+}$ (x = 0, 0.5, 1, 1.5 and 2) powder phosphors were prepared using urea-assisted combustion method. The structure, elemental and molecular species, ultraviolet visible reflectance and photoluminescence properties of the phosphors were studied. The band gap of the doped samples was widened due to the shifting of the Fermi-level into the conduction band by the dopant ions. The photoluminescence study of the phosphors showed that the branching ratio of the $^3P_0$ and $^1D_2$ transitions of Pr^{3+} varies with the crystal field of the host, with x = 0 (La_2SiO_5) favouring $^3P_0$ transition and x = 2 (Y_2SiO_5) favouring

$^1D_2$ transition. The observed variation in branching ratio of the $^3P_0$ and $^1D_2$ transitions was ascribed to the non-radiative transition of $^3P_0 \rightarrow {}^1D_2$, which increases with *x* (i.e. as the ratio of Y increases in the host). It can be concluded therefore, that the inconsistencies observed in the branching ratios of the emission intensities of transitions of Pr^{3+} in different hosts is due to the variable crystal field strength of the hosts. The magnitude of the crystal field influences the interaction between the Pr^{3+} energy levels and the excited configurations and hence the rate of non-radiative $^3P_0 \rightarrow {}^1D_2$ transitions, with higher rate of $^3P_0 \rightarrow {}^1D_2$ non-radiative transitions observed in host lattices with high crystal field strength. Furthermore, it was also shown that the $^3P_0$ transitions are from Pr^{3+} ions occupying La1 and Y1 sites in the La_2SiO_5 and Y_2SiO_5 lattices respectively, while the $^1D_2$ transitions emanated from Pr^{3+} ions occupying the La2 and Y2 sites. The decay curve showed three lifetime components from both $^3P_0$ and $^1D_2$ transition with the latter having higher lifetime values in all cases.

6.5. References

[1] H. Rétot, A. Bessière, B. Viana, B. LaCourse, E. Mattmann, Opt. Mater. 33 (2011) 1008.

[2] M. Rozanski, M. Środa, Cz. Koepke, Time resolved spectroscopy of oxyfluoride glass ceramics activatedby Pr^{3+} ions, Proc. of SPIE. 7120 (2008)71200E-5.

[3] C. De Mello Donegá, A. Meijerink, G. Blasse, J. Phys. Chem. Solids, 56 (1995) 673.

[4] M. Arai, N. Matsuda, M. Tamatani, J. Alloys Compd. 192 (1993) 45.

[5] E.G. Reut, A.I. Ryskin, Phys. Stat. Sol. A 17 (1973) 47.

[6] C. Delsart, N. Pelletier-Allard, J. Phys. C: Solid State Phys. 6 (1973) 1277.

[7] A.A. Kaminskii, S.E. Sarkisov, G.A. Denisenko, V.V. Ryabchenkov, V.A. Lomonov, Y. E. Perlin, M.G. Blazha, D. Schultze, B. Hermoneit, P. Reiche, Phys. Stat. Sol. A 85 (1984) 553.

[8] J.P.M. van Vliet and G. Blasse, Chem. Phys. Lett. 143 (1988) 221.

[9] M. Szymanski, J. Lumin. 29 (1984) 467.

[10] H. Dornauf, J. Heber, J. Lumin. 20 (1979) 271.

[11] W.J. Schipper, M.F. Hoogendorp, G. Blasse, J. Alloys Comp. 202 (1993) 283.

[12] M.J. Weber, J. Chem. Phys. 48 (1968) 4774.

[13] H.E. Hoefdraad, G. Blasse, Phys. Stat. Sol. (a), 29 (1975) K95.

[14] G.C. Aumuller, W. Kostler, B.C. Grabmailer, R. Frey, J. Phys. Chem. Solids, 55 (1994) 767.

[15] L.L. Noto, M.L. Chithambo, O.M. Ntwaeaborwa, H.C. Swart, J. Alloys Compd. 589 (2014) 88.

[16] F.B. Xiong, D.S. Guo, H.F. Lin, L.J. Wang, H.X. Shen, W.Z. Zhu, J. Alloys Compd. 647 (2015) 1121.

[17] V. Vidyadharan, R.P. Mohan, C. Joseph, N.V. Unnikrishnan, P.R. Biju, Mater. Chem. Phys. 170 (2016) 38.

[18] X. Yang, J. Liu, H. Yang, X. Yu, Y. Guo, Y. Zhou, J. Liu, J. Mater. Chem. 19 (2009) 3771.

[19] J.W. Chung, H.K. Yang, B.K. Moon, B.C. Choi, J.H. Jeong, J.H. Kim, J. Nanosci. Nanotechnol. 11 (2011) 6208.

[20] S.N. Ogugua, S.K.K. Shaat, H.C. Swart, O.M. Ntwaeaborwa, J. Phys. Chem. Sol. 83 (2015) 109.

[21] J. Felsche, The crystal chemistry of the rare-earth silicates, In, R.A. Penneman, R.R. Ryan, A. Rosenzweig, R. Reisfeld, J. Felsche, C.K. Jørgensen, "*Structure and Bonding*" Springer, Berlin 13 (1973) p. 99–197.

[22] M. Yin, C. Duan, W. Zhang, L. Lou, S. Xia, J.C. Krupa, J. Appl. Phys. 86 (1999) 3751.

[23] C. Zhu, Y. Ni, T. Cui, C. Lu, Z. Xu, Z. Kang, Mater. Res. Express 2 (2015) 086201.

[24] N.V. Kuleshov, V.G. Shcherbitsky, A.A. Lagatsky, V.P. Mikhailov, B.I. Minkov, T. Danger, T. Sandrock, G. Huber, J. Lumin. 71 (1997) 27.

[25] Y.V. Malyukin, A.A. Masalov, P.N. Zhmurin, Opt. Commun. 239 (2004) 409.

[26] Y.V. Malyukin, A.A. Masalov, P.N. Zhmurin, Phys. Lett. A 316 (2003) 147.

[27] M. Jie, G. Zhao, X. Zeng, L. Su, H, Pang, X, He, J. Xu, J. Cryst. Growth. 277 (2005) 175.

[28] G.D. Dominiak, W. R. Romanowski, R. Lisiecki, P. Solarz, B. Macalik, M. Berkowski, M. Gzowacki, V. Domukhovski, Cryst. Growth Des. 10 (2010) 3522.

[29] R.D. Shannon, Acta Cryst. 32 (1976) 751.

[30] R. Bokolia, O.P. Thakur, V.K. Rai, S.K. Sharma, K. Sreenivas, Ceram. Int. 41 (2015) 6055.

[31] Y. Tang, M.R. DeGuire, R. Mansfield, N. Smilanich, Grain Growth of nanocrystalline Ru-doped SnO_2 in sol-gel derived thin films, In, S.W. Lu, M.Z. Hu, Y. Gogotsi (Ed.), "*Ceramic nanomaterials and nanotechnology III*" The American Ceramic Society, Westerville, Ohio 159 (2005) p. 93–102.

[32] B.D. Cullity, Elements of X-ray diffraction, Addison-wesley publishing company, inc. Reading, Massachusetts, United States (1956) p. 116–122.

[33] P.J. Brown, A.G. Fox, E.N. Maslen, M.A. O'Keefe, B.T.M. Willis, Intensity of diffracted intensities, In, E. Prince (E.d.) "*International tables for crystallography*" C (2006) p. 554–595.

[34] S.N. Ogugua, R.L. Nyenge, P.T. Sechogela, H.C. Swart, O.M. Ntwaeaborwa, J. Vac. Sci. Technol. A 34 (2016) 021520.

[35] A.J. Signorelli, R.G. Hayes, Phys. Rev. B 8 (1973) 81.

[36] E. Coetsee, J.J. Terblans, H.C. Swart, Appl. Surf. Sci. 256 (2010) 6641.

[37] D.F. Mullica, C.K. Lok, H.O. Perkins, Phys. Rev. B. 31 (1985) 4039.

[38] T.H. Yang, Y.W. Harn, K.C. Chiu, C.L. Fan, J.M. Wu, J. Mater. Chem. 22 (2012) 17071.

[39] S. Mickevicius, S. Grebinskij, V. Bondarenka, H. Tvardauskas, B. Vengalis, K. Sliuzienne, B.A. Orlowski, W. Drube, Opt. Appl. XXXVI (2006) 235.

[40] J.F. Moulder, W.F. Stickle, P.E. Sobol, K.D. Bomben, Handbook of X-ray photoelectron spectroscopy, J. Chastain (Ed.), Perkin-Elmer Corporation, Physical Electronics Division, USA, (1992) p. 20.

[41] H. Al Kutubi, L. Rassaei, W. Olthuis, G.W. Nelson, J.S. Foord, P. Holdway, M. Carta, R.M. Evans, N.B. McKeown, S.C. Tsang, R. Castaing, T.R. Forder, M.D. Jones, D. Hea, F. Marken, RSC Adv. 5 (2015) 73323.

[42] E.Y. Konysheva, M.V. Kuznetsov, 3 (2013) 14114.

[43] H.E. Hoefdraad, J. Inorg. Nucl. Chem. 37 (1975) 1917.

[44] P. Boutinaud, E. Pinel, M. Dubois, A.P. Vink, R. Mahiou, J. Lumin. 111 (2005) 69.

[45] J.T.W. de Hair, G. Blass, J. Lumin. 8 (1973) 97.

[46] A. Alemi, S. Khademinia, S.W. Joo, M. Dolatyari, A. Bakhtiari, H. Moradi, S. Saeidi, A. Esmaeilzadeh, Int. Nano. Lett. 4 (2014) 100.

[47] P. Rajeshwaran1, A. Sivarajan, G. Raja, D. Madhan, P. Rajkumar, J. Mater. Sci: Mater. Electron. 27 (2016) 2419.

[48] T. Higuchi, A. Oda, T. Tsuchiya, T. Suetsugu, N. Suzuki, S. Yamaguchi, M. Minohara, M. Kobayashi, K. Horiba, H. Kumigashira, J. Phys. Soc. Jpn. 84 (2015) 114708.

[49] A. Kotani, H. Ogasawara, J. Electron Spectrosc. Relat. Phenom. 60 (1992) 257.

[50] O. Seifarth, J. Dabrowski, P. Zaumseil, S. Müller, D. Schmeißer, H.J. Müssig, T. Schroeder, J. Vac. Sci. Technol. B 27 (2009) 271.

[51] L. Petit, A. Svane, Z. Szotek, W.M. Temmerman, Phys. Rev. B 72 (2005) 205118.

[52] R.C. Karnatak, M. Gasgnier, H. Dexpert, J.M. Esteva, P.E. Caro, L. Albert, J. Less-Common Met. 110 (1985) 377.

[53] R.C. Karnatak, J.M. Esteva, H. Dexpert, M. Gasgnier, P.E. Caro, L. Albert, Phys. Rev. B 36 (1987) 1745.

[54] A. Bianconi, A. Kotani, K. Okada, R. Giorgi, A. Gargano, A. Marcelli, T. Miyahara, Phys. Rev. B 38 (1988) 3433.

[55] S. Kern, C-K. Loong, J. Faber, Jr., G.H. Lander, Solid State Commun. 49 (1984) 295.

[56] G. Kortum, Reflectance Spectroscopy, Springer-Verlag, New York (1969) pp. 103–169.

[57] J. Tauc (Ed.), The Optical Properties of Solids, Academic Press, New York (1966).

[58] M.A. Humayun, M.A. Rashid, F.A. Malek, A.N. Hussain, Journal of Russian Laser Research, 33 (2012) 387.

[59] E. Burstein, Phys. Rev. 93 (1954) 632; T. S. Moss, Proc. Phys. Soc. London Ser. B 67 (1954) 775.

[60] N. F. Mott, Rev. Mod. Phys. 40 (1968) 677; P.P. Edwards, M.J. Sienko, Phys. Rev. B 17 (1978) 2575.

[61] K.F. Berggren, B.E. Sernelius, L. Engstrom, Phys. Rev. B 30 (1984) 3240.

[62] M. Zhuravleva, A. Novoselov, A. Yoshikawa, J. Pejchal, M. Nikl, T. Fukuda, Opt. Mat. 30 (2007) 171.

[63] A. Zych, M. de Lange, C.D. de Mello, A. Meijerink, J. Appl. Phys. 112 (2012) 013536.

[64] Y.C. Li, Y.H. Chang, Y.F. Lin, Y.S. Chang, Y.J. Lin, J. Phys. Chem. Sol. 68 (2007) 1940.

[65] K. Annapurna, R. Chakrabarti, S. Buddhudu, J. Mater. Sci. 42 (2007) 6755.

[66] K.H. Lee, K.W. Chae, C.I. Cheon, J.S. Kim, J. Korean Ceram. Soc. 48 (2011) 183.

[67] Y. Ji, J. Cao, Z. Zhu, J. Li, Y, Wang, C. Tu, Mater. Express 1 (2011) 231.

[68] C. Itoh, K. Tanimura, N. Itoh, J. Phys. C: Solid State Phys. 21 (1988) 4693.

[69] S.N. Ogugua, S.K.K. Shaat, H.C. Swart, O.M. Ntwaeaborwa, J. Lumin. 179 (2016) 154.

[70] Ph. Goldner, O.G. Noël, G. Dantelle, M. Mortier, T.H. My, F. Bretenaker, Eur. Phys. J. Appl. Phys. 37 (2007) 161.

[71] L.E. Cates, F. Li, RSC Adv. 6 (2016) 22791.

[72] A.A. Kaminskii, S.N. Bagayev, K. Ueda, J. Dong, H.J. Eichler, Laser Phys. Lett. 7 (2010) 270.

[73] B.E. Dunina, A.A. Kornienko, L.A. Fomicheva, Cent. Eur. J. Phys. 6 (2008) 407.

[74] F. Auzel, Multiphonon processes, cross-relaxation and up-conversion in ion-activated solids, exemplified by minilaser materials, In, B. DiBartolo, V. Goldberg (Ed.) "*Radiationless processes*" Plenum Press, New York (1980) p. 213-286.

[75] K. Fukuda, T. Iwata, Powder Diffr. 21 (2006) 300.

[76] J. Wang, S. Tian, G. Li, F. Liao, X. Jing, Mat. Res. Bull. 36 (2001) 1855.

[77] T. Justel, W. Mayr, P.J. Schmidt, Tuning the $4f^15d$-$4f^2$ UV emission of Pr^{3+}, 200^{th} meeting of the electrochemical society, San Francisco, CA, USA, September (2001).

[78] L.G. Van Uitert, J. Lumin. 29 (1984) 1.

[79] Y.A. Tanko, S.K. Ghoshal, M.R. Sahar, J. Mol. Struct. 1117 (2016) 64.

[80] L. Marciniak, W. Strek, Y. Guyot, D. Hreniak, G. Boulon, J. Phys. Chem. C 119 (2015) 5160.

[81] S. Dutta, S. Som, S.K. Sharma, RSC Adv. 5 (2015) 7380.

[82] E.L. Cates, F. Li, RSC Adv. 6 (2016) 22791.

[83] E. Dell'Orto, M. Fasoli, G. Ren, A. Vedda, J. Phys. Chem. C 117 (2013) 20201.

CH. 7

Influence of the ratio of rare earth oxyorthosilicate R_2SiO_5 (R = La, Y) hosts on the structure and optical properties of co-doped Pr^{3+} /Dy^{3+} phosphors.

7.1. Introduction

Crystal field determines the chemical nature of the optical center of a phosphor material. Some of the optical advantages of crystal field engineering include shifting of the wavelength ranges of optical transitions, increasing the rates of radiative transitions and minimizing loss by nonradiative decay and excited state absorption. These objectives can be accomplished by manipulating the unit cell containing the optical center. The unit cell can be manipulated by changing its chemical composition [1]. The crystal field strength in any host increases with decreasing ionic radius of the host material relative to that of the dopant due to increased electrostatic interaction of the host lattice with the dopant ion [2]. Therefore, dopant with bigger ionic radius will create stronger electrostatic interaction with the host lattice and hence higher crystal field strength.

The luminescence spectra of phosphors based on Pr^{3+} doped matrices show a strong dependence on the crystal field strength of the host material. For host matrices with weak crystal field strength, the lowest crystal field component of the 4f5d configuration of Pr^{3+} is energetically located above the $^1S_0$ level of the 4f-state and hence after vacuum ultra-vacuum (VUV) excitation, majority of the relaxation path populates the $^1S_0$ level, Fig. 1(a) [3, 4]. When doped into host matrix with crystal field strong enough that the lowest crystal field component of the 4f5d configuration is located slightly below the $^1S_0$ state, Pr^{3+} gives broad emission in the ultraviolet B or UV-B (280–315 nm) and UV–C (100-280 nm) range, Fig. 7.1(b) [4, 5]. However, for a host matrix with a very strong crystal field strength, the 4f5d of Pr^{3+} is far below the $^1S_0$ state and closer to the 4f states. This leads to the population of the 4f states and hence leads to emission in the visible range of the spectrum, Fig. 7.1(c) [4, 6-8].

On the other hand, Dy^{3+} doped matrices show two prominent emission lines around 485 nm (bluish-green) and 575 nm (yellowish), which varies differently with the crystal field around Dy^{3+} ion. Defined as hypersensitive, the yellow emission, which is electric dipole transition, is highly

sensitive to the crystal field around Dy^{3+} ions. On the other hand, the bluish emission is a magnetic dipole transition and hardly varies with the crystal field around Dy^{3+} ions [9].

Variation in the molar ratio of La and Y in $La_{2-x}Y_xSiO_5$ (x = 0, 0.5, 1, 1.5 and 2) host will result in variation of the unit cells of the host and hence tuning of the crystal field strength. These, to large extent, can influence the luminescence properties of Pr^{3+} and Dy^{3+} in the host matrix. Concerning the effects described above, we decided to study the effect of host composition on luminescence properties of R_2SiO_5 (R = La and Y) co-doped Pr^{3+} and Dy^{3+}.

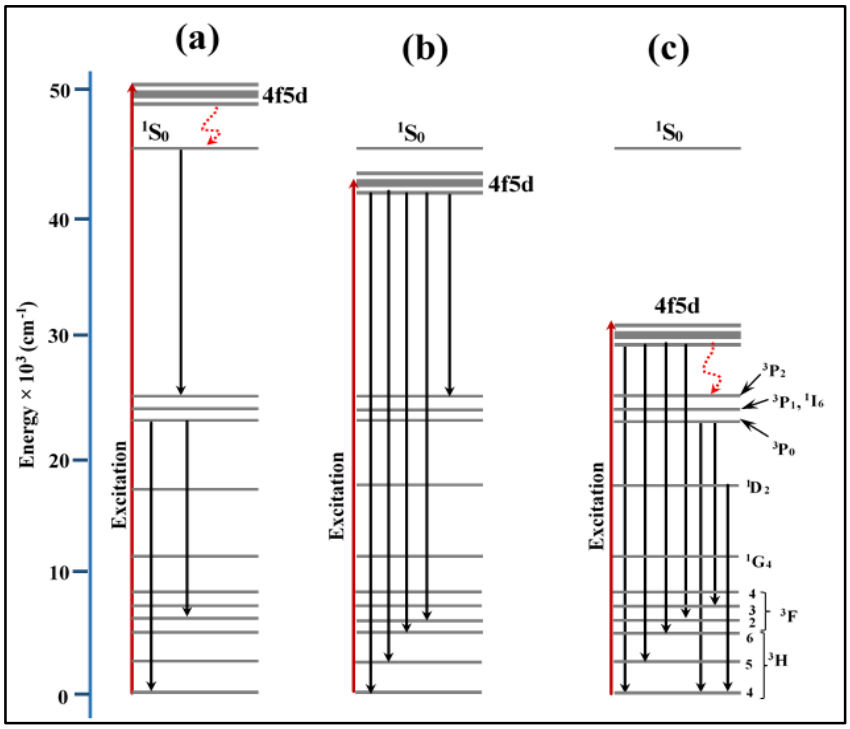

Fig. 7.1: Schematic of energy levels of Pr^{3+} in different hosts.

7.2. Experimental

7.2.1. *Sample preparation*

0.25% of praseodymium (Pr) and dysprosium (Dy) co-doped $La_{2-x}Y_xSiO_5$ (x = 0, 0.5, 1, 1.5 and 2) powder phosphors were prepared by urea-assisted solution combustion synthesis. The starting materials are lanthanum nitrate hexahydrate, $La(NO_3)_3.6H_2O$, yttrium nitrate hexahydrate,

$Y(NO_3)_3.6H_2O$, praseodymium nitrate hexahydrate, $Pr(NO_3)_3.6H_2O$, dysprosium nitrate hexahydrate, $Dy(NO_3)_3.6H_2O$, silicic acid, SiO_2H_2O, urea, $CO(NH_4)_2$ and ammonium nitrate, NH_4NO_3. Urea and ammonium nitrate were used as fuel. Stoichiometric amounts of the above compounds were dissolved in 2 ml of distilled water in a glass beaker and placed in a magnetic stirrer with a hot plate set to 100 ^oC and was stirred for about 15 min to obtain a homogeneous solution. The solution was transferred to ceramic crucible boat and immediately into a muffle furnace pre-heated to 600 ± 10 ^oC. Combustion reaction took place within 2 min after the crucible boat containing the solution was placed into the furnace, resulting in evaporation of gases like CO_2, N_2 and H_2O. The end product (crispy foam-like) was removed from the oven and allowed to cool to room temperature and was ground into a fine powder using an agate mortar and pestle. The powder samples were stored in different sample holders for characterization.

7.2.2. *Characterization*

A Bruker D8 Advanced X-ray diffractometer (XRD) with a monochromatic CuKα radiation of wavelength (λ) = 1.54056 Å was used to study the structure. A Lambda 950 UV-vis spectrometer was used for absorption measurements. A Jeol JSM-7800F field emission scanning electron microscope (FE-SEM) fitted with Oxford Aztec 350 X-Max80 was used to study the morphology and the energy-dispersive X-ray spectroscopy (EDS) for chemical composition analysis. Photoluminescence (PL) measurements were performed using two instruments: (i) the FLS980 spectrometer - Edinburgh instruments equipped with a 450 W Xenon Lamp (Xe1) as the excitation source and the red-cooled photomultiplier tube (PMT) detector. (ii) a PL system consisting of a 325 nm He-Cd gas-cooled laser as source of excitation, PMT detector, a spectrometer and a lock-in amplifier.

7.3. Results and discussion

It has been shown that the crystal structure of La_2SiO_5 and Y_2SiO_5 can crystalize in a pure monoclinic phase. However, La_2SiO_5 fall into the P21/c space group (the large ionic radii rare earth ions) while Y_2SiO_5 fall into the C2/c space group (the small ionic radii rare earth ions) [10, 11]. Dominiak et al reported that mixed oxyorthosilicate $Lu_{2-x}Gd_xSiO_5$ exhibited the Lu_2SiO_5 (C2/c) type structure up to 80 at% of Gd and 20 at% of Lu (Gd_2SiO_5 belong to the P21/c group) [12], while mixed $Gd_{1.99-x}Y_xCe_{0.01}SiO_5$ (x = 0.199) has been shown to crystalize in P21/c space group [13]. The tendency that mixed rare earth host form single or mixed phase can be related to

the ionic radii of the rare earth ions that are incorporated. Considering the similarity between ionic radii of Lu^{3+} and Gd^{3+} ions (Lu^{3+} = 0.1032 and Gd^{3+} = 0.1107 nm) in their nine fold coordinates, [10, 14], substituting these will not have significant effect on the crystal structure of the Lu_2SiO_5. Similarly, Y^{3+} (0.1075 nm) will not have any significant effect on the crystal structure of Gd_2SiO_5. However, the crystal phase of the structure of $La_{2-x}Y_xSiO_5$: $_{0.25}Pr^{3+}$, $_{0.25}Dy^{3+}$ (x = 0, 0.5, 1, 1.5 and 2) can be affected by varying the molar ratio of La^{3+} to Y^{3+} in the matrix as shown in the XRD pattern in Fig. 7.2. By decreasing the La ion content, the matrix can move from P21/c space group to C2/c space group [15]. For x = 0 and 2 we have pure P21/c and C2/c space group respectively. The change in the crystal structure of $La_{2-x}Y_xSiO_5$: $_{0.25}Pr^{3+}$, $_{0.25}Dy^{3+}$ with x can be attributed to a relatively large difference between the ionic radii of La^{3+} (0.1216 nm) and Y^{3+} (0.1075 nm). Considering the ionic radii of the rare earth ions, Pr^{3+} (0.1179 nm) ions can easily substitute La^{3+} (0.1216 nm) sites but will cause expansion in Y^{3+} (0.1075 nm) lattice sites. On the other hand, Dy^{3+} ions (0.1083 nm) can easily substitute both La^{3+} and Y^{3+} lattice sites [10, 14]. However, substitution of Dy^{3+} into La^{3+} lattice sites will lead to shrinkage of the lattice sites (and hence resulting in longer Dy^{3+}–La^{3+} bonds length) and subsequently a weaker crystal field splitting effect [16]. The XRD pattern of the pure La_2SiO_5 (x = 0) and pure Y_2SiO_5 (x = 2) matched with the standard monoclinic structures referenced in JCDPS file no: 40-0234 and 74-2011 respectively. It shows that the diffraction peaks shift to higher angles as x increases, which is ascribed to the change in the crystal structure [15]. For a fixed wavelength (λ), the interplanar spacing (d-spacing) (d_{hkl}) can be estimated from the XRD data using Eq. (7.1) [17].

$$d_{hkl} = \frac{\lambda}{2\sin\theta_{hkl}} \tag{7.1}$$

where $\lambda = 0.15406$ nm is Cu Kα X-ray wavelength; h, k and l are Miller's indices; and θ_{hkl} is the diffraction angle. The estimated d-spacing decreases as x increases and they are compared with the theoretical values in table 7.1. The peaks marked with * are from Y_2SiO_5 while the unmarked peaks are from La_2SiO_5.

Table 7.1: Crystallographic planes and corresponding Bragg angles, the experimental and theoretical *d*-spacing for $La_{2-x}Y_xSiO_5$:$_{0.25}Pr^{3+}$, $_{0.25}Dy^{3+}$ (x = 0, 0.5, 1, 1.5 and 2).

2θ (deg)	La:Y molar ratio/Crystallographic planes					d_{hkl} (nm)	
	x = 0	x = 0.5	x = 1	x = 1.5	x = 2	Experimental	Theoretical
19.5					$(\bar{2}02)$*	0.45485	0.44044
20.51	(200)					0.43268	0.44202
22.58	(111)					0.39397	0.39549
22.61		(111)				0.39294	0.39549
22.75			(111)			0.39056	0.39549
26.86	(021)					0.33165	0.32709
27.89		(021)				0.31963	0.32709
28.58			(121)*			0.31208	0.30357
29.09	(202)					0.30672	0.31978
29.16				(121)*		0.30600	0.30357
29.29		(202)				0.30467	0.31978
29.36					(121)*	0.30396	0.30357
30.67	(121)					0.29127	0.29218
30.84		(121)				0.28970	0.29218
31.02			(121)			0.28806	0.29218
32.57			(213) *			0.27469	0.26469
33.57				(213) *		0.26674	0.26469
33.77					(213) *	0.26521	0.26469
43.73	(321)					0.20684	0.20359
44.07		(321)				0.20532	0.20359
45.97	$(\bar{1}23)$					0.19726	0.19848
48.22				(125)*		0.18857	0.18756
48.62					(125)*	0.18711	0.18756
52.19	$(\bar{5}12)$					0.17512	0.17706
52.82		$(\bar{5}12)$				0.17318	0.17706
57.25				(240)*		0.16079	0.15952
57.65					(240)*	0.15977	0.15952
63.72	$(\bar{4}41)$					0.14593	0.14625

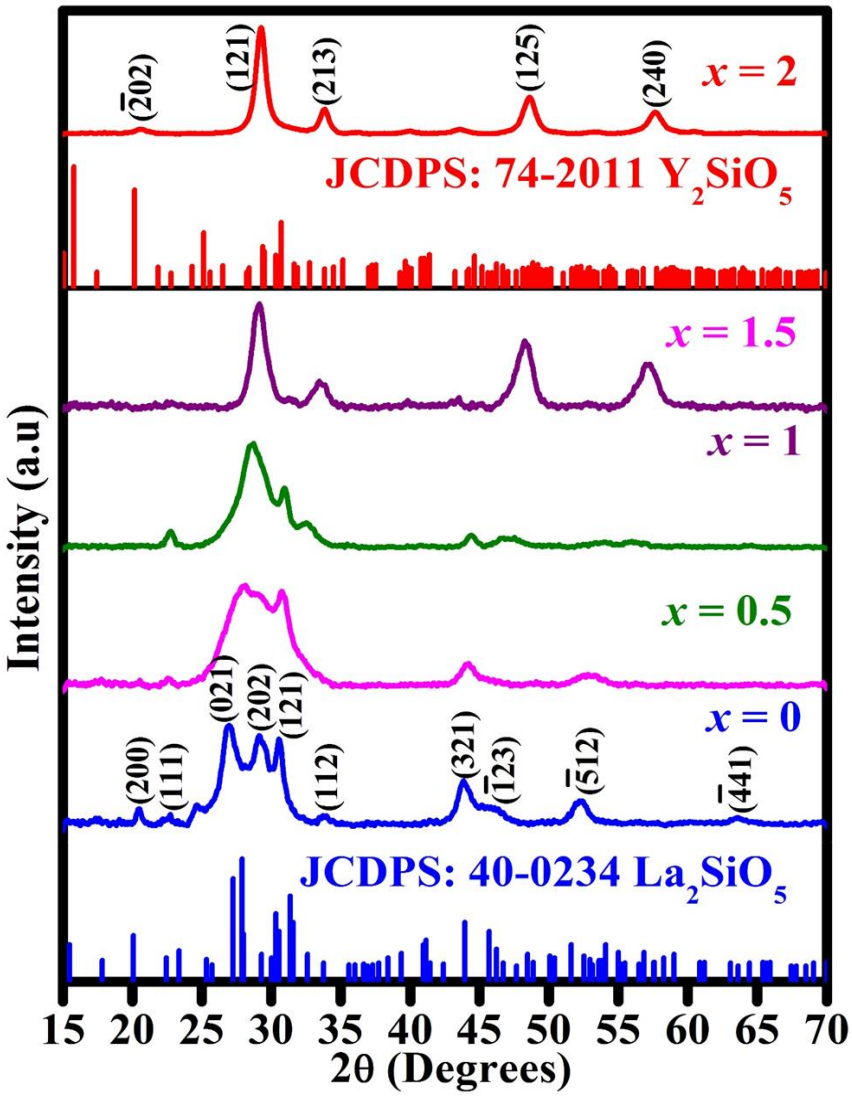

Fig. 7.2: XRD pattern of $La_{2-x}Y_xSiO_5$:$_{0.25}Pr^{3+}$, $_{0.25}Dy^{3+}$ (x = 0, 0.5, 1, 1.5 and 2) compared to the JCDPS files of pure La_2SiO_5 and Y_2SiO_5.

Fig. 7.3 (a-c) show the FE-SEM images of $La_{2-x}Y_xSiO_5$:$_{0.5}Pr^{3+}$, $_{0.5}Dy^{3+}$ (x = 0, 1, 2) powders respectively. The images show that the powders were made up of platelet-like and flake-like structures of different sizes.

EDS spectra recorded from three sample (x = 0, 1 and 2) are shown in Fig. 7.4 (a, c and e) and the corresponding images of elemental mapping are shown in Fig. 7.4(b, d and f). From the EDS spectra, the carbon (C) was probably from the carbon tape used to mount the samples and the atmospheric carbon. Other elements such as La, Y, Si, Dy, and O were observed as expected. The

elemental mapping shows how each element was distributed on the surface of the samples, and it is apparent that all the elements were evenly distributed on the surface.

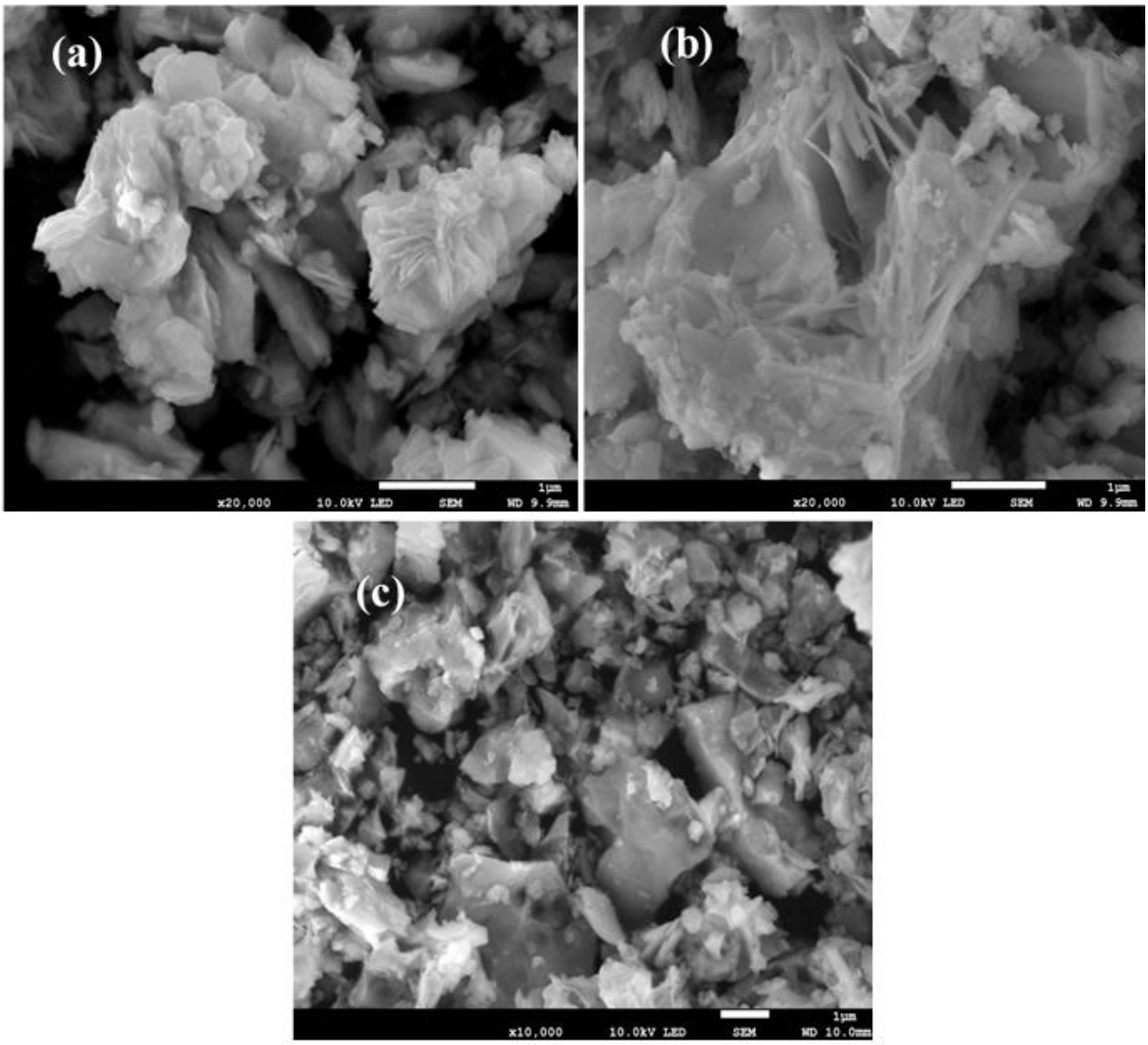

Fig. 7.3: FE-SEM images of (a) La_2SiO_5:$_{0.25}Pr^{3+}$, $_{0.25}Dy^{3+}$ (x = 0), (b) Y_2SiO_5:$_{0.25}Pr^{3+}$, $_{0.25}Dy^{3+}$ (x = 2) and (c) $LaYSiO_5$:$_{0.25}Pr^{3+}$, $_{0.25}Dy^{3+}$ (x = 1).

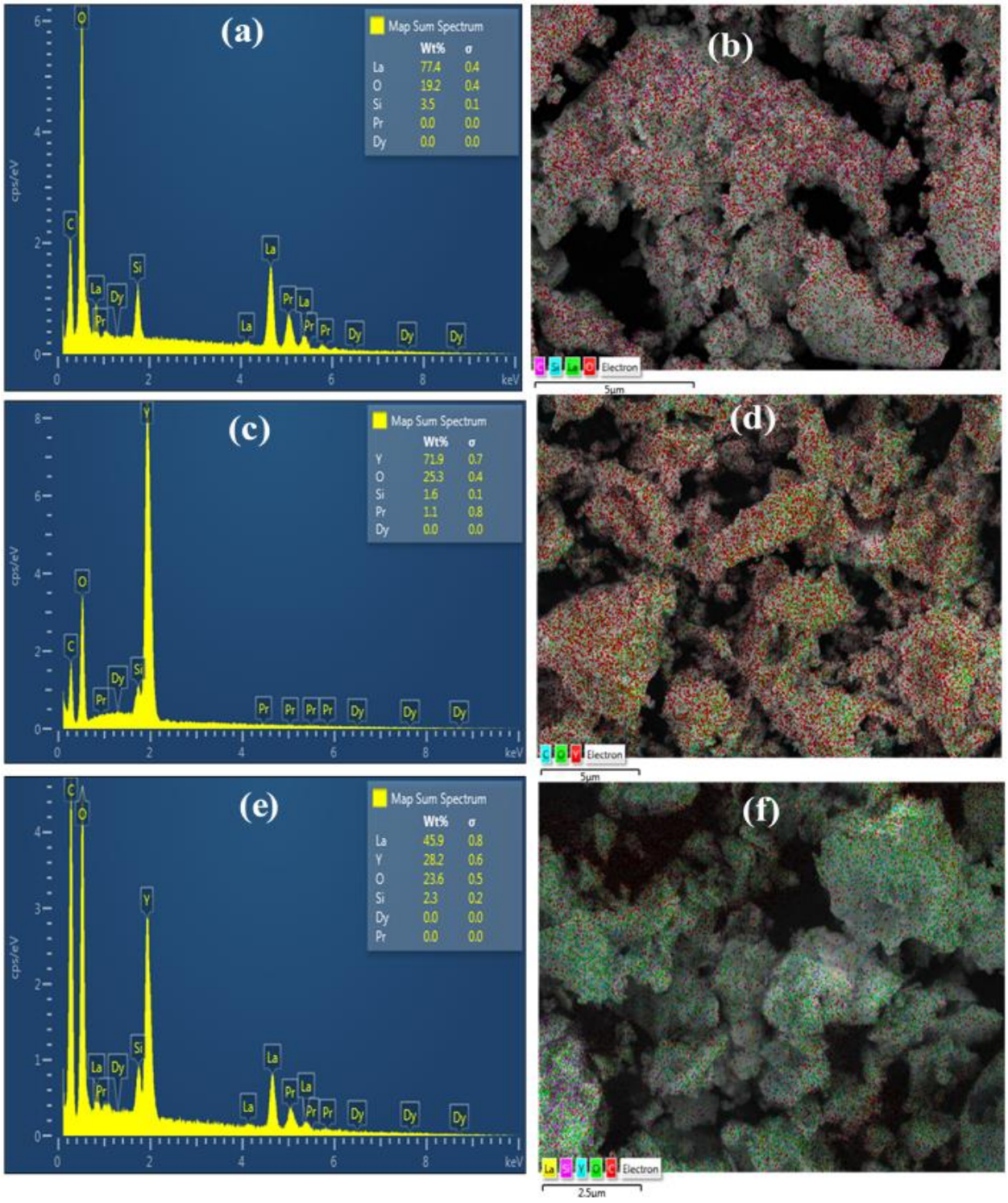

Fig. 7.4: The EDS spectra of (a) La_2SiO_5:$_{0.25}Pr^{3+}$, $_{0.25}Dy^{3+}$, (c) Y_2SiO_5:$_{0.25}Pr^{3+}$, $_{0.25}Dy^{3+}$, (e) $LaYSiO_5$:$_{0.25}Pr^{3+}$, $_{0.25}Dy^{3+}$ and the corresponding elemental maps (b), (d) and (f).

The reflectance properties of La_2SiO_5, Y_2SiO_5, mixed $LaYSiO_5$, and $LaYSiO_5$ doped Dy^{3+} and Pr^{3+} phosphors were investigated using UV-VIS spectrometer at room temperature. Fig. 7.5(a) shows the diffuse reflectance spectra of La_2SiO_5, Y_2SiO_5 and $LaYSiO_5$ while Fig. 7.5(b) shows the diffuse reflectance spectra of $LaYSiO_5$ doped with Dy^{3+} and Pr^{3+}. From the reflectance curve (Fig. 7.5(a)), it is seen that the absorption edge of $LaYSiO_5$ lies at higher wavelength (lower energy) compared to those of Y_2SiO_5 and La_2SiO_5. This could be because of strain induced in the matrix due to mixing of the two host matrices. Both $LaYSiO_5:Dy^{3+}$ and $LaYSiO_5:Pr^{3+}$ show similar absorption edge around 210 nm (Fig. 7.5(b)). Furthermore, the shape of the reflectance curve of $LaYSiO_5:Dy^{3+}$ is similar to the undoped $LaYSiO_5$. However, for $LaYSiO_5:Pr^{3+}$, immense decrease was observed in the reflectance from around 668 nm to 376 nm, and it becomes constant around 310 nm, and then decreases again. This broad absorption band with maxima at 376 nm is ascribed to $O^{2-} \rightarrow Pr^{4+}$ charge transfer band (CTB) and it is usually not accompanied by luminescence [18]. In addition, this charge transfer band suppressed the Pr^{3+} and Dy^{3+} absorptions peaks in the reflectance spectra [18, 19].

The optical band gaps were determined from the reflectance spectra using Tauc plot [20]. According to Tauc, the absorption coefficient α for a given material is related to its band gap (E_g) by

$$(\alpha h\nu)^{1/n} = A(h\nu - E_g) \tag{7.2}$$

where h is Planck's constant, ν is the frequency of vibration, n denotes the nature of material transition and A is a constant which is independent of the chemical composition of the material. According to the Kubelka-Munk function ($F(R_\infty)$), the diffuse reflectance (R_∞) for a semi-infinite medium is given by

$$F(R_\infty) = \left(\frac{(1-R_\infty)^2}{2R_\infty}\right) \tag{7.3}$$

Therefore, for a finite medium with 100 % reflectance,

$$F(R_{100}) = \left(\frac{(1-R_{100})^2}{2R_{100}}\right) = \left(\frac{(1-R)^2/100}{2R/100}\right) \tag{7.4}$$

$F(R_{100})$) is directly proportional to α, hence Eq. (7.2) can be written as

$$(F(R_{100})h\nu)^{1/n} = A(h\nu - E_g) \tag{7.5}$$

The reflectance wavelength in nm λ_{nm} is related to the photon energy $(h\nu)$ in electron volts (eV) by $h\nu = 1240/\lambda_{(nm)}$ [21, 22]. The plot of $h\nu$ versus $[h\nu F(R_{100})]^{1/2}$ for La_2SiO_5, Y_2SiO_5, $LaYSiO_5$ are shown in Fig. 7.6(a), while Fig. 7.6(b) shows the $h\nu$ versus $[h\nu F(R_{100})]^{1/2}$ plot for $LaYSiO_5$ doped Pr^{3+} and Dy^{3+}. The estimated band gaps are 4.65, 5.15, 3.66, 4.72 and 3.71 for La_2SiO_5, Y_2SiO_5, $LaYSiO_5$, $LaYSiO_5$:Dy^{3+} and $LaYSiO_5$:Pr^{3+}, respectively. The value of the band gaps are less than the reported band gap of Y_2SiO_5 (6.10 eV) [22].

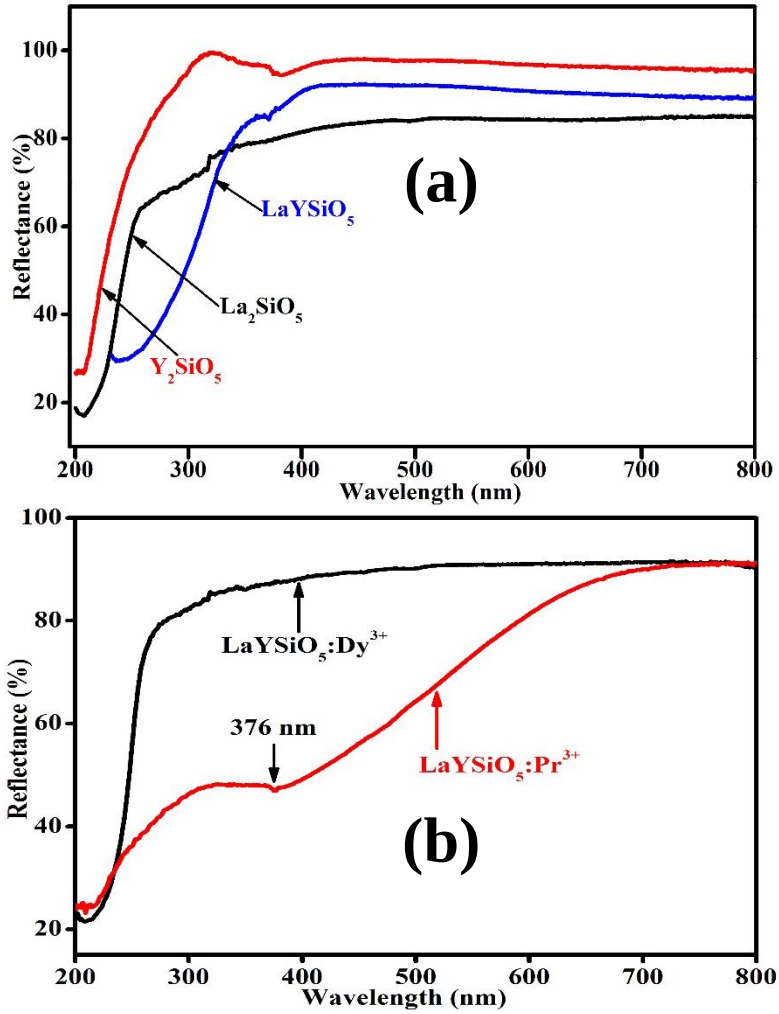

Fig. 7.5: The diffuse reflectance curves of (a) undoped La_2SiO_5, Y_2SiO_5 and $LaYSiO_5$ and (b) $LaYSiO_5$:Dy^{3+} and $LaYSiO_5$:Pr^{3+}.

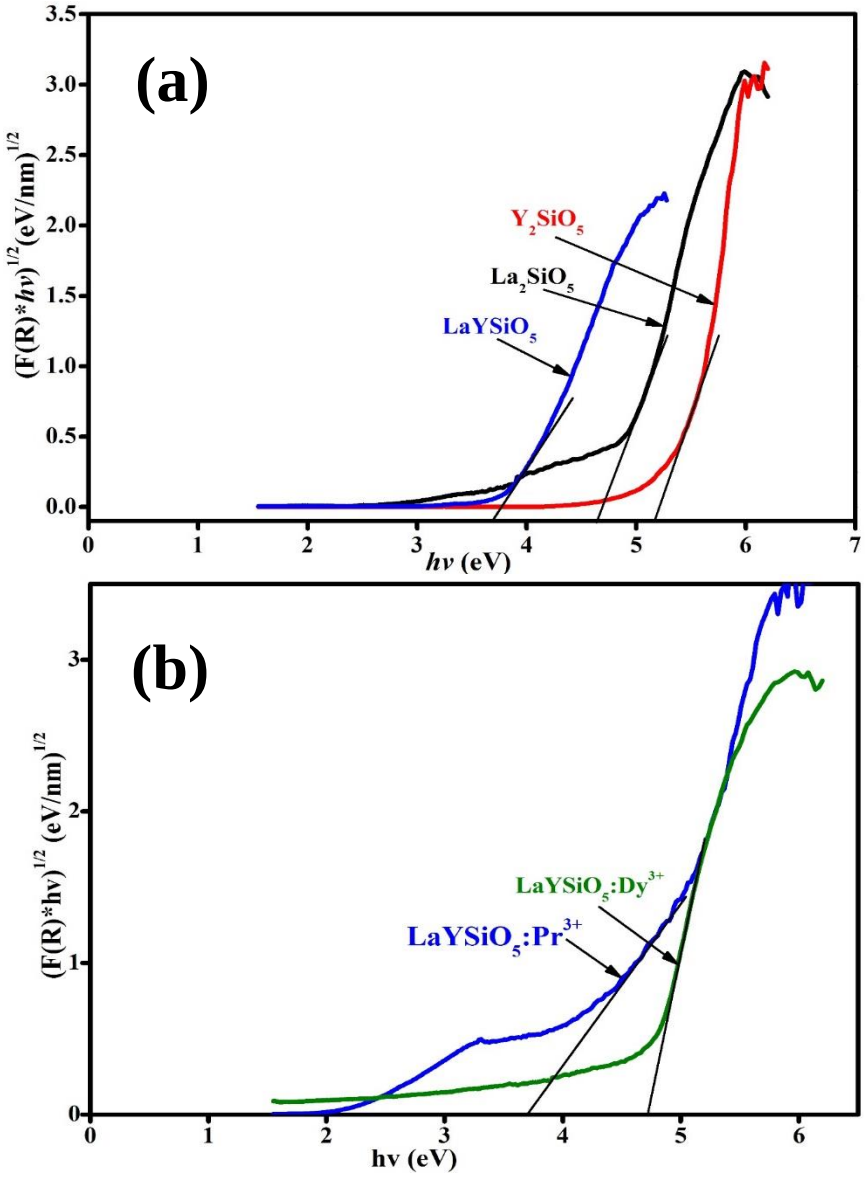

Fig. 7.6: Estimation of the band gaps of (a) La_2SiO_5, Y_2SiO_5 and $LaYSiO_5$, (b) $LaYSiO_5:Dy^{3+}$ and $LaYSiO_5:Pr^{3+}$ using the *hv* versus $[hvF(R_{100})]^{1/2}$.

For the co-doped $La_{2-x}Y_xSiO_5:_{0.25}Pr^{3+}$, $_{0.25}Dy^{3+}$ (x = 0, 0.5, 1, 1.5 and 2), the highest reflectance was obtained when x = 2 ($Y_2SiO_5:_{0.25}P^{3+}$, $_{0.25}Dy^{3+}$) and the lowest when x = 0.5 ($La_{1.5}Y_{0.5}SiO_5:_{0.25}Pr^{3+}$, $_{0.25}Dy^{3+}$), Fig. 7.7(a). It can be seen that the reflectance decreased initially with increasing x (x = 0.5), but started increasing with x from x values of 1, 1.5 and 2. It is expected that, since Y_2SiO_5 have higher reflectance than L_2SiO_5, increasing the molar ratio of Y_2SiO_5 (increasing value of x) in the $La_{2-x}Y_xSiO_5:_{0.25}Pr^{3+}$, $_{0.25}Dy^{3+}$ matrix should lead to increasing

reflectance. Nevertheless, the initial decrease in the reflectance could be due to induced strain due to the mixed phase of La_2SiO_5 and Y_2SiO_5. The absorption edge was constant at 225 nm for x = 0, 0.5 and 1, but changed to 214 and 206 nm for x = 1.5 and 2 respectively. Fig. 7.7(b) shows the hv versus $[hvF(R_{100})]^{1/2}$ curves for $La_{2-x}Y_xSiO5:_{0.25}Pr^{3+}$, $_{0.25}Dy^{3+}$ (x = 0, 0.5, 1, 1.5 and 2) with estimated band gaps of 3.84, 3.23, 3.72, 4.19 and 5.35 eV, respectively.

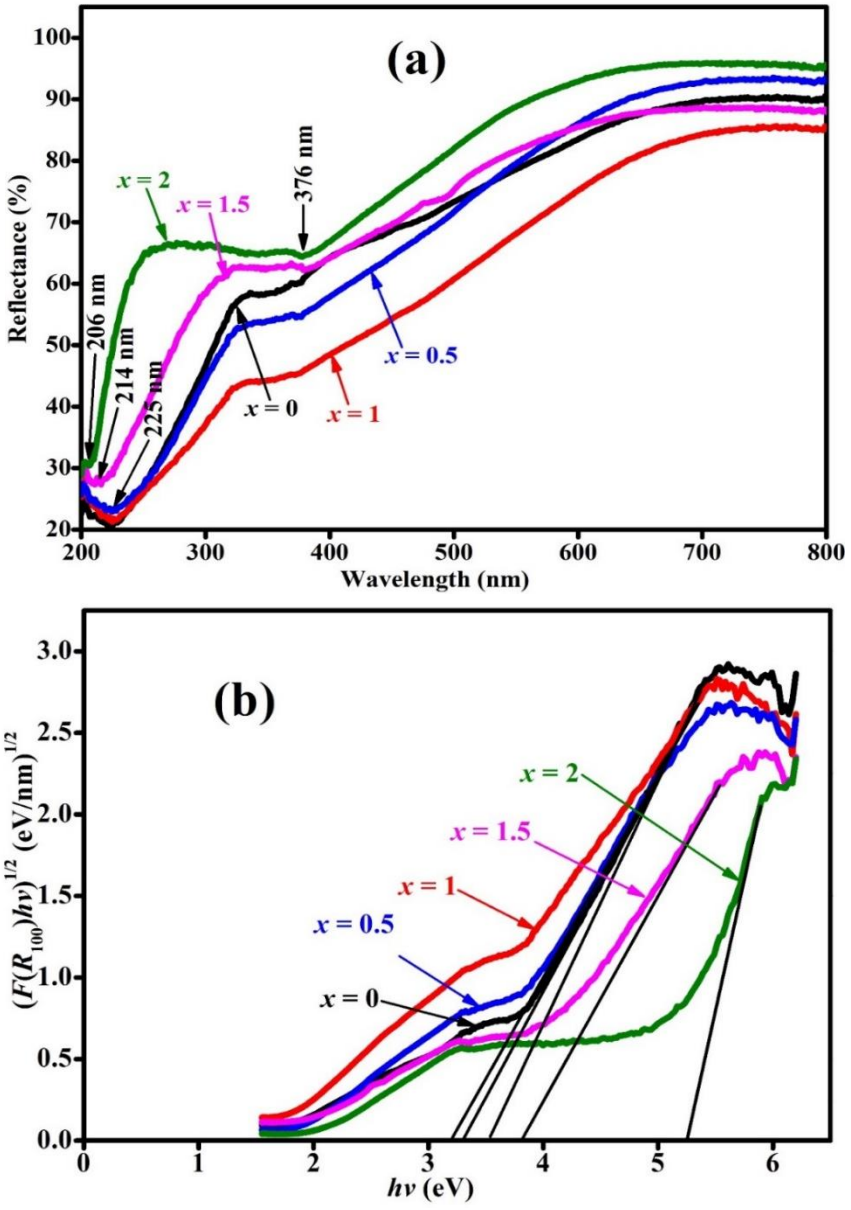

Fig. 7.7: The diffuse reflectance curves of (a) $La_{2-x}Y_xSiO_5:_{0.25}Pr^{3+}$, $_{0.25}Dy^{3+}$ (x = 0, 0.5, 1, 1.5 and 2) and (b) the respective band gaps.

Photoluminescence properties of Dy^{3+} and Pr^{3+} doped $LaYSiO_5$ were measured to confirm the electronic transitions emanating from each of the rare earth ion before co-doping. Fig. 7.8(a) (1 and 2) shows the PL excitation spectra of $LaYSiO_5:Dy^{3+}$ and $LaYSiO_5:Pr^{3+}$ when monitoring the $^4F_{9/2}\rightarrow{}^6H_{13/2}$ (573 nm) and $^1D_2\rightarrow{}^3H_4$ (611 nm) transitions of Dy^{3+} and Pr^{3+} respectively. The excitation spectra of $LaYSiO_5:Dy^{3+}$ and $LaYSiO_5:Pr^{3+}$ show major excitation peaks at 234 and 237 nm, respectively, which are attributed to the electronic transition from the O2p valence band to La(5d6s) and Y(4d5s) conduction band [23, 24]. The inset of Fig. 7.8(a) (1 and 2) are the magnified excitation spectra of $LaYSiO_5:Dy^{3+}$ and $LaYSiO_5:Pr^{3+}$ from wavelength range of 250 – 500 nm. The magnified excitation spectra of $LaYSiO_5:Dy^{3+}$ (Fig. 7.8(a) (1)) shows eight excitation peaks assigned to $^6H_{15/2}\rightarrow{}^4K_{13/2}$ (294 nm), $^6H_{15/2}\rightarrow{}^4K_{15/2}$, $^6P_{3/2}$ (325 nm), $^6H_{15/2}\rightarrow{}^6P_{7/2}$, $^4M_{15/2}$ (349 nm), $^6H_{15/2}\rightarrow{}^6P_{5/2}$ (362 nm), $^6H_{15/2}\rightarrow{}^4I_{13/2}$ (387 nm), $^6H_{15/2}\rightarrow{}^4G_{11/2}$ (424 nm), $^6H_{15/2}\rightarrow{}^4I_{15/2}$ (454 nm), and $^6H_{15/2}\rightarrow{}^4F_{9/2}$ (474 nm) excitation states of Dy^{3+} [25, 26]. The magnified excitation spectra of $LaYSiO_5:Pr^{3+}$, Fig. 7.8(a) (2), shows three peaks at 447, 472, and 486 nm assigned to $^3H_4\rightarrow{}^3P_2$, $^3H_4\rightarrow{}^3P_1$ and $^3H_4\rightarrow{}^3P_0$ transition of Pr^{3+} respectively [27]. The encircled area in the inset of Fig. 7.8(a) (2) is due to 4f→4f5d transition of Pr^{3+} [28-30]. Fig. 7.8(b) (1 and 2) show the emission spectra of $LaYSiO_5:Dy^{3+}$ and $LaYSiO_5:Pr^{3+}$ recorded when exciting at 234 and 237 nm wavelengths respectively. The emission spectrum of $LaYSiO_5:Dy^{3+}$ shows four peaks from Dy^{3+} 4f→4f transition at 484, 573, 665, and 755 nm assigned to $^4F_{9/2}\rightarrow{}^6H_{15/2}$, $^4F_{9/2}\rightarrow{}^6H_{13/2}$, $^4F_{9/2}\rightarrow{}^6H_{11/12}$, and $^4F_{9/2}\rightarrow{}^6H_{9/2}$ respectively [31]. The emission spectrum of $LaYSiO_5:Pr^{3+}$ show three major peaks at 490 nm (with a shoulder at 500 nm), 611 nm (with and shoulder at 630 nm), and 650 nm. The peaks at 490 nm and the shoulder at 500 nm are assigned to double manifold of $^3P_0\rightarrow{}^3H_5$, while the one at 611 nm and the shoulder at 630 nm are double manifold of $^1D_2\rightarrow{}^3H_4$ 4f→4f transitions of Pr^{3+} [32-34]. The other peaks at 650 nm is attributed to $^3P_0\rightarrow{}^3F_2$ transition of Pr^{3+}, while the small broad band peaking at 540 nm is ascribed to manifolds of $^3P_0\rightarrow{}^3H_5$ transitions of Pr^{3+} [35]. The peak at 730 nm is assigned to $^3P_0\rightarrow{}^3F_4$ transition of Pr^{3+} [36]. The broad band shown in the inset of Fig. 7.8(b) (1 and 2) are the magnified PL spectra in the wavelength range of 400 – 470 nm and they are assigned to the self-trapped excitons (STE) in SiO_2 [37, 38].

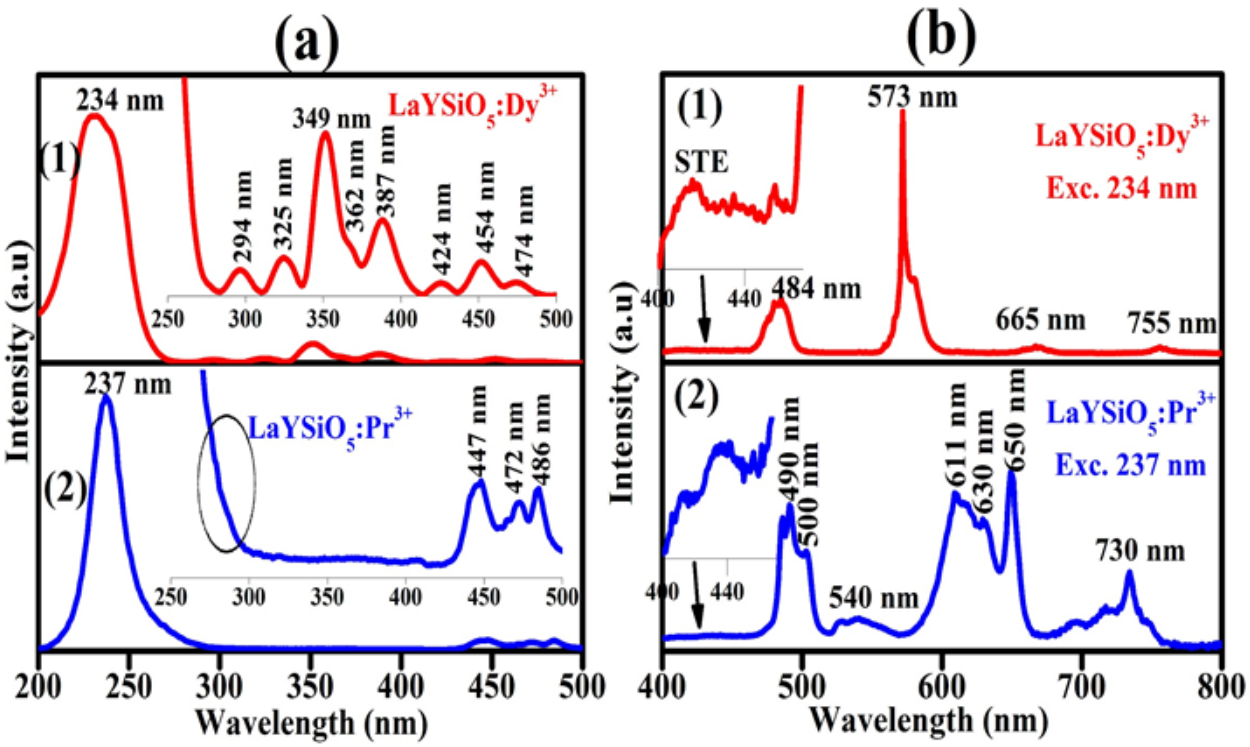

Fig. 7.8: The PL (a) excitation spectra of (1) $LaYSiO_5:Dy^{3+}$, (2) $LaYSiO_5:Pr^{3+}$ monitored under the 573 nm and 611 nm emissions of Dy^{3+} and Pr^{3+} respectively and (b) emission spectra of (1) $LaYSiO_5:Dy^{3+}$, (2) $LaYSiO_5:Pr^{3+}$ under 234 nm and 237 nm excitations respectively.

The PL excitation spectra of the co-doped $La_{2-x}Y_xSiO_5$: $_{0.25}Pr^{3+}$, $_{0.25}Dy^{3+}$ (x = 0, 0.5, 1, 1.5, 2) were measured by monitoring Dy^{3+} $^4F_{9/2}\rightarrow{}^6H_{13/2}$ transition at 573 nm and are shown in Fig. 7.9(a). The excitation spectra comprise of peaks ranging from UV to the visible region. Similarly, eight were observed in the wavelength range of 281– 500 nm in Fig. 7.9(a) as observed from $LaYSiO_5:Dy^{3+}$ (Fig. 7.8(a) (1)). As also observed in Fig. 7.8(a), the broad bands from O 2p valence band to La(5d6s) and Y(4d5s) conduction bands were observed at a lower wavelengths of 228 nm for x = 2 and at 223 nm for x = 1.5, 1, 0.5, and 0 [23, 24] in Fig. 7.9(a). The two insets of Fig. 7.9(a) show the magnified excitation spectrum in the wavelength range of 238 – 300 nm. The two peaks observed at 256 and 278 nm are assigned to the 4f→4f5d transitions of Pr^{3+} [28-30]. Fig. 7.9(b) shows how the UV and the 349 nm excitation intensities varies with each other for each value of x. It is evident that the highest intensities were obtained when x = 2 and the least intensities were obtained when x = 0 for both the UV and 349 nm excitations. The plot in Fig. 7.9(b) shows that the emission intensity of the phosphors decreases with increasing La content (as x decreases) and

increases with increasing Y content (increasing *x*) in the host matrix. This variation in the PL intensity with La can be linked to the differences between the ionic radii of the hosts and the dopants. As observed in the XRD data, substitution of Dy^{3+} into La^{3+} lattice sites will lead to shrinkage of the lattice sites (and hence resulting in longer Dy^{3+}–La^{3+} bonds length) leading to weaker crystal field effect [16]. The weak crystal field interaction leads to decreasing PL intensity as *x* decreases (increasing La^{3+} molar ratio). However, the similarity between the ionic radii of Dy^{3+} and Y^{3+} leads to stronger crystal field interaction and hence leading to increasing PL intensity with increasing Y^{3+} molar ratio (increasing *x*).

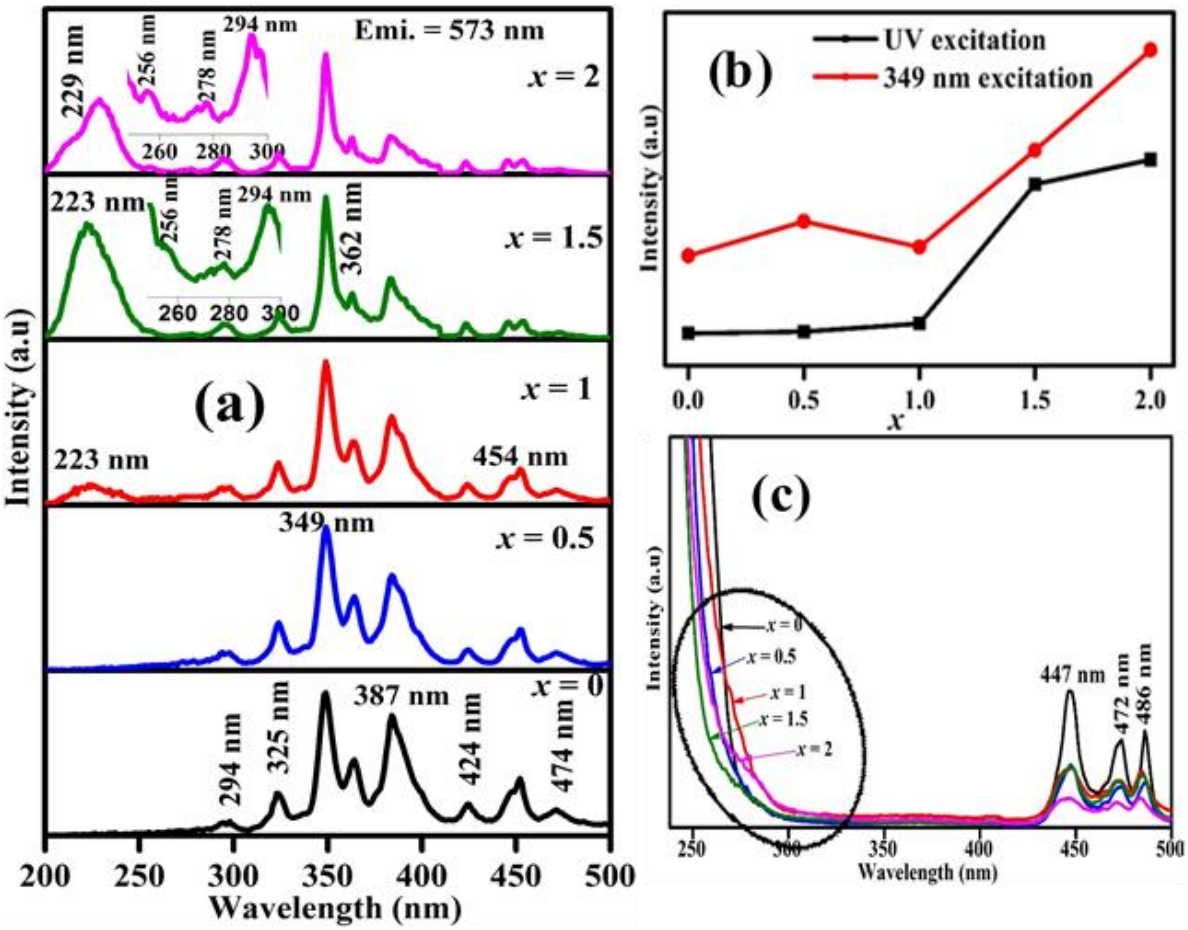

Fig. 7.9: (a) The PL excitation spectra of $La_{2-x}Y_xSiO_5$:$_{0.25}Pr^{3+}$, $_{0.25}Dy^{3+}$ (*x* = 0, 0.5, 1, 1.5 and 2) under the 573 nm emission of Dy^{3+}, (b) compares the variation in the excitation intensities with *x* for the UV (228 and 223 nm) and 349 nm excitation lines, (c) magnified excitation spectra of $La_{2-x}Y_xSiO_5$:$_{0.25}Pr^{3+}$. The insets in (a) is the magnified spectral in the 238 –300 nm spectral range.

The PL emission spectra of the co-doped $La_{2-x}Y_xSiO_5$: $_{0.25}Pr^{3+}$, $_{0.25}Dy^{3+}$ (x = 0, 0.5, 1, 1.5, 2) were recorded by monitoring different excitation wavelengths and the results are shown in Fig. 7.10. The emission spectra of the phosphors when monitoring the excitation at 349 nm are shown in Fig. 7.10(a). Four emission peaks were observed at 484, 573, 665 and 755 nm and are attributed to the $^4F_{9/2}\rightarrow{}^6H_{15/2}$, $^4F_{9/2}\rightarrow{}^6H_{13/2}$, $^4F_{9/2}\rightarrow{}^6H_{11/12}$ and $^4F_{9/2}\rightarrow{}^6H_{9/2}$ f→f electronic transition of Dy^{3+} respectively [31]. The broad band observed from 400 – 470 nm is host related and is assigned to self-trapped excitons (STE) in SiO_2 [37, 38]. Observe that no Pr^{3+} emission was observed in Fig. 7.10(a). However, when the phosphors were excited by using the $^6H_{15/2}\rightarrow{}^4K_{13/2}$ (294 nm) line of Dy^{3+}, both Dy^{3+} and Pr^{3+} emissions were observed as depicted in Fig. 7.10(b). These suggested that Dy^{3+} and Pr^{3+} ions were excited simultaneously when the phosphors were excited at 294 nm. As can be seen from Fig. 7.9(c), 4f→4f5d band of Pr^{3+} extended above 300 nm and hence there is a possibility that when the phosphors were excited at 294 nm, both Dy^{3+} and Pr^{3+} ions were excited concurrently. Also observe from Fig. 7.10(b) is that: (i) when x = 0, only one peak was observed from Pr^{3+} at 540 nm assigned to $^3P_0\rightarrow{}^3H_5$ transition [39]. (ii) When x = 2, six Pr^{3+} emissions were observed at 620, 630, 644, 657, 715 and 750 nm. The four peaks at 620, 630, 644 and 657 nm are the manifolds of $^1D_2\rightarrow{}^3H_4$ transition of Pr^{3+} [40, 41]. The peak at 715 nm is ascribed to $^3P_0\rightarrow{}^3F_3$ transition of Pr^{3+}, while the one at 750 nm is the combination of $^3P_0\rightarrow{}^3F_4$ and $^4F_{9/2}\rightarrow{}^6H_{9/2}$ transitions of Pr^{3+} and Dy^{3+}, respectively [31, 42]. (iii) The luminescence intensity of Pr^{3+} lines in the higher wavelength (620, 630, 644, 657, 715 and 750 nm) decreases with x (i.e. with increasing La content in the host) and vanished completely when x = 0. The decrease in the emission intensity of the peak observed in the higher wavelengths (especially the peaks at 620, 630, 644 and 657 nm) could be due to the $^3P_0\rightarrow{}^1D_2$ non-radiative transitions usually observed in Pr^{3+} doped matrices [15, 43]. The mechanism of $^3P_0\rightarrow{}^1D_2$ non-radiative transitions in Pr^{3+} doped matrices can be explained by $^3P_0\rightarrow{}^1D_2$ relaxation through inter-system crossing via the 4f5d state. It has been shown that the energy level minimum of the 4f5d level of Pr^{3+} can vary with respect to the $^3P_0$ and $^1D_2$ states in different hosts [33, 43]. This variation affects the rate of $^3P_0\rightarrow{}^1D_2$ non-radiative decay, with higher rate observed in host matrices with stronger crystal field strength [44]. Therefore, it is safe to conclude that the variation in the branching ratio of the emission intensities of the emission lines from the $^3P_0$ and $^1D_2$ levels of Pr^{3+} observed in Fig. 7.10(b) is due to the variation of the crystal field strength of the host matrices as the ratio of La:Y is varied. It can also be concluded that the rate of $^3P_0\rightarrow{}^1D_2$ non-radiative decay increases as the ratio of Y increases (as x increases) in the

host. These suggests that Y has higher crystal field strength than La in the $La_{2-x}Y_xSiO_5$: $_{0.25}Pr^{3+}$, $_{0.25}Dy^{3+}$ system. Fig. 7.10(c) shows the emission spectra of the phosphors (x = 1, 1.5 and 2) when monitoring the emission under UV excitation (229, 223 and 223 nm respectively). The spectra show four emission peaks from Dy^{3+} at 484, 573, 665 and 755 nm assigned to $^4F_{9/2}\rightarrow{}^6H_{15/2}$, $^4F_{9/2}\rightarrow{}^6H_{13/2}$, $^4F_{9/2}\rightarrow{}^6H_{11/12}$, and $^4F_{9/2}\rightarrow{}^6H_{9/2}$ respectively [31]. The broad emission band in the wavelength range of 400–472 nm with maximum at 450 nm is a combination of the STE in SiO_2 [37, 38], and Pr^{3+} 4f5d$\rightarrow{}^1D_2$ emission [45]. Observe that the branching ratio of the intensity of the 4f5d$\rightarrow{}^1D_2$ transition of Pr^{3+} to that of the $^4F_{9/2}\rightarrow{}^6H_{13/2}$ (573 nm) transition of Dy^{3+} changes with x, with 4f5d$\rightarrow{}^1D_2$ increasing as x decreases while $^4F_{9/2}\rightarrow{}^6H_{13/2}$ transition increases with x. The variation in the emission intensities of these two peaks could be due to energy transfer from Pr^{3+} to Dy^{3+}. Fig. 7.10(d) shows the excitation and emission spectra of Dy^{3+} and Pr^{3+} respectively, incorporated into $LaYSiO_5$ host. The spectral overlap between the $^6H_{15/2}\rightarrow{}^4I_{15/2}$ (454 nm) excitation peak of Dy^{3+} and the 4f5d$\rightarrow{}^1D_2$ (450 nm) emission band of Pr^{3+} is an evidence that Pr^{3+} can sensitize Dy^{3+}. The possible energy scheme for Pr^{3+} to Dy^{3+} energy transfer in $LaYSiO_5$ host is illustrated in Fig. 7.11. Under UV excitation, electrons are excited from the O 2p valence band to the La(5d6s) and Y(4d5s) conduction band of the host. The excited electrons relax to the 4f5d energy level of Pr^{3+} and higher energy level of Dy^{3+}. Energy transfer from Pr^{3+}:4f5d to Dy^{3+}:$^4I_{15/2}$ level takes place. Energy transfer from Pr^{3+} to Dy^{3+} has been reported in lithium borate glasses co-doped with $Dy^{3+}$and Pr^{3+} [46]. The number of electrons transferred from Pr^{3+} to Dy^{3+} varies with x, probably because of the widening of the energy levels of the Pr^{3+}:4f5d and Dy^{3+}:$^4I_{15/2}$ as a function of x. It has been shown that for divalent and trivalent rare earth ions, the energy level difference between the 4f5d state and the 4f state increases with decrease in the crystal field strength of the host [47]. This suggests that the crystal field strength of the samples probably increased with x; with x = 0 having smallest and x = 2 having the highest crystal field strength.

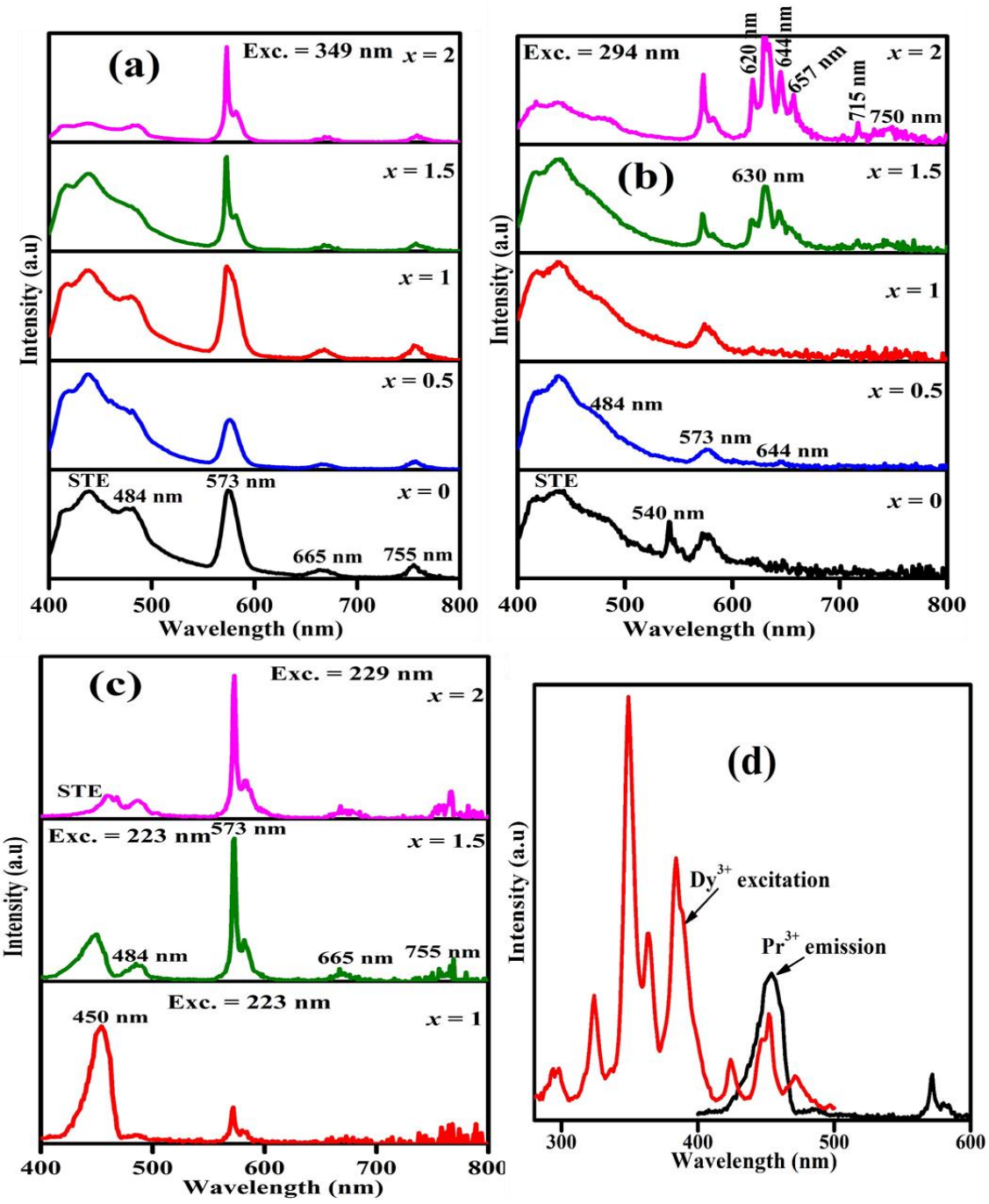

Fig. 7.10: The emission spectra of $La_{2-x}Y_xSiO_5$:$_{0.25}Pr^{3+}$, $_{0.25}Dy^{3+}$ (x = 0, 0.5, 1, 1.5 and 2) monitored using (a) 349 nm excitation (b) 294 nm excitation and (c) 229 and 223 nm excitation, (d) the spectral overlap between Dy^{3+} $^6H_{15/2}\rightarrow{}^4I_{15/2}$ (454 nm) excitation and Pr^{3+} 4f5d$\rightarrow{}^1D_2$ (450 nm) emission band.

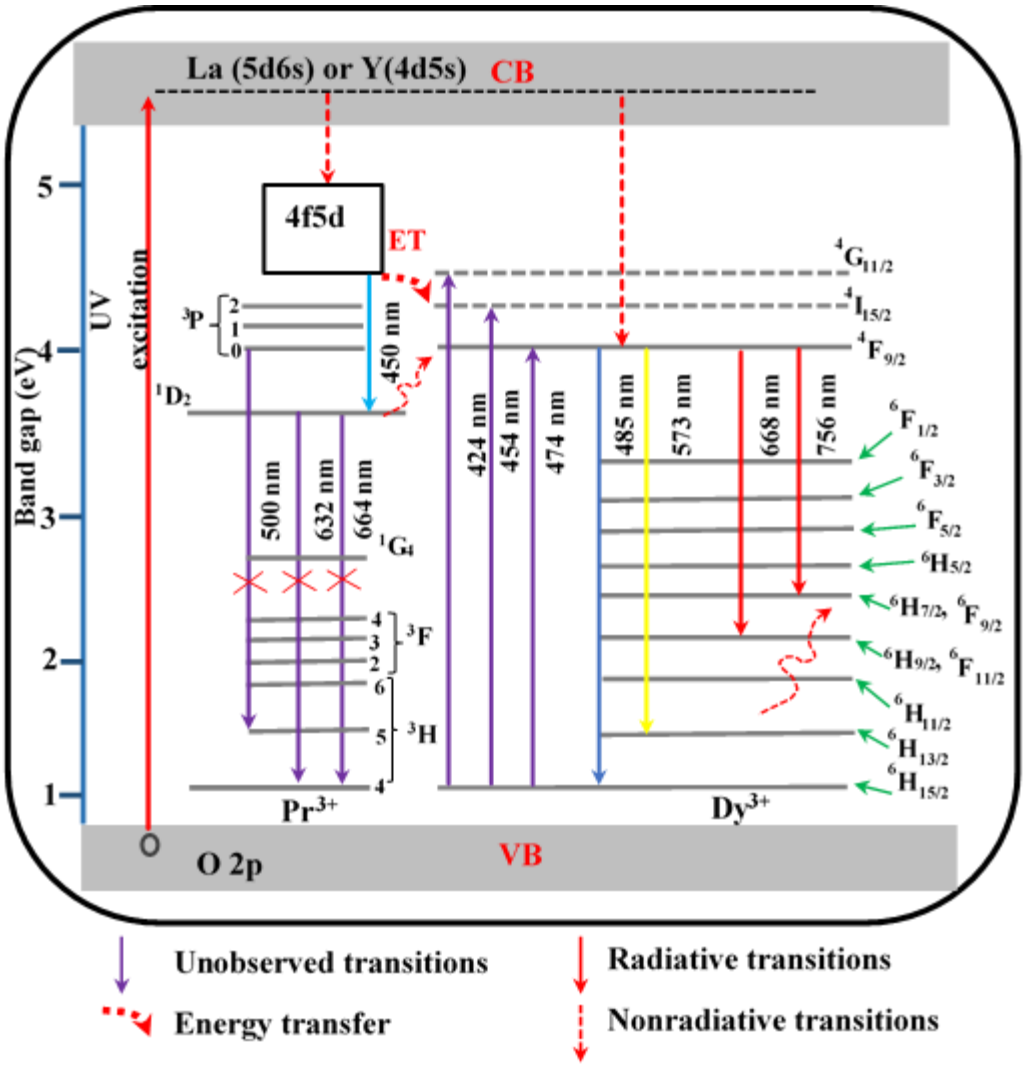

Fig. 7.11: Schematic of energy diagram showing the energy transfer mechanism from Pr^{3+}:4f5d to Dy^{3+}:$^4I_{15/2}$.

The photoluminescence emission properties of the co-doped $La_{2-x}Y_xSiO_5$: $_{0.25}Pr^{3+}$, $_{0.25}Dy^{3+}$ (x = 0, 0.5, 1, 1.5, 2) phosphors were also studied using a 325 nm He-Cd laser as the excitation source and the observed spectra are shown in Fig. 7.12(a). Emission spectra similar to those shown in Fig. 7.9 (b) were obtained including broad emission bands with maximums at 620, 630, 644 and 657 nm (Fig. 7.12(b)) which were observed in only two of the samples (x = 1.5 and 2) assigned to the manifolds of $^1D_2 \rightarrow {}^3H_4$ transition of Pr^{3+} [40, 41]. The STE band is also observed in the wavelength range of 380-470 nm [37]. Fig. 7.12(c) shows a magnified emission spectrum in the wavelength range of 550 to 600 nm. It is clear from Fig. 7.12(c) that the emission maxima at 573 nm gets narrower as the value of x increases in the matrix. This is because the electrostatic field (crystal

field) around rare-earth dopant ions in the host matrix affects the shape and the width of the emission line. The closer the sizes of the ionic radius of the host and the dopant, the stronger the crystal field strength affects the dopant ions and smaller will be the bandwidth of the emission spectra [2, 48, 49]. As discussed in the XRD data, the ionic radius of Y^{3+} (0.1075 nm) is similar to that of Dy^{3+} (0.1083 nm) compared to that of La^{3+} (0.1216 nm) [10, 14]. Therefore, Dy^{3+} ions substituted in Y^{3+} lattice sites will experience greater crystal field effect than Dy^{3+} ions substituted in La^{3+} lattice sites.

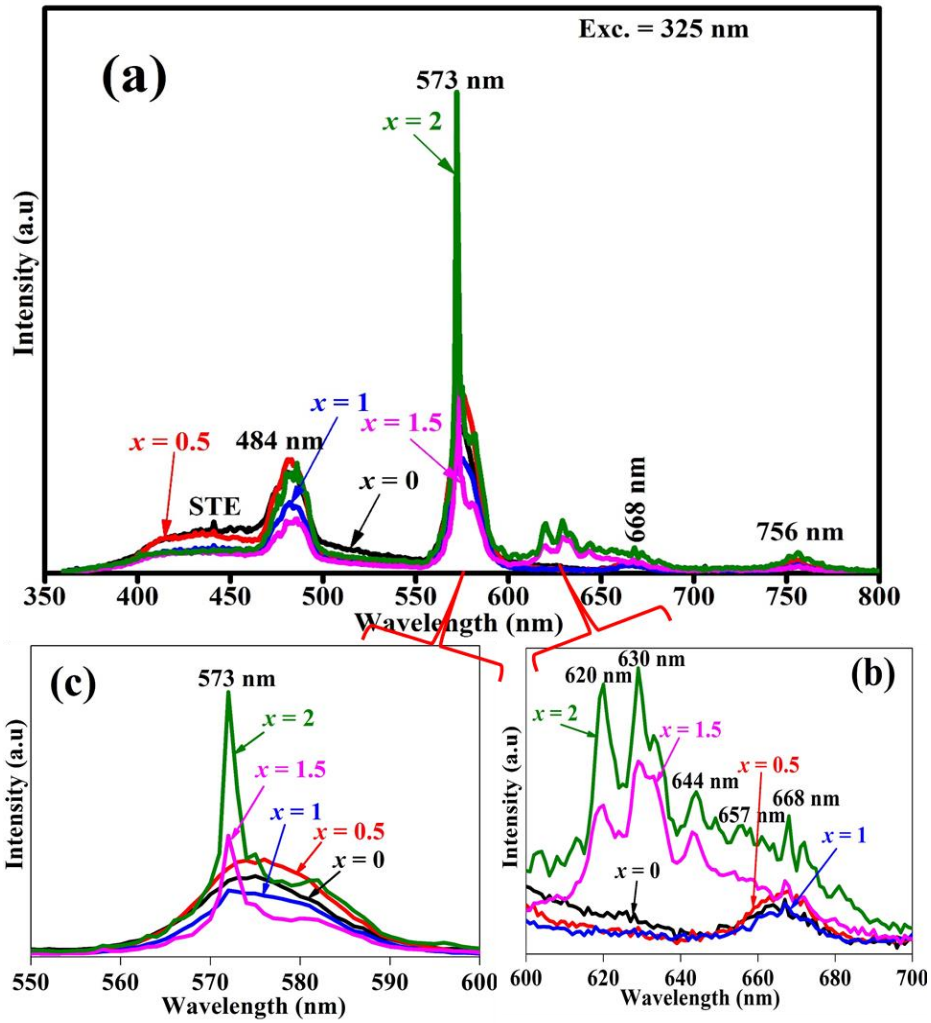

Fig. 7.12: (a) The emission spectra of $La_{2-x}Y_xSiO_5$:$_{0.25}Pr^{3+}$, $_{0.25}Dy^{3+}$ (x = 0, 0.5, 1, 1.5 and 2) under 325 nm He-Cd laser excitation, (b) the magnified spectra in the 500 to 600 nm spectral range and (c) the magnified spectral in the 600 to 700 nm range.

The varied emission properties for different molar ratios of La and Y, particularly the changes of the relative emission intensity observed at 460, 484 and 573 nm is a direct indication that the emitted colours of $La_{2-x}Y_xSiO_5$: $_{0.25}Pr^{3+}$, $_{0.25}Dy^{3+}$ (x = 0, 0.5, 1, 1.5, 2) can be tuned in a controllable manner as confirm by the CIE (x, y) colour coordinates of the phosphors. The CIE chromaticity varies from bluish-white through white to yellowish emission as the ratio of La and Y were varied in $La_{2-x}Y_xSiO_5$: $_{0.25}Pr^{3+}$, $_{0.25}Dy^{3+}$ matrix as shown in Fig. 7.13(a-d) for the samples excited with UV (223 and 229 nm), at 294 nm, 349 nm and 325 nm respectively. The correlated colour temperature (CCT) specifies the appearance of colour emitted by a lamp in comparison with a referenced light source heated to a certain temperature. The CCT of the phosphors were calculated using the McCamy empirical formula [50, 51] given by

$$CCT = -473n^3 + 3601n^2 - 6861n + 5514.31 \quad (7.6)$$

where $n = (x - x_e)/(y - y_e)$ with x_e = 0.3320 and y_e = 0.1858 is the chromaticity epicenter. The calculated CCT values and the corresponding CIE (x, y) coordinates for the phosphors are shown in table 7.2.

Table 7.2. CIE chromaticity coordinates and CCT values of $La_{2-x}Y_xSiO_5$:$_{0.25}Pr^{3+}$, $_{0.25}Dy^{3+}$ (x = 0, 0.5, 1, 1.5, and 2) phosphors under UV, 294 nm, 349 nm and 325 nm He-Cd laser excitation.

$La_{2-x}Y_xSiO_5$: $_{0.25}Pr^{3+}$, $_{0.25}Dy^{3+}$	Chromaticity coordinates (x, y)/ CCT (K)			
	UV	294 nm	349 nm	325 nm
x = 0	-	(0.237, 0.224)/51569	(0.239, 0.218)/65897	(0.313, 0.333)/ 6461
x = 0.5	-	(0.197, 0.144)/6195	(0.207, 0.160)/7102	(0.337, 0.353)/ 5312
x = 1	(0.188, 0.087)/1811	(0.213, 0.181)/2393704	(0.240, 0.207)/138818	(0.339, 0.357)/ 5240
x = 1.5	(0.301, 0.252)/9562	(0.242, 0.154)/5034	(0.215, 0.171)/35397	(0.380, 0.380)/ 4032
x = 2	(0.353, 0.343)/4661	(0.352, 0.228)/3025	(0.294, 0.271)/9329	(0.394, 0.408)/ 3871

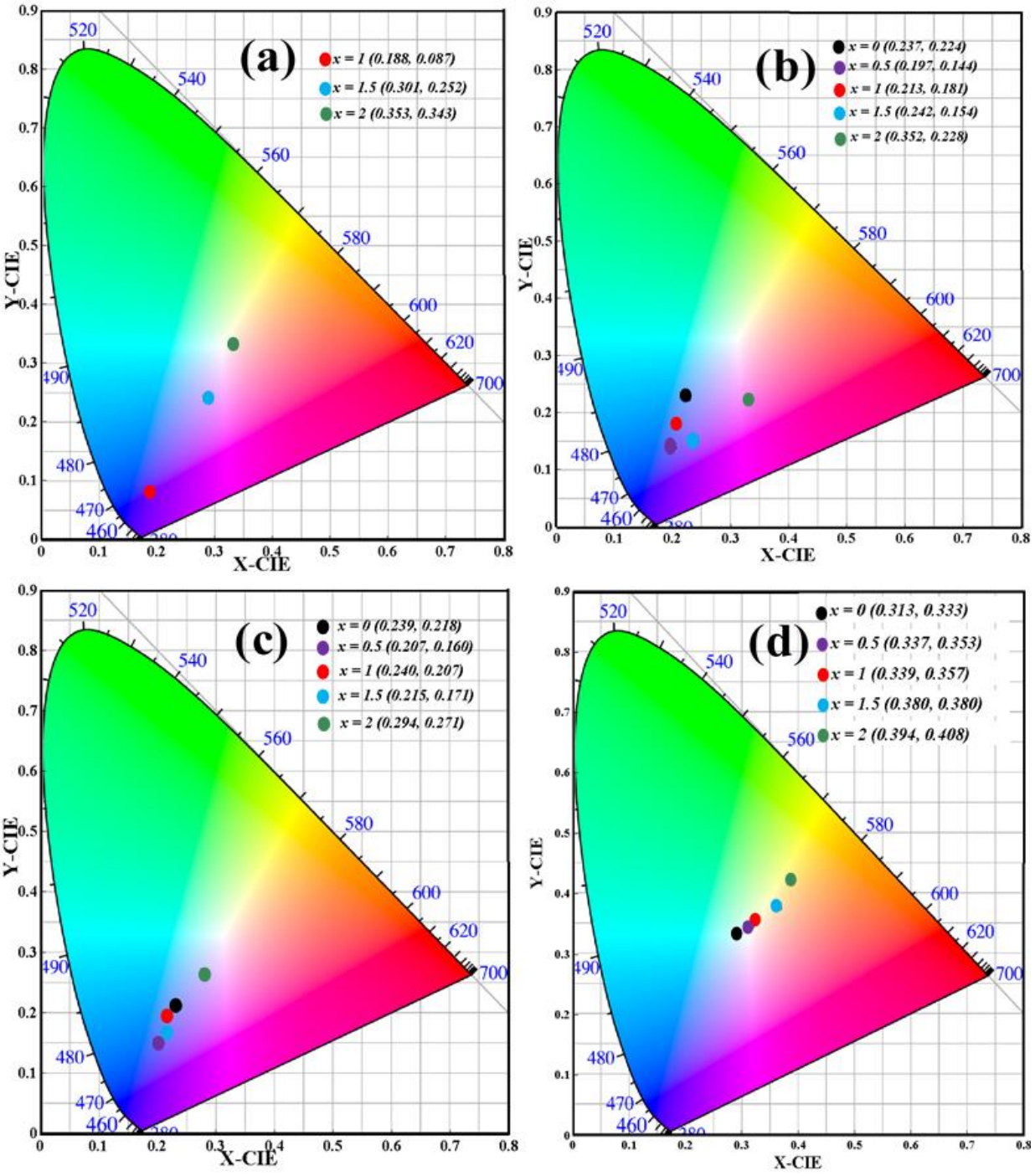

Fig. 7.13: CIE coordinates of $La_{2-x}Y_xSiO_5:_{0.25}Pr^{3+}$, $_{0.25}Dy^{3+}$ (x = 0, 0.5, 1, 1.5, and 2) phosphors under (a) UV (229 and 223 nm) excitation (b) 294 nm excitation (c) 349 nm excitation and (d) 325 nm He-Cd laser excitation.

7.4. Conclusion

The molar ratio of single and mixed host lanthanum and yttrium rare-earth oxyorthosilicate phosphors varied in the following manner: $La_{2-x}Y_xSiO_5$ (x = 0, 0.5, 1, 1.5, 2), (where x = 0 (pure La_2SiO_5) x = 2 (pure Y_2SiO_5) and x = 0.5, 1, and 1.5 are the admixtures of the two compounds) and co-doped with 0.25% Pr^{3+} and 0.25% Dy^{3+} were successfully prepared using urea-assisted combustion method. The change in phase due to the admixture of these two compounds as confirmed by the XRD data was further confirmed by the change in optical properties of the phosphors. The variable optical properties due to the change in the band gaps resulted in a different behaviour in the emission of Pr^{3+} and Dy^{3+} in the host matrices. The position of the 4f5d state of Pr^{3+} relative to the 4f levels of Pr^{3+} and Dy^{3+} in the hosts played major role on the luminescence properties of the phosphors. Our study showed that the 4f5d state of Pr^{3+} lie closer to the 4f levels of Pr^{3+} and Dy^{3+} in the sample when x = 2 (Y_2SiO_5) and further away from the 4f5d state as x decreases from 2 to 0 (La_2SiO_5). This is clear indication that Y_2SiO_5 exerted greater crystal field on the dopants than La_2SiO_5. The tunable colour emission observed when the phosphors were excited at different wavelengths suggest that they can be a promising material for white light and other display applications.

7.5. References

[1] B. Henderson, R. Bartram, Crystal-field engineering of solid-state laser materials, Cambridge University Press, New York (2000) p. 253.

[2] E.A. Fidancev, J. Hölsä, M. Lastusaari, A. Lupei, Phys. Rev. B 64 (2001) 195108.

[3] a) J.L. Sommerdijk, A. Bril, A.W. de Jager. J. Lumin. 8 (1974) 341. b) W.W. Piper, J.A. de Luca, F.S. Ham, J. Lumin. 8 (1974) 344.

[4] F. You, S. Huang, C. Meng, D. Wang, J. Xu, Y. Huang, G. Zhang, 4f5d configuration and photon cascade emission of Pr^{3+} in solids, J. Lumin. 122–123 (2007) 58–61.

[5] G. Blasse, J.P.M. Vliet, J.W. M. Verwey, R. Hoogendam, M. Weigel, J. Phys. Chem. Solids 50 (1989) 583.

[6] J. Ganem, W.M. Denis, W.M. Yen, J. Lumin. 54 (1992) 79.

[7] E. Cavalli, L. Esposito, M. Bettinelli, A. Speghini, K.V. Ivanovskikh, R.B Hughes-Currie, M. de Jong, YAG:Pr^{3+} transparent ceramics for applications in photonics: synthesis and characterization, Mater. Res. Express 1 (2014) 045903.

[8] K. Sreebunpeng, W. Chewpraditkul, V. Babin, M. Nikl, K. Nejezchleb, Scintillation response of $Y_3Al_5O_{12}$:Pr^{3+} single crystal scintillators, Radiat. Meas. 56 (2013) 94–97.

[9] J.C. Zhang, Y H. Wang. Chin. Phys. Lett. 25 (2008) 1453.

[10] J. Felsche, The crystal chemistry of the rare-earth silicates, In, R.A. Penneman, R.R. Ryan, A. Rosenzweig, R. Reisfeld, J. Felsche, C.K. Jørgensen, "*Structure and Bonding*" Springer, Berlin 13 (1973) p. 99–197.

[11] M. Yin, C. Duan, W. Zhang, L. Lou, S. Xia, J.C. Krupa, J. Appl. Phys. 86 (1999) 3751.

[12] G.D. Dominiak, W. R. Romanowski, R. Lisiecki, P. Solarz, B. Macalik, M. Berkowski, M. Gzowacki, V. Domukhovski, Cryst. Growth Des. 10 (2010) 3522.

[13] M. Jie, G. Zhao, X. Zeng, L. Su, H, Pang, X, He, J. Xu, J. Cryst. Growth. 277 (2005) 175.

[14] R.D. Shannon, Acta. Cryst. 32 (1976) 751.

[15] S.N. Ogugua, H.C. Swart, O.M. Ntwaeaborwa, The dynamics of the photoluminescence of Pr^{3+} in mixed lanthanum yttrium oxyorthosilicate hosts, Sens. Actuators B, 250 (2017) 285–299.

[16] W.Y. Huang, F. Yoshimura, K. Ueda, W.K. Pang, B.J. Su, L.Y. Jang, C.Y. Chiang, W. Zhou, N.H. Duy, R.S. Liu, Inorg. Chem. 53 (2014) 12822.

[17] Y. Waseda, E. Matsubara, K. Shinoda, X-ray diffraction crystallography, Springer-Verlag Berlin Heidelberg (2011) p. 74.

[18] H.E. Hoefdraad, J. Inorg. Nucl. Chem. 37 (1975) 1917.

[19] P. Boutinaud, E. Pinel, M. Dubois, A.P. Vink, R. Mahiou, J. Lumin. 111 (2005) 69.

[20] J. Tauc (Ed.), The Optical Properties of Solids, Academic Press, New York (1966).

[21] G. Kortum, Reflectance Spectroscopy, Springer-Verlag, New York (1969) p. 103–169.

[22] H. Pang, G. Zhao, M. Jie, J. Xu, X. He, Mater. Lett. 59 (2005) 3539.

[23] G. Li, C. Li, C. Zhang, Z. Cheng, Z. Quan, C. Peng, J. Lin, J. Mater. Chem. 19 (2009) 8936.

[24] M. Jia, J. Zhang, S. Lu, J. Sun, Y. Luo, X. Ren, H. Song, X. Wang, Chem. Phys. Lett. 384 (2004) 193.

[25] S. Chemingui, M. Ferhi, K.H. Naifer, M. Ferid, J. Lumin. 166 (2015) 82.

[26] S.N. Ogugua, S.K.K. Shaat, H.C. Swart, O.M. Ntwaeaborwa, J. Lumin. 179 (2016) 154.

[27] T.R.N Kutty, A. Nag, J. Mater. Chem., 13 (2003) 2271.

[28] D. Jia, X.J. Wang, W.M Yen, Phys. Solid State, 50 (2008) 1674.

[29] Y. Ji, J. Cao, Z, Zhu, J. Li, Y. Wang, C. Tu, Mater. Express, 1 (2011) 231.

[30] C.H. Huang, L. Luo, Y.T. Yeh, S.M. Janga, W.R. Liu, RSC Adv. 4(2014) 5513.

[31] R. Lisiecki, G. Dominiak-Dzik, P. Solarz, W. Ryba-Romanowski, M. Berkowski, M. Glowacki, Appl. Phys. B 98 (2010) 337.

[32] G.C. Aumuller, W. Kostler, B.C. Grabmailer, R. Frey, J. Phys. Chem. Solids, 55 (1994) 767.

[33] M. Arai, N. Matsuda, M. Tamatani, J. Alloys Compd. 192 (1993) 45.

[34] K. Annapurna, R. Chakrabarti, S. Buddhudu, J. Mater. Sci. 42 (2007) 6755.

[35] K.H. Lee, K.W. Chae, C.I. Cheon, J.S. Kim, J. Korean Ceram. Soc. 48 (2011) 183.

[36] Y. Ji, J. Cao, Z. Zhu, J. Li, Y, Wang, C. Tu, Mater. Express 1 (2011) 231.

[37] C. Itoh, K. Tanimura, N. Itoh, J. Phys. C: Solid State Phys. 21 (1988) 4693.

[38] S.N. Ogugua, S.K.K. Shaat, H.C. Swart, O.M. Ntwaeaborwa, J. Phys. Chem. Sol. 83 (2015) 109.

[39] V.K. Rai, D.K. Mohanty, Appl. Phys. B 109 (2012)599.

[40] G.C. Aumuller, W. Kostler, B.C. Grabmailer, R. Frey, J. Phys. Chem. Solids, 55 (1994) 767.

[41] M. Arai, N. Matsuda, M. Tamatani, J. Alloys Compd. 192 (1993) 45.

[42] K. Annapurna, R. Chakrabarti, S. Buddhudu, J. Mater. Sci. 42 (2007) 6755.

[43] C. De Mello Donegá, A. Meijerink, G. Blasse, J. Phys. Chem. Solids, 56 (1995) 673.

[44] F. Auzel, Multiphonon processes, cross-relaxation and up-conversion in ion-activated solids, exemplified by minilaser materials, In, B. DiBartolo, V. Goldberg (Ed.) "*Radiationless processes*" Plenum Press, New York (1980) p. 213–286.

[45] L. van Pieterson, R.P.A. Dullens, P.S. Peijzel, A. Meijerink, G.D. Jones, J. Chem. Phys. 115 (2001) 9393.

[46] P.P. Pawar, S.R. Munishwar, R.S. Gedam, J. Alloy Compd. 660 (2016) 347.

[47] T. Justel, W. Mayr, P.J. Schmidt, Tuning the $4f^15d$-$4f^2$ UV emission of Pr^{3+}, 200^{th} meeting of the electrochemical society, San Francisco, CA, USA, September, (2001).

[48] A. Najar, H. Omi, T. Tawara, Nanoscale Res. Lett. 9 (2014) 356.

[49] E. Desurvier, Erbium-doped Fibre Amplifiers: principles and applications, Wiley Interscience (2002) p.218- 19, 244–245.

[50] C. S. McCamy, Color Res. Appl. 17 (1992) 142.

[51] G.A. Kumar, M. Pokhrela, A. Martinez, R.C. Dennis, I.L. Villegas, D.K. Sardara, J. Alloys Comp. 513 (2012) 559.

CH. 8

The influence of post-annealing atmospheres on the optical properties and energy transfer between Pr^{3+} and Dy^{3+} in mixed lanthanum-yttrium oxyorthosilicate hosts

8.1. Introduction

White light can be generated from Pr^{3+} and Dy^{3+} when singly doped in different host matrices [1-6]. Dy^{3+} doped materials are of particular interest because of their dual visible emissions around 468−500 nm (blueish) and 565−600 nm (yellowish) associated respectively with the $^4F_{9/2}\rightarrow{}^6H_{15/2}$ and $^4F_{9/2}\rightarrow{}^6H_{13/2}$ transitions [5]. The ratios of these two emissions can be influenced by the symmetry of the host lattice [5, 7, 8]. Visible emission from Pr^{3+} doped materials are dominated by the $^3P_0$ (blueish-green) and $^1D_2$ (red) transitions, whose intensity ratios are dependent on the crystal field strength of the host material [9].

Sensitization of phosphor materials can enhance the luminescence property of the acceptor to a very large degree [10, 11]. This occurs when a donor (activator) absorbs an external radiation and transfers it to an acceptor (sensitizer), causing the emission of the sensitizer to be greatly enhanced [12]. Energy transfer from Pr^{3+} to Dy^{3+} or vice versa have occurred in different host materials [13, 14-16]. However, in other host materials, no evident of energy transfer from either Pr^{3+} to Dy^{3+} or Dy^{3+} to Pr^{3+} were observed [17, 18]. This could be linked to the position of the 4f5d state of Pr^{3+} relative to the 4f states of Dy^{3+} in the host matrix, since energy transfer from Pr^{3+} to Dy^{3+} occurs when the 4f5d state of Pr^{3+} lies close to the 4f states of Dy^{3+} [13]. The variation observed in the gap between the 4f5d state of Pr^{3+} and 4f states of Dy^{3+} could be due to the fact that the energy difference between the 4f5d and 4f states in trivalent and divalent rare earth ions increases with decreasing crystal field strength of the host and vice versa [19].

Pr ions can occur in trivalent (Pr^{3+}) and tetravalent (Pr^{4+}) states. However, only the Pr^{3+} ions are optically active. The Pr^{4+} ions are generally non-luminescence but form luminescence quenching centers in the material [5, 20]. These centers are formed by capturing of holes from the top of the valence band by Pr^{3+} to form Pr^{4+} ($Pr^{3+} + h \rightarrow Pr^{4+}$) [21] and hence reducing the luminescence associated with the trivalent species. The Pr^{4+} ions can act as recombination centers, capturing

electron to form $(Pr^{3+})^*$ (Pr^{4+} + e Pr^{3+}), an excited state, which transits to the ground state and give characteristic emission [22].

Post-annealing can improve the crystallinity of a phosphor material and hence the luminescence [23-25]. Annealing in air can lead to the oxidation of Pr^{3+} ions to form Pr^{4+} ions, which is harmful to the luminescent. Nevertheless, Pr^{3+} doped host materials annealed in air have shown enhancement of luminescence by filling the oxygen vacancies created during synthesis [26, 27]. However, this depend on the annealing temperature [26, 28]. Annealing in reducing atmosphere on the other hand can reduce reasonable amount of Pr^{4+} ions to Pr^{3+} ions, but will create more oxygen vacancies in the material [26]. Pr doped materials annealed in reducing atmosphere have generally enhanced the luminescence compare to the samples annealed in air [26-28].

Pr doped host matrices has shown drastic change in band gap energy under different annealing conditions [29-32]. This change in band gap effects the position of the 4f5d relative to the conduction band of the host, which in turn will determine whether the 4f5d transition will be observe or not. Annealing in different atmosphere will also affect the crystal field of the host material, since it effects the amount of oxygen present in the host. This will influence the position of the 4f5d state of the Pr^{3+} relative to the 4f states of both Pr^{3+} and Dy^{3+}. In the presently work, we studied the influence of different post-annealing environment (air and Ar-H_2) on the photoluminescence properties of $La_{2-x}Y_xSiO_5$:$_{0.25}Pr^{3+}$,$_{0.25}Dy^{3+}$ (x = 0, 0.5, 1, 1.5 and 2) phosphors. We paid particular attention to the energy transfer mechanism from Pr^{3+} to Dy^{3+}, and the influence of molar ratios of the host materials (La_2SiO_5 and Y_2SiO_5) and the different post-annealing atmospheres on the energy transfer. We chose to doped the sample with 0.25 mol% of Dy^{3+} and Pr^{3+} because in our previous study [5], we obtained the best luminescent intensity from the sample doped with 0.25 mol% of Dy^{3+}. Fig. 8.1 shows the plot of mol% Pr^{3+} versus the luminescence intensities. It can be seen from Fig. 8.1 that the best luminescent intensity was attained at the 0.25 mol% Pr^{3+}. We did not dope the samples below 0.25 mol% because Zhmurin et al [33] obtained the best Pr^{3+} luminescence intensity in Y_2SiO_5 host when they doped with 0.1 mol%. Although, they observed luminescence quenching above 0.1 mol%, they did not dope below 0.1 mol%. Furthermore, the intensity they obtained at 0.1 mol% is not much higher than what they obtained at 2 mol % Pr^{3+}. Looking at Fig. 8.1, the intensity obtained at 0.25 mol% is far higher than what

was obtained at 2 mol%, hence since 0.1 and 0.25 mol% are close, we chose not to go lower to 0.25 mol%.

8.2. Experimental

8.2.1. *Sample preparation*

0.25 mol % of Pr^{3+} and Dy^{3+} co-doped $La_{2-x}Y_xSiO_5$ (x = 0, 0.5, 1, 1.5 and 2) phosphors were prepared by urea-assisted solution combustion synthesis. The starting materials were, lanthanum nitrate hexahydrate, $La(NO_3)_3.6H_2O$, yttrium nitrate hexahydrate, $Y(NO_3)_3.6H_2O$, praseodymium nitrate hexahydrate, $Pr(NO_3)_3.6H_2O$, dysprosium nitrate hexahydrate, $Dy(NO_3)_3.6H_2O$, and silicic acid, SiO_2H_2O. A stoichiometric quantity of these reagents was transfer to different beakers labeled x = 0, 0.5, 1, 1.5 and 2. A stoichiometric amount of urea, $CO(NH_4)_2$, and ammonium nitrate, NH_4NO_3, were added to each beaker and 2.0 ml of distilled water was also added. Each beaker was stirred for about 15 min using a hot plate magnetic stirrer set at 100 ^oC to obtain a homogeneous solution. The solutions were transferred to a ceramic crucible boat (cleaned with ethanol and rinsed distilled water) and immediately into a muffle furnace pre-heated to about 600$\pm$10 ^oC. Oxidation was observed in about 2 to 3 min after the crucible boat containing the solution was placed into the furnace, resulting into a crispy form-like product. The product was allowed to cool to a room temperature before it was ground into a fine powder using an agate mortar and pestle. Each set of sample was divided into three parts, and one set of the samples were post-annealed in air and the other set of the samples were annealed in Ar 95%/H_2 5% (Ar-H_2) atmosphere at 950 ^oC for 1 hr. Each set of samples were stored in a different sample holder for characterization.

8.2.2. *Characterization*

A Bruker D8 advanced X-ray diffractometer (XRD) with a monochromatic CuKα radiation of wavelength (λ) = 1.54056 Å was used to analyzed the structure of the phosphors. The electronic states, chemical compositions, and the oxidation states were analyzed using a PHI 5000 VersaProbe X-ray photoelectron spectroscopy (XPS). The ultraviolet visible (UV-vis) measurements were taken using a Lambda 950 UV-vis spectrometer. The photoluminescence (PL) spectra were measured in the steady state mode using Edinburgh instruments FLS980

spectrometer- equipped with a 450 W Xenon Lamp (Xe1) as the excitation source and the red-cooled photomultiplier tube (PMT) detector.

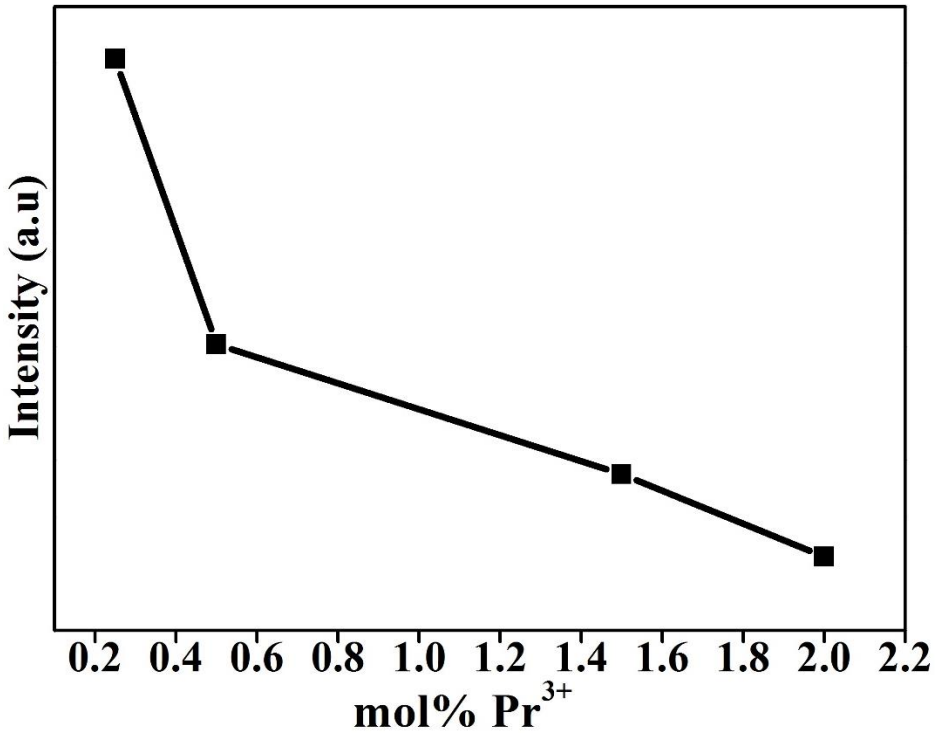

Fig. 8.1: A graph of mol% Pr^{3+} versus luminescent intensity in $LaYSiO_5$ host.

8.3. Results and discussion

Fig. 8.2(a-c) show the XRD patterns of $La_{2-x}Y_xSiO_5$:$_{0.25}Pr^{3+}$,$_{0.25}Dy^{3+}$ (x = 0, 0.5, 1, 1.5 and 2) phosphors for the as-prepared, air-annealed, and Ar-H_2-annealed samples, respectively. The XRD patterns of La_2SiO_5:$_{0.25}Pr^{3+}$,$_{0.25}Dy^{3+}$ (x = 0) and Y_2SiO_5:$_{0.25}Pr^{3+}$,$_{0.25}Dy^{3+}$ (x = 2) are consistent with the standard of the pure monoclinic phases of La_2SiO_5 and Y_2SiO_5 referenced in the JCDPS file no: 40-0234 and 74-2011, respectively. It is therefore reasonable to conclude from the XRD patterns in Fig. 8.2 that the admixtures of La_2SiO_5 and Y_2SiO_5 (x = .5, 1 and 1.5) crystallized as a mixture of the two compounds, with the patterns showing more peaks from the crystal planes of the compound with higher concentration. For instance, when x = 0.5, most of the peaks observed were from La_2SiO_5, and more peaks from Y_2SiO_5 were observed when x =1.5. The dissimilarity in the crystal planes observed from La_2SiO_5 and Y_2SiO_5 was presumed since the two compounds belong to different space group, even though they are both monoclinic. La_2SiO_5 belong to the large ionic radii rare earth ions group (P21/c space group), while Y_2SiO_5 belong to the small ionic

radii rare earth ions group (C2/c space group) [34, 35]. It is apparent that the annealed samples (especially x = 0, 0.5 and 1) are more crystalline than the as-prepared samples. This is confirmed by the higher values of the full width at half maximum (FWHM) of the as-prepared samples (calculated from the (321) peak of La_2SiO_5 and (121) peak of Y_2SiO_5) compared to the annealed samples (Fig. 8.2(d)).

The X-ray photoelectron spectroscopy (XPS) was used to determine the elemental composition, oxidation state, chemical and electronic states of elements in the surface region of the materials. Fig. 8.3(a-c) shows the O 1s fitted XPS spectra of the as-prepared, air-annealed and Ar-H_2-annealed $LaYSiO_5$:$_{0.25}Pr^{3+}$,$_{0.25}Dy^{3+}$ (x = 1) samples respectively. The spectra showed peaks from $LaYSiO_3$ (combination of La_2O_3 and Y_2O_3), SiO_x (x < 2), $LaYSiO_5$ (combination of La_2SiO_5 and Y_2SiO_5), SiO_2 and SiO_4 with binding energy positions shown in table 8.1(a). Observe that the O 1s peak intensity is highest in the air-annealed sample, followed by the as-prepared sample, while the Ar-H_2-annealed sample have the least intensity. Other studies have shown similar results [36, 37]. The reduction of O 1s peak intensity in the Ar-H_2-annealed samples indicates the removal of native oxides from the samples [36], while the enhancement of O 1s peak in the air-annealed sample indicates the oxidation of the sample [28, 36].

The XPS 3d core-level spectra of all rare earths compounds splits into $3d_{5/2}$ (J = 5/2) and $3d_{3/2}$ (J = 3/2) states because of spin-orbit splitting [38]. Fig 8.4 (a) shows the XPS spectrum of Pr 3d for the as-prepared $LaYSiO_5$: $_{0.25}Pr^{3+}$,$_{0.25}Dy^{3+}$ (x = 1). The XPS spectrum show four peaks assigned to Pr $3d_{5/3}$ (932.1 eV), energy loss line (942.6 eV), Pr $3d_{3/2}$ (952.5 eV) and O KLL (975 eV). The $3d_{5/2}$ and $3d_{3/2}$ doublets are located at the lower and higher binding energies with energy separation of 20.4 eV. The small intensity of the Pr 3d peaks in the XPS spectrum reflects the low concentration of Pr in the sample. The energy loss line originates when a photoelectron loss some energy due to its interaction with other electrons [39]. The O KLL peak is an Auger peak and it originates from the ejection of L shell electrons from the atoms owing to the filling of the O 1s state (K shell) by an electron from the L shell [40, 41]. The fitted XPS spectra of Pr $3d_{3/2}$ core-level of the as-prepared, air-annealed and Ar-H_2-annealed $LaYSiO_5$: $_{0.25}Pr^{3+}$,$_{0.25}Dy^{3+}$ (x = 1) samples are shown in Fig. 8.4(b-d). Each spectrum consists two pairs of peaks belonging to Pr^{3+} species (e.g. Pr_2O_3 and $Pr(OH)_3$) and Pr^{4+} species (e.g. PrO_2 and Pr_6O_{11}) [9, 42], with the Pr^{3+} species lying in lower binding energies compared to the Pr^{4+} species. The binding energy positions and the corresponding

Pr species are summarized in table 8.1(b). Observe from Fig. 8.4(b-d) that the average area of Pr^{3+} and Pr^{4+} peaks in the air-annealed sample, Fig. 8.3(c), are almost the same. Moreover, the average area of Pr^{3+} is higher than that of Pr^{4+} in the as-prepared sample, Fig. 8.4(b), and even more in the Ar-H_2-annealed sample, Fig. 8.4(d). This is an indication that more Pr^{3+} were oxidized to Pr^{4+} in the air-annealed samples compare to the as-prepared and Ar-H_2-annealed samples [42]. The broad XPS peaks observed in the lower binding energy and the small peak at the higher binding energy in Fig. 8.4(b-d) are assigned to energy loss lines [39, 43]. The energy loss lines were observed at 942.6 and 959.7 eV for the as-prepared sample, 942.1 and 959.2 eV for the sample annealed in air and at 941. 9 and 959 eV for the samples annealed Ar-He.

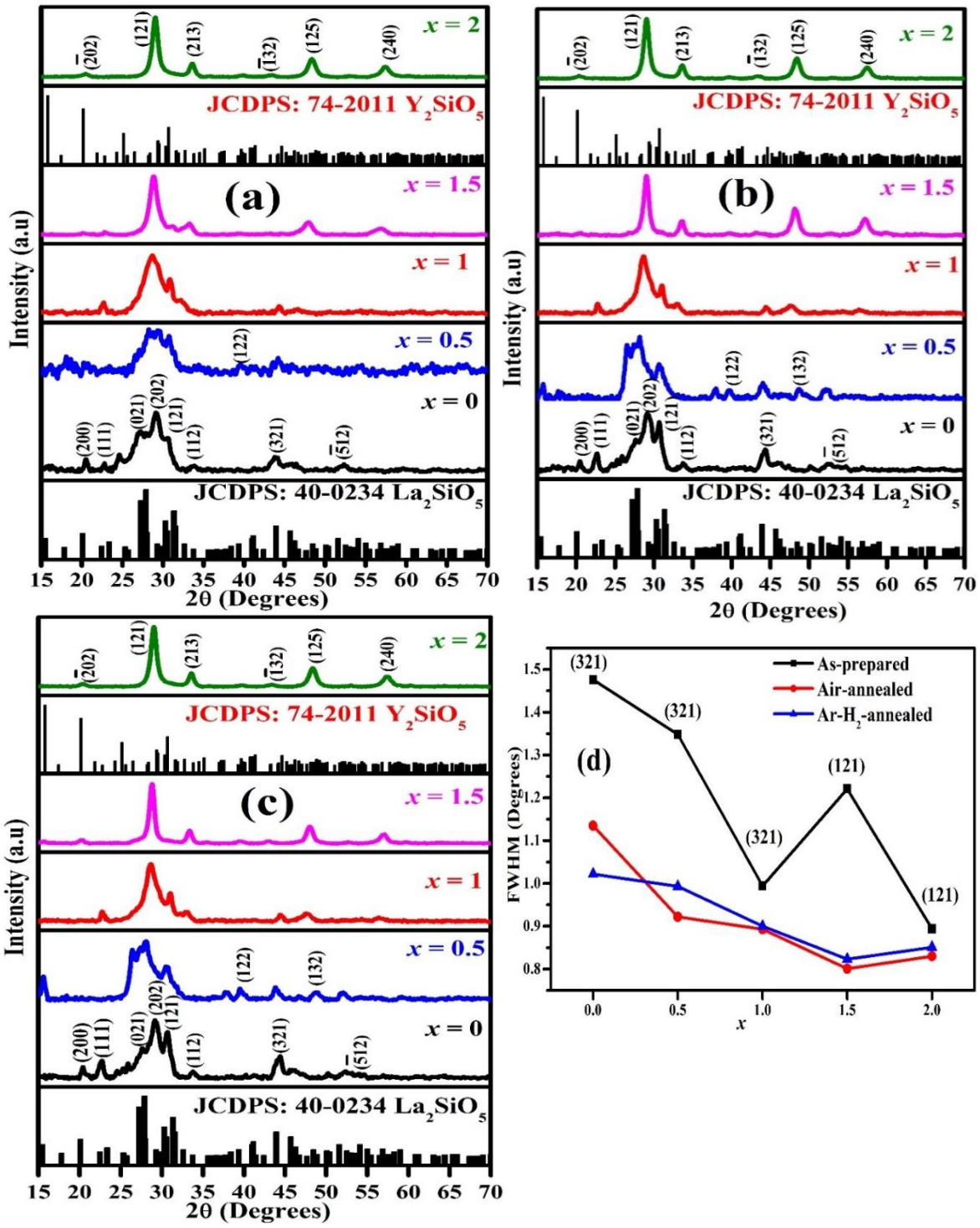

Fig. 8.2: XRD patterns of the (a) as-prepared, (b) air-annealed, and (c) Ar-H_2-annealed $La_{2-x}Y_xSiO_5$:$_{0.25}Pr^{3+}$,$_{0.25}Dy^{3+}$ (x = 0, 0.5, 1, 1.5 and 2) phosphors. (d) a graph of the FWHM against x for the as-prepared, air-annealed and Ar-H_2-annealed samples.

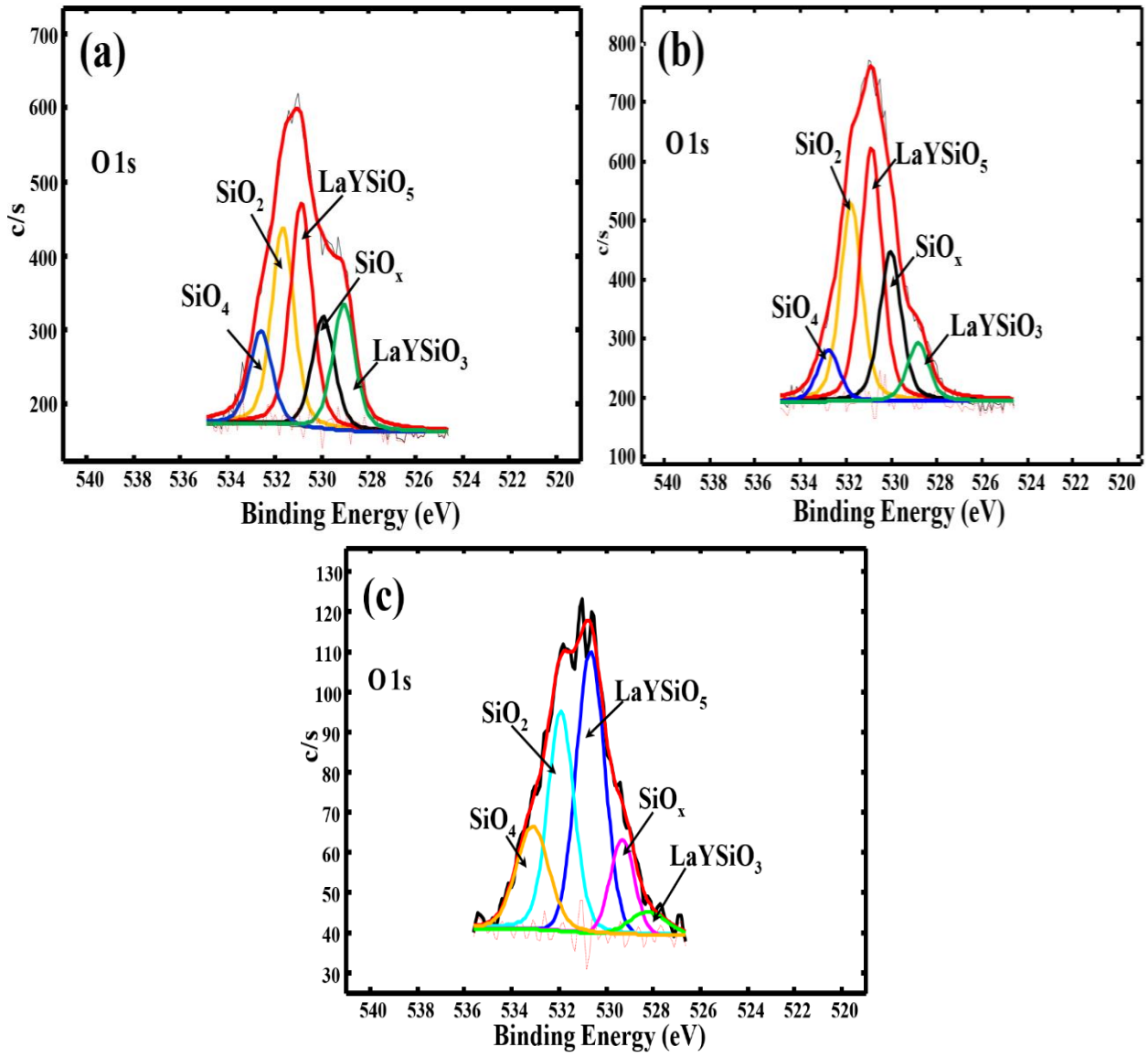

Fig. 8.3: Fitted O 1s XPS spectra of the (a) as-prepared, (b) air-annealed, and (c) Ar-H_2-annealed peaks for $LaYSiO_5$: $_{0.25}Pr^{3+}$,$_{0.25}Dy^{3+}$ (x = 1) phosphors.

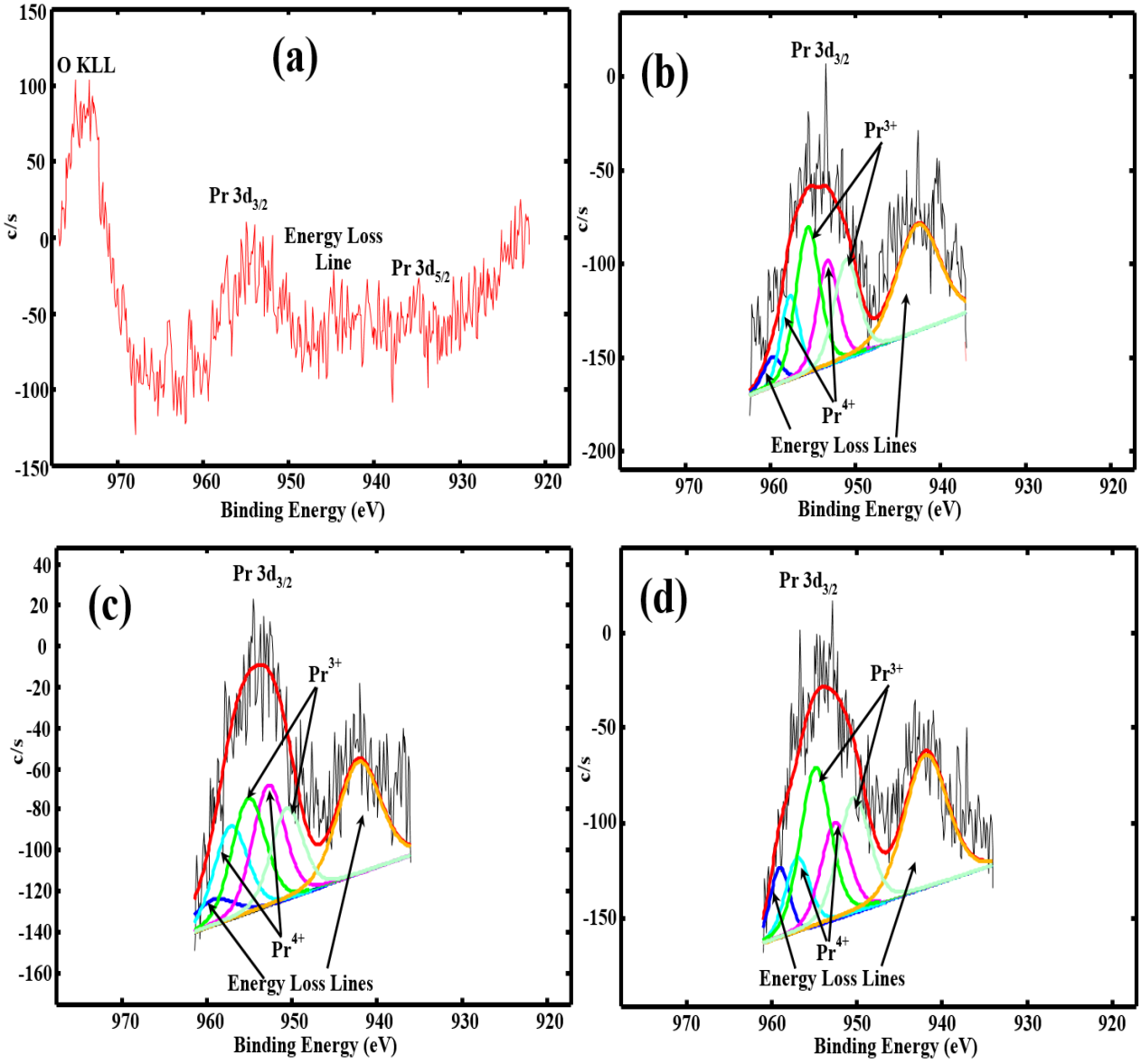

Fig. 8.4: Fitted Pr 3d XPS spectra of the (a) as-prepared, air-annealed, and Ar-H_2-annealed from $LaYSiO_5$: $_{0.25}Pr^{3+}$,$_{0.25}Dy^{3+}$ (x = 1) phosphors.

Table 8.1: The binding energy positions and the corresponding chemical states for (a) O 1s and (b) Pr $3d_{3/2}$ XPS peaks from $LaYSiO_5$: $_{0.25}Pr^{3+}$,$_{0.25}Dy^{3+}$ (x = 1) phosphors.

Chemical state	Binding energy (eV)		
	As-prepared	Air-annealed	Ar-H_2-annealed
(a)			
$LaYSiO_3$	529.1	528.8	528.3
SiO_x (x < 2)	529.9	530.0	529.4
$LaYSiO_5$	530.9	530.9	530.4
SiO_2	531.7	531.8	532.0
SiO_4	532.6	532.8	533.2
(b)			
Pr^{3+} (Pr_2O_3)	951.0	950.5	950.3
Pr^{4+} (PrO_2)	953.2	952.7	952.5
Pr^{3+} (Pr_2O_3)	955.6	955.1	954.8
Pr^{4+} (PrO_2)	957.6	957.2	956.9

The XPS 3d core-level spectrum of La is complicated compare to that of Pr, because the $3d_{5/2}$ and $3d_{3/2}$ states (with spin-orbit splitting of 16.8 eV) split into two final states I and II as depicted in Fig. 8.5(a). The final states I and II are respectively assigned to a core hole state, $3d^14f^0$ and a core hole state, $3d^1f^1$, with an electron transferred from the O 2p valence band to an empty 4f orbital. The final state I is assigned to La-O bond in La_2O_3, while the final state II is ascribed to the La-OH bond in $La(OH)_3$. The final states II, due to electron-hole exchange, splits into two J states, J = 1 (with a strong signal) and J ≠ 1 (with a weak signal). The two broad peaks observed around 848.2 and 863.5 eV are assigned to energy loss lines [39, 44-46]. The binding energies corresponding to each state are shown in table 8.2(a). The I and II final states are due to the two La sites in La_2SiO_5 [9] as depicted in Fig. 8.5(a & c). Fig. 8.5(c) shows the crystal structure of La_2SiO_5, depicting the two La sites, La1 and La2, coordinated by nine and seven oxygen atoms respectively [5]. The I and II final states could be assigned to the La2 and La1 sites respectively. La1 site is expected to have higher binding energy than La2, since it is coordinated by higher number of oxygen atoms [47].

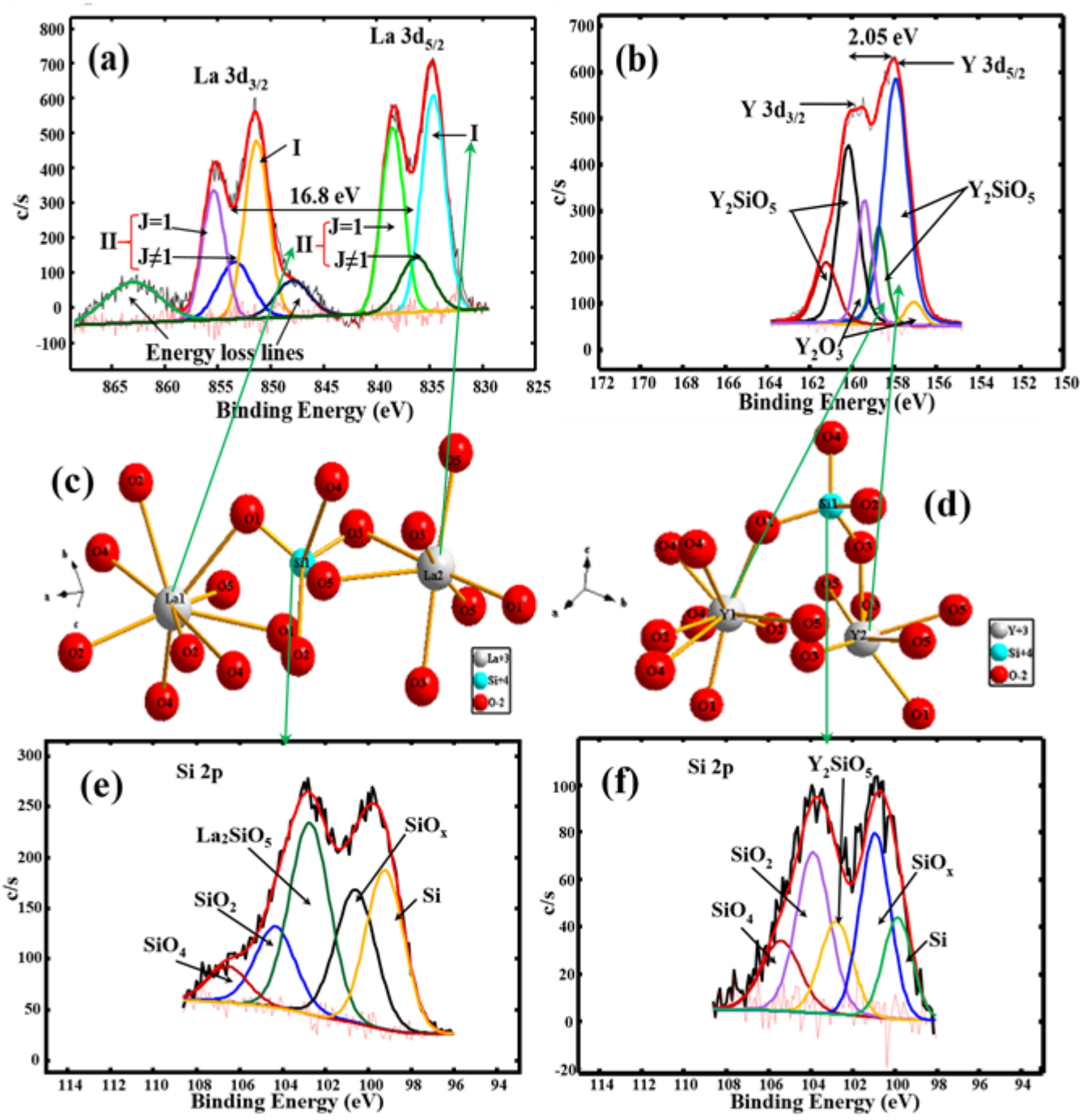

Fig. 8.5: Fitted XPS spectra of (a) La 3d peak, (b) Y 3d peak, (e) Si 2p peak from La_2SiO_5, (f) Si 2p peak from Y_2SiO_5, and the crystal structures of (c) La_2SiO_5, and (d) Y_2SiO_5.

Fig. 8.5(b) shows the XPS spectrum of Y 3d core-level. The $3d_{5/2}$ and $3d_{3/2}$ are separated by spin-orbit splitting of 2.05 eV. Two peaks belonging to Y-O bonds in Y_2O_3 and four peaks belonging to Y-O bonds in Y_2SiO_5 were observed in the spectra. The binding energy position for each photoemission peak is shown in table 8.2(b). The two sets of Y_2SiO_5 peaks observed at the higher and lower binding energies belong to the two Y sites (Y1 and Y2) in Y_2SiO_5 respectively [48], as shown in Fig. 8.5(d).

The Si 2p XPS spectra of La_2SiO_5 and Y_2SiO_5 are shown in Fig. 8.5(e & f) respectively. Five photoemission peaks belonging to Si, SiO_x (x<2), SiO_2 and SiO_4 were observed from both spectra as shown in Fig. 8.5(e & f). Other peaks belonging to La_2SiO_5 and Y_2SiO_5 were also observed as shown in Fig. 8.5(e & f), respectively. The binding energies belonging to these peaks are shown in table 8.2(c & d) for La_2SiO_5 and Y_2SiO_5, respectively. The Si 2p photoemission spectra emanated from the tetrahedra SiO_4 as shown in Fig. 8.5(c & d).

Table 8.2: The binding energy positions and the corresponding chemical states for (a) La 3d peak, (b) Y 3d peak, (c) Si 2p peak from La_2SiO_5, and (d) Si 2p peak from Y_2SiO_5.

Energy level	Chemical state	Binding energy (eV)	Energy level	Chemical state	Binding energy (eV)
(a)			**(b)**		
La $3d_{5/2}$	La_2O_3	834.0	Y $3d_{5/2}$	Y_2O_3	157.0
La $3d_{5/2}$	$La(OH)_3$	836.1	Y $3d_{5/2}$	Y_2O_5	157.9
La $3d_{5/2}$	$La(OH)_3$	837.8	Y $3d_{5/2}$	Y_2O_5	158.7
La $3d_{3/2}$	La_2O_3	850.8	Y $3d_{3/2}$	Y_2O_3	159.4
La $3d_{3/2}$	$La(OH)_3$	853.1	Y $3d_{3/2}$	Y_2O_5	160.2
La $3d_{3/2}$	$La(OH)_3$	855.0	Y $3d_{3/2}$	Y_2O_5	161.2
(c)			**(d)**		
Si 2p	Si	99.2	Si 2p	Si	99.9
Si 2p	SiO_x (x<2)	100.6	Si 2p	SiO_x (x<2)	100.9
Si 2p	La_2SiO_5	102.7	Si 2p	Y_2SiO_5	102.8
Si 2p	SiO_2	104.3	Si 2p	SiO_2	103.9
Si 2p	SiO_4	106.5	Si 2p	SiO_4	105.4

Since the signal intensity from the excitation spectrum reflects the difference in the photons absorbed as a function of wavelength, it is expected that the excitation and absorption spectra

should be identical for the molecule responsible for the luminescence. Therefore, a match of absorption and excitation spectra of a given sample is an evidence of the same absorbing and luminescence species. On the other hand, the absorption and excitation spectra will not match if the molecule responsible for absorption is different from the molecule causing the luminescence [49]. For a non-absorbing material, 100% of the incident radiant energy will be reflected. However, for a reflecting material that selectively absorbs some of the primary excitation energy, the reflectance spectrum deviates from that of the incident radiation [50]. UV-vis diffuse reflectance shows the reflectance and absorption of a material in the ultraviolet-visible spectral region. Fig. 8.6(a-c) shows the UV-vis diffuse reflectance spectra of $La_{2-x}Y_xSiO_5$:$_{0.25}Pr^{3+}$,$_{0.25}Dy^{3+}$ for the as-prepared samples, air-annealed and Ar-H_2-annealed samples in the spectral range of 200-800 nm, respectively. The absorption band in the lower wavelength around 211-220 nm is assigned to band-to-band absorption [51]. The broad absorption band starting from around 620 nm with maxima at 376 nm is due to the $O^{2-}\rightarrow Pr^{4+}$ charge transfer band (CTB). Fig. 8.6(d) shows the diffuse reflectance of $LaYSiO_5$:Pr^{3+} and $LaYSiO_5$:Dy^{3+}. Notice from Fig. 8.6(d) that the absorption band at 376 nm was observed only in the sample doped with Pr^{3+} and not in the sample doped with Dy^{3+}. This confirms that the absorption band at 376 nm is Pr related, mainly due to the $O^{2-}\rightarrow Pr^{4+}$ CTB [28]. The CTB basically introduce extra energy level due to the $4f^1$ (Pr^{4+} state) electrons sitting between the O^{2-} valence band and the host conduction bands [32]. Comparing the diffuse reflectance of the as-prepared samples, Fig. 8.6(a), and the air-annealed samples, Fig. 8.6(b), it can be seen that the samples that are air-annealed tend to oxidize more Pr^{3+} to Pr^{4+} and hence increase the absorption band at 376 nm. As expected, Ar-H_2-annealing caused reduction of Pr^{4+} to Pr^{3+}, which is shown by the decrease of the 376 nm absorption band in Fig. 8.6(c).

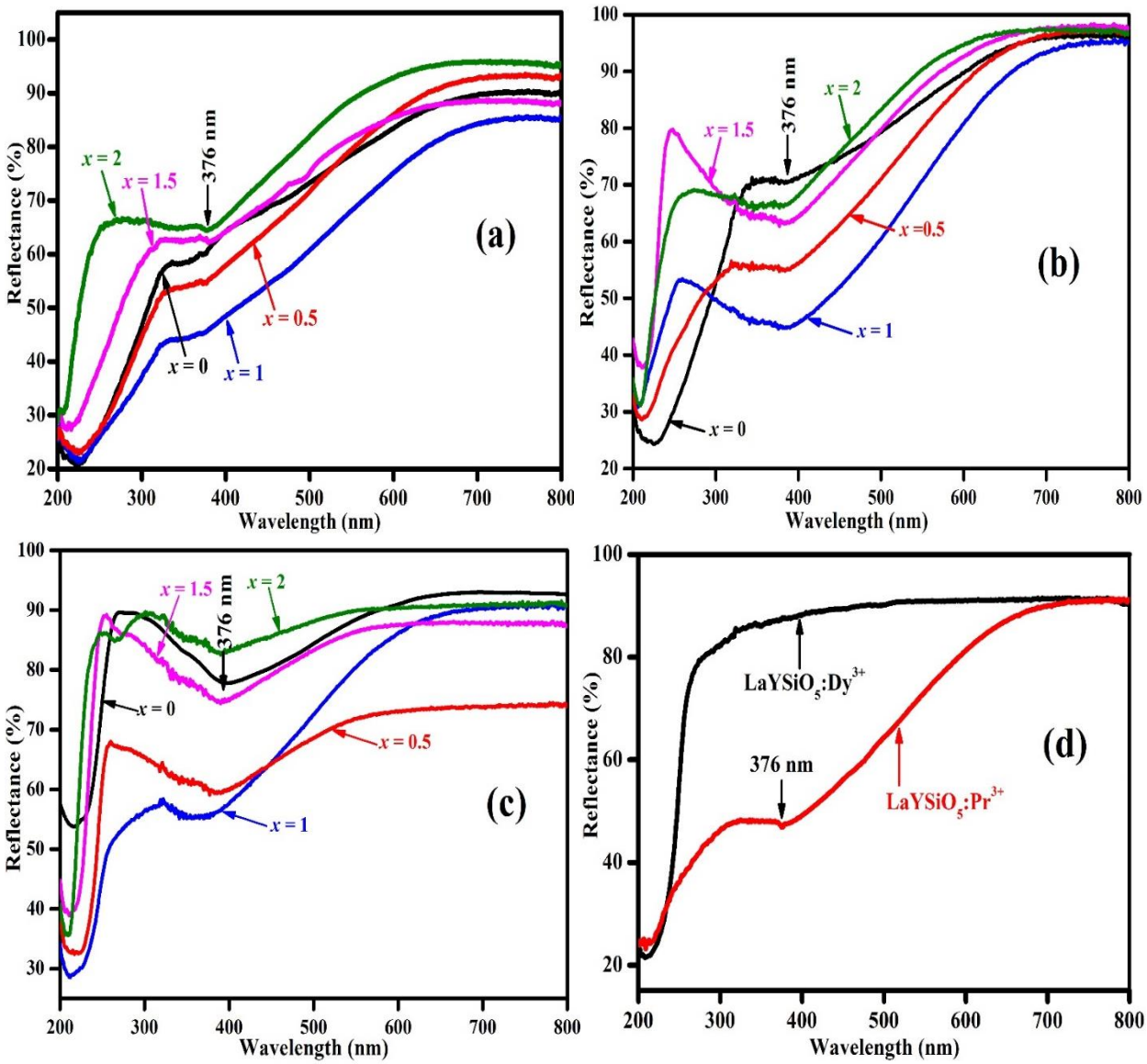

Fig. 8.6: Diffuse reflectance spectra of (a) as-prepared, (b) air-annealed, and (c) Ar-H_2-annealed $La_{2-x}Y_xSiO_5$:$_{0.25}Pr^{3+}$,$_{0.25}Dy^{3+}$ (x = 0, 0.5, 1, 1.5 and 2) phosphors. (d) compares the reflectance of $LaYSiO_5:Dy^{3+}$ and $LaYSiO_5:Pr^{3+}$.

The optical band gap of a material can be determined from the diffuse reflectance curve using the Tauc equation and the Kubelka-Munk function. These two functions are related by Eq. (8.1)

$$(F(R_\infty)h\nu)^{1/n} = A(h\nu - E_g) \tag{8.1}$$

where $F(R_\infty)$ is the Kubelka-Munk function [52, 53] given by Eq. (8.2)

$$F(R_\infty) = \left(\frac{(1-R_\infty)^2}{2R_\infty} \right) \tag{8.2}$$

where R_∞ is the reflectance of a semi-infinite medium. $F(R_\infty)$ is directly proportional to the absorption coefficient (α) of the material [53]. h is Planck's constant, v is the frequency of vibration, n can be 1/2, 3/2, 2 or 3 depending on the nature of the transition, A is proportionality constant and is the band gap of the material. For a finite medium with 100 % reflectance, $R_\infty = R_{100}$, hence Eq. (8.1) can be written as

$$(F(R_{100})h\nu)^{1/n} = A(h\nu - E_g) \tag{8.3}$$

The band gap can be extrapolated from the graph of $[F(R_{100})h\nu]^{1/2}$ against $h\nu$ as shown in Fig. 8.7(a-c) for the as-prepared, air-annealed and Ar-H_2 annealed $La_{2-x}Y_xSiO_5$:$_{0.25}Pr^{3+}$,$_{0.25}Dy^{3+}$ (x = 0, 0.5, 1, 1.5 and 2) phosphors respectively. The estimated values of the band gaps are shown in table 8.3. It can be seen from the table that there is a general increment in the values of the band gap of the air-annealed samples compare to the as-prepared samples. A further increment in the band gap is observe in the Ar-H_2-annealed samples. Studies have shown that the oxidation of trivalent (R^{3+}) to tetravalent (R^{4+}) rare earth ions [31, 32, 54] and oxygen vacancy formation can reduce the band gap of a material [55]. The band gap narrowing could be due to the formation of oxygen defects and Pr 4f levels below the conduction band minimum. The localized band states formed by the 4f electrons and the oxygen vacancies levels restrict the maximum electronic transitions to the conduction band [56]. As stated earlier, air annealing will lead to decrease in the oxygen vacancies, but will oxidize more Pr^{3+} to Pr^{4+}. However, annealing in reducing atmosphere (Ar-H_2) will create more oxygen vacancies in the material, but will reduce a number of Pr^{4+} to Pr^{3+}. Therefore, it is reasonable to conclude that the increment in the band gap for the air-annealed and Ar-H_2-annealed samples are due to filling of the oxygen vacancies and conversion of Pr^{4+} to Pr^{3+} respectively. Furthermore, since these two processes (air-annealing and Ar-H_2-annealing) lead to an increase in the band gap and favour formation of Pr^{4+} and oxygen vacancies, respectively, which causes a decrease in the band gap. It is worth mentioning that there will be an opposing effect between these two processes on the band gap, one increasing and the other decreasing the band gap. It can also be seen from table 8.3 that both processes (air annealing and Ar-H_2 annealing) have more effect on the band gaps of the samples with high ratio of La_2SiO_5 (x = 0 and 0.5) than those with high

ratio of Y_2SiO_5 (x = 1.5 and 2). These effects can be explained by looking at the energy required to form an oxygen vacancy (formation energy) in these two compounds.

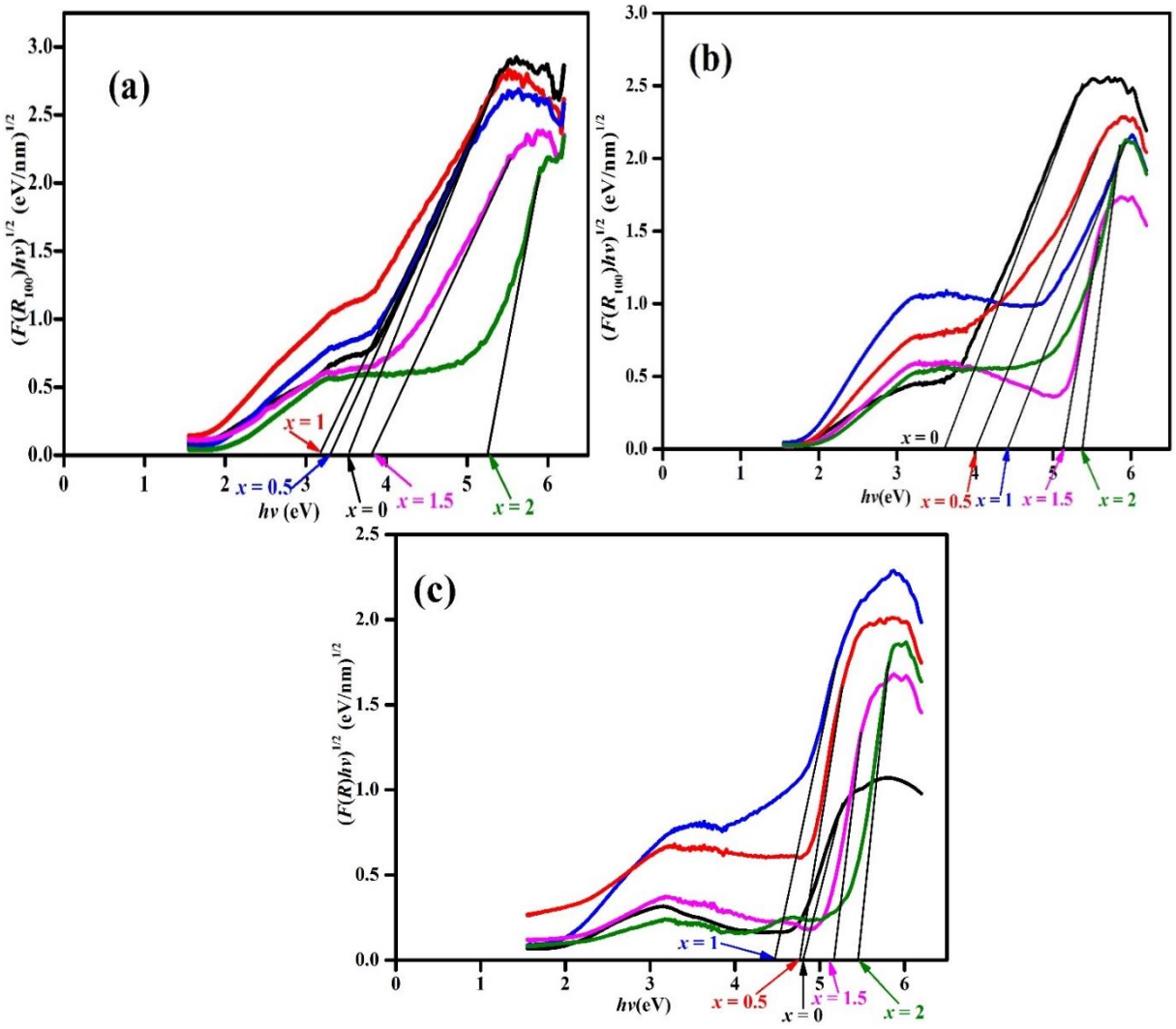

Fig. 8.7: Band gaps graphs of (a) as-prepared, (b) air-annealed, and (c) Ar-H_2-annealed $La_{2-x}Y_xSiO_5$:$_{0.25}Pr^{3+}$,$_{0.25}Dy^{3+}$ (x = 0, 0.5, 1, 1.5 and 2) phosphors.

Table 8.3: Estimated band gap values for the as-prepared, air-annealed, and Ar-H_2-annealed $La_{2-x}Y_xSiO_5$:$_{0.25}Pr^{3+}$,$_{0.25}Dy^{3+}$ (x = 0, 0.5, 1, 1.5 and 2) phosphors.

$La_{2-x}Y_xSiO_5$:$_{0.25}Pr^{3+}$, $_{0.25}Dy^{3+}$	E_g (eV) As-prepared	E_g (eV) Annealed in air	E_g (eV) Annealed in Ar-H_2
x = 0	3.52	3.60	4.82
x = 0.5	3.29	4.00	4.76
x = 1	3.17	4.22	4.47
x = 1.5	3.81	5.13	5.17
x = 2	5.24	5.38	5.46

Fig. 8.8(a) shows the crystal structure of R_2SiO_5 (R = La or Y). R_2SiO_5 consists of SiO_4 tetrahedra and two R sites (R1 and R2) coordinated by 9 and 7 oxygen atoms, respectively. The oxygen sites consist of five distinct oxygen atoms, namely O1 to O5. O1 to O4 atoms are linked to the SiO_4 tetrahedra while the O5 atoms are bonded to only four R atoms forming O5-R4 tetrahedra [57] as shown in Fig. 8.8(b). The formation energy (E_i^f) can be used to determine the preferred vacancy site in each element. Studies have shown that the two R sites (Y1 and Y2) in Y_2SiO_5 have close formation energies. However, the values of the formation energies of the oxygen sites are close for the O1 to O4 sites (7.02−7.14 eV), but is roughly 10 % higher for the O5 site (7.88 eV) [58] (see table 8.4). Hence, more O vacancies are expected to be formed from the oxygen sites O1 to O4 and not from the O5 sites. Although the energy required to break the Si-O bond is higher than that of Y-O, the energy required to break the four Y-O bonds near V_{O5} is higher than the energy required to break one Si-O bond [58]. There is no literature on the formation energies of the lattice sites in La_2SiO_5. However, formation energy for any site in a material is inversely proportional to the bond lengths [59]. Table 8.5 compares the bond length of each site in La_2SiO_5 and Y_2SiO_5. It is apparent that the bond lengths of the sites in La_2SiO_5 are on average longer than the bond lengths of the sites in Y_2SiO_5. This suggests that the formation energies of the lattice sites in Y_2SiO_5 are on average higher than that in La_2SiO_5. The implications of this is that the O1 to O4 atoms on the lattice sites of La_2SiO_5 are likely to form vacancies compare to those of Y_2SiO_5 during synthesis and post-annealing processes. Therefore, it is reasonable to conclude that the rigorous changes observed in the band gaps of the samples with higher ratio of La_2SiO_5 (x = 0 and 0.5) is due to the lower formation energies of O1 to O4 lattice sites in La_2SiO_5 compare to those of Y_2SiO_5.

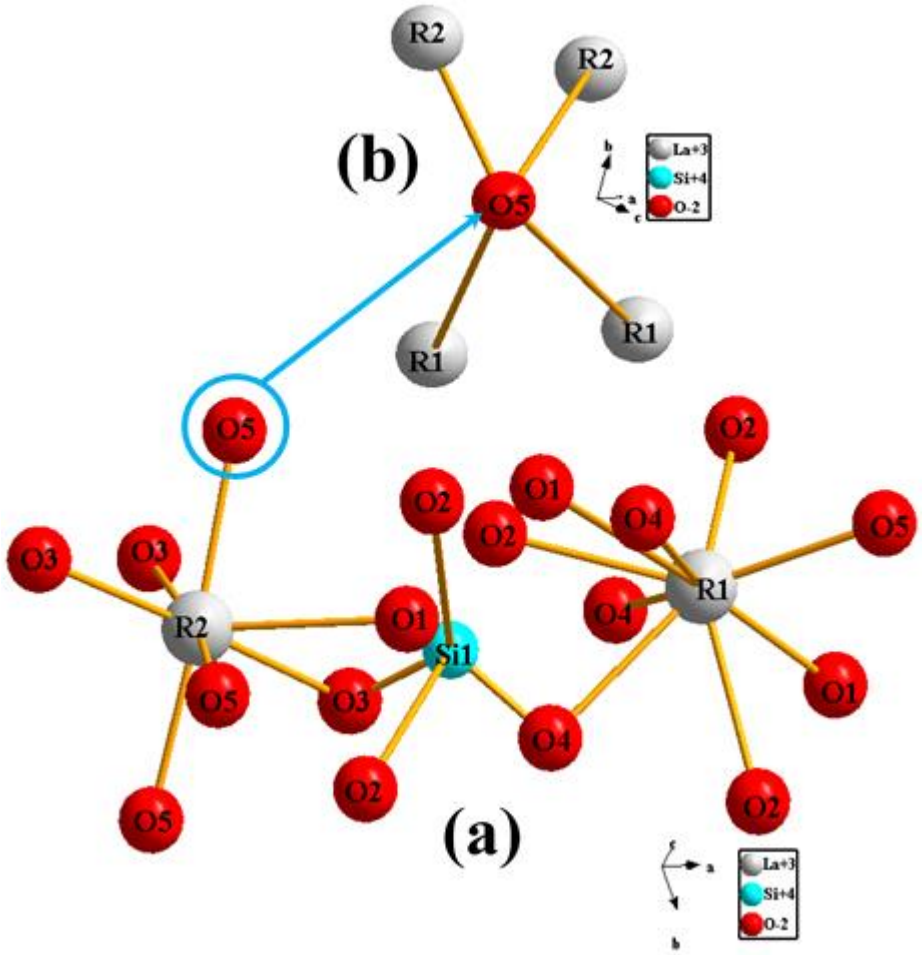

Fig. 8.8: (a) The crystal structure of R_2SiO_5 (R = La or Y) and (b) O5 atom, showing how the atoms are bonded.

Table 8.4: The values of the formation energies of the oxygen sites in O1 to O4 sites compare to the O5 site in Y_2SiO_5 [58].

Species	V_{O1}	V_{O2}	V_{O3}	V_{O4}	V_{O5}	V_{Y1}	V_{Y2}	V_{Si}
E_i^f (eV)	7.02	7.14	7.06	7.06	7.88	13.53	13.57	13.28

Table 8.5: The bond lengths of each site in La_2SiO_5 and Y_2SiO_5.

Nuclear	d (nm)	Nuclear	d (nm)	Nuclear	d (nm)	Nuclear	d (nm)
La1–O1	0.2654	La2–O1[f]	0.2676	Y1–O1	0.2391	Y2–O1[f]	0.2421
La1–O1[a]	0.2370	La2–O3	0.2575	Y1–O1[a]	0.2201	Y2–O3	0.2541
La1–O2	0.2666	La2–O3[f]	0.2656	Y1–O2	0.2611	Y2–O3[f]	0.2562
La1–O2[b]	0.2618	La2–O3[g]	0.2489	Y1–O2[b]	0.2451	Y2–O3[g]	0.2342
La1–O2[c]	0.2516	La2–O5	0.2324	Y1–O2[c]	0.2461	Y2–O5	0.2342
La1–O4[d]	0.3055	La2–O5[h]	0.2506	Y1–O4[d]	0.2561	Y2–O5[h]	0.2302
La1–O4[e]	0.2570	La2–O5[i]	0.2358	Y1–O4[e]	0.2951	Y2–O5[i]	0.2231
La1–O4[b]	0.2695			Y1–O4[b]	0.2251		
La1–O5[c]	0.2509			Y1–O5[c]	0.2231		
Ave.	0.2628	Ave.	0.2512	Ave.	0.2456	Ave.	0.2390

Fig. 8.9(a-c) shows the PL excitation spectra of the as-prepared, air-annealed and Ar-H_2-annealed samples respectively, when monitoring the 573 nm ($^4F_{9/2}\rightarrow{}^6H_{13/2}$ transition of Dy^{3+}) emission. The first broad bands observed in the excitation spectra (whose positions vary from 220–243 nm in the different samples shown in Fig. 8.9(a-c) are host related and are assigned to the electronic transition from the O 2p valence band to the La(5d6s) and Y(4d5s) conduction band [60, 61]. The inset of Fig. 8.9(a) is a magnified excitation spectrum in the wavelength range of 238–300 nm. The peaks observed at 256 and 278 nm are assigned to the 4f→4f5d transitions of Pr^{3+} [62-64]. The other eight peaks in the excitation spectra are assigned to the $^6H_{15/2}\rightarrow{}^4K_{13/2}$ (294 nm), $^6H_{15/2}\rightarrow{}^4K_{15/2}$, $^6P_{3/2}$ (325 nm), $^6H_{15/2}\rightarrow{}^6P_{7/2}$, $^4M_{15/2}$ (349 nm), $^6H_{15/2}\rightarrow{}^6P_{5/2}$ (362 nm), $^6H_{15/2}\rightarrow{}^4I_{13/2}$ (387 nm), $^6H_{15/2}\rightarrow{}^4G_{11/2}$ (424 nm), $^6H_{15/2}\rightarrow{}^4I_{15/2}$ (454 nm), and $^6H_{15/2}\rightarrow{}^4F_{9/2}$ (474 nm) excitation states of Dy^{3+} [5, 6]. It must be pointed out that the observed absorption band with a maximum at 376 nm ($O^{2-}\rightarrow Pr^{4+}$ CTB) appearing in the diffuse reflectance spectra (Fig. 8.6) is not observe in the excitation spectra. This is because the $O^{2-}\rightarrow Pr^{4+}$ CTB is not accompanied by luminescence [65, 66], probably due to the insulating nature of the process [30-32]. Hoefdraad et al. ascribed the absence of luminescence in R^{4+} to be a radiationless process because of the interaction between the R^{4+} and the holes in the ligand molecular orbital [66]. It can also be seen from Fig. 8.9(a-c) that the excitation intensities of the bands due to the O 2p valence band to the La(5d6s) and Y(4d5s) conduction band [60, 61] vary in the three different sets of samples (the as-prepared, air-annealed and Ar-H_2-annealed samples). Fig. 8.9(d & e) show the graphs of intensity versus La_2SiO_5/Y_2SiO_5

ratio (x) for the band-band (the maximum intensity value was taken in that region) and 349 nm excitation peaks, respectively, for the as-prepared, air-annealed and Ar-H_2-annealed samples. It is evident from Fig. 8.9(d & e) that the Ar-H_2-annealed samples have the best excitation intensities followed by the air-annealed samples, with the as-prepared samples having the lowest intensities. In Fig. 8.9(a), the two samples with a high ratio of La_2SiO_5 (x = 0 and 0.5) did not show any host excitation. As stated earlier, oxygen vacancies (VO) formed during synthesis and the Pr^{4+} 4f levels can form defect levels below the conduction band minimum [32, 56] as illustrated in the energy band structure and density of state (DOS) in Fig. 10. These levels can only be measured in the excitation spectrum if they are radiative [49, 67]. Although, the samples (x = 0 and 0.5) showed reasonable absorption peaks from the hosts in Fig. 8.6(a), they did not show any excitation in Fig. 8.9(a). This suggests that the oxygen vacancies and Pr^{4+} levels might have formed luminescence-quenching center below the conduction band minimum and these quenched the electrons excited from the O 2p band. Hence, in a material where the non-radiative species are much greater than the radiative species, the material may be able to absorb but may not luminesce.

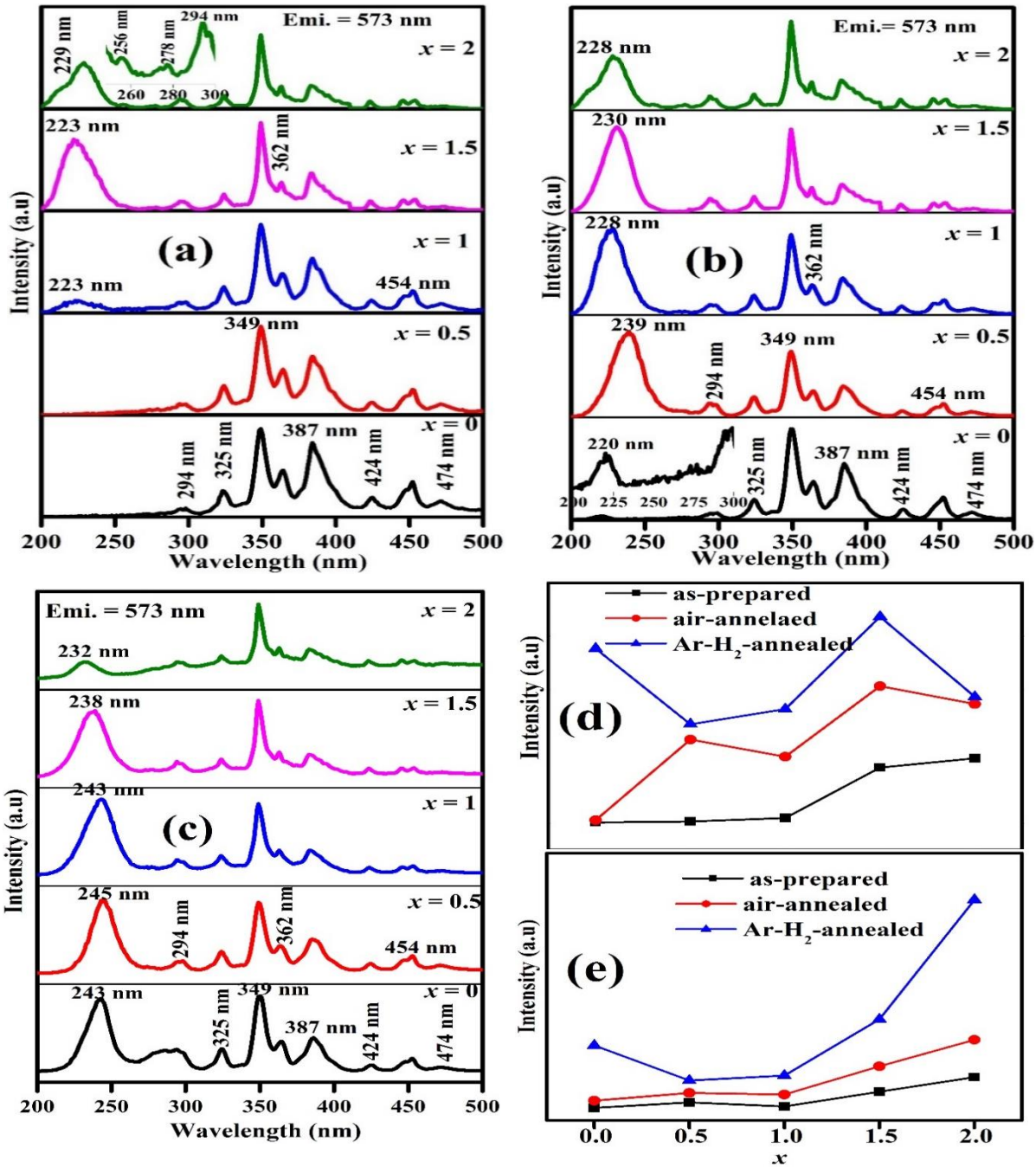

Fig. 8.9: The PL excitation spectra of the (a) as-prepared, (b) air-annealed, and (c) Ar-H_2-annealed $La_{2-x}Y_xSiO_5$:$_{0.25}Pr^{3+}$,$_{0.25}Dy^{3+}$ (x = 0, 0.5, 1, 1.5 and 2) phosphors when monitoring the 573 nm Dy^{3+} emission. The graph of intensity versus x (La_2SiO_5/Y_2SiO_5 ratio) for the (d) band-band (the maximum value was taken in that region), and (e) 349 nm excitation peaks for the as-prepared, air-annealed and Ar-H_2-annealed samples.

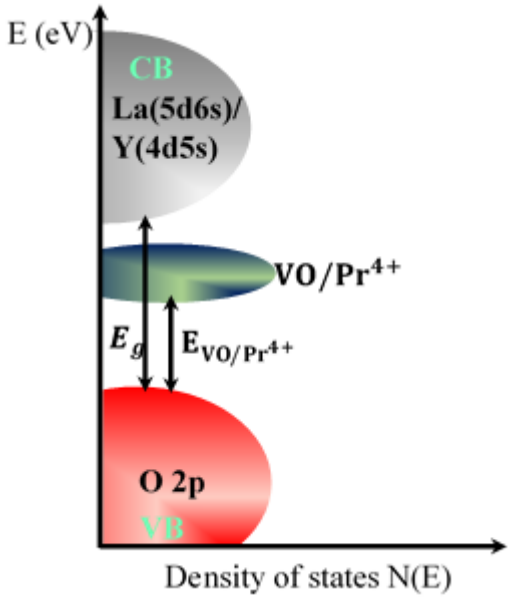

Fig. 8.10: The energy band structure and density of state (DOS), illustrating how the oxygen vacancy (VO) and Pr^{4+} level can form luminescence-quenching center below the conduction band minimum.

The PL emission spectra were measured for the three sets of samples (as-prepared, air-annealed and Ar-H_2-annealed) by monitoring the band-band excitations (O 2p La(5d6s) and Y(4d5s)) and the results are shown in Fig. 8.11(a-c), respectively. Only three of the as-prepared samples (x = 1, 1.5 and 2) are shown since the other two samples (x = 0 and 0.5) did not give excitation in this wavelength region. All the samples showed the four emission peaks from the Dy^{3+} 4f→4f transitions at 484, 573, 665 and 755 nm assigned to $^4F_{9/2}\rightarrow{}^6H_{15/2}$, $^4F_{9/2}\rightarrow{}^6H_{13/2}$, $^4F_{9/2}\rightarrow{}^6H_{11/12}$, and $^4F_{9/2}\rightarrow{}^6H_{9/2}$, respectively [5, 6]. The peaks observed at 450, 440 and 465 nm in Fig. 8.11(a-c), respectively, are assigned to emissions from the Pr^{3+} 4f5d→$^1I_6$, $^3P_{J\ (J\ =\ 0,1,2)}$ manifolds [68], while the peak at 766 nm in Fig. 8.11(c) is assigned to the $^3P_0\rightarrow{}^3F_4$ transition of Pr^{3+} [63]. The other emission peaks at 511 and 667 nm, Fig. 8.11(c), and 630 nm, Fig. 8.11(b & c), are assigned to $^3P_0\rightarrow{}^3H_5$, $^3P_0\rightarrow{}^3F_2$ and $^1D_2\rightarrow{}^3H_4$ 4f→4f transitions of the Pr^{3+} respectively [9].

From Fig. 8.9(d & e), we can conclude that the emission lines are more prominent in the Ar-H_2-annealed samples, Fig. 8.11(c), compare to the as-prepared, Fig. 8.11(b), and air-annealed samples, Fig. 8.11(a), (since the excitation intensity of a material is expected to be equivalent to the emission intensity). This could be due to the presence of more Pr^{3+} ions in the Ar-H_2-annealed samples due

to the reduction of Pr^{4+} to Pr^{3+}. Furthermore, the PL emission intensities of the samples annealed in air are higher than those of the as-prepared samples; this could be due to the filling of oxygen vacancies during annealing in air [26, 27]. The number of oxygen atoms surrounding the dopant determines the effect of the crystal field strength on the dopant, which in turn effects the photoluminescence [69]. In sample x = 1, Fig. 8.11(a), and x = 0, Fig. 8.11(b), the PL emission associated with the 4f5d→$^1I_6$, $^3P_{J\ (J = 0,1,2)}$ manifold transition of Pr^{3+} is prominent. In our previous report, we showed how the crystal field strength effect on the position of the bottom of the 4f5d level can influence the branching ratios of the $^3P_0$ and $^1D_2$ transitions of Pr^{3+} in mixed lanthanum yttrium oxyorthosilicate [9]. However, when Dy^{3+} is introduced into the matrix, the $^6H_{15/2}$→$^4I_{15/2}$ (454 nm) excitation level of Dy^{3+} will overlap with the 4f5d level of Pr^{3+} as shown in Fig. 8.11(d). In the absence of Dy^{3+}, electrons from the 4f5d level of Pr^{3+} can be transferred wholly or partially to its lower energy states ($^3P_0$ and $^1D_2$) and emission can be observed from these states. However, in the present case where Dy^{3+} ions are introduced into the matrix, electrons from the 4f5d level of Pr^{3+} can be partially or wholly emptied into the $^6H_{15/2}$→$^4I_{15/2}$ level of Dy^{3+}, leading to either only Dy^{3+} 4f→4f emission or Dy^{3+} 4f→4f and Pr^{3+} 4f5d/4f→4f emission. This phenomenon is known as energy transfer (from Pr^{3+} to Dy^{3+}). The luminescence mechanism of Pr^{3+} and Dy^{3+} co-doped $La_{2-x}Y_xSiO_5$ host shown in Fig. 8.11 can be understand by considering two cases. Fig. 8.12 provide an explanation for the absence/presence of Pr^{3+} 4f emission in the luminescence spectra in Fig. 8.11.

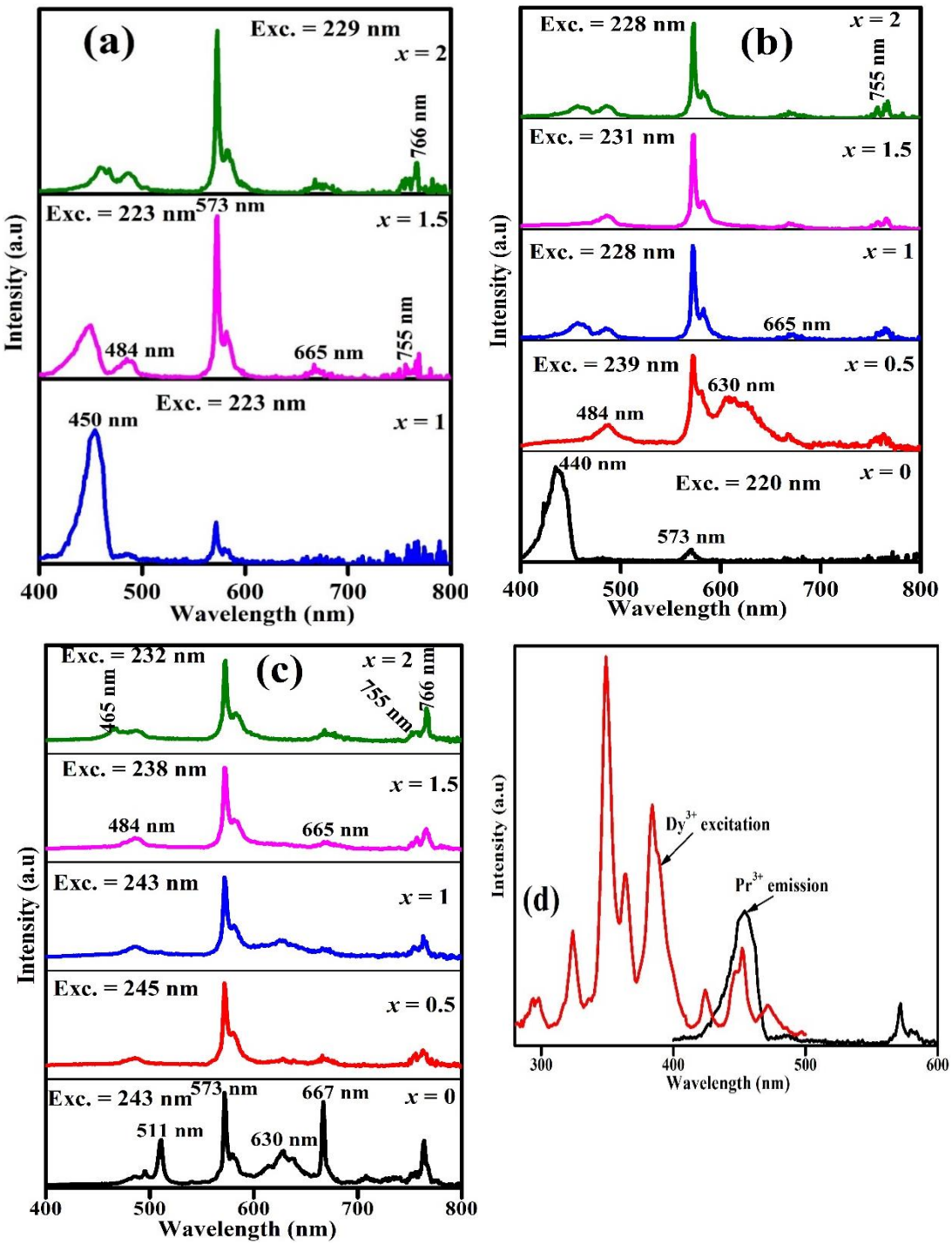

Fig. 8.11: The PL emission spectra of the (a) as-prepared, (b) air-annealed, and (c) Ar-H_2-annealed $La_{2-x}Y_xSiO_5$:$_{0.25}Pr^{3+}$,$_{0.25}Dy^{3+}$ (x = 0, 0.5, 1, 1.5 and 2) phosphors when monitoring the band-to-band excitation. (d) Spectral overlap between the $^6H_{15/2} \rightarrow {}^4I_{15/2}$ (454 nm) excitation level of Dy^{3+} and the 4f5d emission of Pr^{3+} obtained from the as-prepared $LaYSiO_5$:$_{0.25}Pr^{3+}$,$_{0.25}Dy^{3+}$ sample.

Case I: Pr^{3+} 4f5d level lies below the band gap of the host. Fig. 8.12a(1 & 2) shows the schematic illustration of the energy level and the configurational coordinate diagrams respectively of the cases where Pr^{3+} 4f ($^3P_0$ and $^1D_2$) emissions were not observed in Fig. 8.11. According to Fig. 8.12a(1), Pr^{3+} 4f5d state is localized below the conduction band of the host. In this case, there will be an energy overlap between the 4f5d state of Pr^{3+} and the $^4I_{15/2}$ excitation level of Dy^{3+}, but $^3P_0$ and $^1D_2$ states of Pr^{3+} lies below the 4f5d level of Pr^{3+} and the $^4I_{15/2}$ excitation level of Dy^{3+} as illustrated in the configurational coordinate diagram in Fig. 8.12a(2). In such case, under UV excitation, Pr^{3+} will transfer part of its 4f5d energy to the $^4I_{15/2}$ excitation level of Dy^{3+} [4] which transfers it non-radiatively to the $^4F_{9/2}$ level of Dy^{3+} leading to emission from Dy^{3+}, and no emission is observed from the 4f ($^3P_0$ and $^1D_2$) levels of Pr^{3+}.

Case II: Pr^{3+} 4f5d level lies close to or inside the conduction band of the host. In rare earth doped host matrices, when the 4f5d state is very close to or overlap with the bottom of the conduction band of the host, 4f5d electrons are excited into the conduction band of the host under UV excitation [70]. Fig. 8.12b(1 & 2) represents the schematic illustration of the energy level and configurational coordinate diagrams, respectively, for the case were Pr^{3+} 4f ($^3P_0$ and $^1D_2$) emissions were observed in Fig. 8.11. In this case, the 4f5d level of Pr^{3+} lies inside or close to the conduction band of the host. In this instance, the excited electron can delocalize completely in the conduction band, leading to an autoionization process. In this process, the promoted electron can be trapped by a lattice defect or it can be attracted to a Pr^{4+} ion to form a self-trapped exciton state (Pr^{4+}/e-) [71]. Autoionization can result in the partial or complete quenching of the 4f5d luminescence [72, 73]. As illustrated in the configurational coordinate diagram in Fig. 8.12b(2), the 4f5d state of Pr^{3+} lies far above the $^4I_{15/2}$ level of Dy^{3+} hence energy transfer will not occur from Pr^{3+} to Dy^{3+}. However, part or all the excited Pr^{3+} electrons are non-radiatively fed to the $^1D_2$ state from the ^3P_J $_{(= 0,1,2)}$ state t. Here the parabola of the self-trapped exciton state is situated in such a way that any excited Pr^{3+} ion moves the excitation energy to the (Pr^{4+}/e-) state, which bypasses the ^3P_J state and channels the excited energy to the $^1D_2$ state [74]. This will lead to emission either from the ^3P_J and $^1D_2$ state or only from the $^1D_2$ state, depending on whether the ^3P_J state feed all or part of its energy to the $^1D_2$ state (Fig. 8.12b(1)). The emission observed from Dy^{3+} in these cases is due to energy transfer from the host to the higher states of Dy^{3+}.

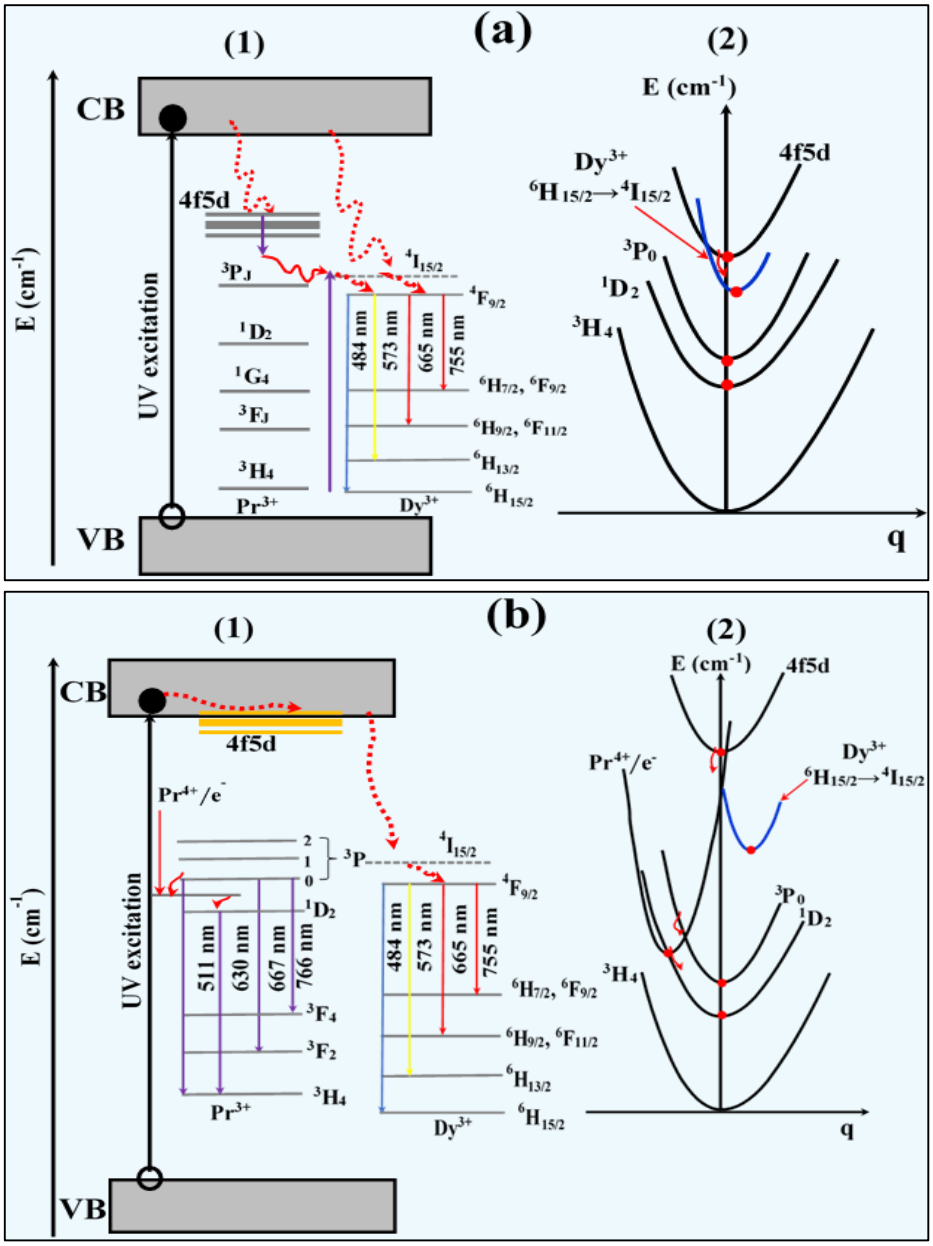

Fig. 8.12: Schematics illustrations of: a(1) energy levels and a(2) configurational coordinate diagrams, where the Pr^{3+} 4f5d level lies below the band gap of the host, and b(1) energy levels and b(2) configurational coordinate diagrams, where the Pr^{3+} 4f5d level lies close to or inside the band gap of the host.

The emission spectra of the as-prepared, air-annealed and Ar-H_2-annealed samples were also measured when monitoring the $^6H_{15/2}\rightarrow{}^6P_{7/2}$, $^4M_{15/2}$ (349 nm) excitation state of Dy^{3+} and are shown

in Fig. 8.13(a-c), respectively. Emission lines were observed at 484, 573, 665, and 755 nm and are assigned to the $^4F_{9/2}\rightarrow{}^6H_{15/2}$, $^4F_{9/2}\rightarrow{}^6H_{13/2}$, $^4F_{9/2}\rightarrow{}^6H_{11/12}$, and $^4F_{9/2}\rightarrow{}^6H_{9/2}$ Dy^{3+} 4f→4f transitions, respectively [5, 6]. A broad band with maximum around 450 nm, which is host related, was also observed and was assigned to the self-trapped excitons (STE) in SiO_2 [75, 76]. The absence of Pr^{3+} emission in Fig. 8.13 is evidence that there was no Dy^{3+} to Pr^{3+} energy transfer.

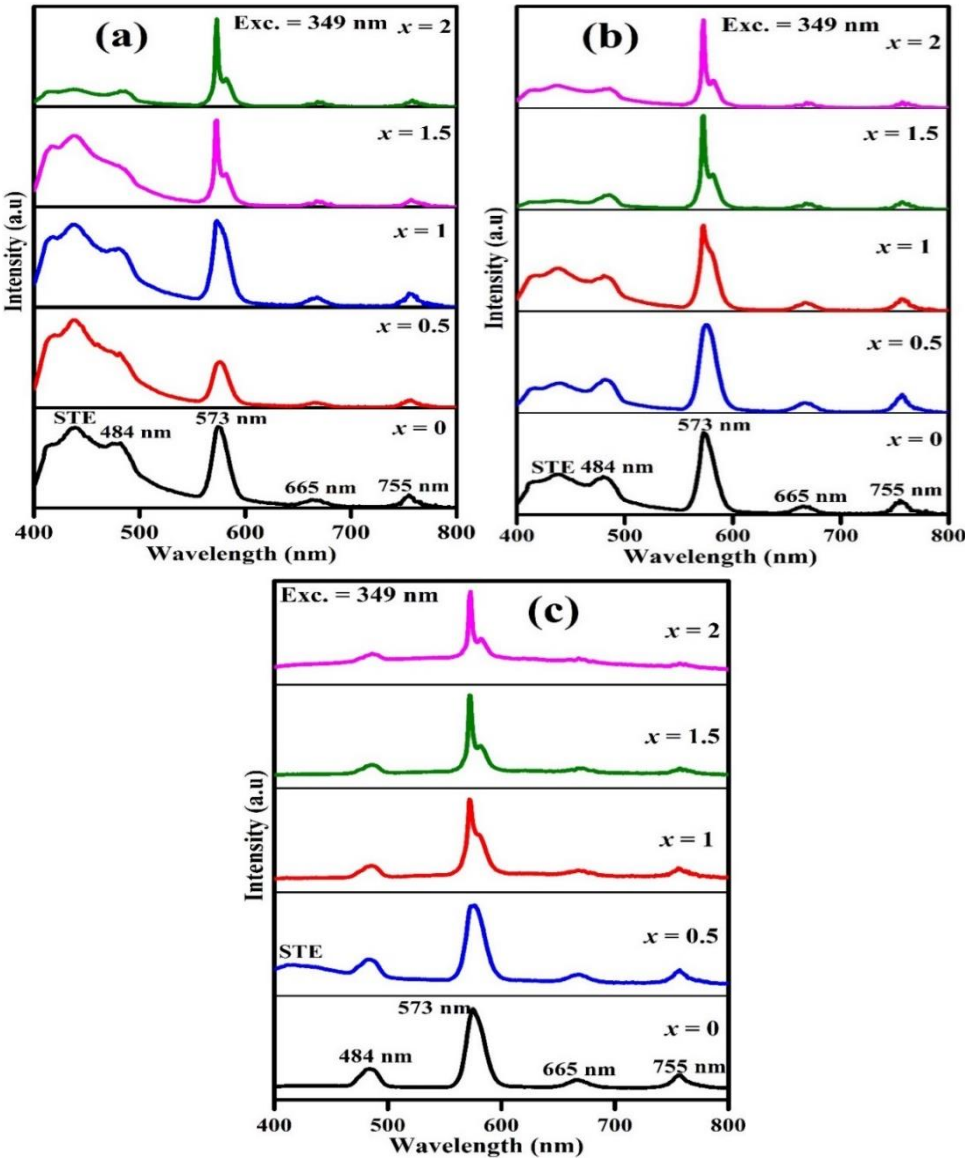

Fig. 8.13: The PL emission spectra of the (a) as-prepared, (b) air-annealed, and (c) Ar-H_2-annealed $La_{2-x}Y_xSiO_5$:$_{0.25}Pr^{3+}$,$_{0.25}Dy^{3+}$ (x = 0, 0.5, 1, 1.5 and 2) phosphors when monitoring the $^6H_{15/2}\rightarrow{}^6P_{7/2}$, $^4M_{15/2}$ (349 nm) excitation state of Dy^{3+}.

The CIE (x, y) colour coordinates for the as-prepared, air-annealed and Ar-H_2-annealed samples taken from the data generated when the samples were excited using the band-to-band (UV) and the 349 nm excitation are shown in Fig. 8.14(a-f), respectively. The variations observed in the CIE coordinates can be related to the changes observed in the intensities of each peak in the emission spectra, because of the change in the ratios of La and Y in the host and different annealing atmospheres. Table 8.6 shows the (x, y) colour coordinates and the corresponding CCT of the phosphors.

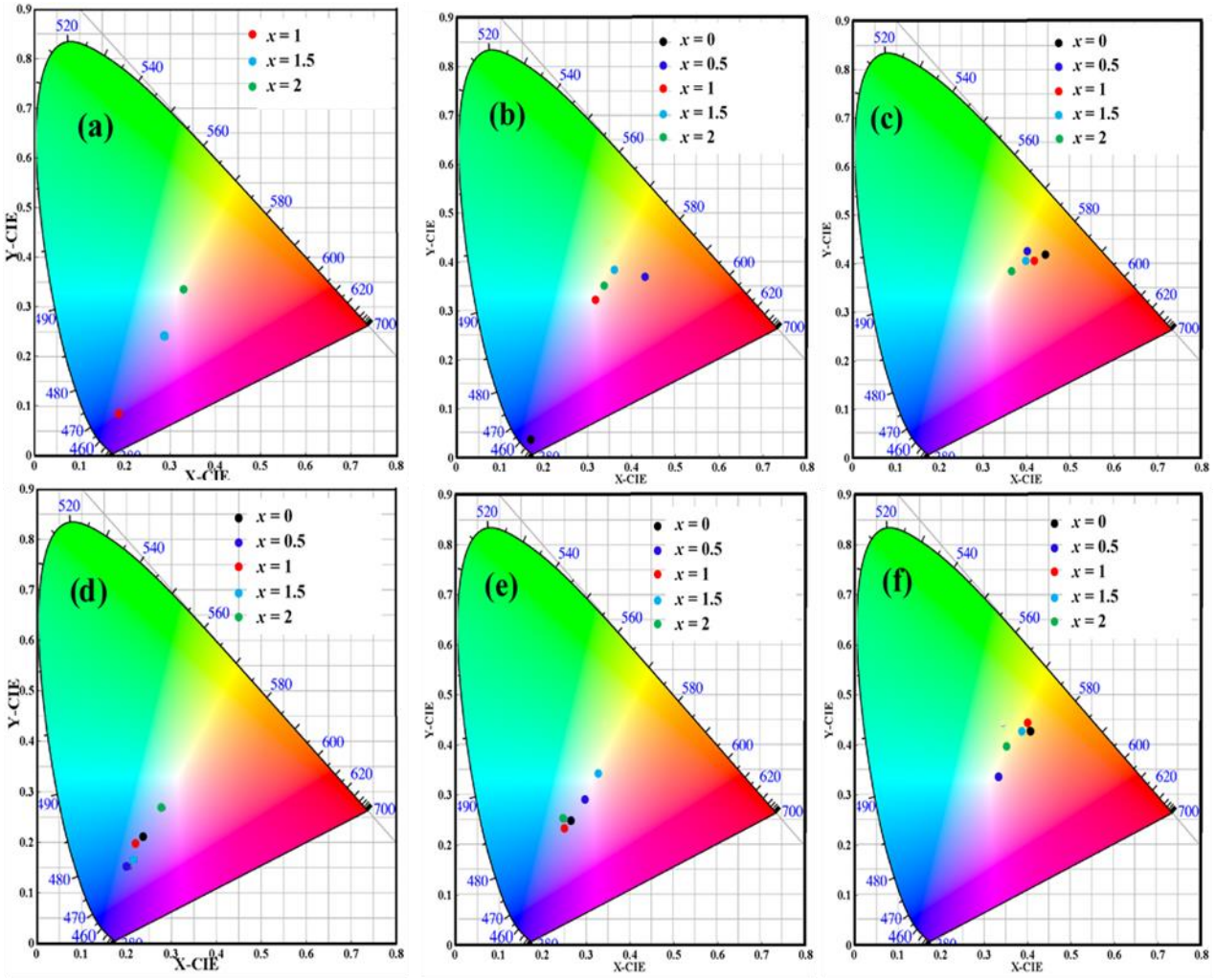

Fig. 8.14: The CIE colour coordinates of $La_{2-x}Y_xSiO_5$:$_{0.25}Pr^{3+}$,$_{0.25}Dy^{3+}$ (x = 0, 0.5, 1, 1.5 and 2) phosphors: (a) as-prepared, (b) air-annealed, and (c) Ar-H_2-annealed excited with UV light and (d) as-prepared, (e) air-annealed, and (f) Ar-H2-annealed excited with 349 nm.

Table 8.6: The CIE colour coordinates and the corresponding CCT values of the as-prepared, air-annealed, and Ar-H_2-annealed $La_{2-x}Y_xSiO_5$:$_{0.25}Pr^{3+}$,$_{0.25}Dy^{3+}$ (x = 0, 0.5, 1, 1.5 and 2) phosphors excited with UV and 349 nm.

$La_{2-x}Y_xSiO_5$: $_{0.25}Pr^{3+}$,$_{0.25}Dy^{3+}$	Chromaticity coordinates (x, y) /CCT (K)		
	As-prepared	Air-annealed	Ar-H_2-annealed
	UV exc.	**UV exc.**	**UV exc.**
x = 0	-	(0.183, 0.051) /1740	(0.470, 0.424) /2663
x = 0.5	-	(0.460, 0.372) /2358	(0.430, 0.423) /3264
x = 1	(0.188, 0.087) /1811	(0.346, 0.329) /4878	(0.448, 0.405) /2827
x = 1.5	(0.301, 0.252) /9562	(0.386, 0.386) /3917	(0.428, 0.420) /3277
x = 2	(0.353, 0.43) /4951	(0.362, 0.353) /4397	(0.390, 0.389) /3839
	349 nm exc.	**349 nm exc.**	**349 nm exc.**
x = 0	(0.239, 0.218)/65897	(0.278, 0.257)/12979	(0.430, 0.433)/3333
x = 0.5	(0.207, 0.160)/7102	(0.316, 0.297)/6577	(0.357, 0.344)/4518
x = 1	(0.240, 0.207)/138817	(0.271, 0.244)/17164	(0.430, 0.437)/3359
x = 1.5	(0.215, 0.171)/39579	(0.356, 0.352)/4597	(0.420, 0.433)/3508
x = 2	(0.294, 0.271)/8970	(0.274, 0.260)/13286	(0.376, 0.399)/4247

8.4. Conclusions

Post-annealing of $La_{2-x}Y_xSiO_5$:$_{0.25}Pr^{3+}$,$_{0.25}Dy^{3+}$ (x = 0, 0.5, 1, 1.5 and 2) phosphors in different annealing atmospheres (air and Ar-H_2) can influence the band gap and the photoluminescence properties of the phosphors. Ar-H_2-annealing enhanced the band gap and photoluminescence intensity of the phosphors compared to the as-prepared and air-annealed samples. The observed enhancement in Ar-H_2-annealed samples could be due to reduction of Pr^{4+} (to Pr^{3+}), formed during synthesis and annealing the samples in air. This suggest that reduction of Pr^{4+} in the $La_{2-x}Y_xSiO_5$:$_{0.25}Pr^{3+}$,$_{0.25}Dy^{3+}$ system will enhance the optical properties (band gap and photoluminescence) more than the formation of oxygen vacancies, since more oxygen vacancies were expected to be present in the Ar-H_2-annealed samples. Furthermore, it was also shown that the energy transfer mechanism from Pr^{3+} to Dy^{3+} in $La_{2-x}Y_xSiO_5$:$_{0.25}Pr^{3+}$,$_{0.25}Dy^{3+}$ (x = 0, 0.5, 1, 1.5 and 2) matrices will depend on the position of the 4f5d energy level of Pr^{3+} in the host matrices. When the 4f5d level of Pr^{3+} lies within the band gap of the host, it overlaps with the $^4I_{15/2}$ level of

Dy^{3+} resulting to energy transfer from Pr^{3+} to Dy^{3+}. On the other hand, if the 4f5d level of Pr^{3+} lies very close to or inside the conduction band of the host, no energy transfer should be observed. The CIE colour coordinates of the phosphors showed tunable colour ranging from red to yellow, including white and blue.

8.5. References

[1] J. Geng, Y. Chen, G. Gu, L. Tian, 36 (2014) 1093.

[2] W. Tang, Y. Sun, M. Yu, X. Liu, Y. Yin, B. Yang, L. Zheng, F. Qin, Z. Zhang, W. Cao, RSC Adv. 5 (2015) 27491.

[3] Y. Ji, J. Cao, Z. Zhu, J. Li, Y. Wang, C. Tu, Mater. Express, 1 (2011) 231.

[4] P.P. Pawar, S.R. Munishwar, R.S. Gedam, Solid State Sci. 64 (2017) 41.

[5] S.N. Ogugua, S.K.K. Shaat, H.C. Swart, O.M. Ntwaeaborwa, J. Lumin. 79 (2016) 154.

[6] S.N. Ogugua, S.K.K. Shaat, H.C. Swart, O.M. Ntwaeaborwa, Physica B 480 (2016) 131.

[7] M.R.N. Soares, M.J. Soares, A.J.S. Fernandes, L. Rino, F.M. Costa, T. Monteiro, J. Mater. Chem. 21 (2011) 15262.

[8] C.R. Kesavulu, C.K. Jayasankar, Mat. Chem. Phys. 130 (2011) 1078.

[9] S.N. Ogugua, H.C. Swart, O.M. Ntwaeaborwa, Sens. Actuators B 250 (2017) 285.

[10] P.P. Mokoena, M.Gohain, B.C.B. Bezuidenhoudt, H.C. Swart, O.M. Ntwaeaborwa, J. Lumin. 155 (2014)288.

[11] M.Y.A. Yagoub, H. C. Swart, P. Bergman, E. Coetsee, AIP Advances 6 (2016) 025204.

[12] K.N. Shinde, S.J. Dhoble, H.C. Swart, K. Park, Phosphate phosphors for solid-state lighting, Springer Heidelberg, New York (2012) p. 57.

[13] P.P. Pawar, S.R. Munishwar, R.S. Gedam, J. Alloys. Compd. 660 (2016) 347.

[14] J. Heo, Rare-earth-doped chalcogenide glass for lasers and amplifiers, In, J.L. Adam, X. Zhang (Ed.) "*Chalcogenide glasses: preparation, properties and applications*" Woodhead publishing limited, Cambridge, UK (2014) p. 367.

[15] K.K. Mahato, A. Rai, S.B. Rai, Spectrochim. Acta A, 61 (2005) 431.

[16] B. Viana, P. Derouineau, L. Gervat, D. Vivien, A.M. Lejus, SPIE French-Israeli workshop on solid state lasers 1182 (1988) 225.

[17] Y. Fangtian, Z. Xinguo, P. Hongshang, H. Shihua, H. Yan, T. Ye, 31 (2013) 1125.

[18] R.S Melltzer, Phosphors for lamps, In, W.M. Yen, S. Shionoya, H. Yamamoto (Ed.) "*Practical Applications of Phosphors*" CRC Press, Taylor and Francis Group, 6000 Broken Sound Parkway, New York (2007) p. 172.

[19] T. Justel, W. Mayr, P.J. Schmidt, Tuning the $4f^15d$-$4f^2$ UV emission of Pr^{3+}, 200^{th} meeting of the electrochemical society, San Francisco, CA, USA, September, (2001).

[20] W. Jiaa, D. Jia, T. Rodriguez, D.R. Evans, R.S. Meltzer, W.M. Yen, J. Lumin. 119–120 (2006) 13.

[21] M.A. Srivastava, C.R. Ronda, Quantum-splitting systems, In C. Ronda (Ed.), "*Luminescence: from theory to application*" WILEY-VCH Verlag GmbH & Co. KGaA, Weinheim, (2008) p. 81.

[22] R.I. Bickley, Photo-induced radiativity at oxide surfaces, In, J.M. Thomas, M.W. Roberts (Ed.) "*A specialist periodical report chemical physics of solids and their Surfaces*" Billing & Sons limited Guildford, London and Worcester 7 (1978) p. 127.

[23] E.I. Anila, M.K. Jayaraj, Effect of post-annealing on structural and photoluminescence properties of SrS:Dy,Cl thin film, Proc. of ASID '06, 8-12 Oct, New Delhi.

[24] T. Morishita, H. Matsuyama, M. Matsui, M. Wakihara, Jpn. J. Appl. Phys. 38 (1999) 6732.

[25] Y.B. Xin, W. Tong, W. Park, M. Chaichimansour, C.J. Summers, J. Appl. Phys. 85 (1999) 3999.

[26] H. Feng, D. Ding, H. Li, S. Lu, S. Pan, X. Chen, G. Ren, J. Appl. Phys. 103 (2008) 083109.

[27] B. Wang, H. Qi, H. Han, Z. Song, J. Chen, J. Shao, Opt. Mat. Express (2015) 155.

[28] S. Yoon, E.H. Otal, A.E. Maegli, L. Karvonen, S.K. Matam, S.G. Ebbinghaus, B. Walfort, H. Hagemann, S. Pokrant, A. Weidenkaff, J. Alloys. Compd 613 (2014) 338.

[29] V.S. Vishnu, G. George, M.L.P. Reddy, Dyes Pigm. 85 (2010) 117.

[30] V.S. Vishnu, M.L. Reddy, Sol. Energ. Mat. Sol. Cells 95 (2011) 2685.

[31] H.Y. He, J. Lu, MRS Communications 3 (2013) 47.

[32] J.J. Kim, S.R. Bishop, N. Thompson, Y. Kuru, H.L. Tuller, Solid State Ionics 225 (2012) 198.

[33] P.N. Zhmurin, N.V. Znamenskii, T.G. Yukina, Y.V. Malyukin, Phys. Stat. Sol. (b) 244 (2007) 3325.

[34] J. Felsche, The crystal chemistry of the rare-earth silicates, In, R.A. Penneman, R.R. Ryan, A. Rosenzweig, R. Reisfeld, J. Felsche, C.K. Jørgensen, "*Structure and Bonding*" Springer, Berlin, 13 (1973) p. 99–197.

[35] M. Yin, C. Duan, W. Zhang, L. Lou, S. Xia, J.C. Krupa, J. Appl. Phys. 86 (1999) 3751.

[36] K. Ueda, Y. Iijima, T. Maruyama, S. Naritsuka, J. Nanosci. Nanotechnol. 10 (2010) 1.

[37] T.P. Rao, M.C.S. Kumar, JCPT. 2 (2012) 72.

[38] A.J. Signorelli, R.G. Hayes, Phys. Rev. B 8 (1973) 81.

[39] J.F. Moulder, W.F. Stickle, P.E. Sobol, K.D. Bomben, Handbook of X-ray photoelectron spectroscopy, J. Chastain (Ed.), Perkin-Elmer Corporation, Physical Electronics Division, USA, (1992) p. 20.

[40] A.V. Shlyakhtina, J.C.C. Abrantes, E. Gomes, A.N. Shchegolikhin, G.A. Vorobieva, K.I. Maslakov, A.V. Knotko, L.G. Shcherbakova, Int. J. Hydrog. Energy, xxx (2016) 1.

[41] Casa Software Ltd (2013), http://www.casaxps.com/help_manual/manual_updates/xps_spectra.pdf.

[42] H. Al Kutubi, L. Rassaei, W. Olthuis, G.W. Nelson, J.S. Foord, P. Holdway, M.Carta, R.M. Evans, N.B. McKeown, S.C. Tsang, R. Castaing, T.R. Forder, M.D.Jones, D. Hea, F. Marken, RSC Adv. 5(2015) 73323.

[43] A. Mekkia, Kh.A. Ziq, D. Holland, C.F. McConville, J. Magn. Magn. Mater. 260 (2003) 60.

[44] D.F. Mullica, C.K. Lok, H.O. Perkins, Phys. Rev. B. 31 (1985) 4039.

[45] T.H. Yang, Y.W. Harn, K.C. Chiu, C.L. Fan, J.M. Wu, J. Mater. Chem. 22 (2012) 17071.

[46] S. Mickevicius, S. Grebinskij, V. Bondarenka, H. Tvardauskas, B. Vengalis, K. Sliuzienne, B.A. Orlowski, W. Drube, Opt. Appl. XXXVI (2006)235.

[47] V. Simon, D. Eniu, A. Takács, K. Magyari, M. Neumann, S. Simon, J. Optoelectron. Adv. M, 7 (2005) 2853.

[48] E. Coetsee, J.J. Terblans, H.C. Swart, Appl. Surf. Sci. 256 (2010) 6641.

[49] R.W. Redmond, Introduction to fluorescence and photophysics, In, M. Mycek, B.W. Pogue, (Ed.) "*Handbook of biomedical fluorescence*" Marcel Dekker, Inc. 270 Madison Avenue, New York (2003) p. 11.

[50] G. Kortum, Reflectance Spectroscopy, Springer-Verlag, New York (1969) p. 55.

[51] L.L. Noto, W.D. Roos, O.M. Ntwaeaborwa, M. Gohain, M.Y.A. Yagoub, E. Coetsee, H.C. Swart, Sci. Adv. Mater. 7 (2015) 1.

[52] G. Kortum, Reflectance Spectroscopy, Springer-Verlag, New York, (1969) p. 103–169.

[53] J. Tauc (Ed.), The Optical Properties of Solids, Academic Press, New York, (1966).

[54] A. Winterstein, S. Manning, H.E. Heidepriem, L. Wondraczek, Opt. Mater. Express 2 (2012) 1320.

[55] Y. Lv, W. Yao, X. Ma, C. Pan, R. Zong, Y. Zhu, Catal. Sci. Technol. 3 (2013) 3136.

[56] B. Choudhury, B. Borah, A. Choudhury, Photochem. Photobiol. 88 (2012) 257.

[57] K. Fukuda, T. Iwata, Powder Diffr. 21 (2006) 300.

[58] B. Liu, J. Wang, F. Li, J. Wang, Y. Zhou, J. Am. Ceram. Soc. 95 (2012) 1093.

[59] B. Liu, Z. Qi, M. Gu, X. Liu, S. Huang, C. Ni, J. Phys. Condens. Matter 19 (2007) 436215.

[60] G. Li, C. Li, C. Zhang, Z. Cheng, Z. Quan, C. Peng, J. Lin, J. Mater. Chem. 19 (2009) 8936.

[61] M. Jia, J. Zhang, S. Lu, J. Sun, Y. Luo, X. Ren, H. Song, X. Wang, Chem. Phys. Lett. 384 (2004) 193.

[62] D. Jia, X.J. Wang, W.M Yen, Phys. Solid State, 50 (2008) 1674.

[63] Y. Ji, J. Cao, Z, Zhu, J. Li, Y. Wang, C. Tu, Mater. Express. 1 (2011) 231.

[64] C.H. Huang, L. Luo, Y.T. Yeh, S.M. Janga, W.R. Liu, RSC Adv., 4 (2014) 5513.

[65] H.E. Hoefdraad, J. Inorg. Nucl. Chem. 37 (1975) 1917.

[66] P. Boutinaud, E. Pinel, M. Dubois, A.P. Vink, R. Mahiou, J. Lumin. 111 (2005) 69.

[67] Y.C. Li, Y.H. Chang, Y.F. Lin, Y.S. Chang, Y.J. Lin, J. Alloys Compd. 439 (2007) 367.

[68] L. van Pieterson, R.P.A. Dullens, P.S. Peijzel, A. Meijerink, G.D. Jones, J. Chem. Phys. 115 (2001) 9393.

[69] E.A. Fidancev, J. Hölsä, M. Lastusaari, A. Lupei, Phys. Rev. B 64 (2001) 195108.

[70] P. Dorenbos, lanthanide level location and its impact on phosphor performance, In, W.M. Yen, S. Shionoya, H. Yamamoto (Ed.) "*Fundamentals of Phosphors*" CRC Press, Taylor & Francis Group, New York (2006) p. 131.

[71] P. Boutinaud, E. Pinel, M. Dubois, A.P. Vink, R. Mahiou, J. Lumin. 111 (2005) 69.

[72] A.V. Sidorenko, P. Dorenbos, A.J.J. Bos, C.W.E van Eijk, P.A. Rodnyi, J. Phys. Condens. Matter 18 (2006) 4503.

[73] P. Lecoq, A. Annenkov, A. Gektin, M. Korzhik, C. Pedrini, Inorganic scintillators for detector systems: physical principles and crystal engineering, Springer-Verlag Berlin Heidelberg (2006) p. 113.

[74] A.M. Srivastava, C.R. Lecuna, D.S. Pérez, F. Rodríguez, R. Valiente, J. Lumin. 146 (2014) 27.

[75] C. Itoh, K. Tanimura, N. Itoh, J. Phys. C: Solid State Phys. 21 (1988) 4693.

[76] S.N. Ogugua, S.K.K. Shaat, H.C. Swart, O.M. Ntwaeaborwa, J. Phys. Chem. Sol. 83 (2015) 109.

CH. 9

Determination of quantum yield of phosphors using integrating sphere

9.1. Introduction

When a phosphor material absorbs a photon of light, an excited state is formed. The excited species undergoes different processes depending on the nature of its surroundings, before it eventually deactivates (loses) the absorbed energy and returns to the ground state. Different ways in which an excited electron can return to the ground state include radiative transition, nonradiative transition such as multiphonon relaxation, and cross relaxation [1].

Phosphors are often graded by their excitation and emission spectra and quantum yield (QY) (also known as quantum efficiency (QE). QY can be internal or external. Internal QY of a photoluminescence material is the ratio of the number of emitted photons to the number of absorbed photons. The external QY is the ratio of the number of emitted photons to the number of incident photons. The external QY is very difficult to determine, since it depends on many factors, namely, excitation wavelength, quantity and particle morphology of a material [2]. Hence it will not be discussed further in this chapter.

QY of luminescence materials have been determined using methods such as, thermal lensing [3], photoacoustic spectroscopy [4], and optically-based methods [5]. The optically-based method for determination of QY can be divided into absolute and relative. The major drawback of the relative method is that it requires a standard sample with similar excitation and emission properties with the sample been studied [5]. The absolute method on the other hand does not require a reference sample but required an integrating sphere. One major advantage of the integrating sphere is its ability to collect all the light emitted and scattered by the photoluminescence material. Many authors have applied this method in determination of the QY of solutions, thin films and powder samples [6-13].

In this chapter, QY values of mixed lanthanum gadolinium oxyorthosilicate ($La_{2-x}Gd_xSiO_5$ (x = 0, 0.5, 1, 1.5 and 2)) doped with 1 mol% Dy^{3+} powder phosphors were determined using an

integrating sphere-based setup. Two approaches can be applied when using the integrating sphere setup for absolute determination of QY, namely two-measurement approach [9-11] and three-measurement approach [6-8]. These two approaches were used in this study.

9.2. Experimental

$La_{2-x}Gd_xSiO_5$ (x = 0, 0.5, 1, 1.5 and 2) doped 1 mol% Dy^{3+} powder phosphors were synthesized using solution combustion method as discussed in section 2.5.3. QY measurements were performed using an FLS980 fluorescence spectrometer. The spectrometer uses a 450 W xenon arc lamp that covers a range of 230 - 1000 nm as an excitation source and a R928P PMT detector in a cooled housing which cover a range of 200 - 870 nm. The integrating sphere has an inner diameter of 120 mm made of a polytetrafluoroethylene (PTFE) material with about 99 % reflectance over a spherical range of 400 - 1500 nm and about 95 % reflectance within 250 - 2500 nm.

9.2.1. *The two-measurement approach*

The integrating sphere setup for the two-measurement approach is shown in Fig. 9.1. This approach involves only two experimental setups; a measurement with no sample in the sphere (Fig. 9.1(a)), and a measurement with a sample in the sphere and in path of the incident beam (Fig. 9.1(b)). The baffle prevents the light from the excited source from exciting the sphere with the scattered radiation through the emission port.

9.2.2. *The three-measurement approach*

The three-measurement approach (Fig. 9.2) involves a measurement with no sample in the sphere (Fig. 9.2(a)), a measurement with a sample in the sphere and in the path of the incident beam (Fig. 9.2(b)) and a measurement with the sample in the sphere but not in the path of the incident beam (Fig. 9.2(c)).

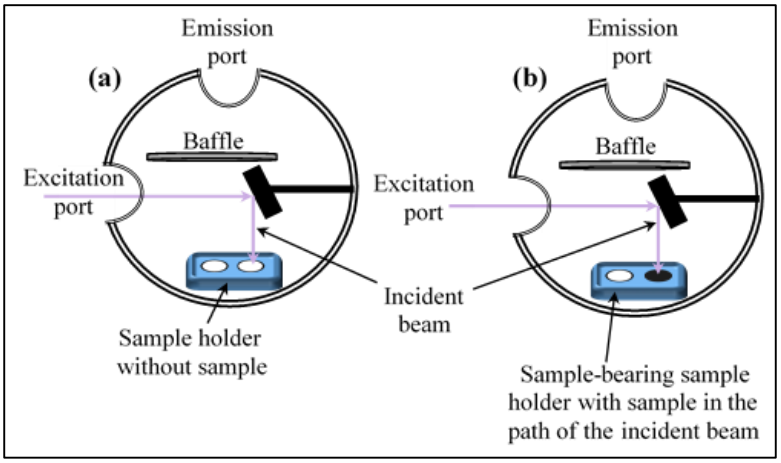

Fig. 9.1: Schematic diagram illustrating two different set-up required for the two-measurement approach, (a) no sample in the sphere and (b) sample in the sphere and in the path of the incident beam.

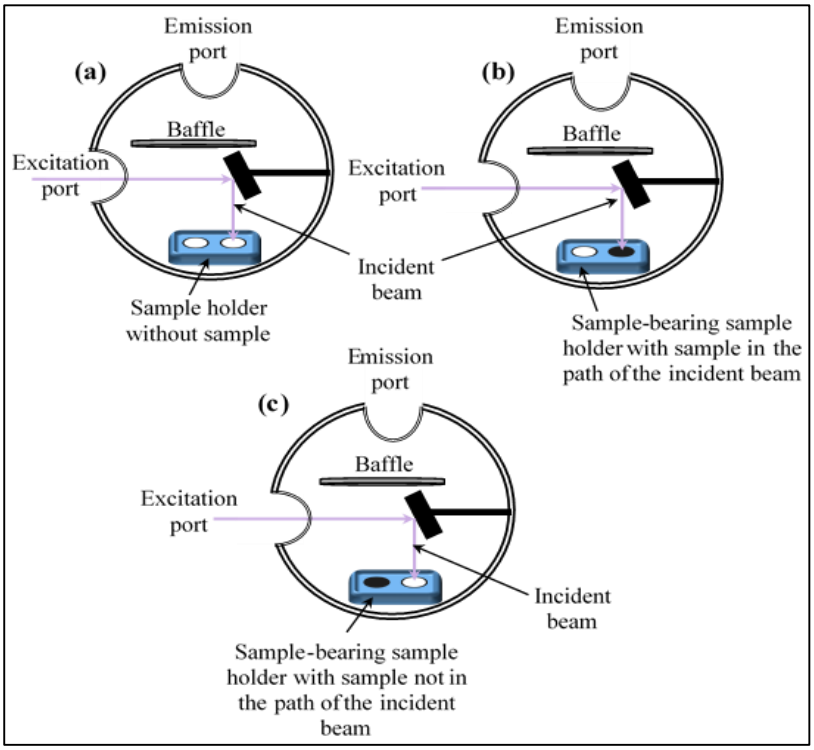

Fig. 9.2: Schematic diagram illustrating three different set-up required for the three-measurement approach, (a) no sample in the sphere, (b) sample in the sphere and in the path of the incident beam and (c) sample in the sphere but not in the path of the incident beam.

9.3. Results and discussion

The two-measurement approach

As shown in Fig. 9.1(a & b), the two measurement approach requires a measurement with an empty sphere and second measurement in which a sample in the integrating sphere is placed in the path of the incident beam. The QY were determined at two wavelengths, 235 nm (electronic transition from the O2p valence band to the La (5d6s) and Gd (5d6s) conduction bands [14, 15]) and 276 nm ($^8S_{7/2} \rightarrow {}^6I_J$ f–f intra configurational transitions of Gd^{3+} [16]). Fig. 9.3 shows the spectra scan for the two measurements approach. Fig. 9.3(a & b) was obtained from $LaGd_2SiO_5:Dy^{3+}$ (i.e. $x = 1$) under 235 and 276 nm excitations respectively, while Fig. 9.3(c & d) were obtained from $Gd_2SiO_5:Dy^{3+}$ (i.e. $x = 2$) under 235 and 276 nm respectively. Each spectrum in Fig. 9.3 can be divided into two regions: "*Ex*" denotes the spectral region for the incident light beam (which covers the excitation wavelength of the sample), "*Emi*" denotes the emission wavelength region [6]. Following the labelling in Fig. 9.1, we can define the following quantities: $Ex_{(a)}$ is the number of photons detected in the excitation wavelength region for the empty sphere measurement, $Ex_{(b)}$ is the number of photons detected in the excitation wavelength region for the measurement where there is a sample in the sphere and it is placed in the path of the beam. Furthermore, $Emi_{(a)}$ is the number of photons detected in the emission wavelength region for the empty sphere measurement, and $Emi_{(b)}$ is the number of photons detected in the emission wavelength region for the measurement where there is the sample in the sphere and it is placed in the path of the beam. From the terms defined above, the QY for the two-measurement approach can be defined by Eq. (9.1) [17]:

$$QY = \frac{Emi_{(b)} - Emi_{(a)}}{Ex_{(a)} - Ex_{(b)}} \tag{9.1}$$

Since the background in the emission wavelength region for the empty sphere measurement, $Emi_{(a)}$, is extremely low Eq. (9.1) can be written as:

$$QY = \frac{Emi_{(b)}}{Ex_{(a)} - Ex_{(b)}} \tag{9.2}$$

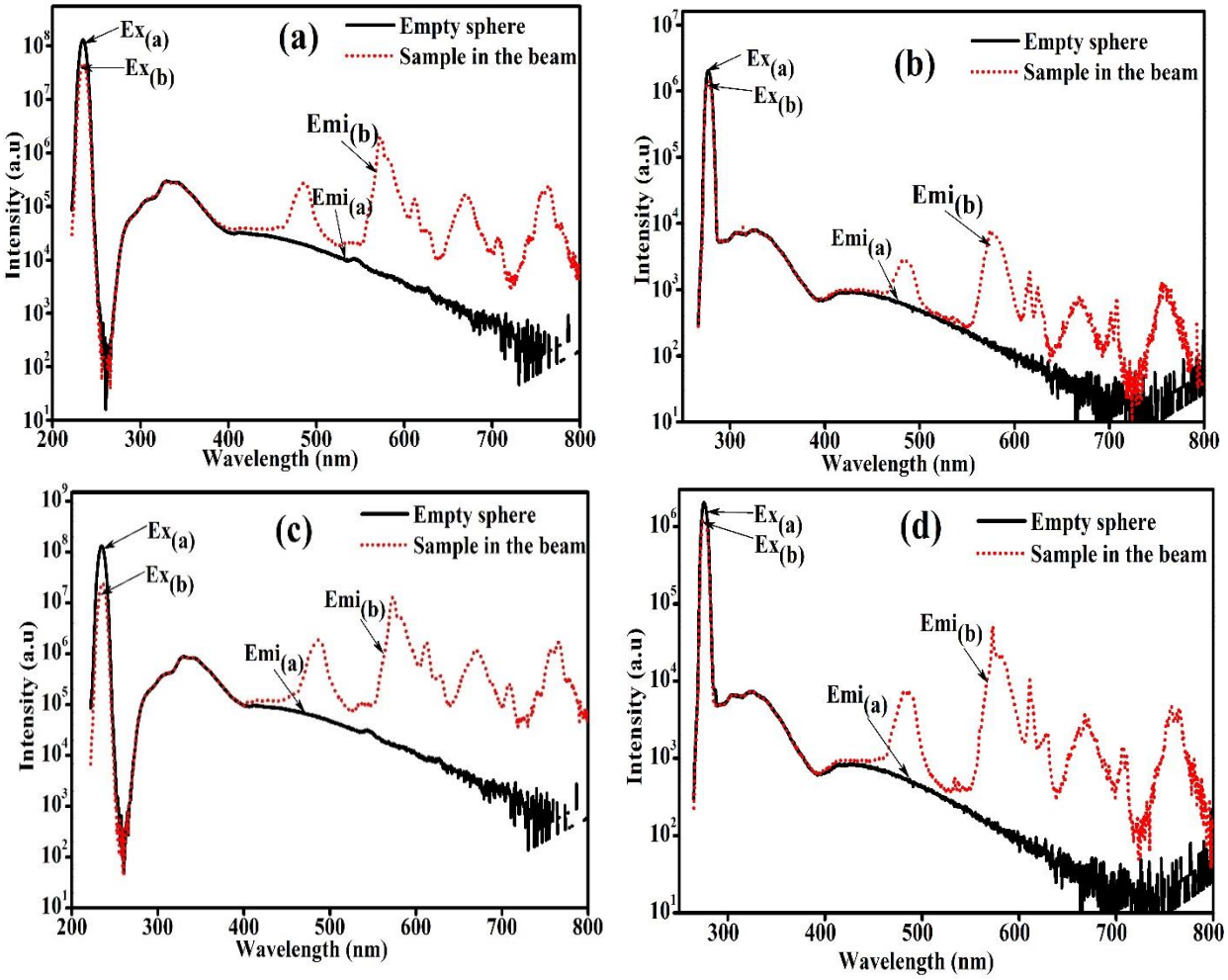

Fig. 9.3: The spectra scan for the two-measurement approach taken from; $LaGd_2SiO_5:Dy^{3+}$ (i.e. x = 1) under (a) 235 and (b) 276 nm excitations, $Gd_2SiO_5:Dy^{3+}$ (i.e. x = 2) under (a) 235 and (b) 276 nm excitations.

The three-measurement approach

By comparing Fig. 9.1 and 9.2, it can be seen that an extra experiment was added in Fig. 9.2 (a measurement with sample in the sphere but pleased out of the incident beam). Hence, we introduce two new terms $Ex_{(c)}$ and $Emi_{(c)}$ in Fig. 9.4, which denote the number of photons detected in the excitation and emission wavelength regions, respectively, in the measurement where there is a sample in the sphere but it is placed out of the path of the incident beam. Fig. 9.4(a & b) was obtained from $LaGd_2SiO_5:Dy^{3+}$ (i.e. x = 1) under 235 and 276 nm excitations respectively, while Fig. 9.4(c & d) were obtained from $Gd_2SiO_5:Dy^{3+}$ (i.e. x = 1) under 235 and 276 nm respectively.

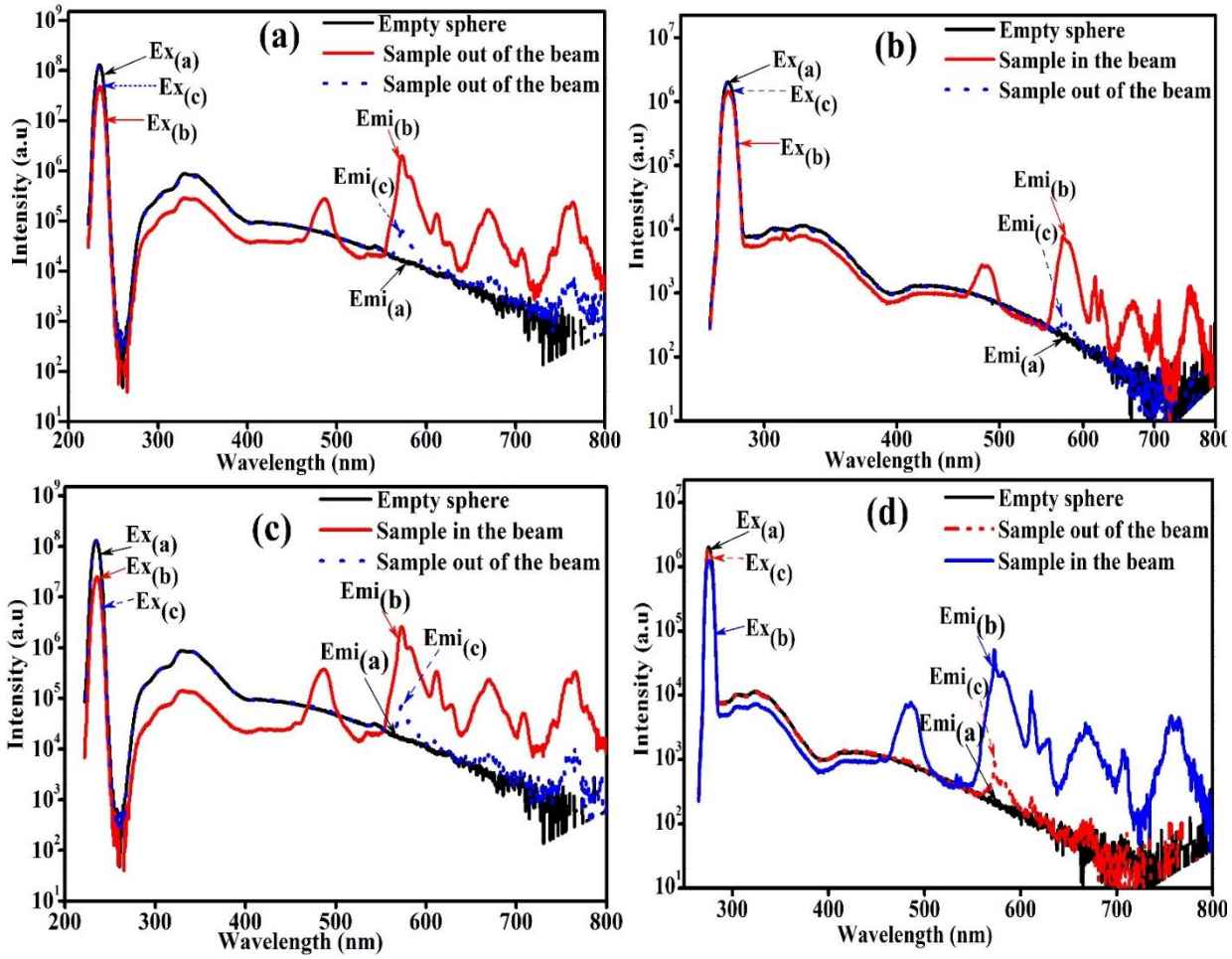

Fig. 9.4: The spectra scan for the three-measurement approach taken from; $LaGd_2SiO_5:Dy^{3+}$ (i.e. $x = 1$) under (a) 235 and (b) 276 nm excitations, $Gd_2SiO_5:Dy^{3+}$ (i.e. $x = 2$) under (a) 235 and (b) 276 nm excitations.

In the three-measurement approach, the QY can be determined using Eq. (9.3) [17]:

$$QY = \frac{Ex_{(b)}(Emi_{(c)} - Emi_{(a)}) - Ex_{(c)}(Emi_{(b)} - Emi_{(a)})}{Ex_{(a)}(Ex_{(b)} - Ex_{(c)})} \tag{9.3}$$

If the background in the emission wavelength region for the empty sphere measurement, $Emi_{(a)}$, is extremely low, Eq. (9.3) can be written as:

$$QY = \frac{Ex_{(b)}Emi_{(c)} - Ex_{(c)}Emi_{(b)}}{Ex_{(a)}(Ex_{(b)} - Ex_{(c)})} \tag{9.4}$$

The QYs were determined in this chapter using Eq. (9.1) and (9.3), and the values are shown in table 9.1.

Table 9.1: QY values for $La_{2-x}Gd_xSiO_5:Dy^{3+}$ (x = 0, 0.5, 1, 1.5 and 2).

$La_{2-x}Gd_xSiO_5:Dy^{3+}$	QY(%)			
	Two measurement approach		Three measurement approach	
	235 nm exc.	276 nm exc.	235 nm exc.	276 nm exc.
x = 0	0.6	-	0.5	-
x = 0.5	3	9.2	2.9	9.2
x = 1	5.9	7.2	6	7.5
x = 1.5	0.9	1.9	0.8	1.8
x = 2	6.5	22.4	6.5	22.4

9.4. Conclusion

The quantum yield (QY) of $La_{2-x}Gd_xSiO_5:Dy^{3+}$ (x = 0, 0.5, 1, 1.5 and 2) powder phosphors were determined using both the two and three-measurement approaches of the integrating sphere technique. Similar values of QY were obtained from the two approaches. Generally, the values of QY obtained when the samples were excited at 276 nm were greater than the values obtained under 235 nm excitation.

9.5. References

[1] K.N. Shinde, S.J. Dhoble, H.C. Swart, K. Park, Phosphate phosphors for solid-state lighting, Springer-Verlag Berlin, Heidelberg (2013) p. 44-48.

[2] S. Leyre, E.C. Gonzalez, J.J. Joos, J. Ryckaert, Y. Meuret, D. Poelman, P.F. Smet, G. Durinck, J. Hofkens, G. Deconinck, P. Haselaer, Rev. Sci. Instrum. 85 (2014) 123115.

[3] J.H. Brannon, D. Magde, J. Phys. Chem. 82 (1978) 705.

[4] E.P. Tomasini, E. San Román, S.E. Braslavsky, Langmuir 25 (2009) 5861.

[5] C. Würth, M. Grabolle, J. Pauli, M. Spieles, U. Resch-Genger, Nat. Protoc. 8 (2013) 1535.

[6] J.C. de Mello, H.F. Wittmann, R.H. Friend, Adv. Mater. 9 (1997) 230.

[7] L.O. Pålsson, A.P. Monkman, Adv. Mater. 14 (2002) 757.

[8] L. Porrès, A. Holland, L.O. Pålsson, A.P. Monkman, C. Kemp, A. Beeby, J. Fluoresc. 16 (2006) 267.

[9] A.R. Johnson, S.J. Lee, J. Klein, J. Kanicki, Rev. Sci. Instrum. 78 (2007) 096101.

[10] H. Ishida, S. Tobita, Y. Hasegawa, R. Katoh, K. Nozaki, Coord. Chem. Rev. 254 (2010) 2449.

[11] C. Würth, C. Lochmann, M. Spieles, J. Pauli, K. Hoffmann, T. Schüttrigkeit, T. Franzl, U. Resch-Genger, Appl. Spectrosc. 64 (2010) 733.

[12] N.C. Greenham, I.D.W. Samuel, G.R. Hayes, R.T. Phillips, Y.A.R.R. Kessener, S.C. Moratti, A.B. Holmes, R.H. Friend, Chem. Phys. Lett. 241 (1995) 89.

[13] P.S. Shaw, U. Arp, K.R. Lykke, Metrologia 46 (2009) S191.

[14] G. Li, C. Li, C. Zhang, Z. Cheng, Z. Quan, C. Peng, J. Lin, J. Mater. Chem. 19 (2009) 8936.

[15] M. Jia, J. Zhang, S. Lu, J. Sun, Y. Luo, X. Ren, H. Song, X. Wang, Chem. Phy. Lett. 384 (2004) 193.

[16] Y. Li, Y. Chang, Y. Chang, Y. Lin, C. Laing, J. Phys. Chem. C, 111 (2007) 10682.

[17] User guide for the FLS980 integrating sphere - Edinburgh instruments, Retrieved September, (2017) from https://www.edinst.com/wp-content/uploads/2016/02/FLS980-Series-Reference-Guide-Integrating-Sphere.pdf.

CH. 10

Summary, future work, presentations and list of publications

10.1. Summary

The result chapters of this thesis (chapter four to nine) are summarized in this section based on the findings discussed in each chapter.

In "*chapter four*", the properties of dysprosium doped mixed lanthanum gadolinium oxyorthosilicate ($La_{1.5}Gd_{0.5}SiO_5:Dy^{3+}$) thin films deposited on Si(111) substrates using the pulsed laser deposition (PLD) technique was studied. The films were deposited in different atmospheres (vacuum, argon (Ar) and oxygen (O_2)), at different deposition temperatures (50, 200, 300, 400 and 500 ºC) in O_2 and at 200 ºC in O_2 for 15, 30 and 50 min. The X-ray diffraction patterns preferentially showed two peaks, one from Gd_2SiO_5 and one from La_2SiO_5. The surface topography and particle morphology of the films were studied using atomic force microscopy (AFM) and field emission scanning electron microscope (FE-SEM). The Rutherford backscattering (RBS) spectra and the energy dispersive X-ray spectroscopy (EDS) spectra confirmed the presence of O, Si, La, Gd, and Dy in the films. The thickness of the films determined from the RBS data were in the micrometer range and changes with the substrate temperature and deposition atmosphere. The electronic states of the films were analysed using X-ray photoelectron spectroscopy (XPS). The photoluminescent (PL) excitation showed a prominent peak around 226 nm from which the emission spectra were measured. The emission spectra showed two prominent peaks at 488 and 578 nm due to f-f electronic transition of Dy^{3+}. The highest PL intensity was obtained from the film deposited in O_2 at the substrate temperature of 200 ºC.

"*Chapter five*" focused on the influence of post-deposition annealing on the structure, particle morphology and photoluminescence properties of the thin films studied in chapter four. The X-ray diffractometer results showed an improved crystallinity after post-annealing. The topography and morphology of the post-annealed films were studied using atomic force microscopy and field emission scanning electron microscopy respectively. The elemental composition in the surface

region of the films were analyzed using energy dispersive X-ray spectroscopy. The photoluminescence studies showed an improved luminescence after post-deposition annealing. The cathodoluminescence properties of the films were also reported. The CIE colour coordinates calculated from the photoluminescence and cathodoluminescence data suggested that the films could have potential application in white light emitting diode (LED) and field emission display (FED) applications.

"*Chapter six*" focused on the effect of the molar ratio of La and Y on the photoluminescence properties of Pr^{3+}. The molar ratio of La:Y were varied in the following manner: $La_{2-x}Y_xSiO_5$ (x = 0, 0.5, 1, 1.5, 2), where x = 0 representing La_2SiO_5, x = 2 representing Y_2SiO_5 and x = 0.5, 1, and 1.5 are the admixtures of the two compounds. The X-ray diffractometer results showed that the La_2SiO_5 and Y_2SiO_5 crystallized in their pure monoclinic phases, while their admixtures are both present in the same phase. The Burstein–Moss (BM) shift was used to explain the increase observed in the band gap after doping. The influence of the host crystal field on the branching ratios of the photoluminescence emission intensities of the $^3P_0$ and $^1D_2$ energy levels of Pr^{3+} were studied. The electronic transition from the $^3P_0$ transition dominated the emission spectra when x = 0, while the $^1D_2$ electronic transition dominated when x = 2. The variation in the branching ratios of the $^3P_0$ and $^1D_2$ emission with the change in the molar ratio of La:Y was assigned to $^3P_0 \rightarrow {}^1D_2$ non-radiative transitions, which increased with the crystal field of the host as the value of x increased (i.e., as the molar ratio of Y increases). Furthermore, it was shown that the $^3P_0$ emission lines emerged from Pr^{3+} ions occupying La1 and Y1 sites of La_2SiO_5 and Y_2SiO_5 respectively, while the $^1D_2$ emission lines emerged from Pr^{3+} ions occupying La2 and Y2 sites. The decay curve showed three lifetime components from both $^3P_0$ and $^1D_2$ emission lines, with the $^1D_2$ lines having higher lifetimes in all cases.

"In *chapter seven*", the influence of different excitation wavelength on the photoluminescence of co-doped Pr^{3+} and Dy^{3+} in $La_{2-x}Y_xSiO_5$ (x = 0, 0.5, 1, 1.5, 2) host was reported. 0.25% of both Pr^{3+} and Dy^{3+} where co-doped into pure and mixed lanthanum and yttrium rare-earth oxyorthosilicates phosphors and were synthesized using the urea-assisted combustion method. The XRD patterns showed the pure monoclinic phases of La_2SiO_5 (x = 0) and Y_2SiO_5 (x = 2) and mixed phases of

lanthanum and yttrium rare-earths oxyorthosilicates ($La_{2-x}Y_xSiO_5$, x = 0.5, 1 and 2). The diffuse reflectance spectral showed a broad absorption peak with a maximum around 376 nm assigned to $O^{2-} \rightarrow Pr^{4+}$ charge transfer band. The band gaps increased from 3.84 to 5.35 eV as the value of x increased from 0 to 2. The PL emission spectra showed tunable emission when monitored at different excitation wavelengths. When the emission was monitored by exciting at 223 and 229 nm, Pr^{3+} 4f5d$\rightarrow{}^1D_2$ transition (450 nm), emission from self-trapped excitons (STE) in SiO_2 and four emission line from Dy^{3+} ($^4F_{9/2}\rightarrow{}^6H_{15/2}$ (484 nm), $^4F_{9/2}\rightarrow{}^6H_{13/2}$, (573 nm), $^4F_{9/2}\rightarrow{}^6H_{11/12}$ (665 nm), and $^4F_{9/2}\rightarrow{}^6H_{9/2}$ (755 nm)) were observed. When the emission was monitored under 294 nm excitation, the STE and the four Dy^{3+} emission including emission from Pr^{3+} peaking at 540 nm ($^3P_0\rightarrow{}^3H_5$), 620, 630, 644 and 657 nm (four manifolds of $^1D_2\rightarrow{}^3H_4$), 715 nm ($^3P_0\rightarrow{}^3F_3$) and 750 nm ($^3P_0\rightarrow{}^3F_4$) were observed. The emission monitored under 349 nm excitation showed the STE peak and the four emission lines from Dy^{3+}. However, when the phosphors were excited using a 325 nm He-Cd laser, the STE emission and the four Dy^{3+} lines were observed in all the samples, but the four manifolds emission from the $^1D_2\rightarrow{}^3H_4$ transition of Pr^{3+} were only observed when x = 1.5 and 2. A possible mechanism of energy transfer from Pr^{3+} to Dy^{3+} was proposed. The International Commission on Illumination (CIE) coordinate diagram demonstrated tunable emission colours of the phosphors.

In "*Chapter eight*", the effect of post-annealing atmospheres on the optical properties of $La_{2-x}Y_xSiO_5$ phosphor powders co-doped with Pr^{3+} and Dy^{3+} were studied. The La to Y ratio was varied according to x = 0, 0.5, 1, 1.5 and 2, while the doping concentrations of Pr^{3+} and Dy^{3+} were fixed at 0.25 mol% of the La and Y. The phosphors were prepared using solution combustion synthesis. Each sample was divided into three parts: one was left as prepared, another was post-annealed in air and the last was annealed in 5% H_2 gas (in Ar). Annealing was performed at 950 ^oC for 1 h. The X-ray diffraction patterns showed that the as-prepared samples have larger full width at half maximum (FWHM) than the annealed samples. The elemental composition, oxidation states, and chemical and electronic states of the phosphors were determined using X-ray photoelectron spectroscopy. The band gap values determined from the diffuse reflectance spectra increased following the post-preparation annealing treatments. The band gap for the sample annealed in the reducing (Ar-H_2) atmosphere was larger than those annealed in air. The photoluminescence

intensities of the phosphors followed the same trend as the band gap values. The CIE colour coordinates of the phosphors showed tunable emission colours (blue, red and white) due to the La to Y ratio and the annealing. Two different cases for the photoluminescence mechanism are possible for the phosphors. In one case, the 4f5d energy level of Pr^{3+} lies below the conduction band of the host and energy transfer was observed from Pr^{3+} to Dy^{3+} via the overlapping 4f5d emission peak of Pr^{3+} and the $^4I_{15/2}$ excitation peak of Dy^{3+}. In the second case, the 4f5d energy level of Pr^{3+} lies very close to or inside the conduction band of the host and energy transfer was not observed. The influence of the La to Y ratio and the annealing on these possibilities are presented.

Lastly, in "*chapter nine*" the quantum yield (QY) of $La_{2-x}Gd_xSiO_5:Dy^{3+}$ (x = 0, 0.5, 1, 1.5 and 2) powder phosphors were determined using the integrating sphere technique. The QY was determined using different approaches−the two-measurement approach and the three-measurement approach. The two approaches produced similar results, but the value of the QY differs when the phosphors were excited at different wavelengths.

10.2. Future work

Luminescence efficiency of a phosphor material is of a major important when considering a material for practical purpose. Hence, our first concern would be to enhance the luminescence efficiency of selected samples. In chapter 5, it was observed that the films are not uniformly distributed on the surface of the substrate due to the formation of some large particulates (droplets) during deposition. To control the amount of these droplets, we will develop an off-axis PLD set-up. In this set-up, two additional substrate holders will be placed horizontally in the upper and lower sides of the on-axis substrate holder.

10.3. List of publications

i. **S.N. Ogugua**, S.K.K. Shaat, H.C. Swart, O.M. Ntwaeaborwa. Structure, Optical Properties and Elemental Analyses of Mixed rare earth oxyorthosilicate (R_2SiO_5, R = La, Gd and Y) doped Dy^{3+} nanophosphors. Journal of Physics and Chemistry of Solids 83 (2015) 109–116.

ii. **Simon N. Ogugua**, Hendrik C. Swart and Odireleng M. Ntwaeaborwa. White light emitting $LaGdSiO_5:Dy^{3+}$ nanophosphors for solid state lighting applications. Physica B 480 (2016) 131–136.

iii. **S.N. Ogugua**, S.K.K. Shaat, H.C. Swart, O.M. Ntwaeaborwa, The Influence of Dy^{3+} ions Concentration and Annealing on the Properties of $LaGdSiO_5:Dy^{3+}$ Nanophosphors, Journal of Luminescence 179 (2016) 154–164.

iv. **Simon N. Ogugua**, Raphael .L. Nyenge, Philip .T. Sechogela, Hendrik C. Swart, and Odireleng M. Ntwaeaborwa. The influence of deposition atmosphere and substrate temperature on the structure, morphology and photoluminescence of pulsed laser deposited $La_{0.5}Gd_{1.5}SiO_5:Dy^{3+}$. J. Vac. Sci. Technol. A 34 (2016) 021520-12.

v. **Ogugua, S.N.** Swart, H.C. Ntwaeaborwa, O.M. The dynamics of the photoluminescence of Pr^{3+} in mixed lanthanum yttrium oxyorthosilicate hosts, Sens. Actuators B, 250 (2017) 285–299.

vi. **Ogugua, S.N.** Swart, H.C. Ntwaeaborwa, O.M. The influence of post-deposition annealing on the structure, morphology and luminescence properties of pulsed laser deposited $La_{0.5}Gd_{1.5}SiO_5$ doped Dy^{3+} thin films, Physica B 535 (2018) 143-148.

vii. **Ogugua, S.N.** Swart, H.C. Ntwaeaborwa, O.M. The influence of post-annealing atmospheres on the optical properties and energy transfer between Pr^{3+} and Dy^{3+} in mixed lanthanum-yttrium oxyorthosilicate hosts. Opt. Mater. 76 (2018) 125-140.

Conference Presentations

i. The 9th African Laser Centre Student Workshop, University of Stellenbosch, 24 – 26 November, 2016.
Presentation topic: Structure, morphology and photoluminescence properties of pulsed laser deposited $La_{0.5}Gd_{1.5}SiO_5:Dy^{3+}$ thin films.

ii. Nanoscience Platform Symposium, School of Public Health, University of the Western Cape, 3 October, 2016.
Presentation topic: A novel tunable emission from dysprosium (Dy^{3+}) doped rare earth oxyorthosilicates, (R_2SiO_5, R = La, Gd, Y) nanophosphors for LED application.

iii. The 7th South African Conference on Photonic Materials, Amanzi Private Game Reserve, 27 - 31 March, 2017.
Presentation topic: Photoluminescent dynamics of Pr^{3+} and Dy^{3+} in R_2SiO_5 (R = La, Y) hosts.

iv. The 10th African Laser Centre Student Workshop, University of Stellenbosch, 30 November–2nd December 2017.
Presentation topic: Influence of post-annealing atmosphere on the optical properties and energy transfer between Pr^{3+} and Dy^{3+} in mixed lanthanum-yttrium oxyorthosilicates.

Awards

i. VACUTEC MSc Student award, 2015: Most outstanding work in the field of condensed matter physics and/or material science by a student, based on a publication in a scientific journal originating from a master dissertation submitted at a South African Institution for Tertiary Education.

ii. An outstanding poster award, Mabula 2015: An outstanding poster presented at the 6th South African Conference on Photonic Materials held at Mabula Game Lodge 4-8 May 2015.